Application of ultrasound for enhanced delivery of biological therapeutics into solid tumours

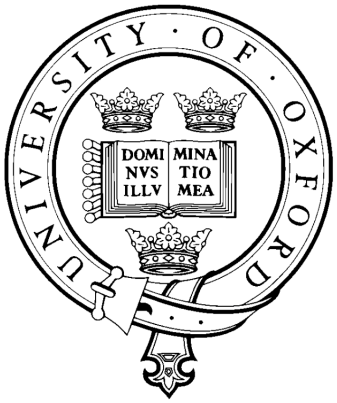

Megan C. Grundy

St John's College

University of Oxford

Supervised by
Professor Robert Carlisle

Submitted: 5th October 2018

A thesis submitted for the degree of Doctor of Philosophy in Engineering Science

Abstract

Drug development for cancer is heading towards increased use of highly-targeted and complex biological therapeutics. As the complexity and costs of drug development increase, the importance of ensuring good tumoural delivery and distribution of these drugs is paramount.

The tumour microenvironment, which possesses many characteristics distinguishing it from healthy tissue, presents both challenges to and opportunities for drug delivery. Countless novel nanoscale formulations or reformulations of existing drugs have been created to harness the potential of the 'enhanced permeability and retention' of tumours. The scale of this effect has, however, come under recent scrutiny, and a clear role for alternative delivery mechanisms has emerged.

Ultrasound-mediated cavitation has been evaluated as a non-invasive external stimulus to improve delivery of drugs to solid tumours. Cavitation nuclei can be used to seed cavitation at relatively low pressures to achieve cavitation levels capable of enabling enhanced drug transport, without safety concerns, suggesting a path for clinical translation.

In this thesis, the effects of ultrasound-mediated cavitation on the delivery of a range of therapeutic drug classes to solid tumours was investigated: a cancer-targeting antibody (cetuximab), an actively targeted nanoparticle (cetuximab-GNP), and an oncolytic virus (ColoAd). Two classes of cavitation nuclei were employed: a microbubble ultrasound contrast agent (SV) and sonosensitive gas-entrapping nanoparticles (SSPs).

Ultrasound-mediated cavitation was shown to enhance the delivery of all therapeutics tested here, though the scale of the effect varied. Cavitation activity achieved with SV or SSPs in vivo showed different characteristics, with SSPs demonstrating more sustained cavitation. Delivery of a long-circulating antibody was significantly more enhanced with SSPs than with SV, but the two cavitation nuclei provided a comparable benefit to the shorter-circulating targeted nanoparticle and oncolytic virus. Furthermore, site-specific density-modification of ColoAd was investigated, in an attempt to further enhance its cavitation-mediated transport, though the conclusion of this work was that the proposed modification strategy was not viable.

The work presented in this thesis highlights the challenge of achieving effective tumoural delivery of systemically administered biological therapeutics, and provides compelling evidence for the further investigation of ultrasound-mediated cavitation as an effective tool for enhancing the delivery of biological therapeutics into tumours.

Statement of Originality

I hereby declare that this submission is my own work and, to the best of my knowledge, it contains no materials previously published or written by another person, or substantial proportions of material which have been accepted for the award of any other degree or diploma at the University of Oxford or any other educational institution, except where due acknowledgement is made in the thesis. Any contribution made to the research by others, with whom I have worked at the University of Oxford or elsewhere, is explicitly acknowledged in the thesis. I also declare that the intellectual content of this thesis is the product of my own work, except to the extent that assistance from others in the project's design and conception or in style, presentation and linguistic expression is acknowledged.

Megan Grundy
October 2018

Acknowledgements

This thesis was made possible by the kindness and support of many people. Firstly, I would like to thank my supervisor Prof. Robert Carlisle for his guidance and patience over the last four years. I am also extremely grateful for the unofficial supervision and mentorship I have received from Prof. Constantin Coussios.

The entire BUBBL group has been wonderful in so many ways, and I count myself extremely fortunate to have completed my DPhil project within this reseach group. In particular I would like to thank Dr. Luca Bau for his unwavering support and guidance – it is quite a feat to have convinced someone with a fear of chemicals to undertake a project in organic chemistry. I would also like to thank Dr. Christophoros Mannaris for being a calm presence during stressful experiments, Claudia Hill for brightening up long lab days, and the entire Seymour group from the Dept. of Oncology – particularly Dr. Margaret Duffy, Dr. Brian Lyons and Egon Jacobus.

I am very grateful to my family back in Canada for their continued long-distance support and encouragement. I would like to in particular thank Joey, whose attempts to explain what my DPhil project is about to others have brought me lots of joy. This thesis would not have been possible without his love and support.

Finally, I would like to thank the Clarendon Fund and OxCD3 for sponsoring my research. PsiOxus Therapeutics and OxSonics Ltd are gratefully acknowledged for the provision of ColoAd and SSPs respectively, and for advice on assays.

Statement of Contributions

I gratefully acknowledge the following who contributed to the research presented in this thesis.

Chapter 3

- Dr. Luca Bau: Contributed significantly to development of a protocol for the synthesis of heterobifunctional PEG linker. Conducted ^{1}H-NMR analysis of all products, and advised on organic and bio-chemistry related topics.
- Dr. Brian Lyons: Acquired TEM images of nanoparticle constructs.

Chapter 4

- Dr. Daniel Lunn and Dr. Luca Bau: Contributed to development of the method used for statistical analysis of in vivo bilateral tumour experiments (also in Chapter 5).
- Catherine Paverd: Operated the US setup for in vivo experiments presented in this chapter.
- Prof. Robert Carlisle: Performed intravenous dosing of mice for in vivo US experiments.
- Sheena Wallington: Performed intravenous dosing and blood sampling of mice for in vivo pharmacokinetic studies.

Chapter 5

- James Fisk: Fabricated tissue-mimicking phantom holder.
- Dr. Christophoros Mannaris and Dr. Margaret Duffy: Collaborated on in vitro investigations of delivery of ColoAdRFP.
- Dr. Christophoros Mannaris and Claudia Hill: Operated the US setup for in vivo experiments presented in this chapter.
- Prof. Robert Carlisle: Performed intravenous dosing of mice for in vivo ultrasound experiments.
- Egon Jacobus: Assisted with interpretation of IHC sections.

Chapter 6

- Dr. Brian Lyons: Optimized HPLC method for analysis of GNP modified viruses, and assisted with chromatographic analysis conducted in this chapter.

Dissemination

Publications

Mannaris, C., Bau, L., **Grundy, M.,** Gray, M., Lea-Banks, H., Seth, A., Teo, B., Carlisle, R., Stride, E., Coussios, C-C. (2018) Microbubbles, nanodroplets and gas-stabilizing solid particles for ultrasound-mediated extravasation of unencapsulated drugs; an exposure parameter optimization study. *Ultrasound in Medicine and Biology*, accepted for publication Oct 31, 2018

Myers, R., **Grundy, M.,** Rowe, C., Coviello, C., Bau, L., Erbs, P., Foloppe, J., Balloul, J-M., Story, C., Coussios, C., Carlisle, R. (2017) Ultrasound-mediated cavitation does not decrease the activity of small molecule, antibody or viral-based medicines. *International Journal of Nanomedicine*, 13, 337-349

Grundy, M., Coussios, C., Carlisle, R. (2016) Advances in systemic delivery of anti-cancer agents for the treatment of metastatic cancer. *Expert Opinion on Drug Delivery*, 13(7), 999-1013
*Portions of this publication appear in Chapter 1 of this thesis.

Conference Presentations

Grundy, M., Mannaris, C., Hill, C., Jacobus, E., Duffy, M., Lyons, B., Seymour, L., Coussios, C., Carlisle, R. (2018, April) Ultrasound-mediated cavitation enhances the delivery of enadenotucirev into tumours. *Poster presented at the 11th International Oncolytic Virus Conference, Oxford, UK*

Grundy, M., Lea-Banks, H., Mannaris, C., Duffy, M., Coussios, C., Carlisle, R. (2016, September) Ultrasound enhanced delivery of a density modified oncolytic virus. *Presented at the meeting of MEIBioEng 16, Oxford, UK*

Contents

1 Introduction and literature review **1**
1.1 Delivery challenge . . . 1
1.1.1 Physical properties of tumour microenvironments . . . 1
1.1.2 Passive targeting . . . 2
1.1.3 Active targeting . . . 5
1.1.4 External stimuli . . . 8
1.2 Biological therapeutics . . . 8
1.2.1 Antibodies . . . 8
1.2.2 Antibody-drug conjugates . . . 11
1.2.3 BiTEs (Bi-specific T cell Engagers) . . . 12
1.2.4 ImmTAC (Immune Mobilizing Monoclonal T cell receptors Against Cancer) . . . 14
1.2.5 Virotherapy . . . 16
1.2.6 Oncolytic viruses . . . 16
1.2.7 Cell-based therapies . . . 20
1.3 Ultrasound for drug delivery . . . 22
1.3.1 Overview . . . 22
1.3.2 Propagation in tissue . . . 22
1.3.3 Therapeutic ultrasound . . . 24
1.3.4 Acoustic cavitation . . . 24
1.3.5 Ultrasound for enhanced drug delivery . . . 25
1.4 Implications for current work . . . 27

2 Methods and materials **30**
2.1 Formulation of heterobifunctional PEG linker . . . 30
2.1.1 Synthesis . . . 30
2.1.2 Purification and deprotection . . . 31
2.1.3 Proton nuclear magnetic resonance spectroscopy . . . 32
2.1.4 TNBS assay for determination of hydrazide concentration . . . 32
2.2 PEGylation of therapeutic antibodies . . . 33
2.2.1 Quantification of aldehydes post-oxidation . . . 34
2.2.2 SDS-PAGE analysis of PEGylated antibodies . . . 35
2.2.3 ELISA analysis of PEGylated antibodies . . . 36
2.2.4 Chromatographic analysis of PEGylated cetuximab . . . 37
2.3 Functionalization and characterization of GNPs . . . 38
2.3.1 Functionalization with PEGylated cetuximab . . . 38
2.3.2 Purification . . . 39
2.3.3 UV-Vis spectroscopy . . . 39
2.3.4 Sizing by DLS . . . 39
2.3.5 TEM imaging . . . 40
2.3.6 SDS-PAGE analysis of cetuximab loading . . . 40

2.3.7 Quantification of cetuximab loading . . . 40
2.4 In vitro characterization of cetuximab-loaded GNPs . . . 41
2.4.1 Cell culture . . . 41
2.4.2 Determination of EGFR expression by flow cytometry . . . 41
2.4.3 Determination of cetuximab binding by flow cytometry . . . 42
2.4.4 Inhibition of EGF binding analysed by flow cytometry . . . 42
2.5 In vivo model for delivery of cetuximab and cetuximab-GNPs . . . 43
2.5.1 Subcutaneous tumour innoculation . . . 43
2.5.2 Animal tumour and welfare monitoring . . . 43
2.6 Determination of circulation kinetics of cetuximab and cetuximab-GNPs . . . 43
2.6.1 Dosing . . . 43
2.6.2 Blood and tissue sampling . . . 44
2.6.3 ELISA for quantification of cetuximab and cetuximab-GNPs . . . 44
2.6.4 Stability of cetuximab-GNPs in plasma . . . 45
2.7 US treatment of tumours . . . 46
2.7.1 US set-up and parameters . . . 46
2.7.2 Dosing with cetuximab/cetuximab-GNPs and US treatment . . . 47
2.7.3 ELISA for quantification of cetuximab/cetuximab-GNPs . . . 48
2.8 In vitro delivery of ColoAd . . . 48
2.8.1 In vitro tissue-mimicking phantom . . . 48
2.8.2 In vitro US setup . . . 49
2.8.3 Analysis of PCD data . . . 51
2.8.4 Microscopy and image analysis . . . 51
2.9 In vivo model for delivery of ColoAd . . . 52
2.9.1 Subcutaneous tumour innoculation . . . 52
2.10 US treatment of tumours . . . 52
2.10.1 US set-up and parameters . . . 52
2.11 IVIS imaging of luciferase production . . . 53
2.12 Ex vivo tumour processing . . . 53
2.12.1 Analysis of luciferase content . . . 53
2.12.2 qPCR analysis of genome copies . . . 54
2.12.3 Immunohistochemistry . . . 54
2.13 Characterization of anti-ColoAd antibodies . . . 55
2.13.1 Western blot analysis . . . 55
2.13.2 Dot blot analysis . . . 56
2.13.3 Infectivity assay . . . 56
2.13.4 ELISA analysis of affinity of ColoAd antibodies . . . 57
2.14 Functionalization and characterization of NHS-GNPs . . . 58
2.14.1 Purification of functionalized GNPs . . . 58
2.14.2 UV-Vis . . . 58
2.14.3 Dot blot analysis . . . 58
2.15 Characterization of antibody-GNP + ColoAd . . . 59
2.15.1 Dot blot test of antibody binding in CsCl and glycerol . . . 59
2.15.2 CsCl density gradient . . . 59
2.15.3 ELISA analysis of affinity in high ionic strength solutions . . . 60

2.15.4 Chromatographic analysis of ColoAd + GNPs 61
2.16 PEGylation of anti-ColoAd antibodies 62
2.16.1 SDS-PAGE analysis 62
2.17 GNP functionalization and characterization 62
2.17.1 UV-Vis 63
2.17.2 SDS-PAGE analysis of antibody loading 63
2.18 Characterization of antibody-PEG-GNP + ColoAd 63
2.18.1 Chromatographic analysis of ColoAd + antibody-PEG-GNPs 63
2.19 Statistical methods 63
2.20 Schematics 64

3 Development and characterization of targeted gold nanoparticles 65
3.1 Formulation of PEG linker 66
3.2 Characterization of PEG linker 70
3.2.1 Reaction monitoring with ^{1}H-NMR 70
3.2.2 TNBS assay for hydrazide content 72
3.3 PEGylation of therapeutic antibodies 73
3.3.1 Lucifer yellow assay 73
3.3.2 Characterization of impact of oxidation on structure and function of antibodies 76
3.4 PEGylation of cetuximab 83
3.4.1 SDS-PAGE analysis of PEGylated cetuximab with PEG staining 83
3.4.2 Chromatographic analysis of PEGylated cetuximab 85
3.5 Functionalization and characterization of GNPs 87
3.5.1 Physical characterization 87
3.5.2 Loading of cetuximab 91
3.5.3 Bioeffect of cetuximab-GNPs 94
3.6 Summary and discussion 97

4 In vivo assessment of cavitation-mediated delivery of antibodies and targeted nanoparticles 100
4.1 Circulation kinetics and tumour accumulation 100
4.1.1 Circulation kinetics of cetuximab and cetuximab-GNPs 101
4.1.2 Passive accumulation of cetuximab and cetuximab-GNPs . . . 104
4.1.3 Plasma stability 106
4.2 Tumoural delivery with US-mediated cavitation 108
4.2.1 Experimental design 109
4.2.2 Statistical analysis 112
4.2.3 Acoustic feedback 113
4.2.4 Quantification of tumoural delivery 116
4.2.5 Relationship between PAM and delivery of cetuximab 120
4.3 Summary and discussion 122

5 In vitro and in vivo assessment of cavitation-mediated delivery of an oncolytic adenovirus 127
5.1 In vitro delivery of ColoAd with US-mediated cavitation 128
5.1.1 Agar tissue-mimicking model 128

5.1.2 Experimental design . . . 128
5.1.3 Delivery of ColoAd with 0.5 MHz US . . . 130
5.1.4 Delivery of ColoAd with 1.6 MHz US . . . 134
5.2 In vivo delivery of ColoAd with US-mediated cavitation . . . 140
5.2.1 Experimental design . . . 141
5.2.2 Statistical analysis . . . 143
5.3 Tumoural delivery of ColoAd with US-mediated cavitation: Regime 1 144
5.3.1 Acoustic feedback . . . 145
5.3.2 Tracking of ColoAd infection . . . 147
5.4 Tumoural delivery of ColoAd with US-mediated cavitation: Regime 2 156
5.4.1 Acoustic feedback . . . 156
5.4.2 Tracking of ColoAd infection . . . 158
5.4.3 Immunohistochemistry . . . 162
5.5 Summary and discussion . . . 165

6 Development and evaluation of a method for modifying the density of an oncolytic adenovirus 170
6.1 Proposed design . . . 171
6.2 Characterization of anti-ColoAd antibodies . . . 173
6.2.1 Specificity of anti-ColoAd antibodies . . . 173
6.2.2 Effect of anti-ColoAd antibodies on infectivity of ColoAdRFP 176
6.2.3 Relative affinities of anti-ColoAd antibodies . . . 178
6.3 Functionalization and characterization of NHS-GNPs . . . 179
6.3.1 Dot blot analysis of antibody-GNP loading . . . 181
6.4 Characterization of GNP + ColoAd constructs . . . 182
6.4.1 Density analysis of GNP + ColoAd constructs: CsCl gradient 182
6.4.2 Chromatographic analysis of ColoAd + GNPs . . . 188
6.5 Functionalization of GNPs with site-specifically PEGylated anti-ColoAd antibody . . . 196
6.5.1 PEGylation of anti-ColoAd antibodies . . . 196
6.6 Functionalization and characterization of GNPs . . . 198
6.6.1 UV-Vis . . . 199
6.6.2 SDS-PAGE analysis of antibody-PEG-GNP loading . . . 200
6.7 Characterization of GNP + ColoAd constructs . . . 201
6.7.1 Chromatographic analysis of GNP + ColoAd constructs . . . 201
6.8 Summary and discussion . . . 206

7 Conclusions and Future Work 211
7.1 Summary of findings and conclusions . . . 211
7.1.1 Development and characterization of targeted gold nanoparticles 212
7.1.2 In vivo assessment of cavitation-mediated delivery of antibodies and targeted nanoparticles . . . 215
7.1.3 In vitro and in vivo assessment of cavitation-mediated delivery of an oncolytic adenovirus . . . 217
7.1.4 Development and evaluation of a method for modifying the density of an oncolytic adenovirus . . . 221
7.2 Future work . . . 222

List of Figures

1.1 Three different methods for enhancing drug delivery or uptake for cancer therapy . . . 7
1.2 Therapeutic classes investigated in this thesis for delivery with US-mediated cavitation . . . 28

3.1 Schematic of functionalization of GNPs with antibodies via site-specific PEG linker . . . 67
3.2 Heterobifunctional PEG linker to site-specifically conjugate antibodies to GNPs . . . 68
3.3 Overview of reaction to synthesize LA-PEG-Hyd-Boc from LA-PEG-COOH . . . 69
3.4 Deprotection of LA-PEG-Hyd-Boc with trifluoroacetic acid (TFA) to give LA-PEG-Hyd . . . 70
3.5 ^{1}H-NMR Spectra of LA-PEG-COOH, LA-PEG-Hyd-Boc, and LA-PEG-Hyd in $CDCl_3$ . . . 71
3.6 Absorbance (500 nm) of product of the reaction of acethydrazide with TNBS over time . . . 72
3.7 Absorbance of LYCH and antibody at wavelengths of 280 and 428 nm. 75
3.8 SDS-PAGE characterization of oxidized and PEGylated cetuximab and trastuzumab . . . 78
3.9 Indirect ELISA analysis of cetuximab and trastuzumab binding to EGFR or HER2 respectively . . . 81
3.10 SDS-PAGE with Coommassie and barium iodide staining for characterization of PEGylated antibodies . . . 84
3.11 Chromatographic analysis of cetuximab, oxidized cetuximab, and PEGylated cetuximab . . . 86
3.12 Absorbance spectrum of GNPs functionalized with cetuximab-PEG-LA and capped with mPEG-SH, and bare GNPs after resuspension in PBS . . . 88
3.13 Sizing of GNPs with dynamic light scattering . . . 90
3.14 TEM of non-modified, mPEG-coated, and mPEG + cetuximab-PEG coated GNPs. . . . 91
3.15 SDS-PAGE characterization of cetuximab-PEG-GNP conjugates . . . 93
3.16 Binding of fluorescent EGF to MCF-7 or MDA-MB-468 cells. . . . 94
3.17 Binding of cetuximab or cetuximab-PEG-LA to MDA-MB-468 cells. . 95
3.18 Inhibition of EGF binding to MDA-MB-468 cells by cetuximab . . . 96
3.19 Inhibition of EGF binding to MDA-MB-468 cells by cetuximab-GNPs 97

4.1 Binding of fluorescent EGF to HT-29 or MDA-MB-468 cells . . . 101
4.2 Plasma concentration of cetuximab over time . . . 102
4.3 Plasma concentration of cetuximab-GNPs over time . . . 104

4.4 Concentration of free cetuximab in cetuximab-GNP samples incubated with whole plasma . . . 107
4.5 Schematic of in vivo US setup . . . 109
4.6 Acoustic data acquired during US treatment of tumour-bearing mice with cetuximab or cetuximab-GNPs + SV or + SSPs . . . 113
4.7 Quantification of acoustic data acquired during US- treatment of tumour-bearing mice dosed with cetuximab + CN or cetuximab-GNPs + CN . . . 115
4.8 Quantification of US-mediated tumour accumulation of cetuximab . . 116
4.9 Quantification of US-mediated tumour accumulation of cetuximab-GNPs . . . 119
4.10 Linear mixed effects model of tumour cetuximab concentration as a function of CN type and cumulative PAM magnitude of cavitation . . 121

5.1 Schematic diagram of the in vitro US exposure setup for testing delivery of ColoAdRFP . . . 129
5.2 Frequency power spectra of acoustic emissions from channels within cell-embedded gel exposed to US at 0.5 MHz and PRFPs 2 - 2.7 MPa. 131
5.3 Brightfield and fluorescence microscopy of cell-embedded gels after delivery of ColoAdRFP + SSPs with US exposure . . . 132
5.4 Brightfield and fluorescence microscopy of cell-embedded gels after delivery of ColoAdRFP + SSPs with US exposure . . . 133
5.5 Frequency power spectra of acoustic emissions from channels within cell-embedded gel exposed to US at 1.6 MHz and peak rarefactional pressures of 3.5 MPa . . . 135
5.6 Brightfield microscopy of channel within agar gel after delivery of ColoAdRFP with US . . . 136
5.7 Fluorescence microscopy of RFP-expression after delivery of ColoAdRFP + SSPs to a cell-embedded gel with and without US exposure . 137
5.8 Quantification of RFP-expression after delivery of ColoAdRFP + SSPs to a cell-embedded gel with and without US exposure . . . 139
5.9 Quantification of RFP-expression after delivery of ColoAdRFP to a cell-embedded gel without US but with SSP or with US but without SSPs . . . 140
5.10 Acoustic data acquired during US- treatment of tumour-bearing mice with ColoAd + SV or SSPs or iSSPs . . . 145
5.11 Quantification of acoustic data acquired during US- treatment of tumour-bearing mice dosed with ColoAd and CN. . . . 146
5.12 Photographs of US-exposed tumours post-treatment with SV, SSPs or iSSPs . . . 147
5.13 In vivo imaging of luciferase expression in tumour-bearing mice . . . 148
5.14 Quantification of in vivo luciferase production over 6 days using IVIS imaging . . . 149
5.15 Quantification of in vivo luciferase production 6 days post-treatment using IVIS imaging . . . 150

5.16 Ex vivo quantification of luciferase and viral genome copies 6 days post-treatment . . . 153
5.17 Acoustic data acquired during US- treatment of tumour-bearing mice with ColoAd + SSPs . . . 157
5.18 Quantification of acoustic data acquired during US- treatment of tumour-bearing mice with ColoAd and CN . . . 157
5.19 Quantification of in vivo luciferase production over 11 days using IVIS imaging . . . 158
5.20 Quantification of in vivo luciferase production 11 days post-treatment using IVIS imaging . . . 159
5.21 Ex vivo quantification of luciferase and viral genome copies 11 days post-treatment . . . 161
5.22 Representative sections of tumours stained for vasculature and viability 163
5.23 Section of tumour showing positive staining for hexon . . . 164

6.1 Schematic of proposed surface modification (1) of ColoAd with GNPs 172
6.2 Schematic of proposed surface modification (2) of ColoAd with GNPs 173
6.3 Western blot analysis of antibody binding to ColoAd . . . 174
6.4 Dot blot analysis of antibody binding to ColoAd. . . . 175
6.5 Impact of MAB8052 : ColoAd and ab7428 : ColoAd ratio on ability of ColoAdRFP to infect A549 cells . . . 176
6.6 Indirect ELISA analysis of ab7428 and MAB8052 binding to immobilized ColoAd . . . 178
6.7 UV-Vis absorbance spectrum of NHS-coated GNPs functionalized with ab7428 . . . 180
6.8 Dot blot analysis of antibody-functionalized GNPs . . . 182
6.9 Dot blot analysis of ab7428 binding to ColoAd in the presence of DPBS, CsCl, or glycerol . . . 183
6.10 CsCl density gradient ultracentrifugation of antibody-functionalized GNPs and ColoAd virus . . . 185
6.11 Indirect ELISA analysis of ab7428 binding to immobilized ColoAd in PBS, CsCl, or glycerol . . . 187
6.12 HPLC analysis of ColoAd and Ad5 . . . 189
6.13 HPLC analysis of ColoAd and GNPs . . . 190
6.14 Indirect ELISA analysis of ab7428 binding to immobilized ColoAd in PBS, or HPLC mobile phase. . . . 191
6.15 HPLC analysis of ColoAd and GNPs . . . 193
6.16 UV-Vis spectrum of peaks of ColoAd and GNPs separated by anion-exchange HPLC . . . 195
6.17 SDS-PAGE and Coommassie/barium iodide staining characterization of PEGylated antibodies . . . 197
6.18 UV-Vis absorbance spectrum of GNPs functionalized with LA-PEG-ab7428 and capped with mPEG-SH . . . 199
6.19 SDS-PAGE and silver staining characterization of antibody-PEG-GNP conjugates . . . 200
6.20 HPLC analysis of ColoAd and GNPs . . . 202

6.21 UV-Vis spectrum of peaks of ColoAd and GNPs separated by anion-exchange HPLC 203
6.22 HPLC analysis of ColoAd and GNPs 204
6.23 UV-Vis spectrum of peaks of ColoAd and GNPs separated by anion-exchange HPLC 206

Abbreviations

- Ad5: Adenovirus type 5
- ADC: Antibody drug conjugate
- BBB: Blood brain barrier
- CMV: Cytomegalovirus
- CN: Cavitation nuclei
- DC: Duty cycle
- DLS: Dynamic light scattering
- EGFR: Epidermal growth factor receptor
- ELISA: Enzyme-linked immunosorbent assay
- EM Means: Estimated marginal means
- EPR: Enhanced permeability and retention
- GNP: Gold nanoparticle
- HIFU: High intensity focused ultrasound
- HRP: Horseradish peroxidase
- IC: Isotype control
- ID: Injected dose
- IFP: Interstitial fluid pressure
- IHC: Immunohistochemistry
- IVIS: In vivo imaging system
- mAb: monoclonal antibody
- MWCO: Molecular weight cut-off
- NHS: N-hydroxysuccinimide
- PAM: Passive acoustic mapping
- PCD: Passive cavitation detector
- PEG: Polyethylene glycol
- PK: Pharmacokinetics

- PRFP: Peak rarefactional focal pressure
- RFP: Red fluorescent protein
- RT: Room temperature
- SA: Splice acceptor
- SDS-PAGE: Sodium-dodecyl sulfate polyacrylamide gel electrophoresis
- SSPs: Sonosensitive particles
- SV: Sonovue
- TEM: Transmission electron microscopy
- UCA: Ultrasound contrast agent
- US: Ultrasound

Chapter 1

Introduction and literature review

1.1 Delivery challenge

The complex biology of cancer gives rise to a number of challenges to successful therapy. A complete understanding of the physiology behind these challenges will be crucial to overcoming them. The following section will focus on the physical aspects of cancer biology that make treatment difficult: specifically, the mechanical properties of solid tumours compared to healthy tissue, and their implications for drug delivery.

1.1.1 Physical properties of tumour microenvironments

Growing tumours co-opt existing blood vessels and over-express pro-angiogenic factors to induce the creation of new vasculature [1, 2]. Tumour microvasculature is markedly different from that of healthy tissue. Comparatively, tumour microvasculature is heterogeneously organized and sized, tortuous, and often 'leaky', due to irregular endothelial cell deposition, and absence of pericytes and a compromised basement membrane [1, 3, 4, 5]. This leakiness contributes to the elevated interstitial fluid pressure (IFP) found in tumours (reviewed in [6]), which can match the 20-25 mmHg pressure within capillaries [7]. In addition to an irregular microvasculature, tumours often present with non-functional lymphatics (abnormal or absent) [8]. The lack of functional lymphatic vessels leads to poor fluid drainage from the tumour, thereby adding to the elevated IFP, which contributes in turn to decreased transcapillary flow [6]. An abnormal tumoural extracellular matrix composition also creates resistance to transcapillary flow [9]. Given these barriers to convective flow out of

capillaries and into and through tumours, delivery of molecules to cells within tumours relies more heavily on diffusion than it does in healthy tissue [7, 10]. Finally, in healthy tissue, all cells are located within ∼100 micrometres of a blood vessel, whereas in tumours, this distance can be considerably greater [11, 12]. When taken together, the increased distance between cells and blood vessels and the abnormal tumoural blood flow result in regions of hypoxia and low pH within tumours [13, 14]. These regions are not only the hardest to deliver therapy to, but are also implicated as the location of cancer stem cells and the site of the epithelial-to-mesenchymal (EMT) transition process [15].

As the tumour microenvironment differs vastly from healthy tissue, it is unrealistic to treat the case of drug delivery to a solid tumour as one would treat drug delivery to typical healthy tissue [11, 16]. Primeau et al. showed in murine tumours, as well as in human cancer xenografts in mice, that when doxorubicin (a commonly-used 'first-line' anticancer drug) is administered with a single intravenous (i.v.) injection, many tumour cells (particularly those in regions of hypoxia) are not even exposed to the drug. Indeed, concentration of drug decreased exponentially with distance from blood vessels [17]. As drugs are distributed sparsely and heterogeneously throughout the target tumour, they are often ineffective at killing cells which can continue to sustain the tumour and allow it to recur, often in a more aggressive and drug resistant form [7, 11, 12].

1.1.2 Passive targeting

The EPR effect

Although tumour physiology poses a formidable challenge to drug delivery, it's unique characteristics also provide opportunities for passive targeting. Leaky vasculature and poor lymphatic drainage allows for passive accumulation of macromolecules within tumours; this is known as the 'enhanced permeability and retention (EPR) effect' [18]. 'Enhanced permeability and retention' means that drugs with

particular characteristics will preferentially accumulate within tumours over healthy tissue, thereby increasing the anti-tumour effect whilst decreasing systemic toxicity (reviewed in [19]). The EPR effect depends on the size, surface charge, biocompatibility and pharmacokinetics of the drug, as well as the specific physiology of the tumour being treated. In particular, if a carrier system is above the size of the gaps between endothelial cells in normal tissue (2–10 nm) and liver (100 nm) but below the size in tumors (typically reported as up to 500 nm) then a window of opportunity is created where accumulation into nontarget tissue can be avoided, providing the extended circulation required to allow passive diffusion into all metastatic tumor deposits [20]. Conventional anti-cancer drugs, such as anthracyclines, typically have low molecular weights, and do not have any tumour selectivity due to the EPR effect [19].

Many existing chemotherapeutics are being reformulated on the nanoscale, in part to capitalize on EPR- mediated passive accumulation within tumors. Nanoparticulate drug formulations can be fine-tuned to achieve a size and surface charge which prevents sieving through hepatic sinusoidal endothelia and capture by the mononuclear phagocytic system (MPS), whilst still allowing EPR-assisted tumor accumulation. Furthermore, nanoparticulate formulations can allow for control of release kinetics of active drug payload, can protect drug from degradation, and can therefore mitigate certain deleterious off-target effects seen with administration of free drug.

Polyethylene glycol (PEG)ylated liposomal doxorubicin (Doxil® or Caelyx® in Europe), for example meaures approximately 100 nm in size, which provides improved pharmacokinetics (PK) and allows levels of EPR-mediated tumor accumulation unattainable by the free drug [21]. The composition of lipids used in PEGylated liposomal doxorubicin - which provide a biocompatible polymer coating to the liposome – reduces sequestration by the MPS and plasma components, leading to an elimination half-life of approximately 2–3 days in humans. Free doxorubicin by com-

parison, is cleared from the plasma with a half-life on the order of hours [22]. Despite these advantages, and the fact that it is approved for use in ovarian cancer, multiple myeloma, and Kaposi's sarcoma, it is only the latter of these indications in which it seems to have gained clinical traction. This may relate to an inefficiency of payload release once within the tumor, a problem which can potentially be addressed by altering the formulation to provide sensitivity to external targetable stimuli such as heat or cavitation [23, 24]. Other liposomal formulations with current FDA approval include liposomal daunorubicin (DaunoXome®, Galen), and liposomal vincristine (Marqibo®, Talon Therapeutics). A non-PEGylated liposomal formulation of doxorubicin (Myocet®, Teva) is approved for use in Europe. In contrast to Doxil®, these three liposomal formulations do not have a coating of biocompatible PEG and are therefore sequestered by the MPS and thus released slowly into circulation [25]. Paclitaxel has also been reformulated, and FDA approved, as a nanoparticle therapeutic. Albumin-bound paclitaxel (Abraxane®, Celgene), measuring approximately 120 nm in size is approved for treatment of breast, pancreatic, and lung cancers. Although the size of albumin-bound paclitaxel imparts nanoparticle-associated delivery benefits (improved circulation time and EPR effect), the main clinical benefit of albumin-bound paclitaxel versus conventional paclitaxel is most likely due the removal of Cremophor as a solvent [26]. Liposomal formulations currently dominate the market-approved nano-therapeutic stage, however a variety of different nanoscale drug formulations are in the clinical testing pipeline. Examples of platforms under current investigation include polymeric micelles (e.g. micellar formulation of paclitaxel) and polymer–drug conjugates (e.g. paclitaxel poliglumex) [27].

Although the EPR effect is predicted to have a positive influence on drug uptake into tumors, it is not yet fully understood and has certain limitations. First, despite most tumors possessing the characteristics conducive to the EPR effect (leaky vasculature and lack of lymphatic drainage), these characteristics are heterogeneous, both within and between tumors, with the levels of perfusion and interstitial fluid

pressure (IFP) varying considerably even between different nodules within the same patient [28]. Furthermore, the true scale of the EPR effect – as well as its impact on intratumoural (i.t.) distribution – warrants further scrutiny. Analysis of EPR enhanced delivery shows perivascular distribution of deposited drug, rather than homogenous distribution throughout the tumor. Hence, a paradox is created where increasing the size of an agent enhances its EPR-assisted accumulation into the perivascular space, but decreases its diffusion-dependent transfer from this site and into the tumor [29]. A recent literature survey by Wilhelm et al. found that across a range of nanoparticle formulations, and tumour models, only a median of 0.7% of an administered dose of nanoparticles is recovered from solid tumours [30].

1.1.3 Active targeting

Unlike the EPR effect, which can be used to 'passively' target drugs, 'actively' targeted therapeutics aim to exploit various hallmarks of cancer by employing ligands targeted to structures typically overexpressed in tumors. Peptides or antibodies can be used in isolation as active agents, or to decorate the surface of drugs in order to improve target-cell recognition and subsequent uptake, consequently reducing uptake of cytotoxic drugs into non-target cells. The use of antibodies as actively targeted agents will be discussed thoroughly in Sections 1.2.1 and 1.2.2, while the rationale and strategies for active targeting, and its limitations, are described here.

Examples of actively targeted therapeutic agents under investigation for cancer therapy include CALAA-01 (a polymer-based nanoparticle containing small interfering RNA (siRNA) and targeted to human transferrin receptor) [31], folate-targeted liposomal doxorubicin [32], trastuzumab (a monoclonal antibody [mAb] targeted to the HER2/neu receptor) [33], and ibritumomab tiuxetan (an antibody–radionuclide conjugate) [34].

In practice, active targeting has certain limitations. In order for ligands to bind to cellular targets, they must be brought in contact with the cells themselves. In tis-

sues, where penetration of molecules is already limited, this represents a substantial challenge. Hence, agents such as the mAb trastuzumab require high and repeated dosing for uniform distribution of drug, while cells located within hypoxic regions of tumors are still often not exposed to drug [35, 36]. Moreover (and independent of any effects due to high IFP and dense tumor interstitium), binding to cellular targets perivascularly can limit the spread of actively targeted therapeutics into tumors; this effect is known as the 'binding site barrier' [37].

Generally, the benefit of 'active' targeting is more efficient drug uptake into target cells (and reduced off-target uptake), rather than an absolute increase in drug dose reaching all regions of the tumour. This is because the main mechanism for drug accumulation within tumours is still EPR-mediated extravasation, regardless of the presence of a targeting ligand. For certain therapeutics, such as siRNA, this advantage can be considerable; but for other therapeutics which enter cancer cells readily, it is unclear whether 'active' targeting confers a definite advantage or not [27, 38].

In response to the difficulty faced in trying to deliver into and throughout the tumour, therapies that target the tumor vasculature rather than the tumour cells themselves, have gained clinical traction. For example, bevacizumab, a mAb targeting vascular endothelial growth factor (VEGF), which plays a significant role in mediating tumor angiogenesis [39], is approved by the FDA for the first and second-line treatment of a range of cancers. The rationale for such vasculature targeting (targeting of the endothelial cells lining angiogenic tumor blood vessels) is clear. First, it should permit drug to more readily contact its target and so avoids the challenge of permeation against the IFP and the 'binding site barrier.' Second, non-transformed vasculature is less capable of mutating away from the mechanism of drug action, and finally, the destruction of just a few endothelial cells should have an amplified effect on the many tumour cells they support. However, it is now clear that this rather simplistic interpretation fails to consider the degree of control needed

to prevent the epithelial–mesenchymal transition which results from vascular inhibition and ultimately causes tumors to become more invasive [15]. Moreover, clinical results of treatment of solid tumors with anti-VEGF agents (such as bevacizumab) as a monotherapy have been underwhelming, while trials with anti-VEGF therapy coadministered with conventional chemotherapy have shown to be significantly more effective than chemotherapy alone [40]. These results support the hypothesis that vascular-targeting approaches will have the most clinical utility when used sparingly to 'normalize' tumour vasculature and allow for better delivery of subsequently systemically administered drugs with direct anti-cancer cell activity [41, 42]. However, there is heterogeneity in the scale and duration of such normalization, making it difficult to predict and control.

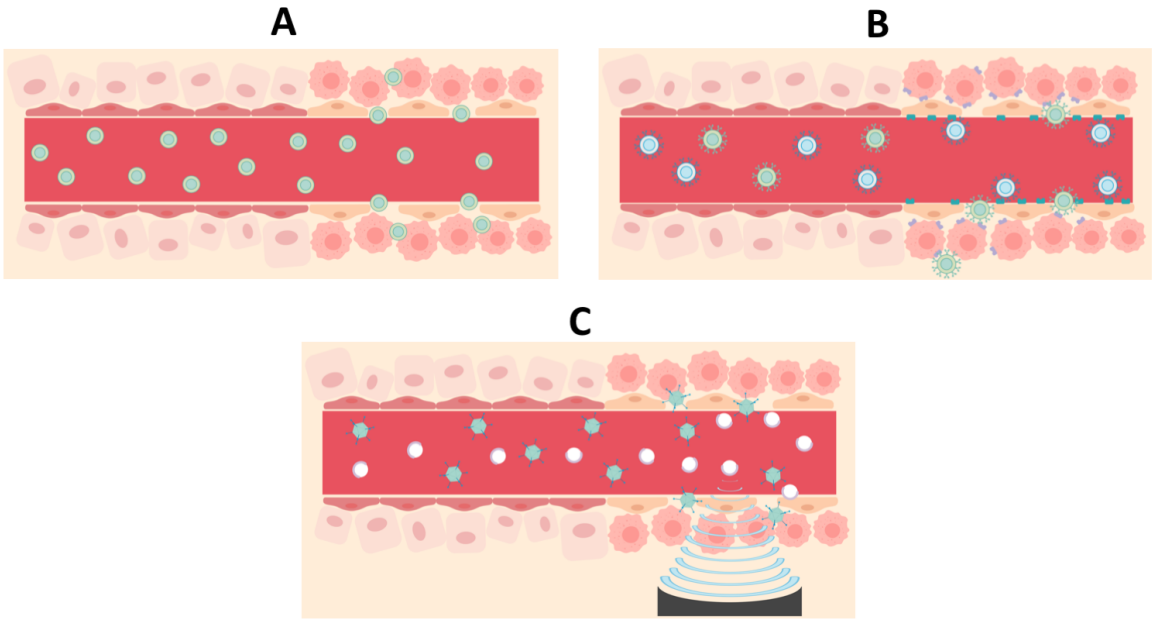

Figure 1.1: Illustration of three different methods for enhancing drug delivery or uptake for cancer therapy. Panel A illustrates passive accumulation of a liposome-type nanoparticle through leaky vasculature. Panel B illustrates delivery of particles actively targeted either to ligands on the tumour vasculature, or to ligands overexpressed on tumour cells. Panel C illutrates delivery of an adenovirus using US-mediated cavitation as an external stimulus.

1.1.4 External stimuli

Non-invasive externally applied stimuli can be used to enhance drug delivery, or potentiate cancer therapy. Physical approaches such as the use of high-intensity ultrasound can enhance the transport of a variety of therapeutics (reviewed in [43]), or provide a stimulus for targeted release of encapsulated drug [24, 44]. The potential for ultrasound as a drug-agnostic technique for improving drug delivery and therapy is further discussed in Section 1.3.

1.2 Biological therapeutics

1.2.1 Antibodies

Although cancer cells cannot, in general, be distinguished by completely unique surface-expressed proteins (as this would lead to rapid immune clearance), they often express or over-express proteins otherwise downregulated in healthy somatic cells, a prime example being HER2 overexpression in breast cancer [45]. Antibodies against cell-surface-expressed antigens can be administered systemically and will achieve extended circulation (as compared to small molecule drugs) allowing them to exert an effect either exclusively or preferentially on all metastatic tumour deposits displaying the target antigen. Antibodies can exert an antitumour effect through a range of modes of action. First, mAb therapies can act directly on cancer cells by acting antagonistically (or agonistically) on receptors involved in crucial cancer cell signalling pathways, or by binding to cytotoxic receptors and thereby triggering apoptotic pathways. The FDA-approved mAb cetuximab targets the epidermal growth factor receptor (EGFR), and when bound to its target, blocks growth factor binding, and can induce internalization of the receptor, as well as downregulation of cell expression of EGFR, ultimately resulting in inhibited cell proliferation [46]. Antibodies can indirectly affect tumour cells by targeting elements of the tumor microenvironment that drive uncontrolled growth. The previously mentioned mAb,

bevacizumab, employs this approach by targeting VEGF expressed by endothelial cells in the tumor vasculature in order to suppress pathophysiological neoangiogenesis [39]. Moreover, mAbs can exert an antitumour effect indirectly through immune-mediated mechanisms. Namely, mAbs targeted to tumor-associated cell-surface antigens can initiate and mediate complement-dependent cytotoxicity (CDC) and antibody-dependent cell-mediated cytotoxicity (ADCC), via the clustering of their Fc regions on the target cell surface. For example, rituximab, a mAb directed toward CD20 (expressed on the surface of B cells), has been shown to instigate both CDC and ADCC (in addition to direct cancer-cell apoptosis) [47]. Additionally, mAbs can be targeted to indirectly regulate T cell function by interfering with 'immune checkpoint' signaling. Notably, antibody therapies are not limited to only one mode of action; cetuximab for instance has been shown to also initiate ADCC by activating cellular components of immunity such as natural- killer cells, dendritic cells, and indirectly, T cells [48, 49]. The exact balance of activity will depend on the mutation profile and immune status of the particular tumour. Systemically administered antibody therapies targeted to tumours and their microenvironments have shown in general, improved safety and lower toxicity as compared to conventional chemotherapeutics [50]. It is important to note, however, that off-target effects can and do occur with antibody therapies and can be due to off-target action of the therapeutic through its intended mechanism. For instance, the cardiotoxicity of trastuzumab has been proposed to be related to binding of HER2 receptors in cardiac tissue [51, 52]. Additionally, the improved specificity of these agents has the downside of reducing how widespread their use can be, with their use and efficacy being restricted by heterogeneous expression of a target antigen within and across patients. Studies on the use of cetuximab in colorectal cancer have shown that patients with tumors bearing a specific mutation (in the K-ras gene) do not benefit from the treatment, while those with the wild-type gene do benefit from improved overall survival and progression-free survival (as compared to current best

supportive care) [53]. As a result, cetuximab was the one of the first therapeutics to be approved for use with a biomarker diagnostic test, which verifies K-ras wild type-status prior to treatment.

Immune checkpoint inhibitors

Numerous studies have shown that the presence of tumor-infiltrating lymphocytes (TILs) is positively correlated with an improved prognosis [54, 55]. While mAbs can indirectly elicit or potentiate antitumour responses by immune cells including T cells, tumours develop mechanisms to evade such immune responses. One such mechanism is to co-opt 'immune check-point' pathways [56]. Briefly, immune checkpoints refer to inhibitory pathways employed by cells to avoid destruction by any self-reactive immune cells. These pathways are key to the maintenance of 'self-tolerance,' but can be misappropriated by cancer cells to avoid the immune system's natural response to tumour-associated antigens (reviewed in [56, 57, 58]). Many of the immune-checkpoint pathways identified so far involve receptor–ligand interactions, and so the blockade of immune-checkpoint receptors or ligands has been identified as a strategy to enhance antitumour immunity. Thus far, clinical research into immune-checkpoint blockade has focused primarily on two pathways: that of cytotoxic T-lymphocyte-associated antigen 4 (CTLA-4), and that of programmed cell-death protein 1 (PD-1) [56]. Although both pathways act on T cells, they function at different levels of the cellular immune response. CTLA-4 is a receptor expressed on the surface of T cells, where it exerts a regulatory effect on the early stages of T cell activation primarily in the lymph nodes [59]. In contrast the PD-1 receptor is expressed after T cell activation and modulates T cell activity locally within tissues [60].

Recent clinical trials have shown blockade of the CTLA-4 pathway, or the PD-1–programmed cell-death protein 1 ligand (PD-L1) interaction, to be highly effective in a certain proportion of patients [61, 62, 59, 63, 64, 65, 66]. These results have generated a great deal of interest and led to the FDA approval of ipilimumab,

nivolumab, pembrolizumab, atezolizumab, avelumab, and durvalumab. Although use of these agents has been demonstrated to provide survival benefits compared to a variety of other therapies, their use in the clinic has also presented a range of challenges unlike those faced by other more conventional therapies [58].

As immune checkpoints are key elements of 'self-tolerance,' blockade of immune checkpoints can produce a range of immune-related adverse effects due to non-specific activation of the immune system (reviewed in [58]). Notably, blockade of CTLA-4 has resulted in more severe/common immune-related adverse effects than blockade of the PD-1 pathway [56]. This is most likely due to the differences in mechanisms of action, with anti-CTLA-4 acting on inactivated T cells in the lymph nodes to produce a more systemic response, while anti-PD-1 and anti-PD-L1 antibodies work on activated T cells in the periphery and may therefore work in a more tumor-selective way [56]. This different site of action may also reveal differing potential limitations, with anti-PD-1 and anti-PD-L1 antibodies potentially requiring passage deep into tumors to contact resident T cells, whereas anti-CTLA-4 antibodies may not face this restriction.

Similar to the other forms of antibody therapy outlined above, treatment by inhibition of immune checkpoints will only be effective in a subset of cancer patients – those who have tumours which use immune checkpoints as a mechanism to escape immune eradication. As such, predictive biomarkers of clinical outcome with immune checkpoint therapy are being actively investigated [67, 68, 69].

1.2.2 Antibody-drug conjugates

In addition to their role as active therapeutics discussed in Section 1.2.1, antibodies can also play a role in metastatic cancer therapy as targeting agents for other therapeutics, such as radioisotopes and cytotoxic drugs. The therapeutic mode of action and efficacy can be altered/enhanced by conjugating a mAb to a cytotoxic drug. Linking a cytotoxic drug to a mAb should allow for administration of more

potent cytotoxic drugs than are currently used in systemic chemotherapy, as the mAb must bind to its target antigen to facilitate uptake of drug, and thus uptake is restricted to cells expressing target antigen. This specificity of action is largely dependent on the linker between drug and mAb. On the one hand, the linker must be stable in circulation to prevent off-target release of drug and to allow for long circulation of drug. The linker must also, however, be able to release drug efficiently once internalized into a target cell. Moreover, the method of attachment of drug (and amount of drug attached) can affect the internalization efficiency of the antibody–drug conjugate (ADC) and must therefore be carefully controlled [70]. The four ADCs with current FDA approval employ different linking strategies and have shown considerable clinical efficacy thus far [71, 72, 73].

ADCs combine the specificity of a mAb and the cytotoxicity of an anti-cancer drug (often too cytotoxic to be administered alone), in theory creating a more targeted, safe, and efficacious therapeutic. Trastuzumab emtansine, for example, has been shown to be efficacious against metastatic breast cancers that were previously treated with the mAb trastuzumab [74], and in a trial comparing the action of the ADC to that of the mAb trastuzumab coadministered with conventional chemotherapy (docetaxel), trastuzumab emtansine showed an improved safety profile [75]. In addition to having robust scientific rationale and some promising clinical data, the ADC approach also benefits from providing a continued income stream for mAbs reaching their patent expiry. In the face of the rise of generic biosimilars, this provides a strong commercial imperative for the development of ADCs.

1.2.3 BiTEs (Bi-specific T cell Engagers)

In the past two decades, novel bi- or multivalent antibody constructs have been engineered to harness the power of T cells in destruction of cancer cells. This approach is exemplified by bi-specific T cell engaging antibodies (BiTEs), composed of two single-chain variable fragments (scFv) linked to form a peptide of approxi-

mately 55 kDa. These BiTEs have been shown to be effective and precise in instigating and mediating T cell destruction of cancer cells, both pre-clinically and in patients [76, 77]. In common with mAbs, or ADCs, BiTEs are specific for target antigens expressed on the surface of cancer cells. Rather than relying on indirect stimulation of the immune system, however, BiTEs incite T cells directly to attack cancer cells, by also binding CD3 (a signaling component of the T cell receptor complex). As many cancers have evolved to avoid normal immune surveillance (through a variety of methods including immune editing and major histocompatibility complex [MHC] downregulation) [78], the ingenuity of the BiTE approach is that T cells can be activated irrespective of their original specificity and in the absence of MHC presentation [79, 80]. BiTE-induced T cell activation should occur only in conjunction with cells bearing the antigen targeted by the BiTEs [80], thus mitigating the safety risk posed by polyclonal activation of T cells. BiTEs have been shown to induce a potent and accelerated form of T cell-mediated cell lysis [81], and are effective even at concentrations orders of magnitude lower than comparable mAb therapeutics [82, 83]. BiTE-redirected T cells form cytolytic synapses with cells bearing target antigens, instigating the formation of perforin pores and the release of cytolytic granule contents. The effectiveness of this redirected T cell-mediated cell lysis has been demonstrated in the clinic with blinatunomab, a bi-specific antibody targeting CD3 and CD19 (CD19 is expressed on the surface of B cells, and while its expression is not increased in cancerous B cells versus normal cells, the transient destruction of healthy B cells expressing CD19 appears to be tolerable). Blinatumomab has shown clinical efficacy against hematological cancer in both disseminated blood and bone marrow deposits of infiltrating disease [83, 84, 85].

Though blinatumomab is currently the only market-approved BiTE, many BiTE formulations directed toward other target proteins have been investigated clinically (e.g. EpCAM, CEA, PSMA) and preclinically (e.g. Her2/neu, EGFR, CD33 [76]) – reviewed in [86]. Despite early clinical success, BiTE technology is limited by

several factors. Clearly, BiTEs face the same challenges as mAbs or ADCs in terms of choosing appropriate target antigens and the same general delivery limitations of any actively targeted therapeutic. Moreover, BiTEs do not contain any Fc regions, which both reduces their recycling and their size, allowing them to be cleared through the kidneys more rapidly than conventional mAbs, and thus their serum half-life is on the order of a couple of hours [76, 87]. This short serum half-life necessitates the administration of BiTEs by continuous i.v. infusion using portable mini-pumps, for periods of 4–8 weeks. However, a size of 55 kDa is still large enough to substantially impede transport deep into solid tumors, especially to the regions rich in T cells with suppressed activity. Finally, though the hallmark of BiTE therapy is a *targeted* redirection of T cell lysis, blinatumomab has shown clinically important adverse side effects, notably including cytokine release syndrome and central nervous system (CNS) disorders [83, 84, 85]. Although the CNS events reported in trials were reversible, they are troubling, as the underlying mechanism behind these events remains unclear. Similar to BiTEs, bi-specific antibodies containing an Fc region, allowing for engagement of Fc receptors on immune cells other than T cells, have been investigated clinically, and catumaxomab (a bi-specific tri-functional antibody directed toward EpCAM and CD3) is approved in Europe for the treatment of malignant ascites [88].

1.2.4 ImmTAC (Immune Mobilizing Monoclonal T cell receptors Against Cancer)

In an approach similar to the antibody-based T cell engagers, ImmTACs (immune mobilizing monoclonal T cell receptors [mTCRs] against cancer) work to redirect autologous T cells to lyse cells presenting specific antigens associated with cancer. Antibody-based therapeutics have been largely restricted by the need for antigen to be surface expressed, with work only recently demonstrating the possibility of designing BiTEs to target specific intracellular peptides presented in the context of

MHC [89]. In contrast, the development of ImmTACs has been based on the principle of targeting cells using affinity-enhanced mTCRs and can thus target the range of endogenously processed tumor-associated antigens. TCRs' natural affinity for cognate antigen is typically orders of magnitude lower than the affinity of antibodies for their target peptides (and affinity for self-derived tumour-associated antigens is even poorer due to mechanisms of T cell selection and central tolerance [90]), and so soluble mTCRs, targeting specific peptides presented in the context of human MHC (pMHC) at greatly enhanced affinities, have been engineered and fused with anti-CD3 single-chain antibody fragments to create a novel class of bi-specific therapeutics, ImmTACs [91]. The potency of ImmTACs directed against a range of target antigens has been demonstrated in vitro and in vivo, with ImmTACs inciting and redirecting a target-specific T cell response, despite low levels of target pMHC presentation on cells tested [91, 92]. Furthermore, ImmTAC redirected cancer-cell lysis (specifically with an IMCgp100 – an ImmTAC specific to the melanocyte differentiation antigen gp100) was shown to lead to antigen cross-presentation by dendritic cells, a process whereby polyclonal T cells can become activated either within the tumour or within draining lymph nodes. Moreover, cross-presentation in the presence of the ImmTAC was shown to enhance the activation of T cells naturally specific for tumour-associated antigens. This exciting finding is significant as antigen cross-presentation and consequent activation of T cells specific for a wider range of tumour-associated epitopes could foster a more robust and self-sustaining immune response against cancer [93].

Although the targeting of intracellular antigens gives rise to a larger pool of possible cancer-specific targets (as compared to surface expressed targets), targeting through MHC restricts the patient population that stands to benefit from therapy with a particular ImmTAC (as MHC alleles vary across individuals, and each ImmTAC is targeted to one allele group) [94]. As with any immunotherapy, the potential for off-target effects (either by destruction of healthy cells presenting target antigen,

or by unpredicted off-target activity) necessitates thorough preclinical testing. This process is, however, considerably more difficult for a therapeutic that specifically targets human proteins (human MHC), as in the case of ImmTACs [94]. The precise location where ImmTAC (and BiTE) molecules interact with T cells has yet to be fully characterized or reported. However, the work of Brischwein et al. suggests that close context of CD3 on T cells and target ligands on cancer cells is required for the multivalent stimulation of CD3 needed for activation [80]. It is likely therefore that effective delivery into and throughout the tumour will be required for these molecules to be fully effective against solid, poorly perfused tumours.

1.2.5 Virotherapy

1.2.6 Oncolytic viruses

Oncolytic viruses are emerging as powerful therapeutics, unrivalled in their capacity for selective self-amplification. Certain viruses are naturally cancer selective, or have become so through many rounds of in vitro culture. In most cases, however, oncolytic viruses are engineered to be cancer specific [95]. This can be accomplished by exploiting the adaptability of the viral genome and the strategies employed by tumour cells to avoid normal mechanisms of cell death and immune destruction [94, 95].

In general, engineering cancer-specific viruses can be achieved in three ways. First, virus-cell entry can be controlled by engineering pathways of virus entry and infection to depend on receptors or proteins with raised or exclusive expression in tumors [96, 97]. Second, as the indefinite division of cancer cells is reliant on upregulation or suppression of many gene products otherwise dormant or active in healthy differentiated somatic tissue, viruses can be engineered to be cancer specific by placing transcription of genes essential to their replication under the control of tumour-specific promoter(s) [98, 99, 100]. Third, specificity can be achieved by regulation through attenuation of virulence in healthy tissue. That is, viruses can be

made cancer selective by attenuating their action in healthy tissue (e.g. engineering virus to be more susceptible to normal mechanisms of immune clearance), while retaining close to wild-type virulence in cancer cells [101, 102]. A variety of viruses have been designed to target a wide range of cancers [103].

In addition to direct cell lysis, oncolytic viruses can have an important therapeutic effect by potentiating or eliciting an antitumour immune response (reviewed in [104]). Studies have demonstrated that efficacy of reovirus, for instance, depends critically on an antitumour immune response [105]. Viruses tend to induce immunogenic cell death; lysed cells release danger signals relating to the viral infection, as well as a range of tumour-associated antigens. These factors displayed in concert by antigen presenting cells can initiate an adaptive immune response against the tumour cells [105, 106]. The benefits of this virus-induced antitumour immunity are elegantly demonstrated by experiments in bilateral syngeneic tumour models in immunocompetent mice, where i.t. injection of an oncolytic virus into one tumour causes a regression of the un-injected lesion (abscopal effect). No effect is observed in un-injected lesions of athymic mice, indicating that the effects in untreated lesions are immune-mediated [107]. These effects have also been observed in humans, in trials for late-stage melanoma, where regression of untreated metastatic nodes was observed after treatment of separate lesions with a modified herpes simplex virus (talimogene laherparepvec [IMLYGIC®]) [108].

To increase their efficacy, oncolytic viruses can be 'armed' with transgenes encoding a variety of useful proteins [109]. Notable examples include transgenes of prodrug converting enzymes [110, 111], immune-stimulating proteins [108], extracellular matrix degrading enzymes [112, 113], syncytia forming proteins [114], and anti-angiogenic proteins [115]. Once infected by an 'armed' oncolytic virus, cancer cells will produce the encoded transgene, in addition to progeny virus. Currently, the only market-approved oncolytic viruses are Oncorine® (H101), a recombinant type 5 human adenovirus [116], and IMLYGIC® (talimogene laherparepvec), a tran-

scriptionally regulated modified herpes simplex virus encoding the gene sequence for human granulocyte-macrophage-colony-stimulating factor (GM-CSF, an inflammatory cytokine) [108]. While oncolytic virotherapy has shown considerable promise in the clinic and has been so far quite safe and well tolerated, the clinical efficacy has, in general, not matched that observed in many preclinical studies [109]. This clinical translation deficit is a consequence of the factors discussed below.

Although oncolytic virotherapy has the potential to elicit a powerful antitumour immune response, there is a balance between the benefits of an antitumour immune response and the detrimental impact of an immune response on the efficacy of viral spread (reviewed in [105]). Despite tumours being, in general, immune-suppressed environments, studies have shown that infection of cancer cells by oncolytic viruses can still activate immune responses which act rapidly to prevent spread of the virus, thereby reducing any therapeutic effect due to viral oncolysis [117, 118]. Administration of immunosuppressive agents has been investigated in an effort to circumvent the immune barrier to viral spread. For instance, treatment of glioma in an immunocompetent rat model with an oncolytic herpes simplex virus can be enhanced by pretreatment with cyclophosphamide, an immunosuppressive agent [119]. A virus-induced immune response thus appears to be a double-edged sword. The immune system is a barrier to viral replication and spread within a tumour; but once infection has occurred and tumour-associated antigens are presented in the context of danger signals due to viral infection, a powerful antitumour response can potentiate tumour debulking [105]. Additionally, although the size of most viruses is ideal for passive targeting via the EPR effect [19], the circulation time required for tumoural accumulation poses a formidable challenge, as the immune system rapidly clears pathogens such as viruses. Systemically administered viruses are coated with antibodies (neutralizing and non-neutralizing), complement, and other serum factors before being sequestered in the liver and spleen by the MPS [120]. This has the added complexity that such clearance is often not predicted by pre-clinical models [121].

The efficacy of these clearance mechanisms means that most oncolytic viruses have very poor circulation half-lives. Of particular concern are neutralizing antibodies in serum of pre-exposed individuals (or in individuals requiring repeated administration), as they can present a significant barrier to systemic delivery and contribute to variation in treatment results across individuals [122, 123]. It is important to note, however, that this limitation varies across virus types – the utility of certain serotypes of adenovirus, for instance, is notably hampered by a high prevalence of pre-existing neutralizing antibodies within the general population [124].

Numerous strategies to circumvent these barriers have been investigated. Examples include the following: immunosuppression [123, 125], serotype switching (applicable to viruses with more than one serotype) [126], engineering of novel serotypes (for monotypic viruses) [127], and chemical modification or 'stealthing' [128]. Enadenotucirev (ColoAd), for example, is a Ad3/Ad11p chimeric adenovirus that was generated using 'directed evolution' to yield a novel potent and cancer-selective virus with improved activity in human blood compared to Ad5 [129, 130]. ColoAd has been administered i.v. in the clinic and positive tumoural delivery was detected, suggesting the feasibility for systemic treatment with an oncolytic virus. Finally, even if a significant proportion of administered virus were to accumulate intratumourally, distribution subsequent to delivery has been shown to greatly impact the ultimate efficacy of an oncolytic virus. In a recent study, i.t. spread of an oncolytic vesicular stomatitis virus following i.v. injection was tracked using NIS expression, and results showed a heterogeneous distribution of infection within tumors and across animals receiving uniform treatments [131]. In response to the challenge of i.v. delivery, many studies have delivered virus via i.t. injection to try to circumvent the barrier posed by the bloodstream and the limitation of poor i.t. distribution [132]. However, i.t. injection is not optimal or even feasible for many tumor locations and is unacceptable for treatment of metastatic cancer, thus impacting the clinical utility of this approach [133]. Physical approaches such as the use of ultrasound-generated

inertial cavitation have offered a means of improving i.t. spread by providing a controllable stimuli to propel viruses deep into tumours [134]. These technologies have provided >100-fold increases in adenovirus delivered i.v. to murine xenograft tumors [135] (discussed in Section 1.3). The challenge will be to see how this technology can scale and translate from preclinical models to humans. The tremendous promise oncolytic viruses have shown in the treatment of cancer both preclinically, and in clinical trials [103], means it is likely that work to overcome the delivery challenge will gather pace. The capacity of these agents to selectively self-amplify within tumours and turn cancer cells into factories for the production of encoded therapeutic protein is unmatched, and it is this functionality which makes them an exciting candidate for combination with the range of biological agents currently being developed. In particular, recent studies showing that efficacy of a measles virus expressing anti-PD-L1 can surpass that of the antibody alone, and match that of the virus (not expressing anti-PD-L1) used in combination with a separately delivered antibody [136], gives an indication of where the field of oncology is heading. Indeed, trials combining oncolytics and checkpoint inhibitors are underway, and although commercial imperatives may initially restrict their use to combination studies, scientific rationale and the need for new parties to carve out freedom to operate are likely to lead to the use of viruses expressing checkpoint inhibitors.

1.2.7 Cell-based therapies

An alternative approach to achieving viral delivery, without instigating vector-induced immunity, is to use cells as carriers to 'hide' viruses from barriers to circulation and systemic delivery. Generally speaking, the cell-carrier-based approach involves the ex vivo loading of a virus into (or onto) the chosen cell carrier, circulation of the loaded carrier cells, and ultimately virus delivery at the tumor site (reviewed in [137]). The success of this complex process is reliant upon an in depth knowledge of the chosen oncolytic virus and cell carrier, and their interactions. A

range of cell types has been tested for the carriage of a range of viruses, including autologous T cells [138, 139], and dendritic cells [140, 141], cytokine-induced killer cells [142], tumour cells [143], and mesenchymal stem cells [144, 145]. The choice of cell carrier rests on a number of factors, notably the tropism (if any) of the cell for metastatic tumors, and the mechanism through which the cell will transport the virus; T cells, for example, have been reported to transport surface-bound reovirus, while dendritic cells will internalize the same reovirus, thereby providing a greater protection from neutralizing antibodies [141]. Using a cell carrier that is permissive to viral replication allows for shielding of virus within the cell and for amplification of dose between loading and delivery stages [146]. However, timing of ex vivo loading and consideration of the time needed for carrier cells to reach (and ideally target) tumors must be measured against the life cycle of the chosen oncolytic virus within that particular cell type, if the cell is survive and effectively prevent immune recognition of virus [137]. Other cell-based treatments focus on the use of adoptively transferred immune cells (natural or genetically engineered) to treat metastatic cancer (reviewed in [147]). In one approach, T cells are taken from a patient, and those with an antitumor specificity are isolated, expanded, then re-introduced into the patient. Although this method of treatment has had impressive clinical results and is currently one of the best available for patients with metastatic melanoma, clinical utility has been dampened by stringent patient-screening requirements and labor-intensive protocols for the selection and isolation of appropriate T cells [148]. Treatments using adoptively transferred genetically engineered T cells share much mechanistic similarity with BiTE and ImmTAC technology. T cells have been isolated and genetically modified to present chimeric antigen receptors (CAR) on their surface, which recognize specific surface antigen; like BiTEs, the specificity of CAR T cells is derived from antibodies [149]. Alternatively, T cells can be engineered to present a modified T-cell receptor, which will instead recognize intracellularly processed protein in the context of MHC [150]. Although the use of genetically en-

gineered T cells removes the need to find autologous tumor-specific T cells to isolate and expand, the resulting engineered T cells have only monoclonalspecificity and are still labor-intensive to produce. The first FDA approved CAR T cell therapy (tisagenlecleucel – Kymriah) costs almost half a million USD for a one-time infusion [151]. Though cell-based therapies show promise, as facilitators to virotherapy, or directly as instigators of cancer immunotherapy, all approaches require extensive manipulation of cells ex vivo prior to treatment. It thus stands to reason that the inherently complicated, labor intensive, and costly process involved in cell-based therapy could preclude its widespread clinical adoption.

1.3 Ultrasound for drug delivery

1.3.1 Overview

Ultrasound (US) has been used clinically since the 1950's, as a diagnostic imaging tool. More recently however, therapeutic US has emerged as an exciting therapy modality, with applications ranging from thermal ablation to enhanced drug delivery to neuro-modulation for brain mapping. US is defined as longitudinal waves of pressure occurng at a frequency greater than 20 kHz, which lead to rarefaction and compression of the medium [152]. This definition is quite broad, and as such, many different regimes fall under this classification. In order to determine which parameter regime best suits a given application of US, an understanding of the physical principles underpinning US propagation in tissue is paramount.

1.3.2 Propagation in tissue

US can travel relatively unimpeded through human tissue [152], although as pressure waves travel from the surface of a transducer, they are modified through interaction with various tissues, and in turn can exert an effect on the tissues themselves.

Tissues within the human body have distinct acoustic properties. When propa-

gating US wave is incident upon a tissue boundary, some of the wave's energy will be transmitted through to the next layer, while some will be reflected back. The amount of energy that is transmitted will depend largely upon the acoustic impedances of the two layers. Most tissues in the body have similar acoustic impedances to water (with the exceptions of lungs, GI tract and bone) [153], allowing for US to be transmitted to great depths within the body. In addition to reflection, energy of a propagating US wave is lost to attenuation, which is a combination of absorption, and scattering. Absorption refers to the absorption of mechanical energy in the form of heat. Scattering occurs when a sound wave is incident upon small (relative to the wavelength) inhomogeneities, and is 'scattered' away from the direction of sound propagation. Both effects decrease acoustic intensity in the direction of sound propagation. The magnitude of attenuation in tissue is a function of both frequency, and material properties of tissue [153].

Although US has relatively low attenuation in tissue [152], attenuation decreases acoustic intensity in a frequency dependent manner. Consequently, lower frequencies are chosen for applications requiring a significant acoustic intensity deep into tissue, while higher frequencies are used in more shallow applications (such as imaging in tissue, which can require the greater resolution afforded by a higher frequency) [153].

When a single-frequency transducer is used to produce a low frequency US wave, non-linear effects can give rise to the generation of higher frequency components, and thus to increased attenuation. As a single-frequency sinusoidal US wave travels through tissue, sound-speed and particles-speed differences in compressed versus rarefied regions lead to the formation of a 'shocked' waveform [153]. Thus, energy is converted from the fundamental frequency of the transducer into ultraharmonic frequencies. The importance of non-linearity in US propagation depends largely on: i) the nonlinearity of the tissue (fat, for instance, is more non-linear than other more aqueous tissues) ii) the pressure amplitude of the incident US wave (at low pressure oscillations, US can be approximated as linear) and iii) the depth of US propagation

into the tissue [153].

1.3.3 Therapeutic ultrasound

As US propagates through tissue, its energy can be converted in a variety of ways (for instance, through absorption, or instigation of cavitation) to produce different therapeutic effects. Thermal effects of US can be used for tissue ablation [154], or to trigger release of drug from thermosensitive drug carriers [44]. Mechanical effects of US can be used to reversibly open the blood-brain barrier [155], or to enhance the action of thrombolytic drugs in treatment of ischemic stroke [156]. At extremely high-amplitudes, US can be used to mechanically disrupt tissue (histotripsy [126]), or even solid urinary stones (lithotripsy [157]).

1.3.4 Acoustic cavitation

Acoustic cavitation is a phenomenon whereby small vapour or gas cavities (bubbles) within a liquid expand and contract in the presence of an acoustic field. Bubbles can be created from dissolved gas within a liquid, can be 'seeded' from gas pockets trapped on surfaces within a liquid, or can be pre-existing [158]. When an US wave interacts with bubbles, they expand during the rarefaction period of the wave, and contract during compression. Though more nuanced than presented here, acoustic cavitation can be classified as either 'non-inertial' or 'inertial'. Inertial cavitation (sometimes called 'transient' cavitation) refers to unsustainable growth of a bubble during rarefaction phase of US wave, followed by a violent collapse under the inertia of the surrounding fluid. Inertial cavitation is short-lived, and typically occurs within a few US cycles [158]. Both inertially and non-inertially cavitating bubbles produce acoustic emissions: non-inertial cavitation gives rise to primarily harmonic acoustic emissions, while inertial cavitation gives rise to broadband acoustic emissions [158]. The detection and examination of the frequnecy spectra of acoustic emissions can therefore be used to distinguish between inertial and non-inertial cav-

itation [159]. Passive acoustic mapping (PAM) is a technique whereby cavitation events are detected passively, and are used to create a spatial map of cavitation activity. This technique can be used to monitor cavitation in real-time, and potentially to allow for treatment monitoring [160, 161]. Broadly speaking, this technique uses the differences in the time of arrival of acoustic emissions to different elements within a linear array to resolve the source location [162, 163].

Microstreaming

Non-inertially cavitating bubbles can give rise to a phenomenon called 'microstreaming', wherein bubble oscillation causes the surrounding fluid to flow [164, 165]. Inertial cavitation can also give rise to microstreaming [166], in addition to other effects such as jetting, free radical production and shock-wave formation [152]. Cavitation-induced microstreaming is thought to be the primary mechanism for US-enhanced extravasation of drugs into solid tumours [152].

1.3.5 Ultrasound for enhanced drug delivery

In the context of cancer therapy, externally-applied US can provide a non-invasive stimulus to increase drug extravasation in solid tumours. Cavitation-induced microstreaming can improve drug transport over orders of magnitude [152]. Inertial cavitation has been shown to be more efficient than stable cavitation at transporting macromolecules [167]. Microbubbles, such as contrast agents used for diagnostic US imaging (UCAs), can be used as cavitation nuclei to decrease the pressures needed to instigate cavitation. These formulations are, however, limited in vivo by short circulation half-lives [168, 24, 169]. These formulations are also of micrometre-scale sizes, and are destroyed by US exposure, preventing their extravasation from vasculature and thus precluding any EPR-mediated accumulation [170]. Alternatively, gas-entrapping nano-scale particles can act as cavitation nuclei and enhance the US-mediated transport of model therapeutics [171, 172]. Specifically, sonosensitive

polymeric particles developed by Kwan. et al. have been shown to sustain cavitation activity longer than microbubbles, and to improve US-mediated transport of a model drug in vitro, and a therapeutic virus in vivo [170, 173]. Other cavitation nuclei under current investigation include acoustically vaporizable liquid droplets. The agents are liquid at body temperature, but undergo a phase change and vaporize when exposed to US (at the appropriate acoustic parameters). These agents are of interest as they can be formulated to be of sub-micrometre sizes, and can also be loaded with drug, allowing for precise colocalization of drug and cavitation activity [174].

US has been used to enhance the transport of a range of different therapeutics, through a variety of mechanisms. High-intensity pulsed US, in the absence of exogenously introduced cavitation nuclei, has been used to enhance the delivery of various agents, including mAbs [175, 176]. Wang et al. demonstrated improved distribution and penetration of radiolabelled trastuzumab into subcutaneous murine xenografts pre-treated with pulsed 1 MHz US at a peak rarefactional focal pressure (PRFP) of 8.95 MPa.

Enhanced transport into tumours can be achieved however, at much lower PRFPs ($\approx$ 1.5-2 MPa) when cavitation nuclei, such as UCAs, are used to seed cavitation, as has been demonstrated in vitro and in vivo with antibodies [170], liposomes [24], and viruses [167, 177, 178, 134]. In addition to increasing transport into tumours, improved i.t. penetration and distribution has been reported for a polymer-stealthed oncolytic virus that was administered with UCA and exposed to US [134]. Sonosensitive particles (SSPs) have also been shown to enhance the delivery of an oncolytic virus: Myers et al. demonstrated the enhanced delivery and efficacy of an oncolytic vaccinia virus after US treatment in the presence of SSPs [173]. Crucially, the US parameters used were shown to have no detrimental impact on the structure or activity of small molecule, antibody, or virus based therapeutics [179].

In an attempt to further enhance cavitation-mediated delivery, Mo et al. inves-

tigated changes that could be made to the therapeutic. Specifically, they demonstrated that US-mediated transport of adenovirus type 5 (Ad5) can be enhanced by increasing the density of the Ad5 with gold nanoparticles. The authors hypothesized that during cavitation-induced microstreaming, increased density would allow the modified Ad5 to travel farther at its terminal velocity due to having greater momentum than the surrounding fluid [135]. This hypothesis was further tested by Lea-Banks et al. who demonstrated through in silico modelling and in vitro testing that within a regime of US-mediated cavitation, denser particles are delivered farther into a visco-elastic matrix.

The combination of US and cavitation nuclei has also been shown to improve delivery of therapeutics to the brain across the blood brain barrier (BBB). Acoustic pressures employed for this type of treatment are typically (but not always) lower than those used in the transport studies described above, and the primary mechanism for enhanced drug delivery is likely transient opening of the BBB [180, 181], though enhanced interstitial convective transport may also play a role [182].

1.4 Implications for current work

The literature shows that while there is a need for more effective and targeted therapeutics, achieving efficient delivery of these therapeutics is an equally challenging yet crucial task. As more time, effort, and money are spent developing complex, targeted, and comparatively large biological therapeutics, the costs and risks of not addressing the limitations to drug delivery increase. The pathophysiology of tumours presents mechanicals barriers to therapy, but abnormal vasculature of tumours also gives rise to the potential for 'passive' targeting and accumulation of therapeutics via the EPR effect. The scale of this effect is unclear however, and recent review of the delivery of nanoparticles (often optimized to capitalize on the promise of the EPR effect) suggests that reliance on passive accumulation of nanoparticles will be insufficient for effective cancer therapy [30]. US-mediated cavitation has been

shown to be a powerful tool for non-invasively enhancing the delivery of biological therapeutics [43], and has the potential to be applied in a safe and 'drug-agnostic' fashion.

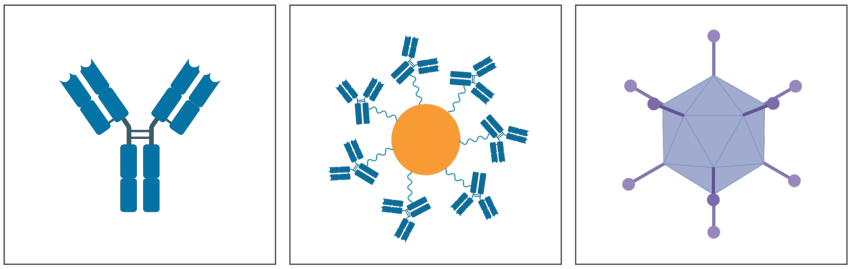

Figure 1.2: Therapeutic classes investigated in this thesis for delivery with US-mediated cavitation.

In this thesis, the use of focused US in combination with cavitation nuclei (CN) to enhance the delivery of a range of biological therapeutics is investigated (Fig. 1.2). Two different classes of CN, microbubble UCAs (SV) and solid gas-entrapping nanoparticles (SSPs), are employed and compared for their ability to enhance the transport of three classes of nano-sized therapeutics into tumours. In the following chapters, the cavitation mediated delivery of a cancer specific mAb, an actively targeted nanoparticle, and an oncolytic virus are examined. The primary aims of this thesis are to:

- Develop and characterize a therapeutically-relevant actively targeted gold nanoparticle by site-specific conjugation to a therapeutic antibody.
- Investigate and compare the cavitation-mediated delivery of an actively targeted nanoparticle, with its corresponding free non-modified therapeutic antibody.
- Investigate the cavitation-mediated delivery of a therapeutically relevant oncolytic virus.

- Evaluate a potential method for further enhancing the cavitation-mediated delivery of an oncolytic virus by increasing its density.

Chapter 2

Methods and materials

This thesis is focused on testing the US-mediated delivery of 1) therapeutic antibodies, 2) actively targed nanoparticles, and 3) oncolytic viruses. This chapter outlines the materials and methods used in the development of assays for testing delivery of these three classes.

2.1 Formulation of heterobifunctional PEG linker

Heterobifunctional PEG (3.4 kDa) was purchased from Nanocs (LA-PEG-COOH PG2-CALA-3k, Nanocs). Early batches of PEG linker were synthesized starting with a heterobifunctional PEG with a lipoic acid group and an n-hydroxy succinimide group (PG2-LANS-3k, Nanocs) which was hydrolysed to give LA-PEG-COOH by dissolving in water and incubating at 40 °C overnight. The hydrolysed PEG was then freeze-dried overnight (VirTis AdVantage Plus), then purified 3 times by precipitation in diethyl ether (296082, Sigma-Aldrich), and finally purified by dissolving in hot isopropanol (65 °C, 190764, Sigma-Aldrich), cooling on dry ice and filtering out the resulting precipitate. The precipitate was blown dry under N_2 gas, and dried completely in vacuo.

2.1.1 Synthesis

The synthesis reaction is depicted in Fig. 3.3, whereby LA-PEG-COOH is ultimately converted to LA-PEG-Hydrazide. First, LA-PEG-COOH was dissolved in dimethylformamide (DMF, 227056, Sigma-Aldrich) to a concentration of 25 mM. 5 equivalents of tert-butyl carbazate (B91005, Sigma-Aldrich) were then added (125 mM), followed by 10 equivalents of 4-(4,6-Dimethoxy-1,3,5-triazin-2-yl)-4-methylmorpholinium

tetrafluoroborate (250 mM,DMTMM BF4, 749613-1G, Sigma-Aldrich). Finally, 1 equivalent of n-methyl morpholine (NMM) was added (25 mM). Reaction mixture was placed on a rotating mixer and left to react for 72 hours at room temperature.

2.1.2 Purification and deprotection

PEG was first purified out of the reaction mixture (in DMF) by precipitating it in cold diethyl ether. The reaction mixture (1 mL) was added dropwise to cold diethyl ether (11 mL) inside of a Supelco SPE tube with 2 PE frit filters. The mixture was kept for 15 minutes on dry ice, before the ether was filtered out of the tube. The remaining precipitate was dried under N_2 gas, then re-dissolved in dichloromethane (DCM, 34856, Sigma-Aldrich) and recovered from the tube. The product was then purified by size-exclusion chromatography. A Pierce 1.8K molecular-weight cut-off (MWCO) Polyacrylamide Desalting Column (ThermoFisher Scientific, 43426) was equilibrated with water. The product was dissolved in 0.5 mL of water, then added to the top of the equilibrated column. Once product had fully entered column, water was added, and 20 fractions of approximately 1 mL were collected. Fractions were tested for the presence of PEG using thin-layer chromatography (TLC). Samples from each fraction were dotted onto silica-coated TLC plates (70643, Sigma-Aldrich). Plates were eluted with 1:9 methanol in DCM and stained with iodine. Fractions that tested positive by TLC for the presence of PEG were freeze-dried overnight (VirTis AdVantage Plus) and then analysed by ^{1}H-NMR (described below).

^{1}H-NMR results indicated the presence of impurities, so the product was further purified by dissolving in hot isopropanol (heated to 65 °C), then cooling slowly to approximately 4 °C. The resulting precipitate was filtered in a Supelco SPE tube with a PE frit filter, dried under N_2 gas, re-dissolved in DCM and recovered from the tube. The product was dried in vacuo and analysed by ^{1}H-NMR (described below).

In order to remove the protecting 'Boc' group to leave the desired hydrazide

group, the product was dissolved in 1 mL of 20% trifluoroacetic acid (TFA) in DCM (Fig. 3.4. The product was left shaking at 200 rpm at RT for 4.5 hours. After this time, the product was dried under N_2 gas, then redissolved in a small amount of DCM and added dropwise to cold diethyl ether in an Supelce SPE tube with PE frit filter. Filtering and recovery were performed as described above. The product was then purified once more using isopropanol (as described above) and sample was analysed by ^{1}H-NMR. Final product was dissolved in water and separated into aliquots of approximately 5 mg. These aliquots were lyophilized (details below) and stored at 4 °C. The product produced through this reaction will be henceforth referred to as LA-PEG-Hyd.

2.1.3 Proton nuclear magnetic resonance spectroscopy

^{1}H-NMR spectra were acquired on a Bruker Ascend 400 spectrometer with 30°pulses and a 5-second relaxation delay on a spectral width of 8,000 Hz. The spectra were referenced to residual $CDCl_3$ (151823, Sigma-Aldrich). Dr. Luca Bau is gratefully acknowledged for acquiring and interpreting the ^{1}H-NMR data.

2.1.4 TNBS assay for determination of hydrazide concentration

A solution of 0.2 M boric acid was made (borate buffer, B6768, Sigma-Aldrich), and pH was adjusted with 1M NaOH to a final pH of 9.3. A standard curve of acethydrazide (A8309, Sigma-Aldrich) was made in water (0.2 mM to 0.04 mM). LA-PEG-Hyd was also dissolved in water at three different concentrations: 0.16, 0.12, and 0.08 mM of PEG (as determined by dry weight of product). 100 μL of borate buffer was added to 100 uL of each standard and each sample (of LA-PEG-Hyd). A working solution of 30 mM 2,4,6-trinitrobenzenesulfonic acid (TNBS, P2297, Sigma-Aldrich) was then prepared in water, and 5 μL of this was added to each sample/standard. The samples/standards were incubated with the TNBS and borate buffer for 30 minutes at room temperature, then were added in duplicate

(90 μL per well) to a UV-transparent 96-well plate (CLS3635, Sigma-Aldrich). The absorbance spectra of the plate was measured on a plate reader (FLUOstar Omega, BMG Labtech) 30, 50 and 70 minutes after the TNBS was added to the samples. The standard curve was used to quantify the concentration of hydrazide groups present in the product.

2.2 PEGylation of therapeutic antibodies

Cetuximab and trastuzumab were obtained from Oxford University Hospitals NHS Foundation Trust. Amicon Ultra-0.5 mL Centrifugal Filters 30K MWCO (UFC503008, Merck Millipore) were used to exchange the suspension buffer of the antibody for an acetate buffer of pH 5.6 (20 mM sodium acetate, 154 mM NaCl). Briefly, antibody (as received from manufacturer) was added to the filter device, which was then topped off with acetate buffer to a final volume of 0.5 mL. Filters were spun in a benchtop centrifuge (5427R, Eppendorf) at 14,000 rcf for 10 mins, the filtrate was removed and the 450 μL of acetate buffer was added to filter. This process was repeated for a total of 3 centrifugation steps. After the final centrifugation at 14,000 rcf, the filters were placed upside-down into a clean microcentrifuge tube and spun for 2 minutes at 1000 rcf to collect the antibody concentrate. The resulting antibody concentrates were diluted with acetate buffer up to a concentration of approximately 2 mg/mL (4 mg/mL for batches scaled up for in vivo experiments). To this solution, sodium metaperiodate ($NaIO_4$, 71859, Sigma-Aldrich) was added to a final concentration of 10 or 5 mM. The antibodies were then incubated with the $NaIO_4$ at room temperature (RT) or at 4 °C for 30 minutes protected from the light. After incubation, the oxidation reaction was quenched by addition of acetate buffer or PBS (early vs late experiments) to a final volume of 0.5 mL per reaction. A 20 μL sample of antibody solution was added to 60 μL of 10 mg/mL Purpald (162892, Sigma-Aldrich) dissolved in 1N NaOH to verify successful oxidation of the antibody. The oxidized antibodies were then washed using the Amicon Ultra-0.5

mL Centrifugal Filters as described above. Two centrifugation steps were completed by replacing the buffer with PBS, as before. A solution of PBS containing the catalyst 5-methoxyanthranilic acid (11.1 mM, pH 5.6, 665118, Sigma-Aldrich) was then added to the concentrated antibodies, and 3 more centrifugation steps were completed with this catalyst-containing buffer. Finally, the filters were placed upside-down into a clean microcentrifuge tube and spun for 2 minutes at 1000 rcf to collect the antibody concentrate. Antibody concentrates were then diluted with catalyst-containing buffer to a concentration of approximately 2 mg/mL (4 mg/mL for batches scaled up for in vivo experiments). A volume of 10% of the final solution volume of 5 mM LA-PEG-Hyd linker solution was then added (or an equivalent volume of water for non-PEGylated antibody controls) to give a final ratio of at least 30 hydrazide-PEG molecules per antibody (15 per antibody for in vivo batches), and 10 mM of 5-methoxyanthranilic acid. The LA-PEG-Hyd (or water) and antibody solutions were incubated overnight at room temperature on a shaking mixer. After incubation the antibody solutions were washed using the Amicon Ultra-0.5 mL Centrifugal Filters (100K MWCO, UFC510096, Merck Millipore) as described above. A total of 5 centrifugation steps were completed, and at each step the buffer was replaced with HEPES buffer (40 mM HEPES [H3375, Sigma-Aldrich], pH adjusted to 8.5 using 1N NaOH). Antibody-PEG solutions were stored in HEPES buffer at 4 °C.

2.2.1 Quantification of aldehydes post-oxidation

Cetuximab and trastuzumab were oxidized as described above in Section 2.2 (10 or 5 mM $NaIO_4$, 30 mins at 4 °C or RT). Oxidized antibodies were washed and oxidation buffer was replaced twice with acetate buffer by centrifugation with Amicon 30K MWCO filters. 20 μL of a 4.346 mg/mL (8.33 mM) lucifer yellow dipotassium salt (LYCH, L1177, ThermoFisher) solution in water was added to 200 uL of oxidized antibody in solution. This corresponded to a molar ratio of approximately 250 LYCH

molecules per antibody. Non-oxidized cetuximab and trastuzumab were treated identically with LYCH as controls for any non-specific binding of LYCH. The samples were incubated overnight at RT. Conjugates were purified as above with antibody-PEG conjugates (5 centrifugation steps, replacing buffer with 40 mM HEPES buffer, pH 8.5). A standard curve of LYCH in HEPES buffer was made, ranging from concentrations of 40 to 2 uM. A standard curve of antibody (cetuximab) was created ranging from concentrations of 1 to 0.2 mg/mL. Standards and samples were added to a UV-transparent 96-well plate, and absorbance spectra were recorded using a plate reader (FLUOstar Omega, BMG Labtech). Concentration of LYCH in samples was determined directly from absorbance of samples at 428 nm, and comparison to absorbance of standard curve of LYCH (antibody alone did not absorb at this wavelength). Concentration of antibody in samples was determined by subtracting the absorbance of LYCH at 280 from the total absorbance of each sample, and using this difference to calculate a protein concentration from the standard curve of antibody at 280 nm.

2.2.2 SDS-PAGE analysis of PEGylated antibodies

Samples were diluted 3:1 in 4X Laemmli Sample Buffer (BioRad, 1610747), neat or supplemented with 10 % 2-mercaptoethanol (BME, Sigma, M6250). Samples containing BME were subsequently heated to 95 °C for 10 minutes. 10μL of each sample was added per well to a 4-20% pre-cast polyacrylamide gel (BioRad, 4561096), and 10 μL of protein standard ladder (BioRad 1610375) was added to the first lane for molecular weight determination. The gel was run in tris–glycine–sodium dodecyl sulfate (TGS) running buffer (BioRad, 1610732) at a constant voltage of 160 V for approximately 45 minutes. The gels were then stained for both PEG and protein, or just protein.

Barium-iodide staining for PEG

The gels were washed with water briefly, then incubated with 5 mL of 5% barium chloride ($BaCl_2$, 342920, Sigma-Aldrich) in 1N HCl and 2 mL of 0.1 N iodine solution (diluted in water, 38084, Sigma-Aldrich). After 10-15 minutes the iodine solution was replaced with water, which was replaced regularly until generic protein staining had disappeared. Gels were photographed at this stage, then were washed in water further until all iodine staining was removed. At this point the gels were restained for protein for at least 2 hours (in Coomassie stain: 0.05 g Coomassie Brilliant Blue R Dye [Sigma, B7920], 45 mL methanol, 10 mL acetic acid and 45 mL water) and finally destained overnight (in a 'destain solution' of 50% methanol, 10% acetic acid and 40% water).

Coomassie staining for protein

If gels were not to be stained for PEG, they were initially fixed for 20 minutes (in 'destain solution'), stained for 2 hours (in Coomassie stain) and finally destained overnight (in 'destain solution').

2.2.3 ELISA analysis of PEGylated antibodies

Recombinant human epidermal growth factor receptor (EGFR, ab155639) was diluted to a concentration of 0.3 μg/mL for cetuximab assays, while recombinant human HER2/ErbB2 (ab215657, abcam) was diluted to a concentration of 0.075 μg/mL for trastuzumab assays. Respective antigens (EGFR or HER2) were diluted in bicarbonate buffer (C3041-50, Sigma-Aldrich), and 100 μL of this solution was added per well to a 96-well Nunc Maxisorp well plate (44-2404-21, ThermoFisher). Plates were covered with an adhesive sheet and incubated at room temperature for 2 hours (all incubations were at room temperature). Wells were then washed 5 times using a solution of PBS and 0.05% Tween-20 (wash buffer). Wells were then blocked for 1 hour using 100 μL of 10% FBS in PBS. Cetuximab/trastuzumab

samples (untreated or PEGylated) were diluted in 10% FBS in PBS to maximum concentrations of 60 ng/mL. Serial 2-fold dilutions were made of each sample to generate a range of concentrations from 0.47 to 60 ng/mL. After blocking, wells were rinsed with wash buffer before 100 μL of each sample was added to the plate. Plates were then incubated for 1 hour, then washed 5 times with wash buffer. Anti-human HRP-conjugated antibody (W403B, Promega) was diluted in 10% FBS in PBS to a final dilution of 1:2500, and 100 μL of this solution was then added per well and incubated for 1 hour. After incubation, plates were washed 5 times with wash buffer. 100 μL of TMB substrate (34029, Thermofisher) was then added to each well and incubated for approximately 15 minutes (until a clear colour change to blue was observed for highest concentration standards). Development of plate was stopped by addition of 100 μL of 0.5M sulphuric acid. Absorbance of the wells at 450 nm was read using a plate reader (FLUOstar Omega, BMG Labtech).

2.2.4 Chromatographic analysis of PEGylated cetuximab

The hydrazone bond of PEGylated cetuximab was first reduced to a more stable hydrazide using the mild reducing agent sodium cyanoborohydride ($NaCNBH_3$, 296945, Sigma-Aldrich). $NaCNBH_3$ (5M in 1 M NaOH) was added to PEGylated, untreated (non-oxidized) and oxidized cetuximab at a ratio of 1:100 v/v. after treatment with $NaCNBH_3$ all antibodies were washed HEPES (40 mM, pH 8.5) with centrifugal filtration as described in 2.2. Interchain disulfide bonds of the antibody samples were reduced by treatment with 50 mM dithiothreitol (DTT) for 10 minutes at RT. Samples were analysed by reverse phase HPLC with an Agilent 1290 Infinity II with a quaternary pump (G7104A) and a diode array detector (G7117B) on a BioResolve RP mAb Polyphenyl column (2.1x100mm, 2.7μm particle size, 450 A pore size). The chromatographic separation was accomplished with a linear gradient of mobile phase A (0.1% TFA in water) and mobile phase B (0.1% TFA in acetonitrile) at a flow rate of 0.5 mL/min and a column temperature of 80 °C, with an 8 μL injection

volume. Elution was monitored at 210 and 280 nm, gradient details are presented in Table 2.1.

Time (min)	% Mobile Phase A	% Mobile Phase B
0	90	10
4	90	10
26.5	45	55
28	20	80
31	20	80
32.5	90	10
40.5	90	10

Table 2.1: Acetonitrile gradient used for elution of cetuximab from BioResolve RP mAb Polyphenyl column.

2.3 Functionalization and characterization of GNPs

2.3.1 Functionalization with PEGylated cetuximab

15 nm spherical bare citrate-capped gold nanoparticles (GNPs) were purchased from Stratech (CG-15-500-CYD, Stratech) at a reported concentration of approximately 1.64 x 10^{12} GNP/mL. GNPs were concentrated to approximately 1 x 10^{14} GNPs/mL, by first centrifuging in a Beckman Coulter Avanti J-26 XP centrifuge (rotor JA-14.50) for 1.5 hours at 15,500 rcf (to concentrate 12x), then further centrifuging these concentrated samples in a benchtop centrifuge (5427R, Eppendorf) for 30 minutes at 16,000 rcf, and removing supernant (5x further concentration). LA-PEG-cetuximab was then added to concentrated GNPs at a molar ratio of approximately 50:1, and incubated for 20 minutes at RT (for control mPEG-GNPs, an equivalent volume of HEPES with no LA-PEG-cetuximab was added). mPEG-SH (2 kDa, PG1-TH-2k-1, Nanocs) dissolved in water was added to the GNP mixtures to a final concentration of approximately 780 μM and incubated at RT for 20 minutes.

2.3.2 Purification

After functionalization, constructs were diluted 10x with wash buffer (PBS + 0.1% Tween-20), and centrifuged at 15,500 rcf for 50 minutes at 10 °C in 1.5 mL lo-bind eppendorf tubes (Z666505, Sigma-Aldrich). Supernatant was removed and GNPs were resuspended in wash buffer (20x dilution). GNPs were washed twice in this fashion, and required sonication with a Eumax Ultrasonic Cleaner (UD150SH-6L, Eumax) after centrifugation to resuspend pellet. Washed constructs were stored in PBS (pH 7.4) + 0.1% Tween-20.

2.3.3 UV-Vis spectroscopy

5 μL of GNP sample was diluted in 95 μL of pure water. Diluted samples were added to a UV-transparent microplate, and UV spectra were acquired by a plate reader (FLUOstar Omega, BMG Labtech) from 200-1000 nm. Acquired spectra were smoothed and baseline corrected (at 920 nm). Absorbance at 522 nm (peak of spectra) was used to estimate GNP concentration (c) from the Beer-Lambert law (2.1), using a molar extinction coefficient (ϵ) of 3.67 x $10^8 M^{-1} cm^{-1}$ as provided by the manufacturer. Path length (l) was estimated using the absorbance of water at 980 nm [183].

$$A = \epsilon l c \tag{2.1}$$

2.3.4 Sizing by DLS

Samples (blank GNPs in citrate buffer, GNPs functionalized with mPEG-SH, and GNPs functionalized with LA-PEG-cetuximab and mPEG-SH) were diluted 70x into pure water in a plastic cuvette, and were sized using dynamic light scattering with a ZetaSizerNano (Malvern Instruments Ltd, UK). Three measurements of size were made per sample, each consisting of approximately 12 runs.

2.3.5 TEM imaging

Samples (blank GNPs in citrate buffer, GNPs functionalized with mPEG-SH, and GNPs functionalized with LA-PEG-cetuximab and mPEG-SH) were deposited on a carbon support film 300 mesh 3mm copper grid (C267/050, TAAB Laboratories Equipment Ltd). Grids were then negatively stained briefly with 2% uranyl acetate. Grids were imaged with and FEI Tecnai 12 Transmission Electron Microscope (TEM). Dr. Brian Lyons is gratefully acknowledged for performing the TEM grid preparation and imaging.

2.3.6 SDS-PAGE analysis of cetuximab loading

SDS-PAGE analysis of antibody loading on GNPs was performed identically to the procedure described above in Section 2.2.2. Gels were stained for protein with Coommassie staining.

2.3.7 Quantification of cetuximab loading

10 μL of 12.5% BME in water was added to 40 μL of GNP samples. Samples were incubated with BME for 20 minutes at 37 °C, before centrifugation at 15,500 rcf for 25 mins. 35 μL was removed from supernatant of samples. A standard curve of cetuximab (1 to 0.1 mg/mL) was also incubated with BME. 5 μL of standards and samples (in triplicate) were added to a microplate. 150 μL of Advanced Protein Assay Reagent (57697, Sigma-Aldrich) was added to each well. Absorbance was read in a plate reader (FLUOstar Omega, BMG Labtech), absorbance at 590 nm was used to calculate protein concentration in supernatants removed from GNP samples.

2.4 In vitro characterization of cetuximab-loaded GNPs

2.4.1 Cell culture

MDA-MB-468 cells were kindly provided by Dr. Jyothi Menon, while MCF-7 cells were kindly provided by Dr. Sandra Nwokeoha. HT-29 cells were kindly provided by Dr. Megan Jackson. All cell types were cultured in high-glucose DMEM (11965-092, Life Technologies). Media was supplemented with 10% fetal bovine serum (FBS; 10270-106, Life Technologies) to give 'growth media'. Cells were incubated in cell culture flasks at 37 °C in 5% CO_2 and were passaged upon reaching ∼80% confluency. To passage cells, a wash with 5 mL of DPBS was followed by incubation with 2.5 mL of trypsin-EDTA (59418C, Sigma-Aldrich). Trypsin was removed, cells were resuspended in growth media and were centrifuged at 181 rcf for 5 minutes to allow for cell debris and residual trypsin to be removed. The cell pellet was then resuspended in growth media and placed either into a new cell culture flask, or used in experiments. Cell counting was performed with a haemocytometer and trypan blue (to exclude non-viable cells from count).

After trypsinization and cell recovery, cells were resuspended in growth media and incubated at 37 °C for 45 minutes (to allow surface receptors to recover from trypsin exposure). Cells were counted, centrifuged and resuspended in cold PBS + 1% BSA to a final concentration of 1 x 10^6 cells/mL.

2.4.2 Determination of EGFR expression by flow cytometry

Fluorescently-tagged EGF (E13345, ThermoFisher) was added to MDA-MB-468, MCF7, or HT-29 cells in PBS + 1% BSA to a final concentration of 2 μg/mL (final concentration of 0.5 μg/mL was used for probing EGFR expression of HT-29 cells compared to MDA-MB-468 cells, as presented in Section 4.1.1). Cells were incubated for 1 hour at 4 °C in the dark. After incubation, cells were centrifuged, supernatant was removed. Cells were washed a total of 3x with cold PBS + 1% BSA. Note, for

analysis of HT-29 EGFR expression, cells were not washed prior to flow cytometric analysis. Samples were run on a BD FACSCalibur Flow Cytometer, and 10,000 events were acquired for each sample. FlowJo v10.5 data analysis software (FlowJo LLC) was used to process the results obtained.

2.4.3 Determination of cetuximab binding by flow cytometry

Cetuximab or LA-PEG-cetuximab was added to MDA-MB-468 cells in PBS + 1% BSA to a final concentration of 10 μg/mL. Cells were incubated for 1 hour at 4 °C. After incubation, cells were centrifuged, supernatant was removed. Cells were washed a total of 3x with cold PBS + 1% BSA. After washing, fluorescently tagged anti-human secondary antibody raised in goat (A-11013, ThermoFisher) was added to cells at a final concentration of 8 μg/mL. Samples were again incubated for 1 hour at 4 °C in the dark, and were washed and analysed as above.

2.4.4 Inhibition of EGF binding analysed by flow cytometry

Cetuximab or cetuximab-GNPs were added to MDA-MB-468 cells in PBS + 1%BSA at concentrations between 5 and 1.25 μg/mL of free cetuximab, and 16 and 4 x 10^{11} cetux-GNPs/mL. At the same time, fluorescently-tagged EGF (E13345, ThermoFisher) was added to a final concentration of 0.5 μg/mL. As a control for non-specific blocking of EGF binding by GNPs, GNPs functionalized with mPEG but not LA-PEG-cetuximab were also incubated with cells and EGF at a concentration of 16 x 10^{11} cetux-GNPs/mL. Cells were incubated for 1 hour at 4 °C. After incubation, samples were analysed as above (no washing).

2.5 In vivo model for delivery of cetuximab and cetuximab-GNPs

Female CD-1 nude mice were purchased from Charles River (Crl:CD1-Foxn1nu (086)). Animals were housed and cared for according to UK Home Office guidelines.

2.5.1 Subcutaneous tumour innoculation

HT-29 cells were cultured and counted as described in Section 2.4.1. Cells were resuspended in serum-free DMEM media and transported to animal facility on ice. Each mouse was anaesthetized using 2-5% isoflurane, and inoculated subcutaneously with one or two injections of between 3-4 x 10^6 cells. If mouse was to be implanted with two tumours, one injection was done on each flank.

2.5.2 Animal tumour and welfare monitoring

Weights of the mice were tracked and tumour growth was monitored by measurements with callipers. Treatment began when the tumours had reached sizes of approximately 100 mm^3 (as calculated by half the product of three dimensions: (l x w x h)/2).

2.6 Determination of circulation kinetics of cetuximab and cetuximab-GNPs

2.6.1 Dosing

Mice were briefly anaesthetized using 2-5% isoflurane, and were injected with 50 or 25 uL of cetuximab GNPs (1.2 x 10^{14} or 6 x 10^{13} GNPs/mL respectively) or cetuximab via the left lateral tail vein. Mice were closely monitored following injection,

and any mice showing signs of adverse effects not immediately improving during recovery in a warmed cage were sacrificed.

2.6.2 Blood and tissue sampling

Blood samples (up to 20 uL) were taken from the right lateral tail vein at specific time points ranging from 5 minutes to 24 hours post-injection. Blood samples were immediately diluted in 180 uL of PBS and centrifuged at 500 rcf for 5 minutes. After centrifugation, plasma was removed from supernatant of centrifuged blood samples and was stored at -80 °C until analysis. After final time point, mice were sacrificed; their tumours, and livers were recovered and stored at -80 °C until analysis.

2.6.3 ELISA for quantification of cetuximab and cetuximab-GNPs

Tissue preparation

Tumours and livers were diluted and homogenized in 1X cell culture lysis reagent (E1531, Promega) supplemented with protease inhibitor cocktail (ab65621, abcam). Tumours were diluted in lysis buffer to a concentration of 40 mg/mL, while livers were diluted to a concentration of 700 mg/mL. After homogenization, liver homogenate was further diluted 100x with PBS. Standards curves were prepared by spiking control homogenate (tumour or liver) or plasma from untreated mice with known amounts of the injectate (of cetuximab or cetuximab-GNPs).

ELISA

Anti-human antibody (A9544, Sigma-Aldrich) was diluted to a final concentration of 1 μg/mL in bicarbonate buffer (C3041-50, Sigma-Aldrich), and 50 μL of this solution was added per well to a 96-well Nunc Maxisorp well plate. Plates were covered with an adhesive sheet and incubated at overnight at 4 °C. After coating, wells were washed 5 times using a solution of PBS and 0.05% Tween-20 (wash buffer). Wells were then blocked for 1 hour with 100 μL of 10% FBS in PBS. After blocking, wells

were rinsed with wash buffer before 50 μL of each sample or standard was added to the plate (in triplicate). Plates were then incubated for a minimum of 2 hours (up to 4 hours), then washed 5 times with wash buffer. Anti-human HRP-conjugated antibody (W4031, Promega) was diluted 1:2500 in 10% FBS in PBS, and 100 μL of this solution was then added per well and incubated for 1 hour. After incubation, plateswere washed, developed, and read as in Section 2.2.3.

2.6.4 Stability of cetuximab-GNPs in plasma

Samples of cetuximab-GNPs were diluted 20x in human plasma (Human plasma EDTA K2 Mixed Gender, Pooled, not Filtered - HMPLEDTA2, Seralab) pre-warmed to 37 °C. Samples were incubated at 37 °C between 5-45 minutes. After incubation samples were centrifuged at 15,500 rcf for 25 minutes. The supernatant was gently removed and diluted 10x in PBS. Standard curve was prepared by spiking 10% human plasma in PBS with known concentrations of LA-PEG-cetuximab.

ELISA

Anti-cetuximab antibody (MAB9626, R & D Systems) was diluted to a final concentration of 1 μg/mL in bicarbonate buffer, and 50 μL of this solution was added per well to a 96-well Nunc Maxisorp well plate. Plates were covered with an adhesive sheet and incubated at overnight at 4 °C. After coating, wells were washed 5 times using a solution of PBS and 0.05% Tween-20 (wash buffer). Wells were then blocked for 1 hour with 100 μL of 10% FBS in PBS. After blocking, wells were rinsed with wash buffer before 50 μL of each sample or standard was added to the plate (in triplicate). Plates were then incubated for a minimum of 2 hours (up to 4 hours), then washed 5 times with wash buffer. Anti-cetuximab HRP-conjugated secondary antibody (HCA228P, BioRad) was diluted to a concentration of 0.5 μg/mL in 10% FBS in PBS, and 100 μL of this solution was then added per well and incubated for 1 hour. After incubation, plates were washed, developed, and read as in Section 2.2.3.

2.7 US treatment of tumours

2.7.1 US set-up and parameters

Fig. 4.5 illustrates the set-up used to expose tumour-bearing mice to ultrasound (US). The water tank was degassed and heated to 37 °C. Two HIFU transducers were mounted in the tank orthogonal to each other, but confocally aligned. The HIFU transducers were single element spherically focused with a fundamental frequency of 0.5 MHz (henceforth referred to as HIFU transducers; H-107C-033 and H-107C-034, Sonic Concepts, USA). HIFU transducers had a focal length of 63 mm, outer diameter of 64 mm, and rectangular cutouts (45 x 18 mm). These rectangular cutouts within the HIFU transducers allowed for two L11-5v 128-element linear arrays with 6.25 MHz centre frequency, 38 mm aperture, and 5-11 MHz bandwidth (Verasonics Inc.) to be mounted within and aligned with the HIFU transducers (so HIFU focus was within elevational plane of arrays). These arrays were used to detect and map cavitation events. Custom made software in MATLab (written by Dr. Christian Coviello, Dr. Calum Crake, and Seán Finn) was used to control a signal generator (33250A , Agilent), which output to a 55 dB power amplifier (1040L, Electronics and Innovation). The output from the power amplifier passed through an impedance matching network (provided by transducer manufacturer, Sonic Concepts) to the HIFU transducers. Voltage was measured at the output from the RF power amplifier with a high-voltage probe and oscilloscope. Synchronisation between transmit and receive signals was enabled by using an output trigger pulse from the Versonics system (Vantage 256 Channel, Verasonics Inc). A HIFU driving frequency of 0.5 MHz, pulse repetition frequency (PRF) of 0.5 Hz, and duty cycle (DC) of 5% (50,000 cycles per burst) were used during US treatment. The peak rarefactional focal pressure (PRFP) was varied between 1.5-2 MPa. During treatment, B-mode imaging was used to monitor correct targeting of HIFU. Interleaved with the B-Mode, acoustic cavitation signals were passively recorded and mapped with

a custom PAM algorithm in order to visualise the magnitude and spatial extent of cavitation activity in real time. The PAM image was created for an area of 20 x 10 mm around HIFU focus. Catherine Paverd, Claudia Hill, and Dr. Christophoros Mannaris are all gratefully acknowledged for operating the US set-up during the studies presented in this thesis.

2.7.2 Dosing with cetuximab/cetuximab-GNPs and US treatment

Mice were anaesthetized using 2-5% isoflurane prior to cannulation of the tail vein. Mice were mounted on a custom made platform and were placed in the pre-warmed (37 °C) water tank. The two orthogonal HIFU transducers were aligned on to one of the tumours on the mouses' flank using the B-mode functionality of the linear arrays for guidance. Mice received a total of either 5 μg of cetuximab in 25 μL of PBS, or 1.5 x 10^{12} cetuximab-GNPs in 25 μL of PBS + 0.1% Tween-20. Within each drug group, half the mice received a total of 50 μL of Sonovue® (SV, Bracco), while the other half received 1.1 mg of sonosensitive particles (SSPs were kindly provided by Dr. Megan Jackson) in 50 μL of 5% glucose. SV was resuspended in PBS according to manufacturers instructions. The full dose of drug was given in one bolus injection at the onset of US treatment. The full dose of SSPs was also given in one bolus injection, immediately following the injection of drug at the onset of US treatment. The dose of SV however, was split into two injections: half at the onset of US treatment, and the other half 4 minutes later. At time t = 0, the HIFU transducers were turned on, and drug + CN was injected. The mouse platform was slowly moved in all three dimensions to 'paint' out the volume of the tumour. The treatment continued for a total of 600 seconds, after which time the mouse was removed from the water tank.

2.7.3 ELISA for quantification of cetuximab/cetuximab-GNPs

After US treatment, mice were culled and tumours were excised, rinsed with PBS, and frozen for analysis. Tumours were homogenized and analysed by ELISA for concentration of cetuximab/cetuximab-GNPs as described above in Section 2.6.3.

2.8 In vitro delivery of ColoAd

A549 cells were obtained from the European Collection of Cell Cultures (86012804, ECACC). All cell types were cultured in high-glucose DMEM (11965-092, Life Technologies, UK), as described in Section 2.4.1.

2.8.1 In vitro tissue-mimicking phantom

The phantom holder was made of a Delrin® rectangular frame, with the same outer dimensions as a standard microplate. The windows of the phantom were covered with Mylar®, and a layer of rubber gasket was placed between each Mylar sheet and plastic frame to create a water-tight seal when MCCell is screwed shut. Each MCCell was fitted with three symmetrically-spaced holes on either side, through which 1.2 mm metal rods were inserted, in order to create a flow channel within a gel cast in the phantom. The two remaining sides contain one hole each, to allow for injection of liquid into the MCCell. Female luer fittings are inserted in each hole, so that tubing can be connected to each flow channel. Phantom holder frame and components were sterilized by immersion in 70% ethanol for approximately 2 hours, followed by irradiation with UV light within a biological safety cabinet. For viral delivery studies, A549 cells were resupended in a growth media consisting of 2x DMEM supplemented with 4% FCS. Cells were counted as described in Section 2.4.1. UltraPure Low Melting Point Agarose (16520050, Thermofisher) was added to deionized water to make a 4.0 or 3.0% agarose solution (for 0.5 MHz and 1.6 MHz experiments respectively). Agarose was dissolved by microwaving, and the

resulting solution was placed in a water bath at 37 °C. Once cooled to 37 °C, it was combined with cell suspension at a 1:1 ratio to make a final solution of 2 or 1.5% or, with a concentration of 8.5 x 10^4 or 2.75 x 10^5 cells/mL (for 0.5 MHz and 1.6 MHz experiments respectively). ∼50 mL of this solution was injected slowly into a phantom holder with a sterile syringe. Once full, the phantom holder was sealed with luer fittings, and kept at 4 °C for approximately 1 hour to allow gel to set. Phantoms were kept in incubator at 37 °C in 5% CO_2 until delivery experiment.

2.8.2 In vitro US setup

Fig. 5.1 illustrates the set-up used to investigate delivery of ColoAdRFP into a tissue-mimicking phantom with US +/- CN. Experiments were conducted in a water tank, filled with deionized, and degassed water at room temperature. The phantom holder and US transducers were mounted in the tank on transversally aligned 3-D positioning systems. A single element spherically focused transducer with fundamental frequency of 0.508 MHz (henceforth referred to as HIFU transducer; H107-D SN13, Sonic Concepts, USA) was driven at its fundamental frequency or third harmonic, while a smaller spherically focused transducer with fundamental frequency of 7.5 (for 0.5MHz exposures) or 15 MHz (1.6 MHz exposures) was used as a 'passive cavitation detector' (PCD; Panametrics). Custom made software in LabView (National Instruments) was used to control a signal generator (CHECK 33220A, Agilent Technologies), which output to a 55 dB, 300 watt, RF power amplifier (A300 RF Power Amplifier, Electronics and Innovation). The output from the RF power amplifier then passed through a matching network (Sonic Concepts) to the HIFU transducer. Voltage was measured at the output from the RF power amplifier with a high-amplitude voltage probe and oscilloscope. Emissions recorded by the PCD were passed through a 5 MHz high-pass filter (FILT-HP2-B, Allen Avionics Inc.). Subsequent to filtering, PCD voltage signals were amplified by a pre-amplifier (SR445A, Stanford Research Systems), and sampled at a frequency of 100 MHz. Data was ac-

quired at the onset of the HIFU burst, and for the duration of 200 μs. The flow-loop for the US experiments is outlined in Fig. 5.1. A MINIPULS Evolution peristaltic pump (Gilson) induces flow through tubing, from a stock solution, through the flow channel created within the agar gel in the MCCell and into a waste container. The pressures generated by the HIFU transducer at its focus were calibrated as a function of the RF power amplifier output using a 75 μm diameter needle hydrophone (Precision Acoustics, UK).

After metal rods were removed from phantom, sterile i.v. extension line tubing with male luer fittings on either end (Braun) was attached to channel inlet and outlet. The holder was then submerged in the water bath and mounted on the 3-D positioning system. Air was flowed through the channel by the peristaltic pump. The HIFU and PCD transducers were both confocally and coaxially aligned to the air-filled channel using a pulser-receiver (DPR300, JSR Ultrasonics) in pulse-echo mode.

ColoAdCMVRFP (kindly provided by Dr. Margaret Duffy) was diluted to a final concentration of 1 x 10^9 virus particles (VP) per mL. Immediately prior to each channel exposure requiring CN, SSPs were added to a final volume of 1.5 mL of virus solution (per channel). The SSPs were diluted to a final concentration of 1 mg/mL.

The solution of virus (with and without CN) was flowed through the phantom. For exposures at 0.5 MHz, the HIFU transducer was driven at its fundamental frequency for for 1000 bursts of 5000 cycles. The channel was thus insonated at each position for a total of 200 seconds. The burst period was 0.2 s (pulse repetition frequency of 5 Hz), and a duty cycle of 5%. The PRFP was varied between 2-2.7 MPa. For exposures at 1.6 MHz, the HIFU transducer was driven at its third harmonic for 500 or 1000 bursts of 4000 cycles. The channel was thus insonated at each position for a total of 50 or 100 seconds. The burst period was 0.1 s (pulse repetition frequency of 10 Hz), and a duty cycle of 2.5%. The PRFP was approximately 3.5

MPa. After insonation, air was flowed through each channel to flush out any virus solution remaining in the channel.

2.8.3 Analysis of PCD data

Voltage data acquired from the PCD was analyzed in MatLab (MathWorks, USA) using code adapted from code written by Dr. Susan Graham. Briefly, voltage traces were truncated to contain an even number of cycles (to minimize FFT leakage) and any DC bias was subtracted. The data was windowed using a Hamming window (to minimize FFT leakage). A single-sided FFT of the windowed data was taken, and was adjusted by the Hamming window energy correction factor. FFT data was truncated to frequencies between 0-15 MHz, as it was assumed that little power would be present in higher frequencies.

2.8.4 Microscopy and image analysis

Following US exposure, the phantom was placed in an incubator at 37 °C in 5% CO_2. 3, 5, or 6 days post-exposure, a section of gel approximately 1-cm wide was excised around each channel. The slices were flipped 90°, and placed on a glass microscope slide. Slices were imaged using a inverted Nikon Ti Eclipse fluorescent microscope (Nikon Instruments, Melville, NY, USA), with CoolLED pE Excitation System (CoolLED, UK). Channels were scanned lengthwise at 4x magnification with brightfield and a TRITC fluorescent filter (Excited HQ545/30x, Dichrioc Q570LP, Emitter HQ620/60m). After imaging the channels length-wise, the channels were sliced orthogonally to the direction of flow and imaged again. Images were stitched using the NIS-Elements Advanced Research software, and processed with ImageJ. Quantification of ColoAdRFP delivery with 1.6 MHz US: for each axial slice of an exposed spot along a given channel, a z-stack of 5 images 500 μm apart was acquired around the area determined to be the US focus (determined by damage seen on brightfield). The maximum intensity pixels of the two adjacent stack slices

with the most in-focus cells were added to create one composite image. The cell counter plugin in ImageJ was then used to label all RFP-positive cells, and calculate the distance of each labelled cell from the centre of the channel.

2.9 In vivo model for delivery of ColoAd

Female CD-1 nude mice were purchased from Charles River (Crl:CD1-Foxn1nu (086)). Animals were housed and cared for according to UK Home Office guidelines. Animal welfare and tumours were monitored as per Section 2.5.2.

2.9.1 Subcutaneous tumour innoculation

DLD-1 cells were kindly provided by Egon Jacobus, and were cultured and counted as described in Section 2.4.1. Tumour innoculation was performed as described in Section 2.5.1.

2.10 US treatment of tumours

2.10.1 US set-up and parameters

US set-up is described in Section 2.7.1. Mice were treated with 1 x 10^{10} VP of ColoAdCMVLuc or ColoAdSALuc (kindly provided by Egon Jacobus), in solution with either i) Sonovue, ii) active sonosensitive particles (SSPs), or iii) inactive sonosensitive particles (iSSPs). Two treatment regimes (Regime 1 and Regime 2) were investigated here. In the first treatment regime (Regime 1), mice were dosed with a co-injection of 1 x 10^{10} ColoAdCMVLuc VP with 1) 1.75 mg of SSPs, 2) 1.75 mg of iSSPs, or 3) 50μL of SV as prepared to manufacturers instructions. The doses for all mice were split into two injections (half at t = 0, half at t = 4 mins). The PRFP was held constant at a value of approximately 1.5 MPa, and mice were treated with US for a total of 10 minutes.

In the second treatment regime (Regime 2), mice were dosed with a co-injection of 1 x 10^{10} ColoAdSALuc particles with 1) 1.75 mg of SSPs, or 2) 50μL of SV as prepared to manufacturers instructions. The doses for all mice were split into two injections (half at t = 0, half at t = 2.5 mins). The PRFP was varied between approximately 1.5-2 MPa, depending on the cavitation output measured during treatment. Mice were treated with US for a total of 5 minutes.

2.11 IVIS imaging of luciferase production

At multiple time points after mice were treated with luciferase-expressing ColoAd they were imaged using an in vivo imaging system (IVIS Lumina, PerkinElmer. Mice were anaesthetized using 2-5% isoflurane and were injected intraperitoneally or intravenously with 100 uL of 15.8 mg/mL luciferin (15225733, ThermoFisher). For intraperitoneal administration of luciferin, the dose was split between two injections of 50 uL on each side of the mouses' abdomen. 5 minutes after dosing with luciferin, the mice were imaged, and images were taken every minute up to a total of 12 minutes.

2.12 Ex vivo tumour processing

Tumours were homogenized in PBS at a concentration of 125 mg/mL.

2.12.1 Analysis of luciferase content

Tumour homogenate was diluted with 5x reporter lysis buffer (E4030, Promega) at a ratio of 4:1. Homogenate in lysis buffer was subject to 1 freeze-thaw cycle, after which 25 μL of homogenate was added (in triplicate when volume of homogenate allowed) to a white opaque microplate. 25 μL of luciferase assay substrate (E151A, Promega) in luciferase assay buffer (E152A, Promega) was added per well, and luminesence was read immediately using a plate reader (FLUOstar Omega, BMG

Labtech).

2.12.2 qPCR analysis of genome copies

Genomic DNA was isolated from homogenized tissue samples and standards (prepared by spiking known amounts of ColoAd into control tumour homogenate) using the GenElute Mammalian Genomic DNA Miniprep Kit from Sigma-Aldrich. Briefly, 200 μL of homogenate from each sample/standard was digested with 20 μL of Proteinase K (P2308, Sigma-Aldrich) and 180 μL Lysis Solution T (B6678, Sigma-Aldrich) at 55 °C. DNA was then extracted from digested samples using GenElute MiniPrep Binding Columns and associated solutions as per manufacturers instructions (G1N350, Sigma-Aldrich). Quantitative polymerase chain reaction (qPCR) was performed with the eluted DNA samples, by combining 5 μL of sample with primers and probes specific for the ColoAd genome, and 2x qPCRBIO Probe Mix Hi-ROX (PB20.22, PCR Biosystems, UK). The primers were as follows: 5'-TACATGCACATCGCCGGA-3' (forward), 5'-CGGGCGAACTGCACCA-3'(reverse). The probe used was: 5'-[6FAM]-CCGGACTCAGGTA CTCCGAAGCATCCT-[TAMRA]-3'. All probes and primers were purchased from Sigma-Aldrich, UK. The qPCR was performed on an Applied Biosystems StepOnePlus^{TM} Real-Time PCR System using the cycle program recommended by the manufacturers of the qPCRBIO Probe Mix Hi-Rox (2 min at 95 °C, followed by 40 cycles of 5 seconds/30 seconds at 95 °C/65 °C).

2.12.3 Immunohistochemistry

Tumours were excised and fixed in 10% neutral buffered formalin (HT5011-15ML, Sigma-Aldrich) for 2 days. After fixing, tumours were washed with and resuspended in 70% ethanol. Fixed tumours were shipped to the pathology service at Bart's Cancer Institute. Here tumours were processed in a Sakura VIP 6AI (Vacuum Infiltration Processor) overnight. Sections were cut at 4μm, at 4 levels

per block. Hematoxylin and eosin staining (H & E) staining was done on a Leica Autostainer XL, while immunostaining was done on a Ventana XT using the OmniMap method. Tumours were stained for hexon (MAB8052, Merck Millipore) and endomucin (Sc-65495, Santa Cruz Biotechnoloy). Slides were scanned using a Hamamatsu NanoZoomer S21. Images were analysed using ImageJ with the BioFormats Plugin.

2.13 Characterization of anti-ColoAd antibodies

An anti-adenovirus monoclonal IgG1 was obtained from Merck Millipore (MAB8052, Merck Millipore, USA). An anti-adenovirus monoclonal IgG2a was obtained from Abcam (ab7428, abcam). An isotype control mouse serum IgG was obtained from Sigma-Aldrich (IC IgG; I5381, Sigma-Aldrich). Suppliers indicated that MAB8052 and ab7428 were raised using isolated hexon polypeptide, or whole Ad3 respectively, and recognize all serotypes of adenovirus.

2.13.1 Western blot analysis

Viral proteins of ColoAd virus (kindly supplied by Dr. Margaret Duffy from the Oxford Department of Oncology) were separated using SDS-PAGE as in Section 2.2.2. Subsequently, proteins were transferred overnight at 30V to a nitrocellulose membrane with 0.2μm pore size (162-0213, BioRad, UK) in a transfer buffer consisting of Tris-Glycine-SDS running buffer with the addition of 20% methanol. Following transfer, membranes were removed and blocked for 1 hour in a blocking buffer of 5% non-fat milk (70166, Sigma-Aldrich, UK) in DPBS (14190094, Life Technologies, UK). Membranes were rinsed once in DPBS, and incubated with either 9C12, ab7428 or MAB8052 at a concentration of 1 μg/mL in DPBS and 10% blocking buffer for 1 hour. Membranes were then washed 3 times with a solution of DPBS and 0.05% Tween-20 (161-0781, BioRad, UK). Membranes were then incubated for 1 hour with an anti-mouse IgG Horseradish Peroxidase(HRP)-conjugated anti-

body raised in goat (HAF007, R&D Systems, USA) diluted 1:1000 from stock in DPBS and 10% blocking buffer. Following incubation with the secondary antibody, membranes were washed 5 times with a solution of DPBS and 0.05% Tween-20. Immobilon Western HRP Substrate (WBKLS0500, Merck Millipore, USA) was used for chemiluminescent detection. Working HRP substrate was prepared by mixing equal volumes of luminol reagent and peroxide solution. 3 mL of HRP substrate was added to each membrane, which were incubated at room temperature for 1 minute. The excess substrate was drained, and the membranes were covered in clear plastic wrap. The membranes were exposed to X-ray film (CL-XPosure^{TM} Film, 34088, ThermoFisher, UK) for approximately 1 second. The films were developed using an Agfa CP 1000 film processor.

2.13.2 Dot blot analysis

Samples of ColoAd were serially diluted 1:10 twice into DPBS, and spotted onto a nitrocellulose membrane (162-0213, BioRad, UK). Membranes were blocked for 1 hour in a blocking buffer of 5% non-fat milk in DPBS. Membranes were rinsed once in DPBS, and incubated with either ab7428, MAB8052 or mouse IgG isotype control at a concentration of 1 μg/mL in DPBS and 10% blocking buffer for 1 hour. Membrane was probed with secondary (anti-mouse IgG HRP), washed, and developed as above in Section 2.13.1.

2.13.3 Infectivity assay

A549 cells were plated in a tissue-culture 96-well plate (10^4 cells in 100 μL DMEM growth media per well), and incubated overnight at 37 °C to allow for cell-adherence. VPs were well mixed with varying concentrations of antibody in growth media and incubated at 37 °C for one hour. 100 μL of virus/antibody solution was added to each well, at a concentration of 1000 VP per cell. Plates were then incubated for 24 hours at at 37 °C and 5% CO_2, before assaying of reporter gene expression.

Flow cytometry for quantification of RFP production

24 hours post-infection, media was removed from each well, cells were washed with 100 μL of DPBS, and were incubated with 25 μL of trypsin-EDTA. Cells were resuspended in 200 μL of growth media, and transferred to round-bottomed tubes for flow cytometry. Cells were analysed using a Becton Dickinson FACSCalibur Flow Cytometer with CellQuestPro analysis (BD Biosciences). 10^4 events were detected per sample, and FlowJo v10.2 data analysis software (FlowJo LLC) was used to process the results obtained. Untreated cells were used as negative controls to set the appropriate gates. The gating tree was set as follows: 1) Polygonal gating of FSCH/SSCH to exclude dead cells and cellular debris to 2) Gating of FL2-H positive cells to identify fraction of live, single cells which express RFP.

2.13.4 ELISA analysis of affinity of ColoAd antibodies

An indirect ELISA was used to compare the relative affinities of MAB8052 and ab7428 for ColoAd. Firstly, Nunc Immunosorp 96-well plates were coated with 100 μL of 200 ng/mL ColoAd (not heat inactivated) in PBS. Plates were covered with an adhesive sheet and incubated at room temperature for 2 hours. Wells were then washed 5 times using a solution of PBS and 0.05% Tween-20 (wash buffer). Wells were then blocked for 1 hour using 100 μL of 1% BSA in PBS. MAB8052 or ab7428 samples were diluted in 1% BSA in PBS to maximum concentrations of 225 ng/mL. Seven three-fold serial dilutions of this top standard were made for each antibody. After blocking, wells were rinsed with wash buffer before 100 μL of ab7428/MAB8052 serial dilutions were added to the plate. Plates were then incubated for 2 hours at 37 °C, then washed 5 times with wash buffer. Anti-mouse HRP-conjugated antibody (HAF007, R&D Biosystems) was diluted in 1% BSA in PBS to a final dilution of 1:1000, and 100 μL of this solution was then added per well and incubated for 1 hour. After incubation plates were washed, developed and read as in Section 2.2.3.

2.14 Functionalization and characterization of NHS-GNPs

Spherical gold nanoparticles (GNPs) were purchased from Nanopartz (C11-20-TNHS-50, Nanopartz,USA) with a stated diameter of 20 nanometers and surface-coating of polymer with N-hydroxysuccinimide (NHS) ester terminal groups. NHS-GNPs were resuspended in DPBS and 10% DMSO (D8418, Sigma-Aldrich, UK), vortexed and sonicated in an ultrasonic water bath (UD150SH-6L Eumax Ultrasonic Cleaner, Eumax) to disperse any aggregates. ab7428 suspended in DPBS was added to the nanoparticles at a molar ratio of 12.4:1. An isotype control IgG (IC IgG) from mouse serum, was also added to separate nanoparticle solutions at the same molar ratio as the ab7428. Equal volumes of antibody solutions and nanoparticles were combined, to create a concentration of 5% DMSO in the final reaction solution. The antibody-GNP solutions were repeatedly sonicated and vortexed, then were left overnight on a shake-plate to allow all remaining NHS groups to hydrolyze.

2.14.1 Purification of functionalized GNPs

Antibody-GNP formulations were purified from free unreacted antibody by centrifugation at 13 300 rcf for 25 minutes in a bench-top Micro Centaur Plus centrifuge (MSE, UK), followed by resuspension in 1% DPBS and 0.1 or 0.05% Tween-20 (161-0781, BioRad, UK) — a process which was repeated between three to six times to ensure purity of final sample. After final spin, samples were resuspended in DPBS.

2.14.2 UV-Vis

UV-Vis spectroscopy was performed as in Section 2.3.3.

2.14.3 Dot blot analysis

Samples were taken from ab7428-GNP or IC IgG-GNP formulations 1) before purification steps, 2) from sample supernatant after first centrifugation, 3) from sample

supernatant after final centrifugation, and 4) from final product resuspended in DPBS. These samples were diluted either 1:10 or 1:40, and spotted onto a nitrocellulose membrane (162-0213, BioRad, UK). Membranes were blocked for 1 hour in a blocking buffer of 5% non-fat milk in DPBS. Membranes were then developed as described above in Section 2.13.1.

2.15 Characterization of antibody-GNP + ColoAd

2.15.1 Dot blot test of antibody binding in CsCl and glycerol

A dot blot was used to test whether the presence of glycerol or CsCl prevents the binding of ab7428 to ColoAd. Samples of ColoAd were spotted onto a nitrocellulose membrane. Membranes were blocked for 1 hour in a blocking buffer of 5% non-fat milk in DPBS. Membranes were rinsed once in DPBS, and incubated with ab7428 at a concentration of 1 μg/mL in 10% blocking buffer and either 1.47 g/cm^3 CsCl solution (C4036, Sigma-Aldrich), 40% glycerol, or DPBS for 1 hour. Membranes were then developed as described above in Section 2.13.1.

2.15.2 CsCl density gradient

ColoAdRFP was mixed at 37 °C for 1 hour with ab7428-GNP and IC IgG-GNP conjugates at a ratio of 100 GNPs per VP in DPBS. Solutions of 1.32 g/cm^3 and 1.47 g/cm^3 caesium chloride (CsCl) were prepared in deionized water and a final concentration of 0.05M Tris-HCl. A 40% glycerol solution was prepared in deionized water with 0.01M Tris-HCl and 0.001M EDTA. All three solutions were sterilized by filtering through a 0.22μm pore-size syringe filter. In two separate Beckman Ultra-Clear centrifuge tubes (334060, Beckman Coulter, UK) a CsCl gradient was made by first adding 3 mLs of 1.32 g/cm^3 CsCl solution to each tube, then carefully underlaying 2 mL of 1.47 g/cm^3 CsCl with a wide-bore needle and 2.5 mL syringe. 2 mL of 40% glycerol solution was then carefully added to the top of the gradient.

GNP-antibody + virus (GNP + ColoAdRFP) constructs were added to the top of the gradient, and the centrifuge tubes were capped and balanced with DPBS. Tubes were centrifuged in a Beckman L8-55 Ultra-Centrifuge with a SW-40τi rotor for 1.5 hours at 25,000 rpm at 10 °C. After spinning, tubes were removed and photographed. Virus bands were carefully aspirated using a wide-bore (21G) needle. A separate needle was then used to carefully remove the GNPs which pelleted to bottom of the centrifuge tube.

qPCR analysis of CsCl banded GNP ColoAdRFP constructs

A standard curve was prepared from a serial dilution of ColoAd in DPBS. Genomic DNA was isolated from samples obtained from CsCl banding of GNP + virus constructs and the prepared standards using the GenElute Mammalian Genomic DNA Miniprep Kit from Sigma-Aldrich as described in 2.12.2. Samples were however, digested with Proteinase K (P2308, Sigma-Aldrich) and Lysis Solution C (B8803, Sigma-Aldrich) (not Lysis Solution T as before). qPCR was performed on extracted samples as in Section 2.12.2.

2.15.3 ELISA analysis of affinity in high ionic strength solutions

ELISAs were conducted largely as described above in Section 2.13.4, with a few differences noted here. Firstly, an ELISA was conducted to determine the effect of CsCl and glycerol on the binding affinity of ab7428 to ColoAd. As compared to Section 2.13.4, Nunc Immunosorp 96-well plates were coated with 100 μL of 400 ng/mL ColoAd in bicarbonate buffer. Two-fold serial dilutions of ab7428 ranging from 60 to 0.47 ng/mL were prepared in PBS, 1.47ρ CsCl or 40% glycerol (prepared as described in Section 2.15.2). A second ELISA was then conducted to determine the effect of salt concentrations corresponding to possible mobile phase compositions in anion-exchange chromatography. This assay was conducted identically to the other ELISA in this section, but samples were diluted in either PBS, or 10% mobile

phase B in mobile phase A, (as described in Section 2.15.4).

2.15.4 Chromatographic analysis of ColoAd + GNPs

Two buffered aqueous mobile phases were made, Mobile Phase A consisted of 50 mM HEPES (H3375, Sigma-Aldrich) and 300 mM NaCl (S7653, Sigma-Aldrich), while Mobile Phase B consisted of 50 mM HEPES and 1.5M NaCl. The pH of both mobile phases was adjusted to 7.4, and the solutions were filtered before use. Chromatographic analysis was performed on a Shimadzu Prominence LC-10 high-performance liquid chromatograph with diode array detection and fluorescence detection. Samples were run on a GE Resource Q anion exchange chromatography column packed with SOURCE 15Q. Samples were eluted using the gradient described in Table 2.2. Dr. Brian Lyons is gratefully acknowledged for his expertise and help with this analysis.

Time (min)	% Mobile Phase A	% Mobile Phase B
0	100	0
2	100	17
17	80	20
22	80	20
24	0	100
26	0	100
26.01	100	0
36	100	0

Table 2.2: Salt gradient used for elution of adenovirus from Resource Q anion exchange chromatography column packed with SOURCE 15Q.

2.5 x 10^9 VPs of ColoAd were pre-incubated for 1 hour with a 100-fold excess of with blank GNPs or GNPs functionalized with ab7428 before being loaded on to anion exchange chromatography column and eluted with gradient described above.

2.16 PEGylation of anti-ColoAd antibodies

Antibodies (ab7428 and IC IgG) were oxidized as described above in Section 2.2 (10 mM $NaIO_4$, 30 mins at RT). Oxidized antibodies were washed (oxidation was verified with Purpald as before) and antibody concentrates were then diluted with catalyst-containing buffer to a concentration of approximately 1 mg/mL. A volume of 20% of the final solution volume of 5 mM LA-PEG-Hyd linker solution was then added (or an equivalent volume of water for non-PEGylated antibody controls) to give a final ratio of at least 115 LA-PEG-Hyd molecules per antibody, and 10 mM of the catalyst (5-methoxyanthranilic acid). PEGylation reaction and subsequent washing and storage was performed as above.

2.16.1 SDS-PAGE analysis

SDS-PAGE analysis of PEGylated antibodies was performed as described above in Section 2.2.2. Gels were stained for PEG with barium iodide staining, and protein with Coommassie staining.

2.17 GNP functionalization and characterization

15 nm spherical bare citrate-capped GNPs (CG-15-500-CYD, Stratech) were functionalized with LA-PEG-ab7428 + mPEG-SH, LA-PEG-IC IgG + mPEG-SH, or simply capped with mPEG-SH. GNPs were concentrated to approximately 1 x 10^{13} GNPs/mL, by centrifuging these concentrated samples in a benchtop centrifuge for 30 minutes at 16,000 rcf, and removing supernant. This was performed twice, and supernatant was replaced with 40 mM HEPES (pH 8.5). LA-PEG-ab7428/IC IgG was then added to concentrated GNPs at a molar ratio of approximately 20:1 or 40:1 (separate experiments), and incubated overnight at RT (for control mPEG-GNPs, an equivalent volume of HEPES with no LA-PEG-cetuximab was added). mPEG-SH (2 kDa, Nanocs) dissolved in water was added to the GNP mixtures to a final

concentration of approximately 80 μM and incubated at RT for 20 minutes. After functionalization, constructs were purified as in Section 2.3.2. After final wash, particles were resuspended and stored in PBS (no Tween-20).

2.17.1 UV-Vis

UV-Vis spectra were acquired as in Section 2.3.3, and used for estimation of GNP concentration.

2.17.2 SDS-PAGE analysis of antibody loading

SDS-PAGE analysis of antibody loading on GNPs was performed identically to the procedure described above in Section 2.2.2. Gels were stained for protein using Silver Stain Plus Kit (1610449, Bio-Rad, UK) and following manufacturers instructions.

2.18 Characterization of antibody-PEG-GNP + ColoAd

2.18.1 Chromatographic analysis of ColoAd + antibody-PEG-GNPs

In two separate experiments, 2.5 x 10^9 VPs of ColoAd were pre-incubated for 1 hour with a 100-fold excess of with blank mPEG-GNPs or GNPs functionalized with LA-PEG-ab7428/IC IgG (at ratio of 20:1 antibodies per GNP), and 5 x 10^9 VPs of ColoAd were pre-incubated for 1 hour with a 130-fold excess of with blank mPEG-GNPs or GNPs functionalized with LA-PEG-ab7428/IC IgG (at ratio of 40:1 antibodies per GNP) before being loaded on to anion exchange chromatography column and eluted with gradient described above in Section 2.15.4.

2.19 Statistical methods

Graphpad Prism (version 7) or R Studio (R Core Team, 2018) were used to perform statistical analysis.

In GraphPad Prism, one-way analysis of variance (ANOVA) with post-hoc multiple comparisons was used to assess significance in data sets with more than two independent groups. All p-values were corrected for multiple comparisons, using either Tukey or Dunnett's correction. For data sets with only two independent groups, two-way unpaired t-tests were used to assess significance. The statistical test used and relevant details are outlined in each figure legend.

For analysis of data from in vivo experiments employing a bilateral tumour model (Chapters 4 and 5), linear mixed effects modelling was employed. The relevant models were constructed in RStudio and were fit with the lmer function of the R package lme4 [184] using the restricted maximum likelihood approach. The Satterthwaite approximation for degrees of freedom was used to determine p-values. All tests were carried out with the R package lmerTest [185]. Type III ANOVA of the fixed effects was performed, with post-hoc multiple t-tests of the model estimated marginal means. All reported p-values from post-hoc tests were corrected for multiple comparisons using the Bonferroni correction. Confidence intervals for model estimated marginal means, and estimated fold-increases, were estimated using parametric bootstrapping.

The assumptions of the linear models were evaluated firstly by the Shapiro-Wilk test of the model residuals and secondly by visual inspection of residual plot to detect deviations from homoscedasticity. Any data sets that did not pass these tests were transformed (Box-Cox or log transform), and tests were performed again on transformed data.

2.20 Schematics

All schematics in this thesis (with the exception of Fig. 5.1) were created using BioRender.

Chapter 3

Development and characterization of targeted gold nanoparticles

As discussed in Section 1.1.3, targeted nanoparticles loaded with therapeutic antibodies have been investigated for a range of applications. It has been shown that therapeutic antibodies including cetuximab and trastuzumab can be conjugated to nanoparticles, which can increase either the direct therapeutic effect of the antibody [186, 187, 188, 189], can have a synergistic effect with alternative therapeutic modalities [190], or can provide labelling for imaging modalities in vivo [191] or ex vivo [192]. Gold nanoparticles (GNPs) in particular have proved an attractive choice of nanoparticle, as they can be easily synthesized to a range of sizes with high monodispersity, their surface provides many easy options for covalent conjugation, and they are considered relatively inert and biocompatible. In the context of cavitation-mediated delivery, the use of gold provides the opportunity to substantially increase the density of the therapeutic antibody thereby potentially increasing the penetration distance achieved [135, 193]. Antibodies can be simply combined with GNPs and conjugated by non-specific interactions [192, 188], or can be conjugated non-specifically via a linker that reacts with many different regions of the antibody (exposed lysine residues, for example) [194]. Alternatively, more refined approaches can be used to achieve site-specific modification via a linker that targets a specific moeity of the antibody [195, 186, 189]. Non-specific antibody conjugation is undesirable as it is likely to result in reduced antibody avidity, as a result of modification of regions of the antibody crucial to antigen binding. Moreover, site-specific conjugation allows for a greater degree of control over labelling, which should give rise to more consistent and reproducible results.

In this chapter, a heterobifunctional linker to provide site-specific conjugation of a therapeutic antibody to GNPs is synthesized and characterized. This linker is then used to attach cetuximab to GNPs, and the resultant constructs are characterized. The work presented in this chapter to develop and characterize an actively-targeted nanoparticle is an essential pre-cursor to the work which follows in the next chapter, wherein the US-mediated delivery of this targeted nanoparticle construct is investigated.

3.1 Formulation of PEG linker

Most naturally produced IgGs have a conserved glycosylation site in the Fc region (at approximately Asn297) [196]. The N-linked glycans can be partially oxidized to generate aldehydes that can be reacted with hydrazines or oxyamines to form hydrazones or oximes respectively. These reactions are commonly used in linker chemistry [197]: hydrazone bonds are more stable than comparable imines, but are pH labile, while oxime bonds are more resistant to hydrolysis even at lower pHs [198]. A proposed linker to site-specifically attach antibodies to the surface of GNPs with a hydrazone is shown in Fig. 3.2. This linker (referred to henceforth as LA-PEG-Hyd) is composed of a polyethylene glycol (PEG) polymer backbone, with a 1,2-dithiane moiety (lipoic acid), and a hydrazide moiety. Thiol groups can effectively chemisorb onto the surface of gold particles, and are thus commonly used to conjugate various species to GNPs, and to increase the colloidal stability of GNPs. Furthermore, it has been shown that the stability of this thiol-gold link can be increased by using multithiolated species or disulfides, versus a single thiol group [199, 200]. Lipoic acid (LA) was chosen here, as it has been used in GNP conjugation/coating and is expected to impart improved stability over monothiol-terminated linkers [201].

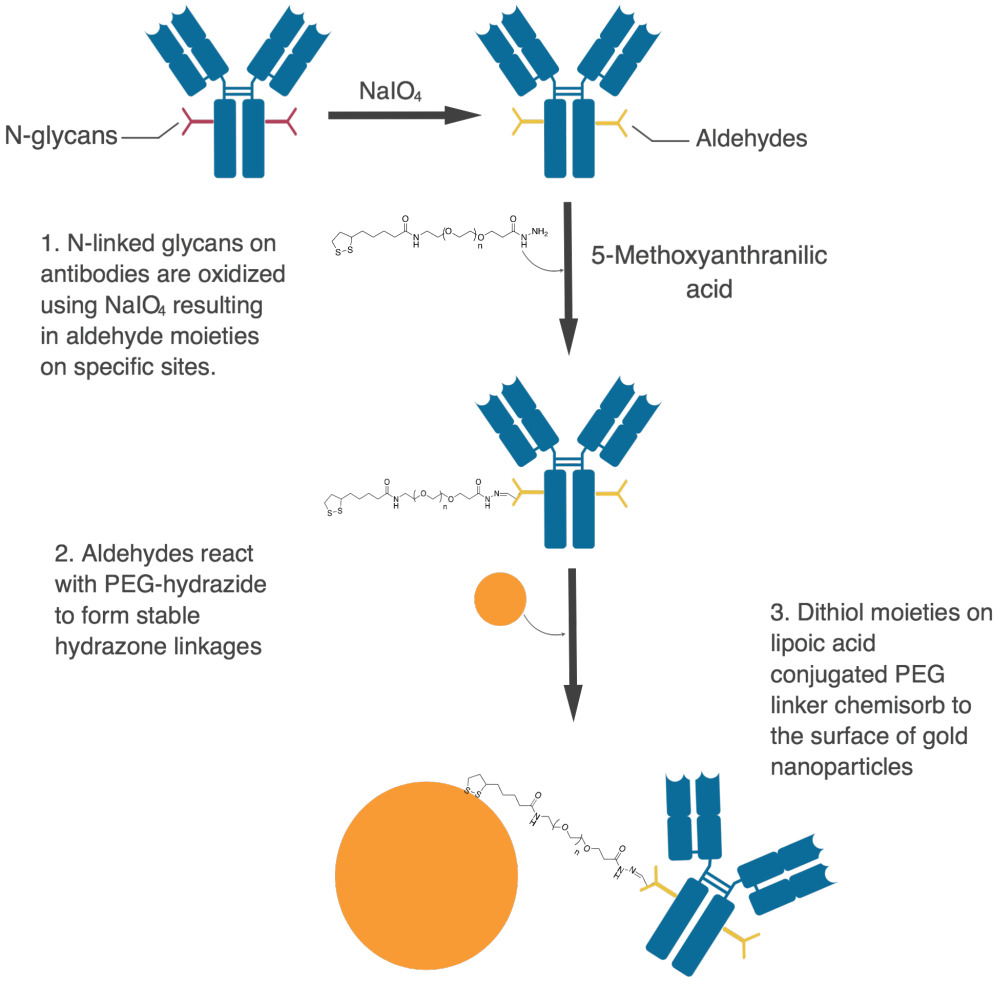

Figure 3.1: Schematic of proposed functionalization of GNPs with antibodies via a site-specific PEG linker.

LA-conjugated PEG with a terminal carboxy group was purchased from a commerical source and all subsequent reactions were performed as described in detail in Section 2.1. In brief, as shown in Fig. 3.3, the starting material LA-PEG-COOH (1) was reacted with tert-butyl carbazate (4) to give a tert-butyloxycarbonyl (Boc)-protected hydrazide (5). Tert-butyl carbazate (which is essentially a Boc-protected hydrazine molecule) offers a significant advantage over hydrazine (a perhaps more obvious choice of reactant) because firstly it is unable to react with two LA-PEG-COOH molecules to form dimers (early attempts at synthesis with hydrazine suggested significant yield of dimers, data not shown).

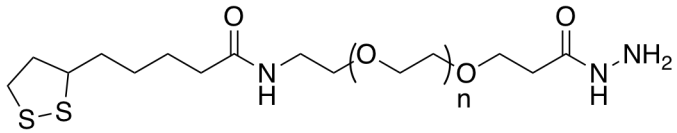

Figure 3.2: Heterobifunctional PEG linker to site-specifically conjugate antibodies to GNPs.

Secondly, it is much safer to handle than hydrazine, and finally the Boc group in the intermediate product formed (Boc-protected hydrazide-PEG-LA) has a distinctive signal by ^{1}H-NMR separate from the signal of the ethylene-glycol repeating unit. The Boc-protected intermediate allows for reaction monitoring by ^{1}H-NMR, and as it is removed in nearly quantitative yields by a simple deprotection step using treatment with trifluoroacetic acid (TFA), does not impact the ultimate yield of LA-PEG-Hyd.

In peptide synthesis, coupling reagents are used to facilitate the formation of an amide bond between the carboxy group on one amino acid and the amino group on the other. In the preparation of DSPE-PEG-Hydrazide with a carboxy-terminated PEG and tert-butyl carbazate as reagents, Zalipsky used dicyclohexylcarbodiimide (DCC) as a coupling reagent and achieved a yield of 98% [202]. Thus, in the first instance, DCC was tested as a coupling reagent, but reaction yields were low and trace amounts of dicyclohexylurea (DCU) proved difficult to remove without substantial loss of product. 4-(4,6-Dimethoxy-1,3,5-triazin-2-yl)-4-methylmorpholinium tetrafluoroborate (DMTMM-BF4) is a triazine-based coupling reagent designed by Kaminski et al. that can be used to activate carboxylic acids via formation of a triazine 'superactive ester', and can be used effectively in organic solvents such as DMF without the need for anhydrous conditions [203]. When DMTMM-BF4 was used as outlined in Fig. 3.3 (step 2), reaction yields after 3 days at room temperature were almost quantitative, as determined by comparison of the ^{1}H-NMR peak area from a proton signal of LA to the ^{1}H-NMR peak area from the Boc protecting group.

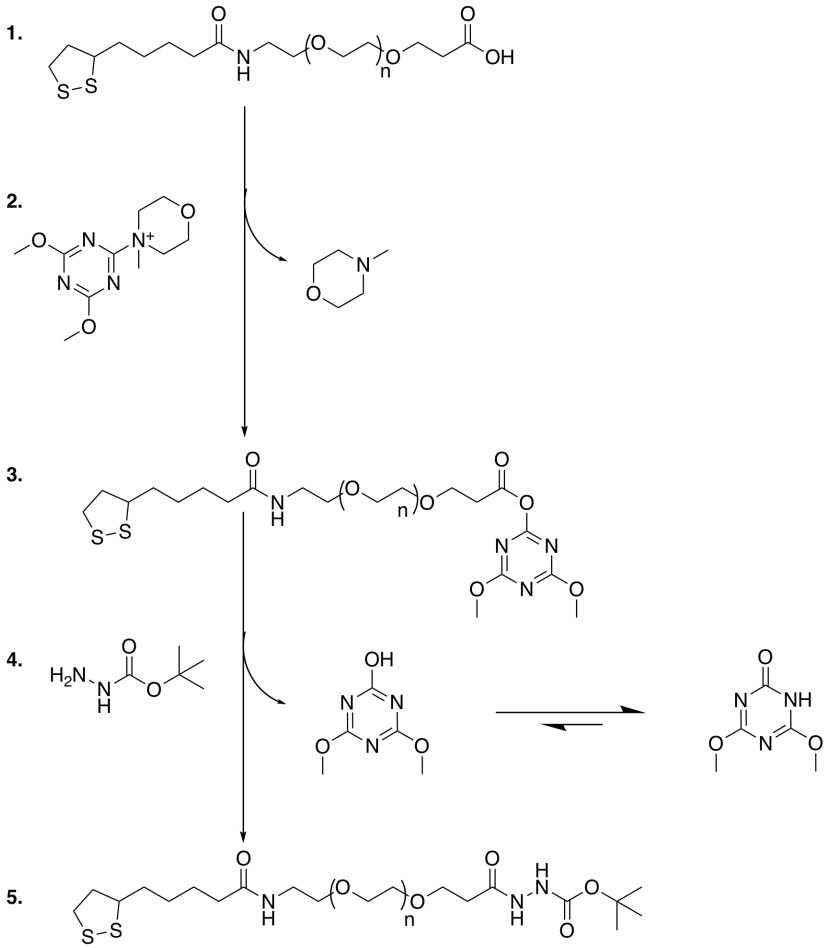

Figure 3.3: Overview of reaction to synthesize LA-PEG-Hyd-Boc from LA-PEG-COOH. Firstly, the terminal carboxy group of starting material (1) is activated with coupling reagent DMTMM-BF4 (2) to yield a reactive intermediate (3). The hydrazine group of tert-butyl carbazate (4) then nucleophilically attacks the electrophilic carbonyl carbon of the activated intermediate PEG (3). The resulting product is a heterobifunctional PEG with a protected hydrazide group (5).

The intermediate Boc-protected hydrazide (step 5), was then deprotected (Fig. 3.4) and the yield was verified with a functional assay (TNBS, see Section 2.1.4) to determine the number of reactive hydrazide groups per unit weight of product. A summary of the synthesis and purification of the final batch of LA-PEG-Hyd created is described in Section 2.1.

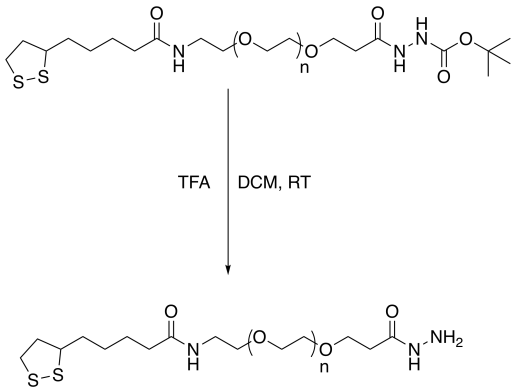

Figure 3.4: Deprotection of LA-PEG-Hyd-Boc with trifluoroacetic acid (TFA) to give LA-PEG-Hyd. LA-PEG-Hyd-Boc was dissolved in 20% TFA in DCM and left for 3 hours at room temperature before purification.

3.2 Characterization of PEG linker

3.2.1 Reaction monitoring with ^{1}H-NMR

In the course of synthesizing LA-PEG-Hyd (Fig. 3.2), ^{1}H-NMR spectroscopy was used to verify the purity of the product, and to estimate the yield of the desired hydrazide-containing heterobifunctional PEG. Dr. Luca Bau is gratefully acknowledged for his assistance with the ^{1}H-NMR analysis presented here. The ^{1}H-NMR spectra shown in Fig 3.5 depict (1) the LA-PEG-COOH starting material as purchased from Nanocs, (2) the LA-PEG-Hyd-Boc protected intermediate (after reaction outlined in Fig 3.3), and finally (3) the final deprotected LA-PEG-Hyd product. For the purpose of clarity, only the portion of the spectrum used for quantification of the Boc signal is shown. The structure of the LA-PEG backbone of the molecule is shown, and protons from lipoic acid used for quantification are assigned and labelled a-d.

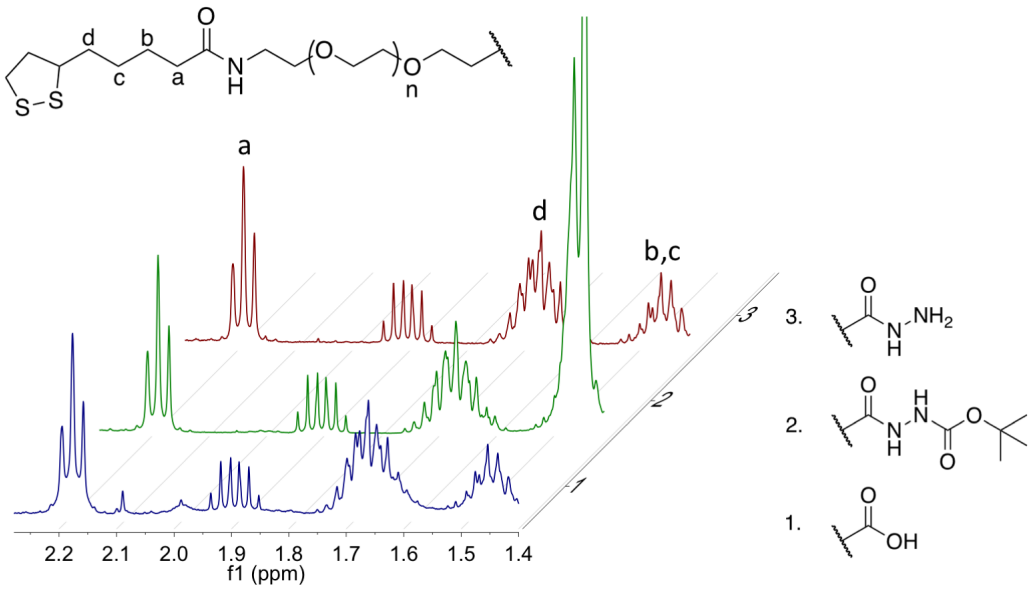

Figure 3.5: ^{1}H-NMR Spectra of (1) LA-PEG-COOH, (2) LA-PEG-Hyd-Boc, and (3) LA-PEG-Hyd in $CDCl_3$. After completion of the first reaction step, the yield of desired product intermediate was monitored by H-NMR (2), and loss of the Boc NMR signal after subsequent treatment with TFA confirmed successful deprotection of intermediate (3). The backbone structure of LA-PEG is shown, and protons used for quantification of Boc protons are labelled **a-d**. The structural assignment was made following Schepkin et al. [204].

The conversion of LA-PEG-COOH into LA-PEG-Hyd was determined from the integrals of the signals from the nine Boc protons at 1.47 ppm and the two lipoic acid protons at 2.2 ppm (a). When the integral of the (a) triplet is normalized to 2, the region between 1.4 and 1.8 ppm, containing the signals from the Boc protons and six other lipoic acid protons (b,c,d) integrates to 16.5. Subtraction of the six lipoic acid protons from this integral gives an integral of 10.5 for the Boc signals, which corresponds to 117% conversion. This excess is likely due to the degree of functionalization of the starting material: if the molar ratio of lipoic acid to PEG-COOH was less than 1:1, then the conversion calculated with this method could exceed 100%. Comparison of the spectrum of the protected intermediate (2) to the spectrum after deprotection (3), provides confirmation of successful deprotection, as the Boc signal at 1.47 ppm in (2) has completely disappeared in spectrum (3). Finally, comparison of the starting material spectrum (1) to the final product spec-

trum (3) confirms that lipoic acid signals have been retained, and the final product is relatively clean of impurities and reaction by-products.

3.2.2 TNBS assay for hydrazide content

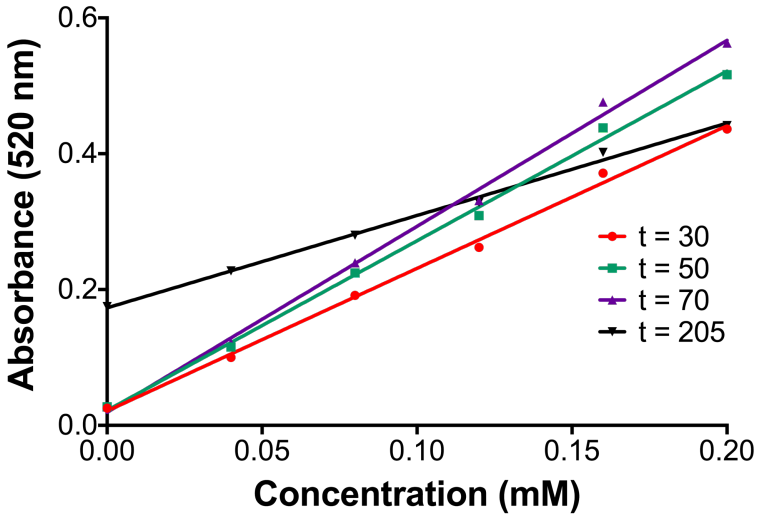

Figure 3.6: Absorbance at 500 nm of colorimetric product of the reaction of acethydrazide with TNBS over time. TNBS (final concentration 0.75 mM) was added to acethydrazide at a range of concentrations in borate buffer at pH 9.3. Samples were incubated at room temperature for a total of 205 minutes, absorbance readings were taken at 30 (circular markers, red trace), 50 (square markers, green trace), 70 (triangular markers, purple trace) and 205 (triangular markers, black trace) minutes post-addition of TNBS reagent.

Though ^{1}H-NMR analysis was useful for roughly estimating completion of the conversion of LA-PEG-COOH to LA-PEG-Hyd, the most important metric to ascertain was the number of moles of hydrazide per unit weight of final product: this represents the proportion of functional PEG able to react with antibody aldehyde groups, and informs calculations for future conjugations. 2,4,6-trinitrobenzenesulfonic acid (TNBS) is a reagent commonly used in a colorimetric assay for determining concentrations of amino groups. This assay can be adapted to measure both hydrazides and hydrazines [205]. Zalipsky and Menon-Rudolph (1997) describe a simple TNBS assay to determine the hydrazide concentration of a PEG-Hyd compound, this method was used here. A calibration curve of acethydrazide was prepared in

a range from 0.2 mM to 0.04 mM, and samples of LA-PEG-Hyd were prepared at concentrations of 0.16, 0.12, and 0.08 mM (as determined by the dry weight of the product and nominal MW of LA-PEG-COOH from the manufacturer). After incubation with TNBS reagent, a colour change from yellow to orange/brown was observed in top standards and samples. The progress of the reaction with TNBS was monitored by UV-Vis absorption spectroscopy after addition of TNBS, with an absorption peak at 500 nm corresponding to the colourimetric product of TNBS and hydrazide. Fig. 3.6 shows the absorbance at 500 nm of the calibration curve of acethydrazide at time points between between 30 and 205 minutes after addition of TNBS. The standard curve remained approximately linear up until 70 minutes after addition TNBS, but at the time point of 205 minutes there was clear degradation of the colorimetric product. Thus, all calculations of hydrazide concentration were made from measurements taken 70 minutes after addition of TNBS. The final batch of LA-PEG-Hyd synthesized (same batch as analysed above by ^{1}H-NMR spectroscopy) was determined to have a degree of functionalization with hydrazide of 77±7% based on a nominal LA-PEG-COOH MW of 3400 Da. As the actual number-average molecular weight can vary substantially from batch to batch and was not provided by the manufacturer, this estimate can only be used as a rough indication of successful functionalization. What is more important is the hydrazide loading of LA-PEG-Hyd, which was determined to be 0.23±0.02 mmol/g.

3.3 PEGylation of therapeutic antibodies

3.3.1 Lucifer yellow assay

In addition to a conserved N-linked glycan within the Fc region, approximately 20% of human monoclonal antibodies have an additional N-linked glycan within the variable region [196]. Both glycosylation sites are located on the heavy chain of the antibody. Glyco-profiling of cetuximab has revealed a second glycosylation

site (at Asn88 within the Fd domain), in addition to a conserved glycosylation (at Asn299) [206, 207]. Studies in the literature have used carbohydrate oxidation as a method for site-specific modification of cetuximab [186, 191, 189], however many do not address the possibility of attachment through the second glycan in the Fab region, which could potentially hinder effective binding to EGFR, reducing the effective affinity of cetuximab, and potentially its therapeutic benefit. Trastuzumab, however, contains only the one conserved glycosylation site, and it is situated within its Fc region [208]. For greater yields of PEGylated antibody, a greater number of aldehyde groups is desired, though greater oxidation and generation of aldehydes could lead to an excessive number of PEG molecules attached (raising the risk of cross-linking), or could cause damage to the antibody through damage to glycosylations, or oxidation of amino acid residues (methionine for example [209, 210]). Wolfe et al. investigated antibody oxidation by periodate at various reaction times, pHs, temperatures and periodate concentrations, and showed that the number of aldehydes generated increased with decreasing pH, increasing temperature, and increasing periodate concentration [211].

As part of the optimization process here, the oxidation of cetuximab and trastuzumab was investigated at a pH of 5.6, a concentration of sodium metaperiodate ($NaIO_4$) of 5 mM or 10 mM, and a temperature of 4 °C or 20 °C (room temperature: RT). After oxidation, antibodies were washed 5 times with a centrifugal spin filter with a MWCO of 30 kDa to ensure removal of the oxidant. Oxidized antibodies were then reacted overnight with a 250-fold molar excess of lucifer yellow CH (LYCH), an aldehyde reactive hydrazide-containing dye. After incubation, antibodies were washed again 5 times with a centrifugal spin filter with a MWCO of 30 kDa to ensure removal of unbound LYCH from the trastuzumab- or cetuximab-LYCH. Non-oxidized samples of cetuximab and trastuzumab were incubated with LYCH and washed identically, as controls for non-specific binding, and the effectiveness of the washing procedure. After each spin, the buffer was replaced with 40 mM HEPES, at pH 8.5

to prevent hydrolysis of the hydrazone bond and freeing of the LYCH. Concurrently, serial dilutions of LYCH and dilutions of non-oxidized cetuximab were prepared separately, and the absorbance of the oxidized and labelled antibodies were compared at 280 and 480 nm to the standard curves (Fig. 3.7) in order to determine a molar ratio of LYCH molecules bound per antibody.

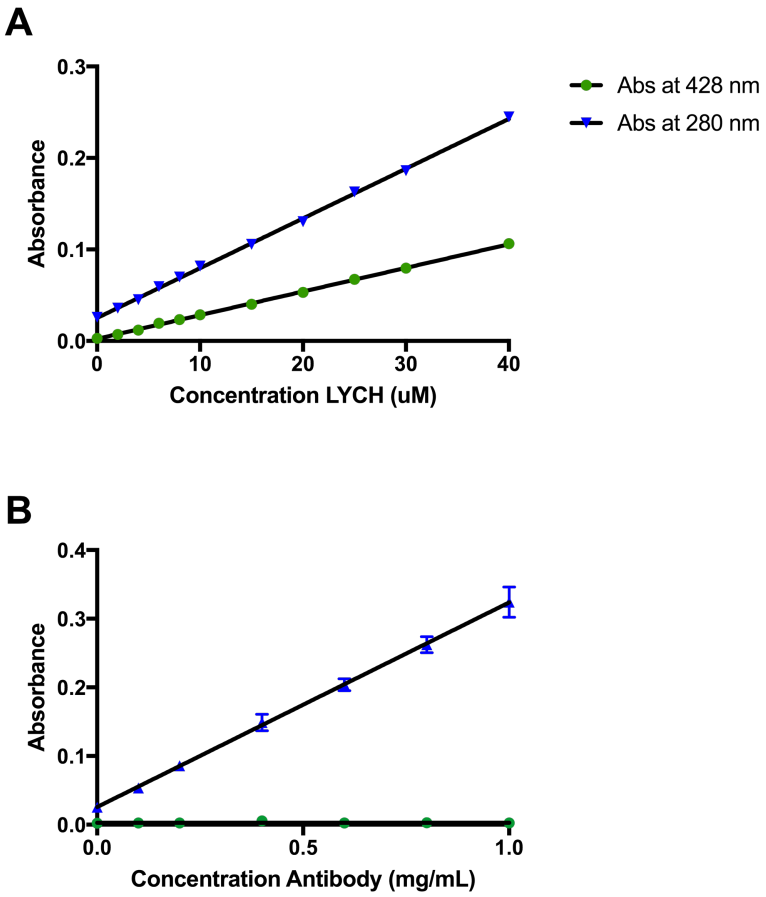

Figure 3.7: Absorbance of LYCH (A) and antibody (B) at wavelengths of 280 and 428 nm. Serial dilutions of LYCH and non-oxidized cetuximab were prepared (separately) in 40 mM HEPES buffer (pH 8.5) and added to UV-transparent 96-well microplate, and absorbance spectra were acquired.

From Table 3.1, the effects of temperature and periodate concentration clearly mirror those described in the literature [212, 213, 211], confirming predicted results based on the glycoprofiles of cetuximab and trastuzumab, i.e. higher levels for cetuximab which has a greater number of glycosylation sites.

Antibody	[NaIO4] mM	Temperature	Molar Ratio LYCH:Ab
Cetuximab	10	RT	17 ± 4
	5	RT	12 ± 2
	5	4 °C	10 ± 1
	0	RT	0.1 ± 0.2
Trastuzumab	10	RT	5.3 ± 0.3
	5	RT	4.3 ± 0.2
	5	4 ° C	3.5 ± 0.2
	0	RT	-0.01 ± 0.08

Table 3.1: Quantification of aldehydes on cetuximab and trastuzumab post-periodate oxidation.

3.3.2 Characterization of impact of oxidation on structure and function of antibodies

Abraham et al. tested periodate oxidation of 8 different mAbs (from different classes and isotypes) and showed that there was a large variety in the number of aldehydes generated with identical oxidizing conditions, and demonstrated that periodate oxidation can lead to antibody crosslinking and a reduction in antibody avidity (functional affinity) [213]. To test this, after oxidation and PEGylation, sodium dodecyl sulfate polyacrylamide gel electrophoresis (SDS-PAGE) was used to verify the structure and of cetuximab and trastuzumab, while an indirect enzyme-linked immunoassay (ELISA) was used to examine functional antibody affinity. These tests were performed after cetuximab and trastuzumab were oxidized using harsh (10 mM $NaIO_4$ at RT) or mild (5 mM $NaIO_4$ at 4 °C) conditions.

After oxidation, antibodies were washed 5 times with a centrifugal spin filter with a MWCO of 30 kDa to ensure removal of the oxidant. During these washing steps, the buffer was replaced with a solution of 5-methoxyanthranilic acid in PBS (pH 5.6). Equilibrium kinetics of hydrazone formation are quite slow [214, 215], but water-

soluble organocatalysts can be used to increase the rate of reaction, and thus increase the relative yield of hydrazone. Crisalli et al. report that 5-methoxyanthranilic acid can be used to increase the percent conversion of an aldehyde-containing compound (1 mM 4-nitrobenzaldehyde) reacted with 18 μM of a hydrazone-forming substrate from approximately 0.7% (uncatalyzed) to 55.5% (1 mM 5-methoxyanthranilic acid) after 2 hours of reaction at pH 7.4 and RT [215]. Here, 1 mM LA-PEG-Hyd was added to a 13.3 μM (2 mg/mL) solution of cetuximab or trastuzumab in PBS with 10 mM 5-methoxyanthranilic acid, and allowed to react at RT overnight. PEGylated antibodies were then washed 5 times with a centrifugal spin filter, and were resuspended in a solution of 40 mM HEPES buffer at pH 8.5 to prevent hydrazone hydrolysis on storage. As controls, samples of oxidized cetuximab and trastuzumab were washed and treated identically, but were incubated overnight with pure water instead of LA-PEG-Hyd.

SDS-PAGE

After completion of the PEGylation reaction and subsequent washing, the PEGylated cetuximab and trastuzumab were analysed by SDS-PAGE, as described in Section 2.2.2. The gels were stained with Coommassie stain for protein, and PEGylated antibodies were compared to oxidized and non-oxidized controls. In Fig. 3.8 panel A, lanes 2 and 3 show cetuximab, oxidized with mild (lane 2) or harsh (lane 3) conditions and run on the gel with non-reducing conditions (i.e. no cleavage of heavy and light chains). A small degree of antibody aggregation (possibly cross-linked antibody) is noted. These aggregates are more readily apparent when the oxidized antibodies are reduced with β-mercaptoethanol (BME) and heat (lanes 9 and 10). No substantial qualitative difference is observed between the mild and harsh oxidation, and the majority of antibody still migrates to the appropriate MW ($\approx$150 kDa), and the heavy and light chain bands match the corresponding bands of non-oxidized (reduced) cetuximab (lane 11).

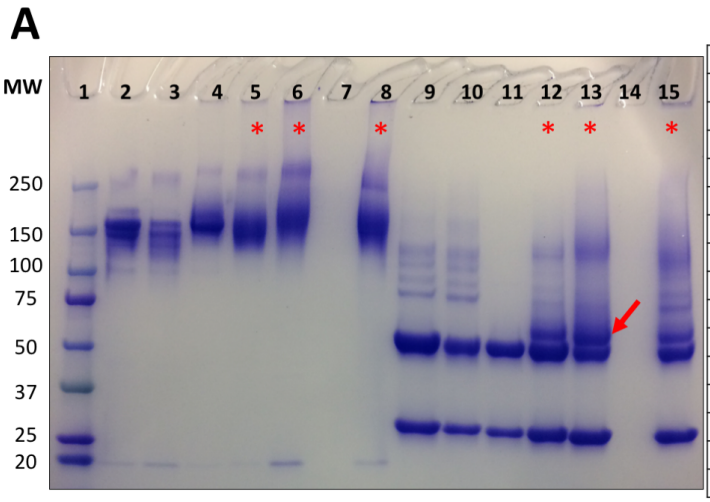

Lane #	Sample Identity
1	Molecular weight marker
2	Cetuximab + Mild Oxidation
3	Cetuximab + Harsh Oxidation
4	Non-oxidized Cetuximab + LA-PEG-Hyd
5	Cetuximab + Mild Oxidation + LA-PEG-Hyd
6	Cetuximab + Harsh Oxidation + LA-PEG-Hyd
7	LA-PEG-Hyd
8	Cetuximab + Harsh Oxidation + LA-PEG-Hyd (old)
9	Cetuximab + Mild Oxidation
10	Cetuximab + Harsh Oxidation
11	Non-oxidized Cetuximab + LA-PEG-Hyd
12	Cetuximab + Mild Oxidation + LA-PEG-Hyd
13	Cetuximab + Harsh Oxidation + LA-PEG-Hyd
14	LA-PEG-Hyd
15	Cetuximab + Harsh Oxidation + LA-PEG-Hyd (old)

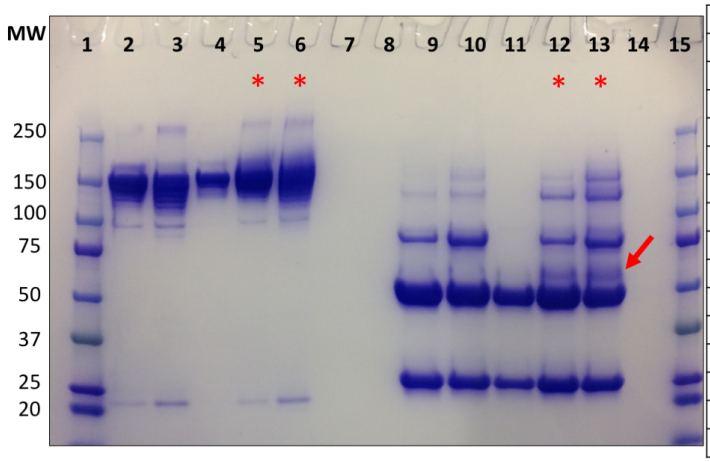

Lane #	Sample Identity
1	Molecular weight marker
2	Trastuzumab + Mild Oxidation
3	Trastuzumab + Harsh Oxidation
4	Non-oxidized Trastuzumab + LA-PEG-Hyd
5	Trastuzumab + Mild Oxidation + LA-PEG-Hyd
6	Trastuzumab + Harsh Oxidation + LA-PEG-Hyd
7	LA-PEG-Hyd
8	
9	Trastuzumab + Mild Oxidation
10	Trastuzumab + Harsh Oxidation
11	Non-oxidized Trastuzumab + LA-PEG-Hyd
12	Trastuzumab + Mild Oxidation + LA-PEG-Hyd
13	Trastuzumab + Harsh Oxidation + LA-PEG-Hyd
14	LA-PEG-Hyd
15	

Figure 3.8: SDS-PAGE and Coommassie staining characterization of oxidized and PEGylated cetuximab (A) and trastuzumab (B). Samples run in non-reducing conditions samples (lanes 2–8) were diluted 3:1 in 4x Laemmli sample buffer, while samples run in reducing conditions (lanes 9-15, denoted with text box filled in blue) were diluted 3:1 in 4x Laemmli sample buffer supplemented with 10% β-mercaptoethanol, and heated to 95 °C for 10 minutes. Gels were run as described in Section 2.2.2. Red stars denote lanes containing antibody-PEG conjugates.

PEGylated cetuximab samples (lanes 5 and 6) are similar to non-oxidized cetuximab spiked with LA-PEG-Hyd (lane 4) when run in non-reducing conditions, except for the presence of smearing at MW greater than 150 kDa, which may indicate the formation of a conjugate. When PEGylated samples were run in reducing

conditions (lanes 12 and 13), a thick band was observed slightly above the unmodified heavy chain band (see red arrow), this band was not evident in any of the oxidized (but not PEGylated) samples (lanes 9 and 10), suggesting this band corresponds to a PEGylated heavy chain. As the LA-PEG-Hyd has a MW of only 3.4 kDa, it would not be predicted to alter the MW of an antibody heavy chain (approximately 50 kDa unmodified) considerably (though it is important to note that PEG in the presence of SDS does not migrate linearly with size [216]). The migration pattern of the light chain of the PEGylated antibody has not changed, this is in keeping with the fact that no glycosylation sites are found on the light chain, and so there is no opportunity for modification with LA-PEG-Hyd. Finally, lanes 8 and 15 (non-reducing and reducing conditions) contain a sample of PEGylated cetuximab that was PEGylated 4-weeks prior to the SDS-PAGE analysis and stored at 4 °C in 40 mM HEPES (pH 8.5). The continued presence of the second heavy-chain band suggests persistence of the hydrazone bond under these storage conditions.

Fig. 3.8 panel B, shows an identical analysis of PEGylated trastuzumab (with the exception of the 4-week old samples). Notable differences between the SDS-PAGE of trastuzumab and cetuximab are firstly the reduced intensity of the second heavy-chain PEG-conjugate band (see lanes 12 and 13) for trastuzumab compared to cetuximab, and secondly the presence of a band of significant intensity at a MW of approximately 75 kDa, seen for all oxidized (PEGylated or not) samples of trastuzumab. Taken together, these results suggest a lower degree of PEGylation of trastuzumab, coupled with a greater degree of antibody aggregation.

ELISA

ELISA analysis can be used to determine the relative binding affinities of antibodies to their antigens, as measured by their relative dissociation constants, K_d. From the law of mass action, a simple relationship between free ('A') and substrate bound antibody ('AS') can be derived (Eq. 3.1). If the amount of antibody bound in an

ELISA is small compared to the total antibody added to each well, the concentration of free antibody can be approximated by the total concentration of antibody, and Eq. 3.3 can be used to determine a relative K_d with ELISA. From Eq. 3.3, in these conditions K_d is equal to the concentration of antibody at half-maximal saturation (S_{tot}). A lower K_d value indicates a higher affinity of an antibody for its antigen.

$$\mathrm{A} + \mathrm{S} \underset{\mathrm{k_{off}}}{\overset{\mathrm{k_{on}}}{\rightleftharpoons}} \mathrm{AS}$$

$$\frac{k_{off}}{k_{on}} = K_d = \frac{[A][S]}{[AS]} \tag{3.1}$$

$$[S_{tot}] = [S] + [AS] \tag{3.2}$$

Combining 3.1 and 3.2 yields Eq. 3.3, where $y = [AS]$, and $x = [A] \approx [A_{tot}]$

$$y = \frac{x[S_{tot}]}{K_d + x} \tag{3.3}$$

In a conventional indirect ELISA as conducted here, antigen and antibody are in separate phases (here antigen is immobilized by adsorption to the microplate well), and thus the assay might not accurately reflect the affinity of an antibody for its antigen in solution [217]. Generally, it is more precise to determine antibody affinity using methods such as surface plasmon resonance, however for determination of relative binding affinities [217], ELISA utilizing an immobilized antigen can be an appropriate method, and is easy to implement and analyse.

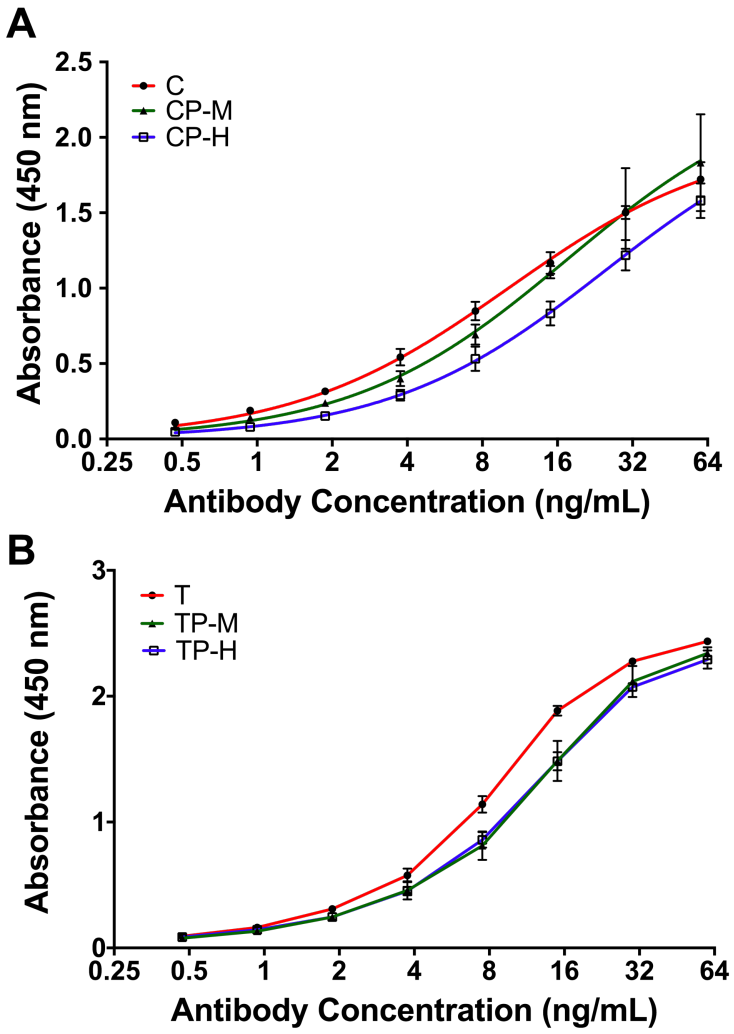

Figure 3.9: Indirect ELISA analysis of cetuximab and trastuzumab binding to immobilized recombinant human EGFR or HER2 respectively. Panel A shows binding curves for cetuximab while panel B shows binding curves for trastuzumab. Both panels show binding of non-modified antibody (red trace and circular markers), PEGylated antibody with mild oxidation (green trace with triangular markers), and PEGylated antibody with harsh oxidation (blue trace with square markers). Least-squares nonlinear regression in GraphPad PRISM was used to fit cetuximab binding data, and these fits are depicted by the coloured traces. See Section 2.2.3 for method details.

Fig. 3.9 shows the binding curves of cetuximab (A) and trastuzumab (B) to their respective antigens (EGFR and HER2). The binding of PEGylated antibody (after mild or harsh oxidation) is compared to the untreated (stored as per manufacturers instructions) antibody. For both cetuximab and trastuzumab, a change in binding is observed after PEGylation. The binding of cetuximab or PEGylated

cetuximab is fit well with Eq. 3.3, and the estimated relative dissociation constants (K_d) are displayed in Table 3.2. PEGylation of cetuximab after harsh oxidation leads to an approximate 2.4-fold increase in K_d, indicating a decrease in the avidity (functional affinity) of cetuximab for EGFR. The binding of trastuzumuab or PEGylated trastuzumab is, however, not well fit with Eq. 3.3. This is consistent with the findings of Suarez et al., who found in a similar indirect ELISA assay that the shape of the binding curve of trastuzumab to HER2 differed from that of cetuximab to EGFR, and was best fit with a polynomial model [218]. Regardless, from panel B of Fig. 3.9, the half-maximal saturation concentration of PEGylated trastuzumab is clearly lower than untreated trastuzumab, indicating a decrease in functional affinity.

Cetuximab Treatment	**Relative K_d (ng/mL)**	**95% CI of K_d (ng/mL)**
Untreated	10.25	9.10 to 11.55
Mild oxid. + LA-PEG-Hyd	17.60	12.97 to 24.18
Harsh oxid. + LA-PEG-Hyd	24.76	20.66 to 29.87

Table 3.2: Estimates of relative dissociation constants of cetuximab and PEGylated cetuximab from indirect ELISA.

From the characterization of oxidation with LYCH and SDS-PAGE analyses, cetuximab was shown to have more potential binding sites after oxidation, greater PEGylation of its heavy chain and a lesser degree of antibody aggregation. Furthermore, (although difficult to quantify) PEGylation of cetuximab showed comparable reduction in functional affinity by ELISA as compared to PEGylated trastuzumab (despite the presence of a second glycosylation of cetuximab within the variable region). Thus, the remainder of the work presented here will focus on modification of cetuximab, and ultimately delivery of cetuximab and cetuximab-GNPs with cavitation-mediated US. Additionally, as the harsh oxidation conditions still gave rise to a high-affinity cetuximab-PEG conjugate, these conditions were used for all remaining conjugations.

3.4 PEGylation of cetuximab

3.4.1 SDS-PAGE analysis of PEGylated cetuximab with PEG staining

Although the SDS-PAGE analysis presented in Fig. 3.8 suggested successful modification of the heavy chain of cetuximab, this was demonstrated indirectly by a change in MW of the heavy chain. Barium chloride combined with iodine has been used in assays to quantify PEG concentration [219], and in gel electrophoresis to stain for PEG [220], as barium iodide can form a coloured complex with PEG. Here, PEGylated cetuximab samples (and oxidized/untreated controls) were separated by SDS-PAGE, and the gel was stained first with barium iodide for PEG, then with Coommassie stain for protein. As a control, untreated (non-oxidized) cetuximab was combined with LA-PEG-Hyd, subjected to the same washing procedure as oxidized cetuximab combined with LA-PEG-Hyd, and run on the same gel. Briefly, the gel was immersed in a solution of 5 mL of 5% $BaCl_2$ in 1M HCl, to which 2 mL of a 0.1N iodine solution was added, according to the procedure described by Kurfurst [220]. After approximately 15 minutes of incubation with the barium iodide, the gel appeared to be stained for both protein and PEG (i.e. bands were visible in lanes that contained protein but did not contain any PEG). The staining solution was replaced with pure water, and the gel was rinsed multiple times until all protein bands had disappeared and the only remaining staining occurred in lanes where PEG had been loaded – the gel was photographed at this point. Subsequently, the gel was washed until all staining had disappeared, then was immersed in Coommassie stain for a minimum of 2 hours, destained, and photographed. Fig. 3.10 is a composite of the photographs of the gel after barium iodide staining and Coommassie staining – the brown staining is barium iodide staining, while the blue/violet staining is protein stained with Coommassie stain.

Examples from the literature of barium iodide staining for detection of protein PEGylation indicate that attachment of PEG can change apparent MW of the pro-

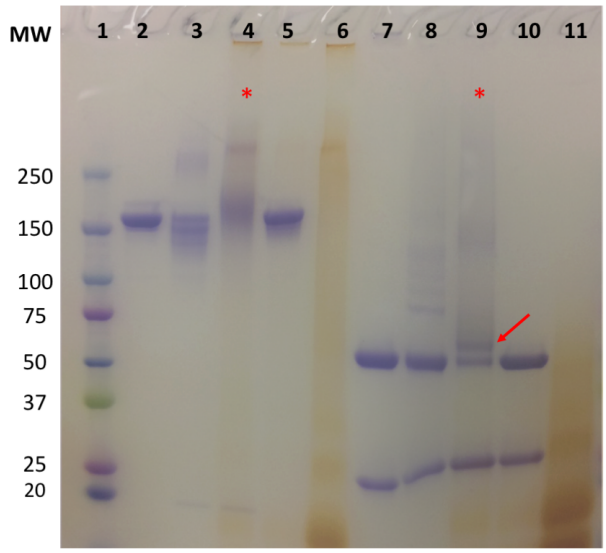

Lane #	Sample Identity
1	Molecular weight marker
2	Non-oxidized cetuximab
3	Oxidized cetuximab
4	Oxidized cetuximab + LA-PEG-Hyd
5	Non-oxidized cetuximab + LA-PEG-Hyd
6	LA-PEG-Hyd
7	Non-oxidized cetuximab
8	Oxidized cetuximab
9	Oxidized cetuximab + LA-PEG-Hyd
10	Non-oxidized cetuximab + LA-PEG-Hyd
11	LA-PEG-Hyd

Figure 3.10: SDS-PAGE with Coommassie and barium iodide staining for characterization of PEGylated antibodies. Samples run in non-reducing conditions (lanes 2–6) were diluted 3:1 in 4x Laemmli sample buffer, while samples run in reducing conditions (lanes 7-11, denoted with text box filled in blue) were diluted 3:1 in 4x Laemmli sample buffer supplemented with 10% β-mercaptoethanol, and heated to 95 °C for 10 minutes. Gels were run as described in Section 2.2.2. Staining was performed first for PEG (barium iodide stain), and second for protein (Coommassie stain), and images of the gel after the two separate staining steps are co-registered and overlaid here. $\star$ denotes lanes containing antibody-PEG conjugates.

tein (though this is not linear with actual MW, particularly when the sample and running buffer contain SDS) [216], and that barium iodide staining overlaps with Coommassie staining of a PEGylated protein [220] [216] [190]. In Fig. 3.10, non-reduced PEGylated cetuximab (lane 4) runs as a smeared band (see $\star$), especially when compared to untreated cetuximab spiked with LA-PEG-Hyd (lane 5), which gives rise to a sharp band at a MW of approximately 150 kDa. From the barium iodide staining, it is clear when comparing lanes 4 and 5 to lane 6 (which contains LA-PEG-Hyd alone) that the procedure of washing with centrifugal filtration with a MWCO of 100 kDa is an effective means of removing free LA-PEG-Hyd. Furthermore, there is a faint brown stain in lane 4 ($\star$) overlapping with the Coommassie stain of the non-reduced antibody. This suggests association of LA-PEG-Hyd with

the antibody. No similar signal was seen in lane 5 where LA-PEG-Hyd was simply mixed with non-oxidized antibody (and then washed). This staining is however, faint, so cannot be considered definitive proof of PEGylation. However, when combined with the MW change of the heavy chain (seen again here in lane 9, see red arrow), this adds to the evidence of successful PEGylation of cetuximab.

3.4.2 Chromatographic analysis of PEGylated cetuximab

Reverse-phase (RP) liquid chromatography can be used to analyze monoclonal antibodies including cetuximab [221, 222], and to analyze PEGylated proteins [223]. Here, a wide-pore RP-column with phenyl-based stationary phase was used for analysis of cetuximab, oxidized cetuximab, and oxidized and PEGylated cetuximab. Antibody was eluted from the column using a linear gradient of acetonitrile in water (both with 0.1% trifluoroacetic acid, TFA), as described in Section 2.2.4. The column was kept at a temperature of 80 °C during antibody elution, as high temperatures help to reduce secondary interactions between the column and positively charged biomolecules [224]. However, given that the analysis was conducted at high temperature and low pH, a large degree of hydrazone hydrolysis was predicted with these conditions, which would make it difficult and/or impossible to determine whether the antibody is PEGylated when subject to milder conditions (i.e. RT and pH 8.5). In order to facilitate the analysis, the hydrazone bond of PEGylated cetuximab was first reduced to a more stable hydrazide using the mild reducing agent sodium cyanoborohydride ($NaCNBH_3$). Untreated (non-oxidized) and oxidized cetuximab were also treated with $NaCNBH_3$, and after treatment with $NaCNBH_3$ all antibodies were washed with centrifugal filtration. After treatment with $NaCNBH_3$, the interchain disulfide bonds of cetuximab were reduced by treatment with 50 mM DTT for 10 minutes at RT. Samples were run on a Agilent 1290 Infinity II LC system, gradient details are presented in Section 2.2.4, and chromatographs are shown in Fig. 3.11.

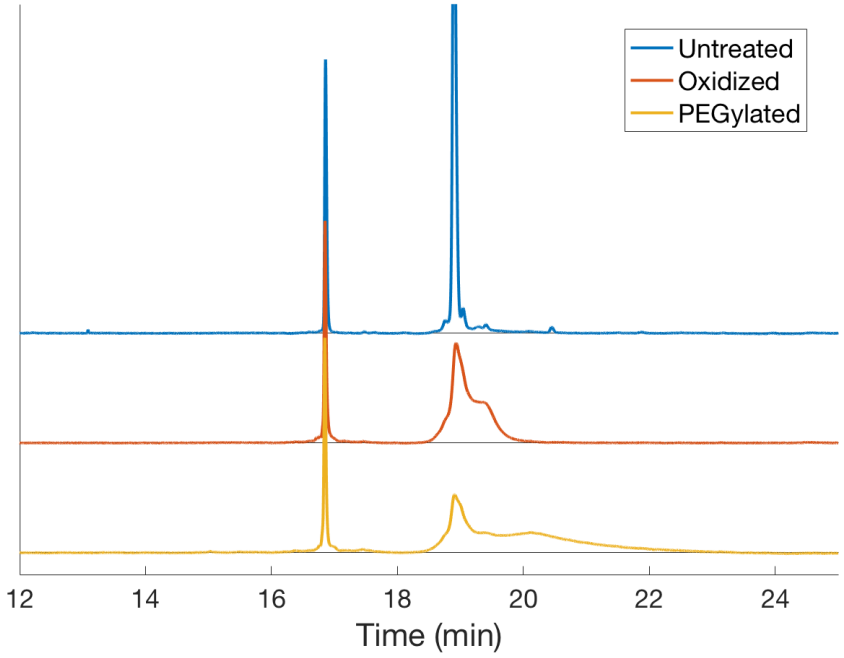

Figure 3.11: Chromatographic analysis of cetuximab, oxidized cetuximab, and PEGylated cetuximab. Samples of untreated (non-oxidized) cetuximab (blue trace), cetuximab oxidized with metaperiodate (orange trace), and cetuximab oxidized and PEGylated with LA-PEG-Hyd (yellow trace) were loaded on to a Waters® BioResolve™ Reversed-Phase mAb Polyphenyl Column and were eluted with a linear gradient of acetonitrile in water (with 0.1% TFA, gradient details in Section 2.2.4). Column was kept at 80 °C during runs. Chromatographs shown here were acquired at an absorbance of 280 nm, were normalized to the area of the light chain peak of untreated antibody (retention time of 16.8 minutes), and were baseline corrected.

In Fig. 3.11, each trace has two peaks: the light chain of cetuximab eluting at a retention time of 16.8 minutes, and the heavy chain eluting at approximately 18.9 minutes (for untreated cetuximab) [222]. For untreated cetuximab (blue trace), the peaks for both heavy and light chains are sharp and well-resolved. For oxidized cetuximab (orange trace), and oxidized and PEGylated cetuximab (yellow trace), the light chain peak is identical in retention time and shape to the untreated antibody, but the heavy chain peak is altered in retention time and shape. This is consistent with the SDS-PAGE analysis which indicated the light chain remained unmodified after treatment with metaperiodate, and after subsequent PEGylation, and consistent with site-specific modification of cetuximab via n-glycans on the heavy chain.

In both oxidized cetuximab and PEGylated cetuximab samples, a small sharp peak was still seen at a retention time of 18.9 minutes, perhaps indicating that a proportion of heavy chains remain non-oxidized (and thus non-PEGylated). The oxidized (non-PEGylated) cetuximab appears to have a second, relatively broad peak centred around approximately 19.3 minutes, while the PEGylated cetuximab has an extremely broad peak centred around 20 minutes. The broadness of these peaks could possibly be explained by a distribution of oxidized antibodies (with a varying number of aldehydes) reacting with PEG to give a distribution of PEGylated antibodies. This broadness could be compounded in the case of the PEGylated antibody by the fact that LA-PEG-Hyd will be a population of polymers with a range of MWs centred around the nominal reported MW of 3.4 kDa. Regardless, RP UP-LC analysis clearly indicates a difference between the heavy chains of untreated, oxidized (non-PEGylated), and oxidized and PEGylated cetuximab, providing strong evidence of successful site-specific PEGylation of cetuximab through the proposed mechanism.

3.5 Functionalization and characterization of GNPs

After achieving site-specific modification of cetuximab with LA-PEG-Hyd, these modified antibodies were combined with bare citrate-capped gold nanoparticles (GNPs) to give rise to a therapeutic antibody-loaded GNP construct, as described in Section 2.3.1.

3.5.1 Physical characterization

Citrate-capped GNPs with a diameter of 15 nm were reacted with PEGylated cetuximab for 20 minutes at room temperature, after which time 2 kDa mPEG-SH was added to cap remaining reactive surface of GNPs and provide colloidal stability. mPEG-SH was added at a ratio 2-fold greater than the amount predicted to provide complete coverage of the GNP surface (calculated from surface area of GNP and the

lower-bound estimate of Nuzzo et al. that a small thiolated molecule can occupy 21.6 $\mathring{A}^2$ of space on a gold surface [225]). 20 minutes after the addition of mPEG-SH, GNPs were washed with a solution of 0.1% Tween-20 in PBS by centrifugation at high rcf (rcf $>$ 15 500).

UV-Vis

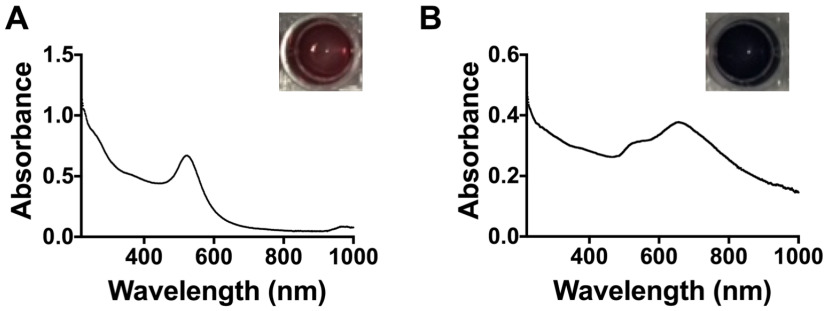

Figure 3.12: Absorbance spectrum of (A) GNPs functionalized with cetuximab-PEG-LA and capped with mPEG-SH, and (B) bare GNPs after resuspension in PBS. Samples were loaded in a UV-transparent microplate, and spectra were acquired with BMG Labtech microplate reader. Photos show appearance of GNPs after washing and resuspension in PBS. Note, samples A and B do not contain the same concentration of GNPs.

After washing, functionalized GNPs were resuspended in PBS. GNPs were added to a UV-transparent 96-well microplate, and a UV-Vis absorbance spectrum was acquired using a microplate reader. As a control, non-PEGylated GNPs were washed in the same manner and resuspended in PBS. Monodisperse GNPs of sizes 5-100 nm display one single absorbance peak at a wavelength corresponding to the surface plasmon resonance (SPR) band for that particular size [226]. For 15 nm particles, the SPR band occurs at approximately 520 nm (though this exact value is sensitive to changes in capping ligands), and this peak is clearly visible for the GNPs functionalized with cetuximab-PEG-LA in Fig. 3.12 panel A (with peak at approximately 523 nm). Bare GNPs however, when resuspended in a high-salt solution such as PBS, are prone to aggregation as shown in Fig. 3.12 panel B. This aggregation is readily visibly to the naked eye, as the GNP solution turns from a deep burgundy

colour to dark purple.

Dynamic light scattering

Dynamic light scattering (DLS) is a technique used to determine the size distribution of a population of particles in the 10-1000 nm range in suspension. Small particles in solution are in constant random (Brownian) motion, at a speed related to their size. To obtain a size measurement, monochromatic polarized light is directed through a sample of small particles in solution. The resulting speckle pattern produced by constructive and destructive interference due to light scattering off of the particles is then correlated over time to provide an estimate of size. Small particles will move more quickly than larger ones, and thus the speckle pattern will de-correlate more rapidly. Fig. 3.13 panel A shows the intensity-weighted distribution of GNP sizes for blank (in citrate), mPEG coated, and mPEG + cetuximab-PEG-LA coated GNPs. There is a clear increase in size when GNPs are coated with cetuximab-PEG-LA (red trace), as compared to blank GNPs (green trace) and mPEG coated GNPs (blue trace). The z-average sizes determined for three sample types were 24.9, 28.5 and 87.8 nm (average of three measurements), with corresponding polydispersity indices of 0.43, 0.29 and 0.34 for blank, mPEG coated, and cetuximab-PEG-LA coated GNPs (Cetux-PEG) respectively. The size value of the blank non-modified GNPs does not match the stated particle diameter as supplied by the manufacturer (15 nm). However, it is well established that DLS measurements of the hydrodynamic radius gold nanoparticles can give rise to different results than more direct techniques such as transmission electron microscopy (TEM), as GNPs have unique optical absorption and scattering properties, and measurements by DLS are extremely sensitive to the presence of a small number of large aggregates [227] [228]. Panel B of Fig. 3.13 clearly shows (without making any of the possibly erroneous assumptions needed to calculate a size value) a clear difference in the autocorrelation functions of cetuximab-PEG-LA coated GNPs, and mPEG coated GNPs,

compared to blank non-modified (citrate capped) GNPs. This suggests successful surface coating of GNPs with cetuximab-PEG.

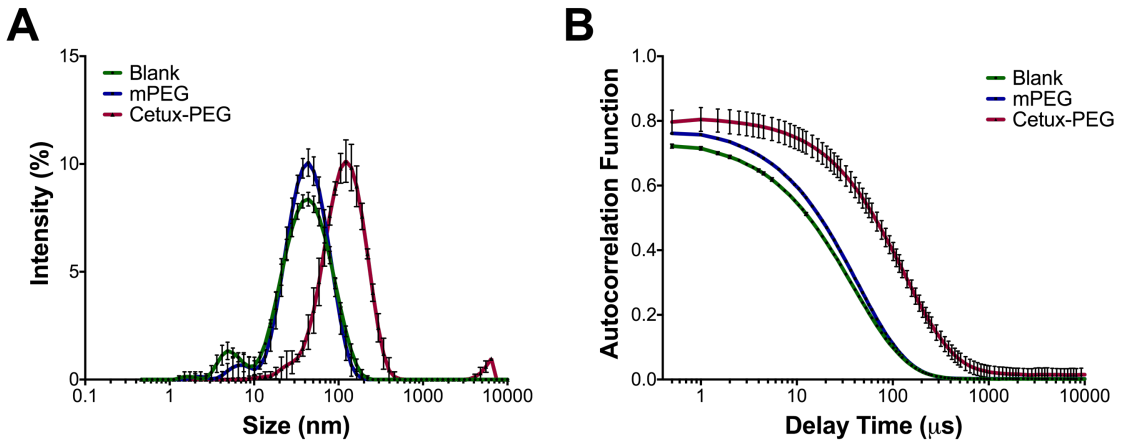

Figure 3.13: Sizing of GNPs with dynamic light scattering. Samples were added to pure water in a plastic cuvette, and were sized using dynamic light scattering with a ZetaSizerNano (Malvern Instruments Ltd, UK). Three measurements of size were made per sample (each measurement is of 12 runs), traces shown here are the mean over three measurements, while error bars are the corresponding standard deviations. Panel A shows the intensity-weighted sizes of GNPs, while panel B shows the autocorrelation function of GNPs as a function of delay time. The green traces are blank (citrate-capped) GNPs, blue traces are mPEG-coated GNPs, while red traces are GNPs coated with mPEG and cetuximab-PEG-LA.

Transmission electron microscopy

Transmission electron microscopy (TEM, see Section 2.3.5) of GNPs showed that the blank non-modified GNPs are indeed approximately 15 nm in diameter (Fig. 3.14 panel A), and relatively monodisperse. When mPEG-SH was added to GNPs (Fig. 3.14 panel B), very little change was observed, in keeping with the DLS results shown above. When GNPs were loaded with cetuximab-PEG-LA however (panel C), a clear change was evident. At lower magnifications (top image), agglomeration of GNPs is seen, though it is unclear whether this agglomeration reflects the state of the particles in solution, or is an artefact of sample drying on the TEM grid. At higher magnifications, a corona of grey staining is clearly seen around each GNP, indicating a uniform coating around each GNP of protein.

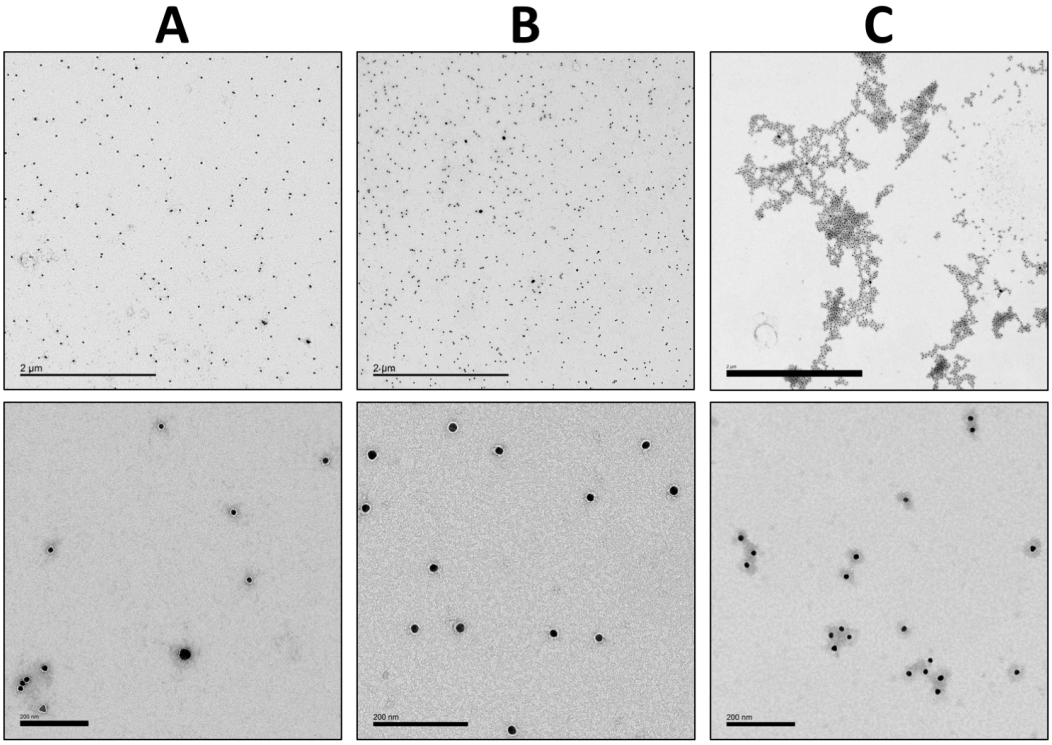

Figure 3.14: TEM of blank non-modified (panel A), mPEG-coated (panel B), and mPEG + cetuximab-PEG-LA (panel C) coated GNPs. Samples were deposited on a carbon support film 300 mesh 3 mm grid, and negatively stained with 2% uranyl acetate before TEM imaging with a FEI Tecnai 12 Transmission Electron Microscope.

3.5.2 Loading of cetuximab

SDS-PAGE analysis of loading

Loading of cetuximab onto GNPs was verified by SDS-PAGE analysis with Coomassie staining for protein, as shown in Fig. 3.15. GNPs were reacted with cetuximab-PEG-LA and washed with PBS and 0.1% Tween-20 then combined with non-reducing Laemmli sample buffer and added to lane 2. An identical sample of cetuximab-PEG-LA functionalized GNPs was added to Laemmli buffer supplemented with 2.5% BME (reducing Laemmli buffer). This sample was heated to 95 °C for 10 minutes, before loading into lane 3. Free cetuximab-PEG-LA (at concentrations between 2 to 0.125 mg/mL) was also heated with reducing Laemmli buffer, and was added to lanes 4-8. Very faint protein staining is observed in lane 2, but no distinct

bands are seen. Though as discussed previously, the presence of PEG can affect the migration of a protein, and these samples could contain not only LA-PEG-Hyd, but also mPEG-SH and Tween-20, and so the faint staining seen here could in fact correspond to a small amount of free cetuximab left in solution after the GNPs were washed. In lane 3 however, very distinct heavy and light chain protein bands are evident. In addition to cleaving the interchain disulfide bonds (and thus releasing the light chain from the PEGylated heavy chain attached to the GNP), addition of a large excess of thiol-containing BME will displace the lipoic acid anchoring the PEGylated antibodies to the GNP surface. Taken together, the staining patterns in lanes 2 and 3 indicate that a significant amount of cetuximab-PEG has been loaded onto the GNPs through the proposed mechanism, and that very little free cetuximab is left in solution after washing. From the standard curve of free cetuximab-PEG in lanes 4-8, it is clear that staining intensity closely relates to protein concentration. However, the protein bands from GNP-released cetuximab-PEG (which must contain also mPEG-SH and Tween-20) do not precisely resemble the free cetuximab-PEG bands, and so an accurate quantification was not possible. Based on staining intensity however, antibody concentration in the GNP solution tested here appeared to be in the range greater than or equal to 0.5 mg/mL. GNP concentration was estimated from the UV-Vis absorbance at the SPR peak and the molar extinction coefficient provided by the manufacturer (3.67 x 10^8 $M^{-1}cm^{-1}$), and for the batch of GNPs tested here was calculated to be approximately 1.2 x 10^{14} GNPs/mL. This would imply a loading of at minimum 16 cetuximab molecules per GNP.

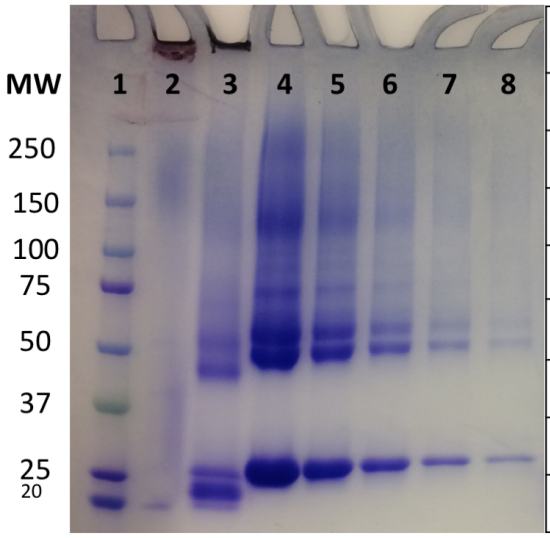

Lane #	Sample Identity
1	Molecular weight marker
2	Cetux-PEG-GNPs
3	Cetux-PEG-GNPs
4	Cetux-PEG (2 mg/mL)
5	Cetux-PEG (1 mg/mL)
6	Cetux-PEG (0.5 mg/mL)
7	Cetux-PEG (0.25 mg/mL)
8	Cetux-PEG (0.125 mg/mL)

Figure 3.15: SDS-PAGE and Coommassie staining characterization of cetuximab-PEG-GNP conjugates. SDS-PAGE and Coommassie staining were performed with samples as described in Section 2.2.2. Sample in lane 2 was diluted in non-reducing Laemmli sample buffer, while the remaining samples are in reducing Laemmli buffer and were heated to 95 °C for 10 minutes (denoted with text box filled in blue).

Estimation of cetuximab loading

The lower limit of cetuximab loading was quantified by incubation of GNP samples with BME to release antibodies attached via LA-PEG, centrifugation, and quantification of protein content in supernatant. This quantification method provides only a lower estimate of loading, as it was not possible to confirm complete release of cetuximab from the particles, and it is possible that the centrifugation conditions used to pellet the GNPs create a gradient of antibody concentration within the tube, such that the supernatant taken from the top of the tube is a lower concentration than the true free antibody concentration. Nonetheless, estimates of cetuximab loading were calculated for both batches of cetuximab-GNPs used in vivo in Chapter 2. The batch of GNPs analysed by SDS-PAGE in Fig. 3.15 were found to have a minimum concentration of 0.62±0.06 mg/mL cetuximab, which corresponded to a minimum loading of approximately 20 cetuximab molecules per GNP. The second

batch of cetuximab-GNPs synthesized for use in vivo contained half the concentration of GNPs, and a minimum cetuximab concentration of 0.26±0.02 mg/mL, corresponding to approximately 17 cetuximab molecules per GNP.

3.5.3 Bioeffect of cetuximab-GNPs

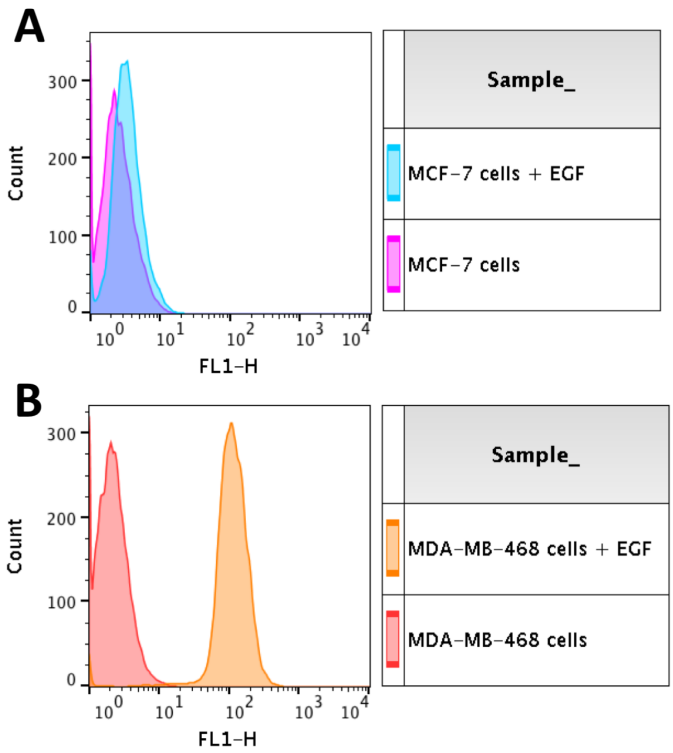

Figure 3.16: Binding of fluorescent EGF to MCF-7 or MDA-MB-468 cells. MCF7 or MDA-MB-468 cells were incubated with fluorescently-tagged EGF (in a solution of 1% BSA in PBS). Cells were washed after 1 hour of incubation before flow cytometric analysis with a BD FACSCalibur Flow Cytometer as described in Section 2.4.2.

Thus far it has been shown that cetuximab can be site-specifically PEGylated, and retain the ability to bind to its target, the EGF receptor (EGFR). Furthermore, it was proven that GNPs could be loaded effectively with cetuximab. As discussed in Section 1.2.1 when cetuximab binds to EGFR, it blocks EGF binding, can induce internalization of the receptor, and downregulate of cell expression of EGFR [46]. Although ELISA (Fig. 3.9) analysis demonstrated that cetuximab-PEG-LA retains EGFR antigen binding capacity, it was also important to demonstrate retention of

binding to the EGFR in its native state on cell membranes.

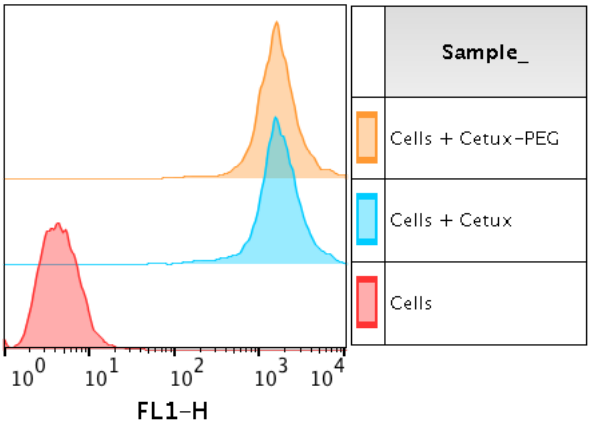

Figure 3.17: Binding of cetuximab or cetuximab-PEG-LA to MDA-MB-468 cells. MDA-MB-468 cells were incubated with cetuximab or cetuximab-PEG (in a solution of 1% BSA in PBS). Cells were washed after 1 hour of incubation, and were incubated with a Alexafluor488-tagged anti-human secondary antibody for an hour before washing and flow cytometric analysis with a BD FACSCalibur Flow Cytometer as described in Section 2.4.2.

As shown in Fig. 3.16, MDA-MB-468 cells express a high level of the EGFR, as compared to MCF7 which express low levels of EGFR. Fig. 3.17 shows successful binding of both untreated cetuximab (blue) and cetuximab-PEG-LA (orange) to MDA-MB-468 cells. In order to then determine if cetuximab-loaded GNPs can induce a similar bioeffect to unmodified cetuximab, their ability to block binding of fluorescently-labelled EGF to MDA-MB-468 cells was investigated.

First, cells were incubated for one hour with: 5, 2.5 or 1.25 μg/mL of untreated cetuximab (Fig. 3.18), or 16, 8 or 4 x 10^{11} of cetuximab-GNPs/mL Fig. 3.19 and 0.5 ug/mL of fluorescently-tagged EGF. After incubation, samples were analysed using flow cytometry, and cellular fluorescence was used as a metric to quantify the degree of EGF-binding.

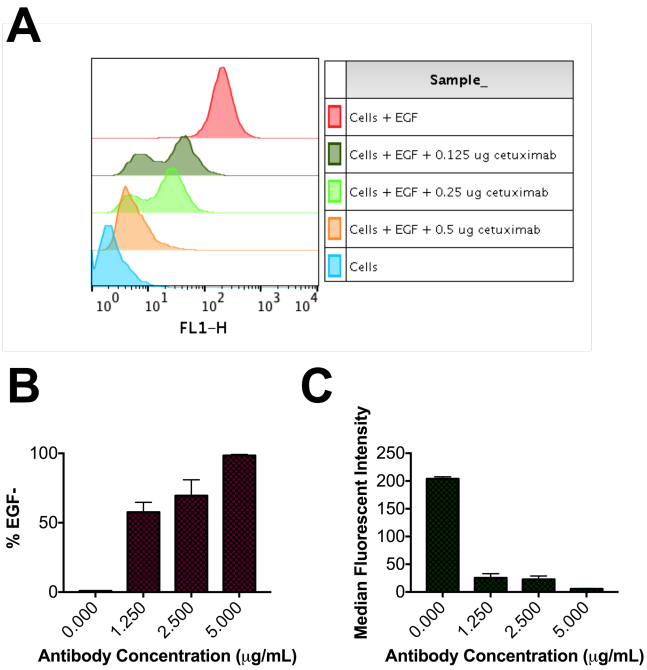

Figure 3.18: Inhibition of EGF binding to MDA-MB-468 cells by cetuximab. 100 μL of MDA-MB-468 cells were incubated for one hour with: 0.5, 0.25 or 0.125 μg of untreated cetuximab and 0.5 ug/mL of fluorescently-tagged EGF. Single cells were gated for with polygonal gating in samples of untreated cells. Panel B shows the percentage of cells with fluorescence lower than the control sample, cells + EGF ('% EGF-'). The median fluorescent intensity of each sample was quantified and plotted in panel C.

Figs. 3.18 and 3.19 show the results of this analysis. Firstly, single cells were gated for with polygonal gating of untreated cells. Panel A shows a representative histogram for each concentration of cetuximab or cetuximab-GNP tested, compared to cells alone (no EGF) and cells incubated with EGF but no cetuximab or cetuximab-GNP. It is clear that both cetuximab and cetuximab-GNPs block binding of EGF in a dose-dependent fashion. Cells with fluorescence lower than the control sample (EGF only, no cetuximab) were gated for, and the percentage of cells that fell within this gate were quantified and denoted '% EGF-'. Finally, the median fluorescent intensity of each sample was quantified and plotted, indicating again successful dose dependent inhibition of EGF binding with cetuximab. Fig. 3.19 panel B shows that incubating cells with blank GNPs (mPEG-coated, but no cetuximab) has no effect on EGF binding, indicating that the effect of cetuximab-GNPs on EGF

binding of MDA-MB-468 cells is due to the activity of the conjugated cetuximab.

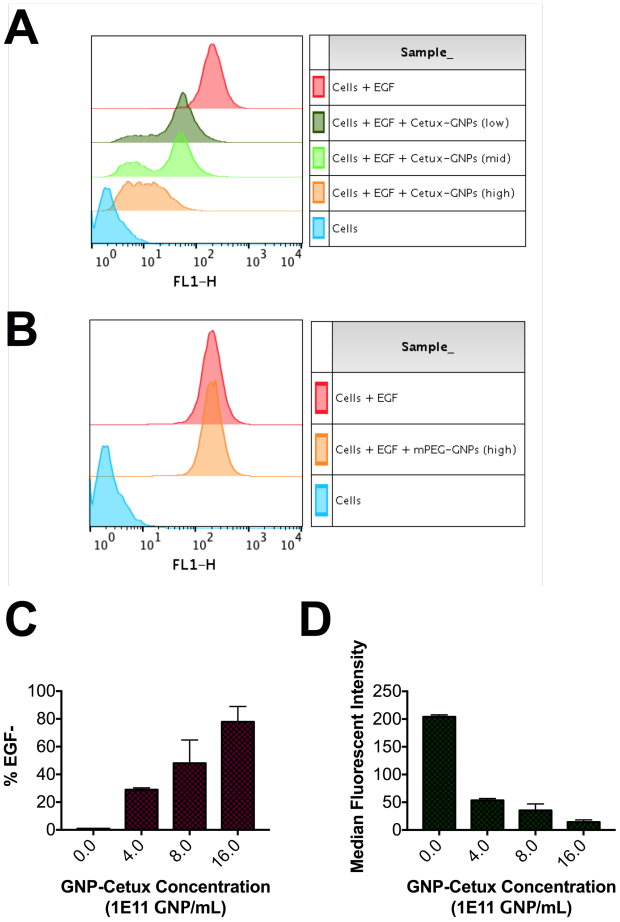

Figure 3.19: Inhibition of EGF binding to MDA-MB-468 cells by cetuximab-GNPs. 100 μL of MDA-MB-468 cells were incubated for one hour with: 16, 8 or 4 x 10^{11} cetux-GNPs/mL (panel A, denoted here as high, mid and low respectively), or 16 x 10^{11} mPEG-GNPs/mL (panel B), and 0.5 μg/mL of fluorescently-tagged EGF. Single cells were gated for with polygonal gating in samples of untreated cells. Panel C shows the percentage of cells with fluorescence lower than the control sample Cells + EGF ('% EGF-'). The median fluorescent intensity of each sample was quantified and plotted in panel D.

3.6 Summary and discussion

Examples in the literature of site-specific conjugation of therapeutic antibodies to GNPs have suggested that these conjugates can be more cytotoxic to target cells, and can lead to greater internalization of GNPs into target cells. Yokoyama et al. and Garcia-Fernandez et al. both created a cetuximab-GNP construct utilizing a

heterobifunctional linker with a dithiol moeity for GNP attachment and hydrazide for antibody attachment, and both groups demonstrated enhanced bioeffects with their cetuximab-nanoparticle constructs [186, 189].

The work in this chapter sought to optimize, validate, and as far as possible quantify the process of conjugating therapeutic antibodies to GNPs. In light of the potential loss of antigen binding capacity resulting from non-site specific modification of the antibody, a site-specific methodology (reported by Kumar et al. [195] and used by others with cetuximab [186, 189]), was optimized and used here.

Specifically, a new heterobifunctional PEG linker (LA-PEG-Hyd) was designed to provide covalent linkage to the surface of GNPs and formation of a stable hydrazone bond with oxidized glycan moieties created on the antibodies (though this linker could theoretically be used with any aldehyde-containing or oxidizable glycoprotein). Oxidation and PEGylation (with LA-PEG-Hyd) of two therapeutic monoclonal antibodies (cetuximab and trastuzumab) were then investigated, and generated evidence suggesting that cetuximab could be more readily PEGylated with LA-PEG-Hyd, while retaining a high affinity for EGFR (though decreased from unmodified cetuximab). SDS-PAGE and liquid chromatographic analyses were used to confirm site-specific modification of the heavy chain of cetuximab. Cetuximab-PEG-LA was then combined with bare citrate capped GNPs to yield cetuximab-loaded GNPs that were stable in PBS, and SDS-containing buffer (in the absence of BME), but could be released upon addition of thiol-containing reducing agent such as BME. DLS and TEM microscopy revealed a size increase to the GNPs after loading with cetuximab-PEG. Finally, flow cytometric analysis revealed that cetuximab-GNPs could block the binding of EGF in a dose dependent fashion. The totality of this data provides one of the most robust and thorough demonstrations of such work in terms of the evidencing of site selective modification and the analysis performed to characterize the impact on antibody structure and binding of the antibody to its target. Indeed, though Garcia-Fernandez et al. and Yokoyama et al. have

demonstrated successful conjugation of cetuximab to GNPs through a hydrazide linker [186, 189], these studies did not examine the potential effect of conjugation through the glycosylation site of cetuximab within the antibody binding domain on antigen binding, and did not seek to optimize PEGylation through use of organocatalysts and optimized oxidation conditions. No investigation of the characteristics of PEGylated cetuximab was performed in these studies.

Given the potential for enhanced therapy with antibody-loaded GNPs, and the delivery challenges faced by large nanoparticulate therapeutics, it was hypothesized that US-mediated cavitation could enhance the delivery of these actively (and passively) targeted therapeutics, particularly as nanomedicine density has been recently identified as a potential positive factor in US-enhanced transport [135, 193]. In the next chapter, the US-mediated delivery of the cetuximab-GNP developed and characterized here is investigated.

Chapter 4

In vivo assessment of cavitation-mediated delivery of antibodies and targeted nanoparticles

As discussed in Chapter 1, there is a clear argument for improving the delivery of nanomedicines through use of externally-applied stimuli, as the benefits provided by passive targeting due to the EPR effect are limited [30]. Even therapeutics with extended circulation such as mAbs are limited by heterogenous distribution and poor tumour penetration, especially at lower doses [35, 36]. In this chapter, the effect of US-mediated cavitation on delivery of cetuximab-GNPs and free cetuximab is investigated and compared to the passive accumulation achieved as a possible result of the EPR effect.

4.1 Circulation kinetics and tumour accumulation

In order to interpret and assess the effects of US-mediated cavitation on tumoural delivery of cetuximab-GNPs and cetuximab, it was important to first determine the circulation kinetics of these two therapeutics, and determine the degree of passive tumoural accumulation achieved. The circulation kinetics of cetuximab are well established in the literature [229], but were investigated here nonetheless to firstly provide a comparison for cetuximab-GNPs in an identical mouse model, and to determine levels of passive accumulation for the specific tumour model chosen here.

4.1.1 Circulation kinetics of cetuximab and cetuximab-GNPs

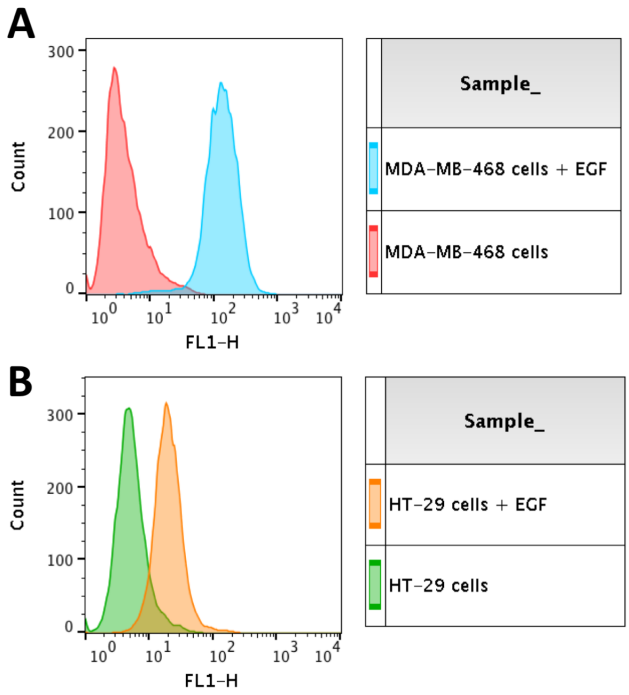

Figure 4.1: Binding of fluorescent EGF to HT-29 or MDA-MB-468 cells. HT-29 or MDA-MB-468 cells were incubated with fluorescently-tagged EGF (in a solution of 1% BSA in PBS) for 1 hour. Flow cytometric analysis was performed with a BD FACSCalibur Flow Cytometer as described in Section 2.4.2.

HT-29 cells were chosen here as a subcutaneous tumour model, as they have relatively high EGFR expression (as shown in Fig. 4.1), and have been used with cetuximab in pre-clinical models of colorectal cancer [230]. CD-1 nude mice were implanted subcutaneously with HT-29 cells, and once tumours had reached a mean size between 100-150 mm^3, mice were dosed i.v. with cetuximab or cetuximab-GNPs. Although it was predicted that the cetuximab-GNPs would be well tolerated based on numerous reports in the literature of successful in vivo administration of targeted GNPs [188, 187], the injectate was very concentrated (approximately 1.2 x 10^{14} GNP/mL), and the GNPs appeared to be (reversibly) flocculating at these concentrations. The reversibility of this flocculation was evidenced by the SPR peak on the UV-Vis absorbance spectra which remained at 522 nm with no visible

broadening, following sonication in an ultrasonic bath to disperse clumps. After functionalization and washing by centrifugation, GNPs were resuspended in PBS supplemented with 0.1% Tween-20, to provide surfactant to reduce flocculation. The first three mice to receive cetuximab-GNPs (6 x 10^{12} cetuximab-GNPs) were closely observed after recovery from anaesthesia, and no ill-effects were seen. Three mice were also injected with cetuximab alone (25 μg). Blood was sampled from mice in both groups at 3, 6 and 24 hours post-injection. Treatment with the cetuximab-GNPs was staggered so that safety in the first mouse was confirmed, before dosing of the remaining mice in the group was performed. Despite this, toxicity concerns raised in subsequent short-term PK experiments resulted in these short-term studies being performed with 1/4 the amount of cetuximab-GNP than was used in the long-term PK studies. For short-term PK study of cetuximab-GNPs (1.5 x 10^{12} cetuximab-GNPs) and non-modified cetuximab (25 μg) blood samples were taken 5, 10, 30 and 60 minutes post-injection.

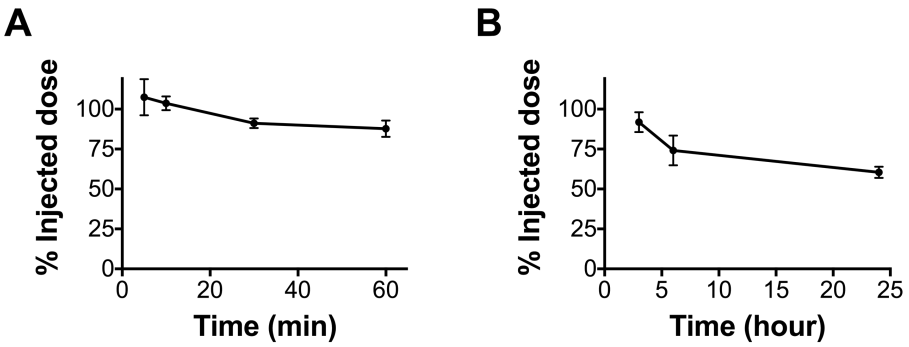

Figure 4.2: Plasma concentration of cetuximab over time. Two cohorts of mice (n=3) were injected with 25 μg of cetuximab. Blood samples were taken at fixed time points post injection, and analyzed for cetuximab-GNP concentration using a sandwich ELISA to detect human antibodies. Panel A: 0-60 minutes, panel B: 0-24 hours. Points represent mean of 3 mice, and error bars represent standard deviations.

Fig. 4.2 shows the percentage of injected dose (ID) in plasma at fixed time points after injection of 25 μg of free cetuximab. Plasma concentration of cetuximab was determined by sandwich ELISA. To convert determined plasma amounts to a per-

centage of the ID, a standard curve was made by spiking control plasma (from an untreated animal) with known amounts of the injectate. As predicted, cetuximab shows extended circulation, with approximately 60% of the ID remaining in circulation after 24 hours.

As the dose used to investigate the long-term circulation kinetics of cetuximab-GNPs raised some safety concerns, a fresh batch of cetuximab-GNPs were prepared, and diluted to half the concentration of the batch used to test long-term clearance (approximately 6 x 10^{13} GNP/mL). These GNPs were sonicated immediately prior to dosing to prevent the injection of large flocculates. Three mice were treated with 25 μL containing 1.5 x 10^{12} cetuximab-GNPs (1/4 of the original dose, as 50 μL was given of the higher dose at twice the concentration), and no adverse reactions were observed. Blood samples were taken at 5, 10, 30 and 60 minutes post-injection, and analyzed by sandwich ELISA using the injectate of cetuximab-GNPs to generate a standard curve. Fig. 4.3 shows the percentage of the ID in plasma at fixed time points after injection of either the high dose of 6 x 10^{12} cetuximab-GNPs (panel B) or the low dose of 1.5 x 10^{12} GNPs (panel A). From these curves, it is clear that cetuximab-GNPs are cleared much more rapidly than free cetuximab, as only 14% of the ID was in circulation 1 hour after injection (of the lower dose). 24 hours after injection of the higher dose, only 4% of the ID remained in the plasma.

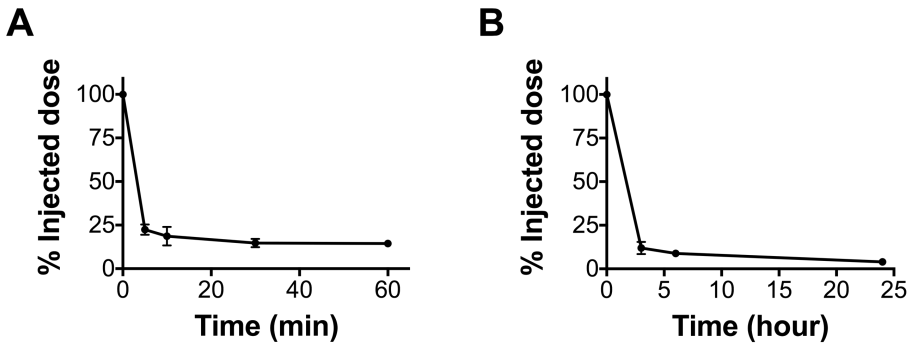

Figure 4.3: Plasma concentration of cetuximab-GNPs over time. Mice (n=3) were injected with 1.5 x 10^{12} (panel A) or 6 x 10^{12} (panel B) of cetuximab-GNPs. Blood samples were taken at fixed time points post injection, and analyzed for cetuximab-GNP concentration using a sandwich ELISA to detect human antibodies (see Section 2.6.3). Panel A: 0-60 minutes, panel B: 0-24 hours. Points represent mean of 3 mice, and error bars represent standard deviations.

4.1.2 Passive accumulation of cetuximab and cetuximab-GNPs

After mice treated with cetuximab or cetuximab-GNPs were culled (at 1 hour or 24 hours post-injection), tumours and livers were immediately excised and frozen until analysis. Tissues were homogenized and lysed, and cetuximab or cetuximab-GNP concentration was quantified using a sandwich ELISA. Percentage of the ID was determined from a standard curve created with control tumour homogenate or liver (from untreated mouse) spiked with known amounts of the appropriate injectate.

Time (hrs)	Tissue	% ID/g tissue	% ID
1	Tumour	6.5±2.2	0.91±0.72
	Liver	26.0±7.7	32.6±6.1
24	Tumour	15.6±4.5	1.87±0.80
	Liver	12.3±5.1	17.1±5.7

Table 4.1: Quantification of passive tumour accumulation of cetuximab over time. Two cohorts of mice (n=3) were injected with 25 μg of cetuximab. After 1 or 24 hours, tumours were excised, homogenized, and analyzed for cetuximab concentration using a sandwich ELISA (see Section 2.6.3)

.

Table 4.1 shows the percentage of the ID of cetuximab recovered from the tumours and livers of mice 1 and 24 hours post-injection. Predictably, free cetuximab passively accumulates well within tumours, with close to 2% (1.87±0.80) of the ID accumulating in tumours after 24 hours. Liver concentration decreased from 32.6±6.1 to 17.1±5.7% of the ID between 1 and 24 hours post-injection. As the blood was not 'flushed' from the livers with PBS before measurement, this may be explained by the decrease in circulating dose of cetuximab between these times (from approximately 88% to 60% of the ID). It may also be a consequence of the breakdown of the cetuximab antibody within the murine liver.

Time (hrs)	**Tissue**	**% ID/g tissue**	**% ID**
1	Tumour	0.2±0.1	0.03±0.01
	Liver	17.6±5.8	16.3±4.9
24	Tumour	1.0±0.1	0.13±0.08
	Liver	0.06±0.05	0.08± 0.08

Table 4.2: Quantification of passive tumour accumulation of cetuximab-GNPs over time. Mice (n=3) were injected with 1.5 x 10^{12} (1 hr group) or 6 x 10^{12} (24 hr groups) of cetuximab-GNPs. After 1 or 24 hours, tumours were excised, homogenized, and analyzed for cetuximab-GNP concentration using a sandwich ELISA (see Section 2.6.3)

Table 4.2 shows the percentage of the ID of cetuximab-GNP, recovered in tumours and livers of mice 1 and 24 hours post-injection, as measured by a sandwich ELISA (see methods Section 2.6.3). Evidently, cetuximab-GNPs do not passively accumulate well within tumours, with only 0.13±0.08% of the injected dose accumulating in tumours after 24 hours. As the data for tumour and liver accumulation after 1 hour were acquired from mice which received a lower dose, it is difficult to say whether the % of ID recovered after 1 hour is comparable to the % of ID recovered after 24 hours, or if in fact, tumour accumulation is dose dependent. Liver concentration decreased from 16.3±4.9% to almost 0% of the ID between 1 and 24 hours post-injection. As only 15% of the ID of cetuximab-GNPs remained in circulation

after 1 hour, this figure indicates liver accumulation of GNPs, which is consistent with other studies in the literature. GNP clearance routes and mechanisms have been shown to depend on size [231] and surface-coating [201], and studies with similarly sized GNPs (uncoated, PEGylated, or targeted with cetuximab) have shown the liver to be the major clearance route [231] [232] [187] [233]. The complete reduction in the levels of cetuximab-GNPs detected in the liver by 24 hours indicates that the capture and processing pathways of cetuximab-GNP may differ from those involved in the processing of free cetuximab.

4.1.3 Plasma stability

Though analysis with SDS-PAGE (Section 3.5.2) revealed only a very small proportion of free antibody in solution with the washed GNPs, the conditions in circulation might affect this equilibria, as the pH is lower (7.4 vs 8.5) and temperature is higher (37 °C vs storage at 4 °C). Thus the stability of the cetuximab-GNPs was investigated in whole plasma heated to 37 °C. Pre-warmed samples of human plasma were spiked with cetuximab-GNPs to a final concentration of 5% v/v (GNPs/plasma). Samples were incubated at 37 °C for varying amounts of time, before centrifuging at 15,500 rcf for 25 minutes at 4 °C. Fig. 4.4 reveals a slight but significant increase in concentration of free antibody after incubation with warm plasma, from approximately 0.028±0.004 to 0.038±0.003 mg/mL after 15 minutes (at 37 °C, plus 25 minutes at 4 °C in centrifuge). From estimates of the lower limit of cetuximab-loading (approximately 0.26±0.02 mg/mL, Section 3.5.2), this measure of free cetuximab represents at most approximately 15% of cetuximab in the cetuximab-GNP sample.

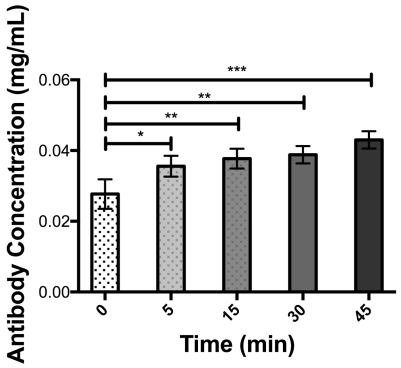

Figure 4.4: Concentration of free cetuximab in cetuximab-GNP samples incubated with whole plasma. Samples of cetuximab-GNPs were diluted 20x in human plasma, and incubated at 37 °C between 5-45 minutes. After incubation samples were centrifuged at 15,500 rcf for 25 minutes. Supernatant was assayed for cetuximab concentration by ELISA (see 2.6.4). Statistical significance was assessed with one-way ANOVA followed by post-hoc Dunnett's multiple comparisons test. *** = $p < 0.001$, ** = $p < 0.01$, * = $p < 0.05$, all p-values were adjusted for multiple comparisons.

From this study of circulation kinetics and passive tumour accumulation of cetuximab-GNPs and cetuximab it is clear that these two therapeutics have vastly different characteristics in vivo. As expected, free cetuximab has an extended circulation time and accumulates reasonably well within EGFR-expressing tumours (approximately 2% of the ID present in tumours after 24 hours). In contrast, cetuximab-GNPs were cleared rapidly and after 24 hours only approximately 0.1% of the higher ID had accumulated. 1 hour after injection of a lower well-tolerated dose, only 0.03% of the ID had accumulated within the tumour, while 85% of the ID had already cleared from circulation. If these GNPs (or any other NPs with similar circulation and poor tumoural deposition) are to be effective anti-tumour agents, it is clear that their tumour delivery needs to be improved. The delivery of free cetuximab also stands to benefit from enhanced delivery, but there is clearly a large area of opportunity for improving delivery of (and hopefully thus therapy with) of poorly-circulating/accumulating nanoparticles, such as the cetuximab-GNPs studied here.

4.2 Tumoural delivery with US-mediated cavitation

As discussed in Section 1.3, US-mediated cavitation can provide a mechanical stimulus to improve the transport of therapeutics into solid tumours. Cavitation nuclei (CN) can be used to seed cavitation, and obviate the requirement for extremely large US pressures, which can be damaging to tissue. Many studies using US-mediated cavitation to enhance delivery of a therapeutic have used clinically-approved ultrasound contrast agents (UCAs), such as Sonovue® (SV) as CN [167, 177, 134, 24, 135]. SV is a formulation of lipid-shelled microbubbles of sulfur hexafluoride gas, with a size distribution between 0.7 to 10.0 μm [234]. Though microbubbles have proven effective at enhancing delivery of therapeutics both in vitro and in vivo, their efficacy (particularly in vivo) is limited by their rapid clearance, and their relatively large size. Firstly, the short half-life of formulations such as SV is suboptimal for treatment of larger regions of metastatic disease. In humans, 40-50% of the i.v. injected dose is eliminated within 1 minute after injection, with 80-90% eliminated after 11 minutes [168]. This rapid clearance necessitates continual re-dosing to ensure sustained levels of cavitation [24, 169]. Secondly, even in pre-clinical models, the micron-sized bubbles might be less effective at ensuring delivery deep into hypoxic tumour regions than a smaller nano-scale CN, as microbubbles are too large to extravasate from the blood stream and 'follow' a nanomedicine pushed into a tumour by cavitation. In response to these limitations, Kwan et al. developed polymeric gas-stabilizing nanoparticles, capable of sustained cavitation when exposed to high-intensity US, and small enough to potentially extravasate from 'leaky' tumour vasculature [171]. These sonosensitive particles (SSPs) were shown to sustain cavitation in an in vivo tumour model 4-fold longer than SV microbubbles, and increase delivery of a model drug (fluorescently-labelled dextran) in an in vitro model [170]. Furthermore, the use of SSPs as CN was shown to enhance the delivery of an oncolytic vaccinia virus to an in vivo tumour model 6-fold as compared to the delivery

achieved with SV as a CN [173]. Here, both SV and SSP are used to investigate US-mediated cavitation for delivery of a therapeutic antibody (cetuximab) and actively-targeted nanoparticle (cetuximab-GNPs).

4.2.1 Experimental design

In any in vivo experiment, there is inherent variability due to natural differences between organisms. Between mice, for example, GNPs will likely circulate with slightly different kinetics - and this variability is in addition to small differences in the initial injectate concentration and volume due to unavoidable operator error. A bilateral tumour model within a single animal provides an elegant way to isolate the effects of US and cavitation on virus delivery, while controlling for other variables which contribute to variance in delivery between animals. The bilateral tumour model also allows for a reduction in the number of animals needed to reach a given sample number for each combination of factors. Previous studies of Ad5 delivery using US + CN employed this bilateral tumour model, and were able to demonstrate increased transgene expression [178], and accumulation of (polymer-coated) virus [134] in US-treated tumours as compared to non-US-treated control tumours.

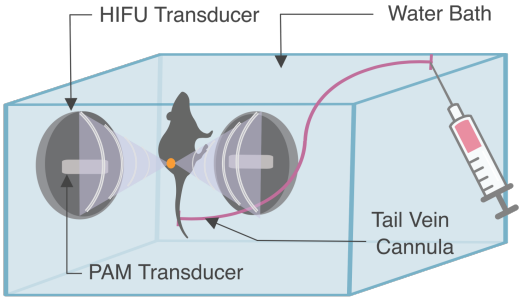

Figure 4.5: Schematic of in vivo US setup. Mice were placed in warm water bath to facilitate coupling of US. Two HIFU transducers were aligned on the tumour to be treated, and resulting cavitation signals were detected with Passive Acoustic Mapping (PAM) transducers.

A schematic of the US set-up is shown in Fig. 4.5, and parameters used are described in Table 4.3. Two HIFU transducers (with centre frequencies of 0.5 MHz)

were mounted orthogonally, and confocally aligned. Each transducer contained a rectangular cut-out, in which a linear transducer array was mounted. The ultrasound arrays were used to provide a real-time passive acoustic map (PAM) of any cavitation activity occurring within the tumours – this allowed for treatment monitoring, and post-treatment analysis of cavitation activity. Cavitation data acquired by the arrays was processed using custom generated MatLab code written by Dr. Christian Coviello, Dr. Calum Crake, and Seán Finn. This 'bistatic' configuration of transducers offers multiple advantages over use of a single HIFU trandsucer and single array. Primarily, the bistatic configuration of arrays affords greater PAM resolution in the axial direction, allowing for more accurate localization of cavitation activity [235] [162]. Secondly, the overlapping focal region of the two HIFU transducers (and region of greatest PRFP) is smaller than it would be for a single transducer generating a similar focal pressure, allowing for more precise localisation of cavitation.

Frequency (MHz)	**PRF (Hz)**	**DC (%)**	**Cycles/Burst**	**PRFP (MPa)**
0.5	0.5	5	50 000	1.5-2

Table 4.3: Parameters for in vivo US treatment of mice dosed with cetuximab or cetuximab-GNPs + SV or SSPs.

.

Table 4.4 outlines the dose of free cetuximab and cetuximab-GNPs administered to mice. The dose of cetuximab-GNPs was set by toxicity limits established during PK studies. The dose of free cetuximab was chosen for two reasons. Firstly, to match a lower-limit estimate of cetuximab-loading onto cetuximab-GNPs; and secondly, to maximize the chances of seeing an effect of cavitation on delivery, as results in Section 4.1.2 showed that passive tumoural accumulation of free cetuximab is substantial. Finally, a separate cohort of mice (with only 1 subcutaneous HT-29 tumour) was treated with an i.v. injection of this low dose of cetuximab (5 μg), without administration of CN or treatment with US, in order to be able to compare

US-mediated delivery to passive accumulation at the same dose.

Drug	Dose of Drug	Dose of SV	Dose of SSP
Cetuximab	5 μg	50 μL	1.1 mg
Cetuximab-GNPs	1.5 x 10^{12} GNPs	50 μL	1.1 mg

Table 4.4: Administered dose of drug and CN. Mice were injected first with drug (25 μL), followed by CN. Dose of SV was split into two separate injections of 25 μL at the start of treatment, and after 4 minutes, while 50 μL of SSPs were injected in one bolus at start of treatment.

Mice were cannulated and positioned on a custom holder, which was then placed into a pre-warmed and degassed water tank, such that both tumours were fully submerged, but the mouse's head remained above water. The two HIFU transducers provided the high-intensity US for 'treatment' of the tumours and were operated in concert using a signal generator. Once the mouse was placed into the water tank, the US arrays were used for B-mode imaging to allow for alignment of the HIFU transducers on the tumour to be treated. A detailed description of the US treatment platform can be found in Section 2.7.1. Animals were dosed i.v. with cetuximab + CN or cetuximab-GNPs + CN. Doses of CN (SV and SSPs) were informed by previous studies with these CN [173] [134]. Immediately after dosing one of two bilateral tumours was treated with focused US. At the onset of treatment (following drug + CN injection), the transducers were focused on the largest region of the tumour, but after injection of CN, the mouse holder was slowly moved in 3 dimensions, in order to allow the HIFU focus to treat all regions of the tumour. PRFP was continually adjusted based on real-time PAM feedback, to keep PAM magnitude constant between 10-20 units (arbitrary units). Post-treatment, the tumours were examined for any signs of bruising or other damage, mice were culled and tumours were collected for ex vivo ELISA quantification of tumoural concentration of cetuximab or cetuximab-GNPs.

4.2.2 Statistical analysis

Analysis and comparison of PAM data of cavitation events (see Fig. 4.7) is compatible with the use of standard one-way ANOVA. However, comparison of the effect of such cavitation on the tumour delivery requires more consideration. In the experimental design used here, it was hypothesized that the response variable (tumoural concentration of drug) was a function of two factors: treatment with a type of CN and exposure to US. In standard ANOVA (and other linear statistical analyses), an important assumption is independence of errors – if this assumption is violated, the results of statistical testing can be invalid. Measurements of tumours within the same subject would not result in independent errors: if, for example, one subject in this experiment received a slightly higher dose of cetuximab, *both* the untreated and treated tumours could be expected to show higher concentration of cetuximab, and thus the errors (deviation from the population mean) would be correlated. Mixed effects models can account for this correlation, as they incorporate both fixed and random effects. In the context of this experiment, a fixed effect is a model parameter constant across subjects, while a random effect is a random variable that is drawn for each subject from a common normal distribution – we might expect that CN and US should have a constant effect on tumoural delivery of drug, but that there will be variability observed in this effect between subjects due to random (or unquantifiable) differences in subjects (in addition to stochastic variation that is truly random and independent, and is thus accounted for in a mixed effects model as a simple error term) [236]. In addition to resolving the issue of non-independent error, mixed effect modelling (also known as multilevel modelling) can be a powerful tool for resolving within- and between-group differences (here, the between-group factor is CN type, while the within-group factor is US treatment). Thus, a mixed-effect model was constructed to describe the response variable (% of the ID recovered in the tumour) in terms of the fixed effects of CN, US, the interaction of CN and US, and a random intercept of Subject. Here CN has two levels (SSPs, and SV), and

US had two levels (+ or -). The model was constructed in RStudio (R Core Team, 2018) and in R syntax has the following form, where ϵ is an error term:

$$[\text{Drug}] \sim \text{CN*US} + (1 \mid \text{Subject}) + \epsilon \tag{4.1}$$

The model was fit with the lmer function of the R package lme4 [184] using the restricted maximum likelihood approach. The Satterthwaite approximation for degrees of freedom (which are non-trivial to determine for mixed effects models [237]) was used to determine p-values, though similar results were obtained using other methods for evaluating significance, such as using likelihood ratio tests. All tests were carried out with the R package lmerTest [185].

4.2.3 Acoustic feedback

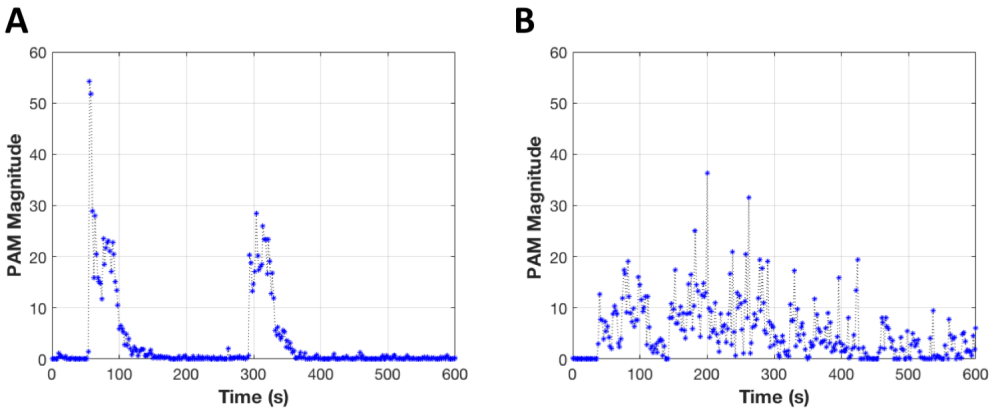

Figure 4.6: Acoustic data acquired during US- treatment of tumour-bearing mice with cetuximab or cetuximab-GNPs + SV (A) or + SSPs (B). The magnitude of the maximum PAM pixel is plotted over time for duration of US-treatment of mice with cetuximab or cetuximab-GNPs + SV (A) or + SSPs (B).

As introduced in Section 1.3.4, passive acoustic mapping (PAM) is a technique for spatially mapping cavitation events, and can be used for real-time feedback of acoustic cavitation during US treatment of tumours. During US exposure, treatment was monitored with B-mode imaging co-registered with PAM imaging to show location

and strength of any cavitation events. For every PAM frame, the pixel with maximum energy (in arbitrary units, denoted as PAM magnitude) was extracted and plotted against time. Representative traces of this PAM magnitude over time from treatment of mice with SV or SSPs are shown in Fig. 4.6. With SV (panel A), a peak in the PAM magnitude was observed immediately following injection (at the onset of treatment, and after approximately 4 minutes), which decayed rapidly back to baseline values. With SSPs cavitation activity was quite consistent over time, as HIFU PRFP was adjusted in real-time to maintain a consistent PAM magnitude. From these PAM traces, multiple metrics were quantified in order to compare the features of the cavitation recorded, with the hope of determining the optimal levels of cavitation required for successful enhancement of antibody or nanoparticle delivery (Fig. 4.7).

Firstly, the maximum PAM magnitude and total (integrated) PAM magnitude recorded throughout treatment were compared for the different CN. The maximum PAM magnitudes were not significantly different ($p>0.05$) between SV and SSPs in either of the treatment groups (cetuximab or cetuximab-GNPs), while the total (cumulative) PAM magnitude was significantly higher with SSPs than with SV for both treatment groups ($p<0.05$). Secondly, as one of the reported advantages of SSPs versus SV is their ability to sustain cavitation over time, the percentage of treatment time for which the PAM magnitude was over a threshold value was quantified. Two separate thresholds were identified: a PAM magnitude of 1 (Fig. 4.7 panel C) and a PAM magnitude of 10 (Fig. 4.7 panel D). A threshold of 1 was deemed a lower cut-off for a 'positive' detection of cavitation. A threshold of 10 however, was chosen as a cut-off in order to quantify the duration of higher energy PAM readings, indicating the presence of substantial cavitation. The percentage of treatment time with cavitation activity over a threshold of 1 was significantly greater with SSPs than SV ($p<0.0001$). Finally, percentage of treatment time above a threshold of 10 was comparable between SV and SSPs, though was significantly greater ($p<0.05$) for

mice treated with cetuximab + SSPs than for mice treated with cetuximab-GNPs + SV or SSPs.

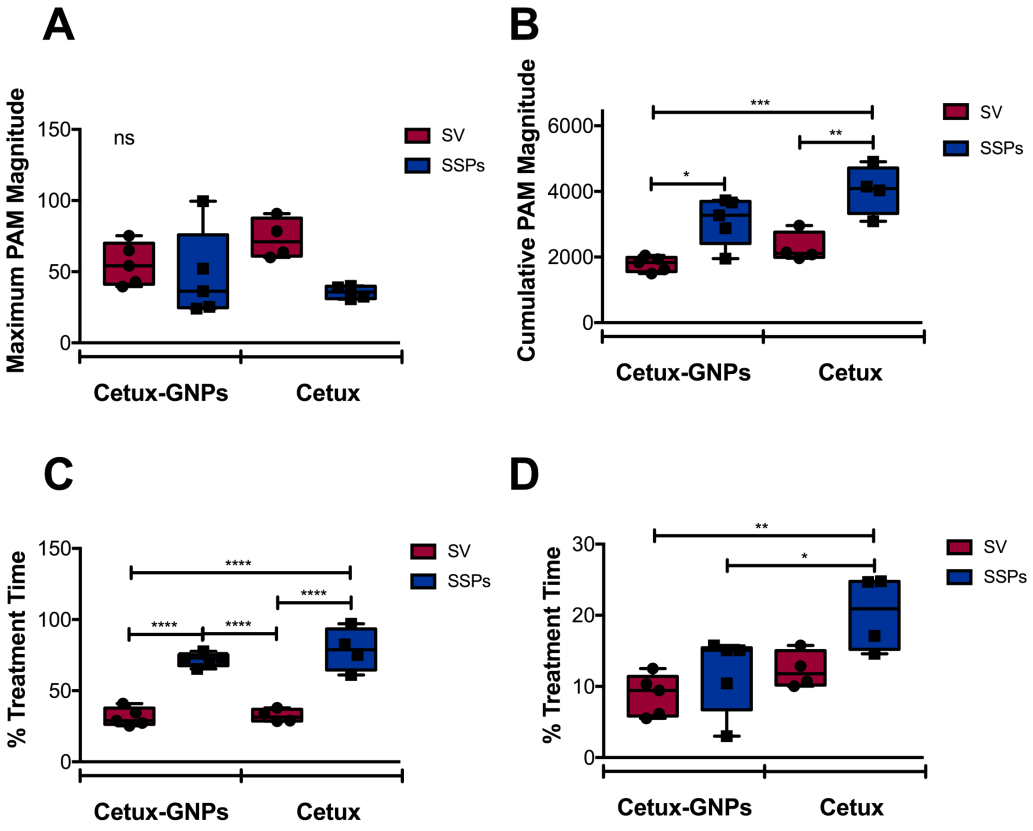

Figure 4.7: Quantification of acoustic data acquired during US- treatment of tumour-bearing mice dosed with cetuximab + CN or cetuximab-GNPs + CN. The maximum (panel A) and cumulative (panel B) PAM magnitudes are shown, as well as the percentage of treatment time that PAM magnitude was above a threshold of 1 (panel C) or a threshold of 10 (panel D). Box and whisker plots show median, first and third quartiles, and maximum and minimum values, while points show data from individual mice (n = 4 for treatment with cetuximab, and n = 5 for treatment with cetuximab-GNPs). Statistical significance was assessed with one-way ANOVA followed by post-hoc Tukey's multiple comparisons test. **** = $p < 0.0001$, *** = $p < 0.001$, ** = $p < 0.01$, * = $p < 0.05$, ns = $p > 0.05$, all p-values were adjusted for multiple comparisons, the means of all columns were compared but only significant comparisons are noted.

Immediately post-treatment, tumours were inspected for damage to the exposed area. There was significant bruising evident in tumours treated with SSPs + US, and very minimal bruising observed with SV. No other adverse events were observed as a result of US-treatment or treatment with cetuximab-GNPs at this dose.

4.2.4 Quantification of tumoural delivery

Mice were culled after US-treatment (approximately 12 minutes after injection of cetuximab or cetuximab-GNPs and initiation of US exposure), tumours were excised and frozen until analysis. Tumours were homogenized and cetuximab concentration was quantified using a sandwich ELISA (see Section 2.6.3).

Quantification of cetuximab

Panel A of Fig. 4.8 shows the results of the ELISA quantification of delivery of free cetuximab. In 8 out of 8 mice treated with cetuximab + CN, the application of US caused a substantial increase in the percentage of injected dose recovered from the tumour immediately after treatment. The mean percentage of the ID recovered from tumours treated with SSPs + US was greater than the dose recovered from tumours treated with SV + US (5.9±1.6% versus 3.0±0.7% of the ID per gram of tumour).

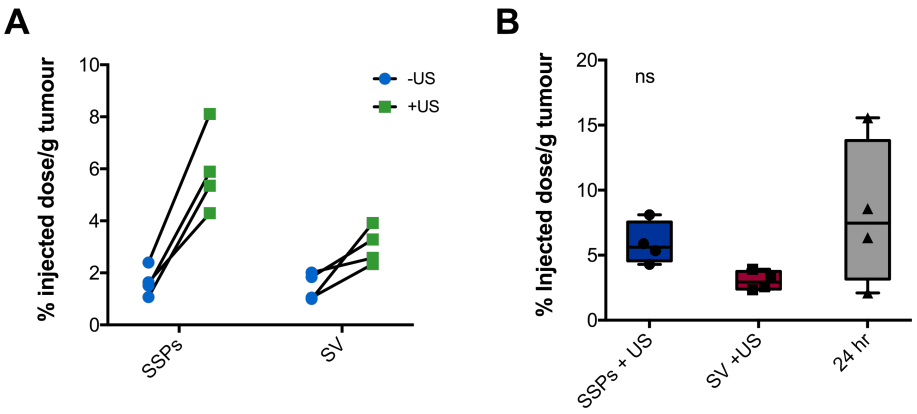

Figure 4.8: Quantification of US-mediated tumour accumulation of cetuximab. Mice (n=4) were injected i.v. with 5 μg of cetuximab, followed by 1.1 mg of SSPs, or 50 μL of SV. After 10 minutes of US treatment, tumours were excised, homogenized, and analyzed for cetuximab concentration using a sandwich ELISA (see Section 2.6.3). Panel A shows the impact of CN and US on the % of the ID/g recovered from tumours, tumours from the same mouse are linked by a continuous line. Panel B shows the % of the ID/g from tumours treated with SSPs + US, SV + US, or with no US but with 24 hours of passive accumulation. Statistical significance of groups in panel B was assessed with one-way ANOVA, ns = $p > 0.05$.

The raw ELISA concentration data from mice treated with cetuximab SV or SSPs was analysed using the linear mixed effects model described above. Assumptions of this linear model were met with raw data as model residuals were normally distributed (p-value from Shapiro-Wilk test of 0.7096), and no obvious deviation from homoscedasticity was observed from residual plot (variance of data should be the same across range of values).

ANOVA of the fixed effects of the fitted model revealed significant main effects of US ($p = 0.0003$) and CN ($p = 0.0316$), and a significant interaction between US and CN ($p = 0.0145$). Post-hoc t-tests of the estimated marginal means (EM means) from the model were used to compare 4 groupings of interest (Table 4.6). Two pairwise comparisons were found to be statistically significant: SSP +US versus SSP -US, and SSP +US versus SV +US.

The fold increase between tumours treated with and without US was estimated from the model, and was found to be approximately 2.0-fold for SV + US (95% CI from 1.3- to 3.7-fold) and 3.6-fold for SSPs + US (95% CI from 2.5- to 6.2-fold). Confidence intervals (CI) of these fold-increases were estimated by parametric bootstrapping (5000 simulations).

In order to compare US-mediated delivery of cetuximab to passive accumulation, a separate group of mice (with only one tumour) were injected with the same dose of cetuximab (5 μg), but received no CN and no US treatment. These mice were culled 24 hours post-injection, tumours were excised and analysed with ELISA as above. Panel B of Fig. 4.8 compares the percent of the injected dose of cetuximab recovered per gram of tumour for tumours treated with SSPs + US, with SV + US, or with no CN or US but exposed to circulating cetuximab for 24 hours. The mean percentage of injected cetuximab recovered per gram of tumour after treatment with SSP + US or SV + US were 73$\pm$54%, and 37$\pm$27% respectively of the mean percentage recovered after allowing 24 hours of passive accumulation by the EPR effect. As all tumours considered in this analysis came from separate subjects, a

Fixed Effect	p
CN	**p = 0.0316**
US	**p = 0.0003**
CN:US	**p = 0.0145**

Table 4.5: Type III ANOVA of fixed effects of tumoural concentration of cetuximab from ex vivo ELISA of tumours from mice dosed with cetuximab with SV or SSPs.

Comparison	Day 6
SVY vs. SVN	p = 0.1307
SSPY vs. SSPN	**p = 0.0011**
SVY vs. SSPY	**p = 0.0055**
SVN vs. SSPN	p = 1.00

Table 4.6: Post-hoc multiple t-test comparisons of EM means from mixed effects model of tumoural concentration data from ex vivo ELISA of tumours from mice dosed with cetuximab with SV or SSPs. All reported p-values are corrected for multiple comparisons using the Bonferroni correction.

simple one-way ANOVA was used to assess statistical significance. No statistically significant difference between groups was found, possibly because of large variability within the 24-hour accumulation. These results indicate that treatment with US + CN can achieve a tumour uptake of cetuximab after only 12 minutes that is comparable to that achieved after a full 24 hours of passive accumulation. Moreover, the standard deviations of the percent recovery of US-treated groups was found to be substantially lower than the standard deviation of the passive accumulation group (1.6 and 0.7% of the ID for SSPs and SV respectively, compared to 5.6% of the ID for passive accumulation), suggesting that cavitation-mediated delivery might provide more consistent delivery than passive accumulation alone. It could also be argued that the US-mediated approach achieves greater 'burst' delivery kinetics (perhaps providing higher peak tumour concentrations), could give better tumour penetration [134], and may still allow for passive accumulation via the EPR effect to conitnue beyond the 10 minutes of US exposure, providing an additive rather than alternative approach.

Quantification of cetuximab-GNPs

Panel A of Fig. 4.9 shows the results of the ELISA quantification of delivery of cetuximab-GNPs. In 9 out of 10 mice treated with cetuximab-GNPs + CN, the application of US caused an increase in the percentage of the ID recovered from the tumour immediately after treatment. Notably, 8 out of 10 tumours that did not receive US had absorbance values at or below the 'blank' or untreated control homogenate. Therefore, it would appear that US-mediated cavitation has an 'enabling' effect: without US, the dose recovered from the tumour is approximately at the limit of detection of the ELISA assay, which here could detect down to approximately 0.08 % of the ID/g tumour. The median percentage of the ID/g of tumour recovered from tumours treated with SSPs + US (0.90%, range from 0.11 to 5.43%) was greater than the median percentage of the ID recovered from tumours treated with SV + US (0.62%, range from 0.01 to 1.39%).

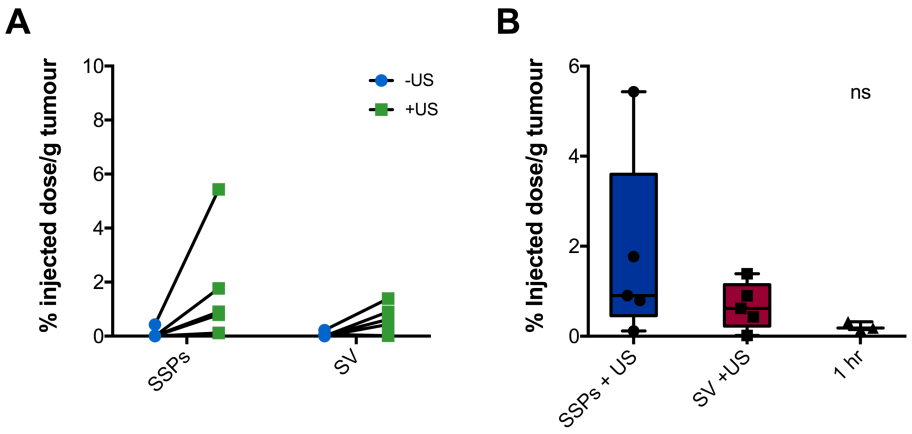

Figure 4.9: Quantification of US-mediated tumour accumulation of cetuximab-GNPs. Mice (n=5) were injected i.v. with 1.5 x 10^{12} of cetuximab-GNPs, followed by 1.1 mg of SSPs, or 50 μL of SV. After 10 minutes of US treatment, tumours were excised, homogenized, and analyzed for cetuximab-GNP concentration using a sandwich ELISA (see Section 2.6.3). Panel A shows the impact of CN and US on the % of the ID/g recovered from tumours, tumours from the same mouse are linked by a continuous line. Panel B shows the % of the ID/g from tumours treated with SSPs + US, SV + US, or with no US but with 1 hour of passive accumulation. Statistical significance of groups in panel B was assessed with one-way ANOVA, ns = $p > 0.05$.

As the % ID recovered from such a large proportion of tumours not treated with US was below the limit of detection of the assay, accurate estimates for the true concentrations could not be calculated. Thus, analysis with the mixed effects model as performed for cetuximab delivery was not deemed appropriate, as the estimate of the variance within this group would be incorrect if concentrations below the limit of detection were all set to zero, or to the lower limit of detection. Clearly, there is a positive effect of cavitation on delivery of cetuximab-GNPs. To further elucidate the benefits of this effect, the tumoural accumulation of cetuximab-GNPs with US and CN was compared to passive accumulation over 1 hour (of the same dose of cetuximab-GNPs). This is shown in Fig. 4.8 panel B, and when analysed with one-way ANOVA, no statistically significant difference between the groups was found. The effect of US, particularly in conjunction with SSPs, was extremely variable, with one mouse accumulating 0.5% of the ID in the tumour exposed to US (and only 0.03 %ID without US-exposure). The median %ID per gram of tumour after treatment with US + SSPs was 0.90% (range from 0.11 to 5.43%), compared to 0.62% (range from 0.01 to 1.39%) for US + SV, and 0.22% (range from 0.15 to 0.32%) for passive accumulation over 1 hour.

4.2.5 Relationship between PAM and delivery of cetuximab

One of the advantages of using linear regression models for statistical analysis over a standard ANOVA, is that predictors can be continuous rather than categorical. In the interpretation above, it was helpful to input US as a categorical variable (+US or -US), as it allowed meaningful comparisons to be made between groups, and corresponding conclusions to be drawn. However, with the acoustic feedback recorded during treatment, US, or more accurately 'cavitation activity', can also be considered a continuous variable or predictor. Inputting a metric of cavitation activity as a continuous variable gives physical meaning to the parameters estimated by the model, and could help elucidate a relationship between observed cavitation

activity and delivery of a therapeutic [238].

The cumulative PAM magnitude (Fig. 4.7 panel B) for each treated tumour was input into the linear mixed effects model. Tumours that were not exposed to US were assigned a cumulative PAM magnitude of 0, as they did not receive any cavitation. Fig. 4.10 shows the cetuximab quantification data plotted and overlaid with the estimated mixed effects model of tumour cetuximab concentration as a function of cumulative PAM magnitude.

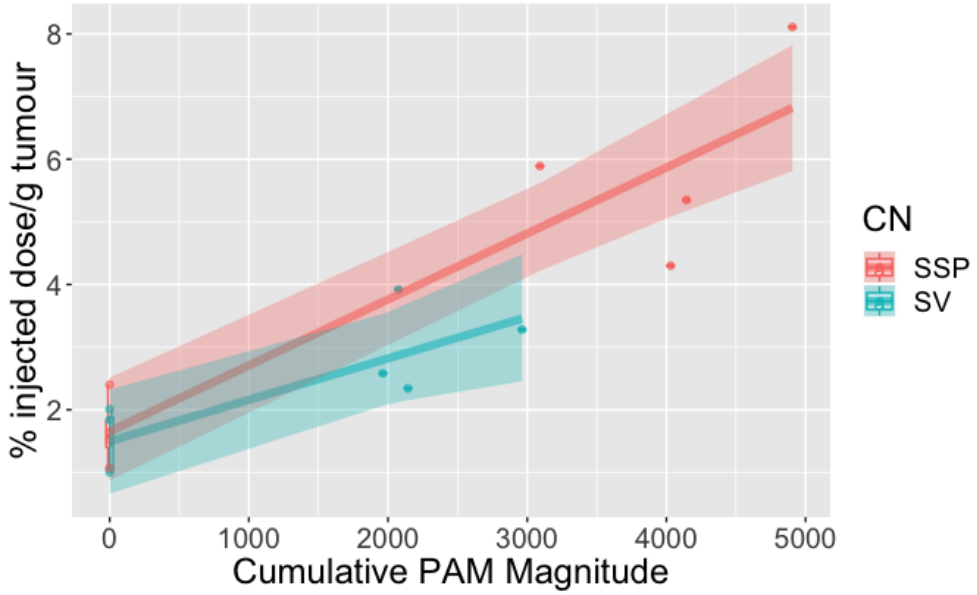

Figure 4.10: Linear mixed effects model of tumour cetuximab concentration as a function of CN type and cumulative PAM magnitude of cavitation. Points show data from individual mice (n = 4). The red and blue line traces show the estimated marginal means from a linear mixed effects model fitted to the data, while the red and blue shading denote the 95% CI of these predicted values, estimated from parametric bootstrapping.

ANOVA of the fixed effects (Table 4.7) revealed a significant main effect of cumulative PAM magnitude ($p = 0.0006$), no significant main effect of CN ($p = 0.7973$), and while the interaction term between PAM magnitude and CN was not significant ($p = 0.1943$), it was not largely so, and visual inspection of the data (Fig. 4.10) suggests there could be a small difference in the effect of cavitation (as measured by cumulative PAM magnitude) on cetuximab delivery depending on whether SV or SSP were used. A larger study with greater power would be required

to definitively prove or disprove the existence on this interaction. The results of this experiment suggest however, that cumulative PAM magnitude (as a metric for cavitation activity) is an important predictor of cetuximab delivery, potentially irrespective of CN type used to seed cavitation.

Fixed Effect	**p**
CN	p = 0.7973
PAM Mag	**p = 0.0006**
CN:PAM Mag	p = 0.1943

Table 4.7: Type III ANOVA of the fixed effects of a mixed model incorporating acoustic feedback data as a predictor of tumoural concentration of cetuximab from from ex vivo ELISA of tumours from mice dosed with cetuximab with SV or SSPs.

4.3 Summary and discussion

In this chapter, the in vivo pharmacokinetics of the cetuximab-GNPs designed and characterized in Chapter 3 were investigated and compared to free cetuximab. Cetuximab-GNPs were cleared rapidly, and concentrations in the liver 1 hour post-injection suggest the liver as a clearance route, in line with reports in the literature [231, 232, 201, 187, 233]. A small proportion of the injected dose of cetuximab-GNPs passively accumulated in tumours (0.13±0.08 % of ID after 24 hours), compared to free cetuximab (1.87±0.80 % of ID after 24 hours). This poor passive accumulation suggests a large area of opportunity for enhancing delivery of poorly-circulating therapeutic nanoparticles using external stimuli.

US-mediated delivery of cetuximab and cetuximab-GNPs with cavitation seeded by SV and SSPs was then investigated in vivo in a murine bilateral tumour model of subcutaneous tumours that overexpress EGFR. During US-treatment, cavitation was detected in real-time using two orthogonally mounted linear arrays, and was mapped using passive acoustic mapping techniques (Section 1.3.4). A maximum

magnitude PAM signal was extracted at each time point during the treatment, and this PAM magnitude was used to characterize cavitation during treatment of mice receiving SV, or SSPs.

US-mediated delivery of cetuximab or cetuximab-GNPs was investigated using treatment with US (0.5 MHz driving frequency and a PRFP between 1.5-2 MPa) over 10 minutes. Analysis of acoustic feedback data revealed that cavitation with SSPs was significantly more sustained than with SV, and the maximum PAM magnitudes were not significantly different. The cumulative PAM magnitude was significantly increased during US treatment with SSPs than with SV.

Delivery was assessed using a sandwich ELISA to quantify tumoural concentration of cetuximab, and was converted to % of ID by use of a standard curve made with injectate (of either cetuximab or cetuximab-GNPs). For treatment with free cetuximab, a clear benefit of US was observed, as 8 out of 8 mice had a greater concentration of cetuximab in the tumour that received US treatment. ANOVA of a the fixed effects revealed significant main effects of US and CN type, as well as a significant interaction effect. Post-hoc testing revealed a significant difference between the EM means of SSP + US and SSP - US, and SSP + US and SV + US. Treatment with SSP +US gave rise to an estimated 3.6-fold increase (95% CI from 2.5 to 6.2-fold) in tumour cetuximab concentration, while treatment with SV +US gave rise to a 2-fold increase (95% CI from 1.3 to 3.7-fold).

A benefit of US was also observed for mice treated with cetuximab-GNPs, though variability between mice within the same group was very large. The effect of US + CN appeared to be 'enabling': only 2 out of 10 tumours receiving CN but no US had a tumoural concentration of cetuximab-GNPs above the detection limits of the ELISA. Tumours treated with US (and thus having a quantifiable concentration of cetuximab-GNPs) were compared to tumours from mice where cetuximab-GNPs were allowed to circulate and accumulate passively for 1 hour post-injection. No statistically significant differences were found between any of the groups by 1-way

ANOVA (SV +US, SSP +US, and passive accumulation for 1 hour), though median tumoural concentrations of cetuximab-GNPs were greater for tumours treated with US than for those with only passive accumulation.

It should be noted that one limitation of ELISA analysis of tumours treated with cetuximab-GNPs is that it is an indirect measure of *particle* concentration, and will be unable to distinguish a signal from cetuximab-GNPs from free cetuximab. Analysis of the stability of cetuximab-GNPs in plasma showed that some degree of antibody separation from the particles can be expected to occur over the 10 minutes of US treatment, so it must be acknowledged that the tumour concentration quantification will include the concentrations of both free and GNP-loaded cetuximab. This is an important limitation of any indirect measurement of particles in vivo, whether it be a measurement of a loaded protein, a fluorescent tag, or a radioactive ligand [187, 201]. Direct measurements of gold concentration, by inductively coupled plasma mass spectrometry (ICP-MS) for example [231], would provide more compelling evidence of GNP delivery, but with this technique it can be difficult to optimize tissue digestion and gold recovery to ensure accurate quantification [239].

Finally, the linear mixed effects analysis of cetuximab delivery was extended to include a measure of cavitation activity as a predictor of tumoural delivery of cetuximab. The cumulative PAM magnitude metric was chosen, as it absorbs the most information about the cavitation activity (duration and magnitude). Cumulative PAM magnitude was input into the model as a continuous predictor, and ANOVA of the fixed effects revealed that it had a significant main effect. In this updated model, the main effect of CN was highly non-significant. The interaction between CN and PAM was also found to be non-significant. Though this analysis was only completed on a small data set, and a study with greater power would be required to fully determine the relationship between PAM quantification of cavitation activity and therapeutic delivery, this analysis provides compelling evidence that feedback of cavitation activity can be used to predict therapeutic delivery. Application of the

same analysis to delivery of cetuximab-GNPs would require greater delivery without cavitation, or a more sensitive detection method to provide non-zero readings to compare against.

The results presented in this chapter clearly demonstrate that US-mediated cavitation can be used to increase the delivery of both a therapeutic antibody, and a targeted nanoparticle. Two CN types were investigated, solid gas-entrapping nanoparticles (SSPs) and more conventional UCA microbubbles (SV). The cavitation profiles of both CN were different by multiple metrics, and though both CN gave rise to an increase in therapeutic delivery, the magnitude of this effect was greater with SSPs. This is possibly due to the overall increased cavitation 'dose' delivered to the tumour (as approximated by the cumulative PAM magnitude). Additionally, tumour regions treated with US + SSPs showed signs of greater bruising post-treatment, than those exposed to US + SV.

Past studies of antibody delivery with cavitation (mostly to the brain after BBB opening with US) have used fluorescence imaging of tumour sections to look at antibody delivery, and did not directly quantify the percentage of injected dose delivered to tumours after US exposure [180, 240, 167, 176]. Kinoshita et al. determined the amount of Herceptin delivered to mouse brains after BBB opening with US and microbubbles using a microagglutination assay kit to detect human antibodies [181]. Delivery in this study was largely due to reversible BBB opening, and the US parameters (0.69 MHz driving frequency, PRFP between 0.6-0.8 MPa before attenuation by the skull, no broadband emissions indicating inertial cavitation) were much milder than those employed here to generate microstreaming and consequent drug transport. To the best of the author's knowledge, the studies presented in this chapter represent the first reported direct quantification of therapeutic antibody delivery to a solid tumour (outside the brain) with ultrasound-mediated cavitation. The results presented here help to increase understanding of the relationship between cavitation 'dose' and the level of therapeutic delivery achieved.

However, although cavitation provided a benefit to delivery of both cetuximab and cetuximab-GNPs, therapeutic antibodies (including cetuximab) circulate extremely well in vivo, and when the same dose of cetuximab was given to mice and allowed to circulate and accumulate passively for 24 hours, the median % of the ID that accumulated after 24 exceeded that achieved with US delivery (though not statistically significantly so). Hence it could be argued that the benefit of this cavitation approach represents a costly and technically challenging approach to achieve the same ultimate result. However, this ignores several important aspects. Firstly, there is a possibility that cavitation-mediated delivery may combine with further passive accumulation due to the EPR effect, and so had accumulation been measured 24 hours after US exposure, a greater delivery level may have been achieved than by relying solely on EPR. Secondly, achieving a 'burst' delivery profile with potentially deeper and more widespread tumour penetration using cavitation, over a matter of minutes, rather than EPR assisted delivery over hours (as discussed in [36, 35]), may provide improved therapeutic outcomes. Thirdly, while passive accumulation may be expected to be sensitive to changing and unpredictable perfusion levels, cavitation might provide a more reliable and consistent approach. All these aspects require further research but are outside the scope of the studies reported here.

In contrast, the effect of US on delivery of cetuximab-GNP was enabling (within the limits of the assay used here), and increased tumoural concentration of cetuximab-GNPs compared to passive accumulation over 1 hour, suggesting a larger area of opportunity for US-enhanced transport of poor-circulating therapeutics with low tumoural-passive accumulation. This is in accordance with work reported using oncolytic viruses [177, 134, 173], and is of relevance considering the large amount of research being committed to the development of nano-sized therapeutic carrier systems. In the next chapter, cavitation-mediated delivery of another (relatively) poor-circulating nanomedicine – an oncolytic virus – is investigated.

Chapter 5

In vitro and in vivo assessment of cavitation-mediated delivery of an oncolytic adenovirus

In Chapter 4, the potential for US + CN to enhance the delivery of both short- and long-circulating nanomedicines was demonstrated. Externally applied focused US in combination with i.v. dosed cavitation nuclei (US + CN) has been shown to improve delivery of adenovirus type 5 (Ad5) into tumours following i.v. dosing in pre-clinical models [134]. However, the clinical utility of Ad5 has been restricted to i.t. injection, and its use as an i.v. delivered monotherapy has shown limited efficacy [241]. Thus, use of US + CN will likely have more impact when applied to a virus more amenable to intravenous delivery with an extended blood clearance profile. Enadenotucirev (ColoAd) has demonstrable clinical delivery and virus activity after i.v. administration, and is a potent and selective option for the treatment of colon cancer [242]. In this chapter, the delivery of ColoAd using US and CN is discussed. Firstly, ColoAd delivery with US + CN in vitro is examined using a tissue-mimicking flow phantom model. Delivery is then examined and tested in a murine bilateral tumour model, wherein delivery is compared between tumours within each mouse: one exposed to US and the other not exposed.

5.1 In vitro delivery of ColoAd with US-mediated cavitation

5.1.1 Agar tissue-mimicking model

In order to reduce the number of animals used in research, and to allow for more in-depth analyses of specific variables, in vitro models mimicking human tissue can be used in lieu of in vivo tumour models to study the effects of US and US-mediated cavitation on drug delivery to cancer cells. Modelling the tumour and its microenvironment is a challenging task, and most models represent at best a gross approximation of the true characteristics of a tumour (especially when the heterogeneity between deposits of even the same cancer type is considered). Agarose gel has been used as a tissue-mimicking gel in experiments investigating US enhanced drug delivery [167, 177, 135], as it has similar acoustic properties to human tissue [243], and contains pores of similar size to the 'leaky' vasculature often found in solid tumours [244, 245]. Additionally, human cancer cells can be immobilized and sustained in agar gel supplemented with cell culture growth media. Here a ColoAd variant expressing a red fluorescent protein (RFP) reporter gene (ColoAdRFP) was used in to allow for tracking of infected cells, as cells produce RFP once infected with the virus.

5.1.2 Experimental design

Past studies of in vitro US-mediated cavitation to enhance delivery of adenovirus have used clinically-approved UCAs, such as SV as CN [167, 177, 135]. To date, US-mediated delivery of the combination of adenovirus + SSPs has not been investigated, and so here the effect of US-mediated cavitation seeded by SSPs on delivery of ColoAd to a tissue-mimicking flow phantom is examined. In vitro testing of US-mediated delivery requires robust, reusable, acoustically and optically compatible and cell growth amenable phantoms — preferably incorporating flow vessels to

investigate delivery under the more realistic condition of flow. Since none of the phantom holders available met these criteria, a new holder was designed and constructed. The reusable tissue-mimicking phantom holder consisted of a rectangular frame, with the outer dimensions of a standard microplate to facilitate imaging. The windows of the phantom were covered with Mylar® — an optically and acoustically transparent plastic sheet. The holder was fitted so that 1.2 mm metal rods could be inserted to create three separate flow channels within the gel cast in the holder. Female luer fittings were inserted in each hole, so that tubing could be connected to each flow channel, and the holder could be easily sealed to maintain sterility and survival of cells within.

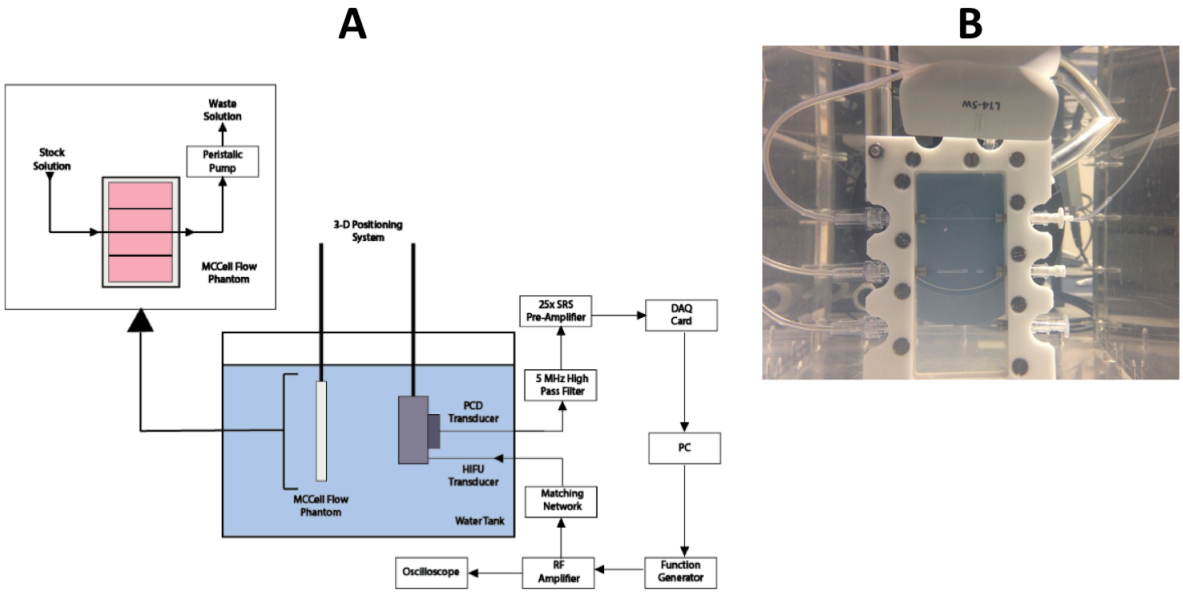

Figure 5.1: Schematic diagram of the in vitro US exposure setup and flow channel loop used for testing delivery of ColoAdRFP to cell-embedded agar gel.

A schematic showing the phantom holder in the experimental US set-up is shown in Fig. 5.1, and is decribed by Mannaris et al [172]. The phantom holder was placed in a degassed and deionized water tank, and the confocally aligned HIFU and passive cavitation detector (PCD) transducers were aligned on one channel (filled with air

initially) of the gel. Once aligned, a solution of ColoAdRFP with or without SSPs was flowed through the channel at a constant rate, and the channel was insonated at a frequency of either 0.5 or 1.6 MHz. After US treatment, the tissue-mimicking phantoms were stored in an incubator at 37°C until imaging. The resulting acoustic data and microscopy are presented below.

5.1.3 Delivery of ColoAd with 0.5 MHz US

Many of the previous studies investigating delivery of adenovirus (and other biological therapeutics) with SV or SSPs have used an US driving frequency of 0.5 MHz [167, 177, 178, 134, 171, 170, 173]. As such, initial ColoAdRFP delivery experiments were conducted with a driving HIFU frequency of 0.5 MHz. As described in Section 2.8.2, the HIFU transducer was driven at its fundamental frequency for 1000 bursts of 5000 cycles (200 seconds total insonation). The pulse repetition frequency was set at 5 Hz, which gives a duty cycle of 5% (note that a low duty cycle is used to promote US-mediated cavitation and extravasation while minimizing heating effects of US exposure). Three different PRFPs were tested: 2 MPa, 2.36 MPa, and 2.7 MPa, 1 exposure spot per channel was insonated, and each pressure condition was tested on n = 2 channels. Passive cavitation detection was used in real time to detect cavitation, and in post-analysis to assess the amount of cavitation over time.

Acoustic feedback

Fig. 5.2 shows the frequency power spectra of acoustic emissions recorded by the PCD confocally aligned with the HIFU transducer onto the channel within the tissue-mimicking phantom during insonation of ColoAdRFP + SSPs under flow. Broadband emissions characteristic of inertial cavitation were recorded throughout the duration of insonation for each of the PRFPs tested, which was expected as the lowest PRFP tested here (2 MPa) is above the threshold for inertial cavitation of SSPS at 0.5 MHz [171].

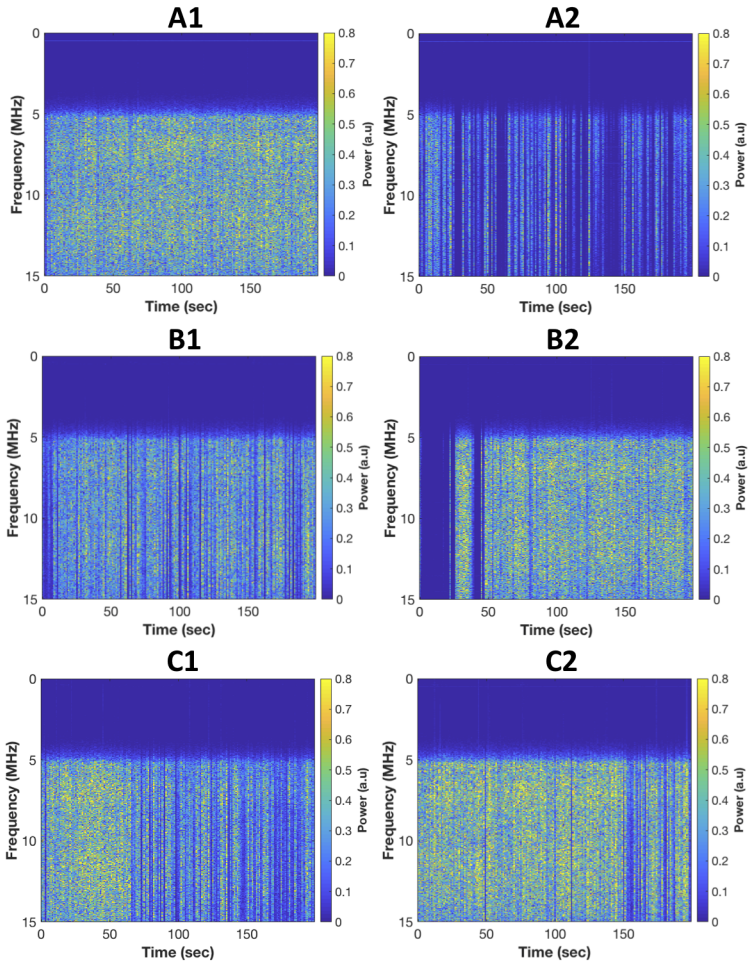

Figure 5.2: Frequency power spectra of acoustic emissions from channels within cell-embedded gel exposed to US at 0.5 MHz and peak rarefactional pressures between 2 - 2.7 MPa. ColoAd and SSPs were flowed through channels within a cell-embedded gel, where one spot along each channel was exposed to focused US at a PRFP of 2MPa (A), 2.36 (B) or 2.7 MPa (C), for a duration of 200 seconds.

Microscopy of viral transgene expression and agar damage

After US-treatment, the gels were kept (in their holders) in an incubator at 37°C, and were imaged after 2 and 3 days using brightfield and fluorescence microscopy (TRITC filter). The length of each channel was scanned under brightfield to detect any damage caused to the channel, while fluorescence microscopy was used to detect cells successfully infected with ColoAdRFP. Channels exposed to 2 MPa (Fig. 5.3) showed no sign of damage to the agar surrounding the channel, but also showed

no delivery of ColoAdRFP beyond the region immediately surrounding the channel. As Fig. 5.3 is taken from an orientation where the direction of US-propagation is in the z-axis, a z-stack of images was acquired, as maximal delivery may be expected in the direction of exposure [177]. However, even this analysis failed to show areas of localized cavitation mediated infection (data not shown).

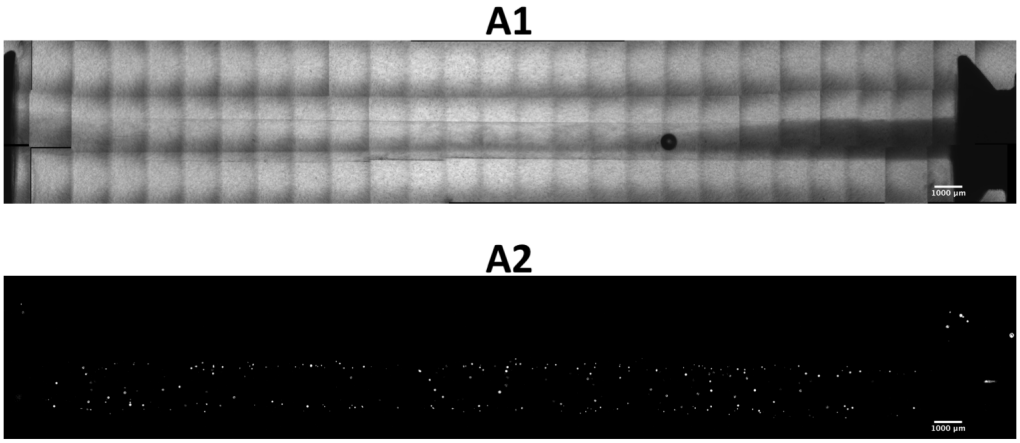

Figure 5.3: Brightfield and fluorescence microscopy of cell-embedded gels after delivery of ColoAdRFP + SSPs with US exposure. ColoAd and SSPs were flowed through channels within a cell-embedded gel, where one spot along each channel was exposed to focused US at a PRFP of 2 MPa for a duration of 200 seconds. 2 days post exposure to ColoAdRFP, channels were excised from gel and imaged with fluorescence (A2) and brightfield (A1) microscopy. The resulting images were processed in ImageJ, a representative set of images is shown here. In these images, the direction of US propagation is into the plane of the page. The fluorescence image shown here (A2) was thresholded in ImageJ for ease of visualizing infected cells, as signal was very weak in original images.

Fig. 5.4 shows representative brightfield and fluorescence microscopy images from channels with ColoAdRFP + SSPs exposed to 0.5 MHz US at PRFPs of 2.36 (B) and 2.7 (C) MPa. From the brightfield images it is clear to see that the US-exposure caused cracking of the agar in the direction of US propagation. From the fluorescence microscopy images it appears that ColoAdRFP tracked along the cracks and voids created by the agar damage, and pooled at the interface of the gel and the Mylar sheet.

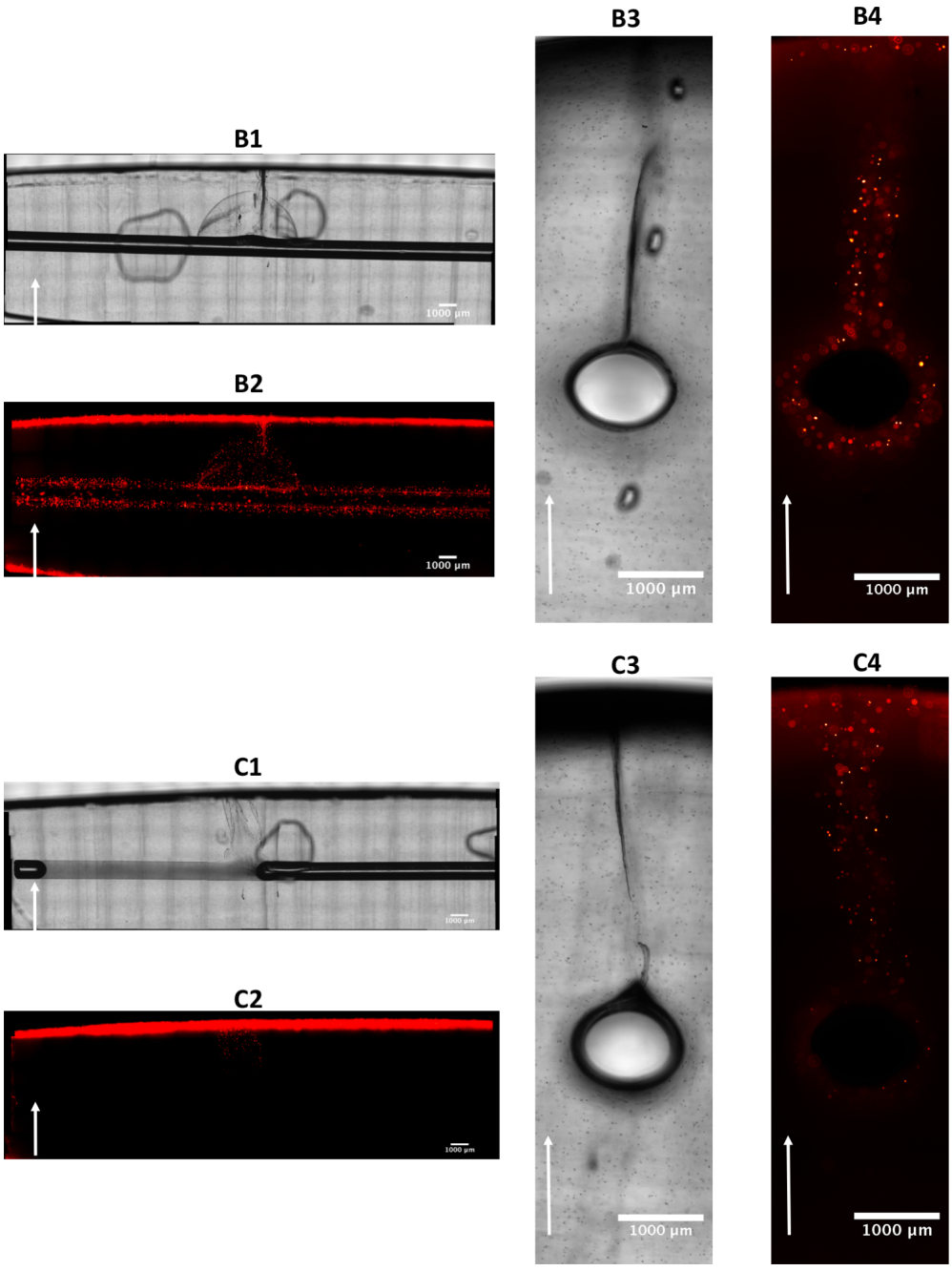

Figure 5.4: Brightfield and fluorescence microscopy of cell-embedded gels after delivery of ColoAdRFP + SSPs with US exposure. ColoAd and SSPs were flowed through channels within a cell-embedded gel, where one spot along each channel was exposed to focused US at a PRFP of 2.36 (B) or 2.7 MPa (C), for a duration of 200 seconds. 3 days post exposure to ColoAdRFP, channels were excised from gel and imaged with fluorescence and brightfield microscopy. Images B3-B4/C3-C4 were taken of an axial slice from the centre of the agar damage shown in B1-B2/C1-C2 respectively. The resulting images were processed in ImageJ, a representative set of images is shown here. The white arrows show the direction of US propagation.

Although this shows, in a sense, enhanced transport of ColoAdRFP due to US-mediated cavitation, the 'cracking' phenomenon displayed by the gel is likely not representative of the behaviour of real tissue under similar conditions. At these US parameters, (i.e. at 0.5 MHz and at the three PRFPs tested here – all of which gave rise to inertial cavitation) there were two outcomes. Either no damage to the agar was evident, and consequently a low-level of 'background' infection along the length of the channel was seen (2 MPa). Or alternatively, the US-exposure caused significant cracking and damage to the agar gel, causing ColoAdRFP to likely flow out of the channel and into the cracks and voids in the agar and infect cells along the track of damage (2.36 and 2.7 MPa). Enthusiasm generated by the dramatically improved and efficiently targeted deposition of ColoAdRFP in these experiments therefore has to be tempered by concerns over the translatability of the parameters and results to the in vivo situation.

In these experiments, an agar percentage of 2% – which is higher than those used in similar experiments in the literature [167, 177] – was used, as optimisation experiments conducted with a cell-embedded gel of lower agar percentage had a high rate of channel bursting and experiment failure. It is possible that the higher agar percentage made the gel more 'brittle' and prone to damage and cracking. For experiments with US at 1.6 MHz, the agar concentration of the gel was decreased to 1.5%. Additionally, the concentration of embedded cells was increased to improve the resolution of infection tracking.

5.1.4 Delivery of ColoAd with 1.6 MHz US

Kwan et al. demonstrated that SSPs could nucleate sustained cavitation at 0.5 MHz or 1.6 MHz [171]. Studies were therefore performed to investigate whether a 1.6 MHz exposure could provide ColoAd delivery without agar damage. For exposures with 1.6 MHz, the HIFU transducer was driven at its third harmonic for either 500 bursts or 1000 bursts of 2000 cycles (50 or 100 seconds total insonation). The pulse

repetition frequency was set at 10 Hz, which gives a duty cycle of 2.5%. The PRFP was fixed at 3.5 MPa. Multiple spots per channel were insonated to give an n = 3 or 4 per condition. As controls, one spot per channel was exposed to ColoAdRFP + SSPs and not insonated, while one whole channel was exposed to ColoAdRFP alone (no SSPs) and insonated in three separate locations (to control for any effect of US alone in the absence of SSP-seeded cavitation). It should be noted that the power (a.u.) of detected emissions should not be directly compared for the 0.5 and 1.6 MHz exposures, as different PCDs were used (7.5 MHz and 15 MHz frequency transducers respectively).

Acoustic feedback

Fig. 5.5 shows that in the absence of SSPs (panel A), no inertial cavitation is detected upon insonation with US at 1.6 MHz and a PRFP of 3.5 MPa. The broadband acoustic emissions shown in panels B and C however, demonstrate sustained inertial cavitation over both 500 and 1000 bursts when ColoAdRFP is flowed with SSPs.

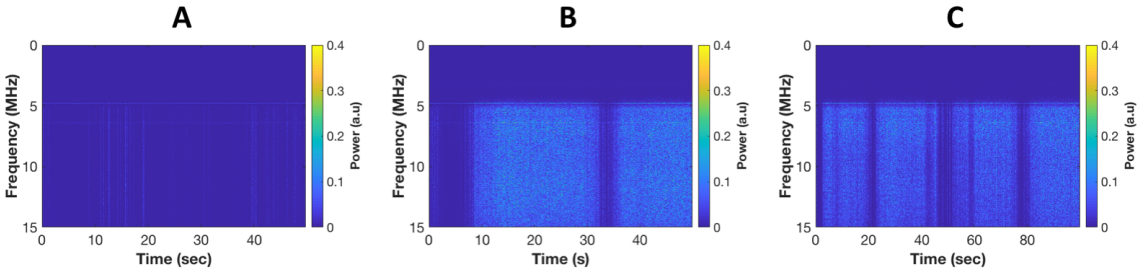

Figure 5.5: Frequency power spectra of acoustic emissions from channels within cell-embedded gel exposed to US at 1.6 MHz and peak rarefactional pressures of 3.5 MPa. ColoAd with and without SSPs were flowed through channels within a cell-embedded gel, where multiple spots along each channel were exposed to focused US, for a duration of 50s (500 bursts - panels A and B) or 100s (1000 bursts - panel C). In panel A, the acoustic response of a channel containing ColoAd in solution but no SSPs is shown, while in panels B and C exposed channels contained ColoAd + SSPs.

Microscopy of viral transgene expression and agar damage

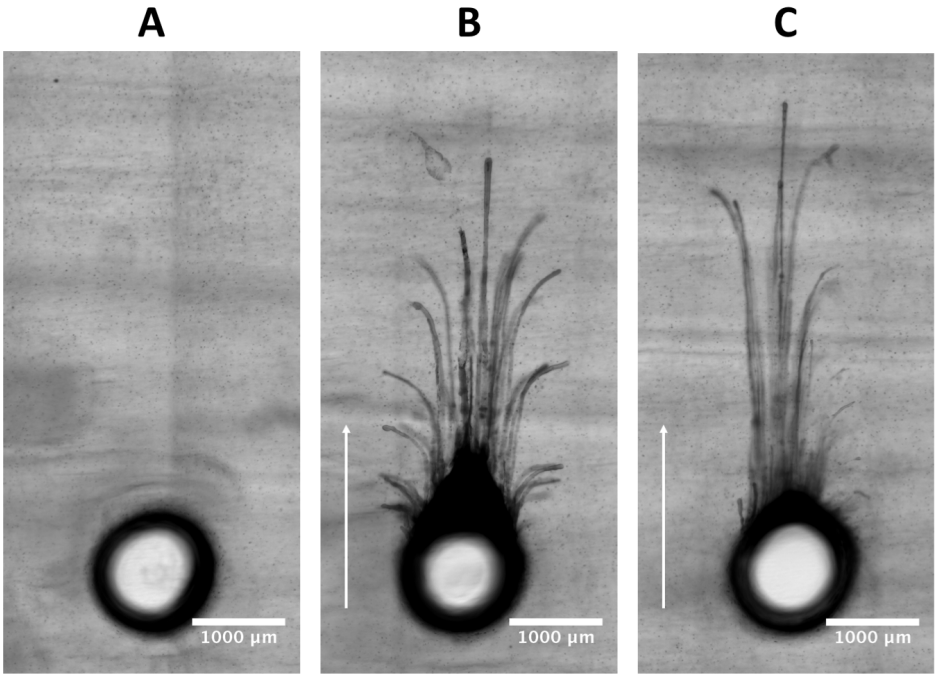

Figure 5.6: Brightfield microscopy of channel within agar gel after delivery of ColoAdRFP with and without US exposure. ColoAd and SSPs were flowed through channels within a cell-embedded gel, where multiple spots along each channel were exposed to focused US, for a duration of 0 (no US - panel A) 50s (500 bursts - panel B) or 100s (1000 bursts - panel C). 6-days post exposure to ColoAdRFP, channels were excised from gel and imaged with brightfield microscopy. The resulting images were processed in ImageJ, a representative set of images is shown here. The white arrows show the direction of US propagation.

After US-treatment with 1.6 MHz US, the gels were kept (in their holders) in an incubator at 37°C, and were imaged after 6 days with brightfield and fluorescence microscopy (TRITC filter). Fig. 5.6 shows representative brightfield images taken from axial slices from three separate spots along one channel. All three spots were exposed to ColoAdRFP + SSPs, while the second and third spots (panels B and C) were also exposed to US (images were excised at approximately the US focus). A clear pattern of damage in the direction of US propagation is seen in panels B and C, however the damage does not appear to be in the form of large cracks and voids

as seen with 0.5 MHz US. Fig. 5.7 shows the corresponding fluorescence images, and infection of cells with ColoAdRFP appears to correlate with agar damage, and is markedly increased in the direction of US propagation. In the absence of US (panel A), the only cells successfully infected with ColoAdRFP are those immediately surrounding the channel, indicating that delivery of ColoAd to depth by diffusion alone is extremely limited, again emphasizing the scale and importance of the challenge faced.

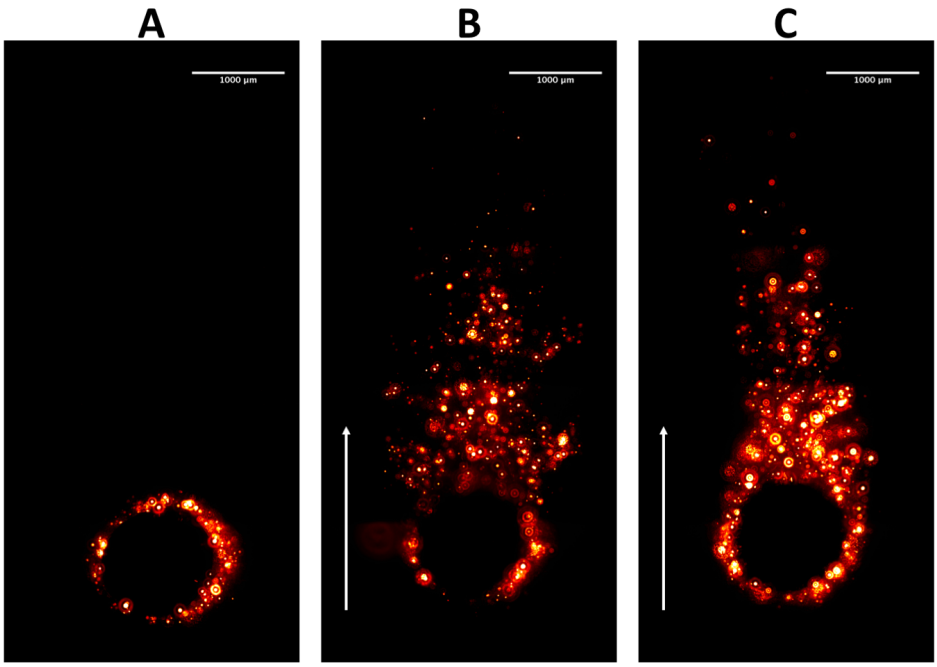

Figure 5.7: Fluorescence microscopy of RFP-expression after delivery of ColoAdRFP + SSPs to a cell-embedded gel with and without US exposure. Briefly, ColoAd and SSPs were flowed through channels within a cell-embedded gel, where multiple spots along each channel were exposed to focused US, for a duration of 0 (no US - panel A) 50s (500 bursts - panel B) or 100s (1000 bursts - panel C). 6-days post exposure to ColoAdRFP, channels were excised from gel and imaged with fluorescence microscopy. The resulting images were processed in ImageJ, a representative set of images is shown here. The white arrows show the direction of US propagation.

The number and spread of RFP-positive cells with and without US-mediated cavitation was quantified using the images acquired with fluorescence microscopy (as described in Section 2.8.4). The total number of infected cells was counted, and

their distances from the centre of the channel were measured. Fig. 5.8 shows that insonation with 1.6 MHz US for both 500 and 1000 bursts in the presence of SSPs significantly ($p < 0.05$) increases the mean, median and maximum delivery distance of ColoAdRFP to a tissue-mimicking phantom (approximated by distance to an RFP+ cell). Note that the distance values shown in Figs. 5.8 and 5.9 are distances from the centre of a 1.2 mm diameter channel. The red dashed lines approximate where the edge of the channel is. The increase in the total number of infected cells after US-exposure was not statistically significant ($p > 0.05$), though this is likely due to variability between the density of RFP+ cells detected in images of the 3 replicate channels.

As mentioned above, to control for any possible effect of US in the absence of SSP-seeded cavitation, one channel was exposed to only ColoAdRFP (no SSPs) and insonated at three spots. 5-days post-treatment, this channel was excised and sliced axially and RFP+ cells were quantified as described in Section 2.8.4. Fig. 5.9 shows that the exposure to 1.6 MHz US in the absence of SSPs does not affect the mean, median, or maximum delivery distance of ColoAdRFP to the tissue-mimicking gel, as compared to delivery of ColoAdRFP with SSPs in the absence of US. The total number of RFP+ cells was significantly different in the absence of US, but this is again likely due to the inter-channel variability in cell density.

Exposure to US at a driving frequency of 1.6 MHz, in the presence of SSPs, led to increased delivery of ColoAd to a cell-embedded tissue mimicking phantom. A similar trend was seen with US exposure at 0.5 MHz, however properties of the in vitro model gave rise to non-realistic 'cracking' of the gel and consequent pooling of the ColoAd solution. Whilst both frequencies tested provided impressive enhancement of delivery and consequent infection (with different degrees of damage to the agar matrix), the pressure levels used here at 1.6 MHz made translation to in vivo studies using this frequency more challenging. For this reason, and due to the successful use of 0.5 MHz in previous studies (including delivery of cetuximab and

nanoparticles in Chapter 4), this frequency was selected for further studies. These studies provided a useful first demonstration that SSPs could be used to enhance the delivery of a clinically relevant adenoviral vector.

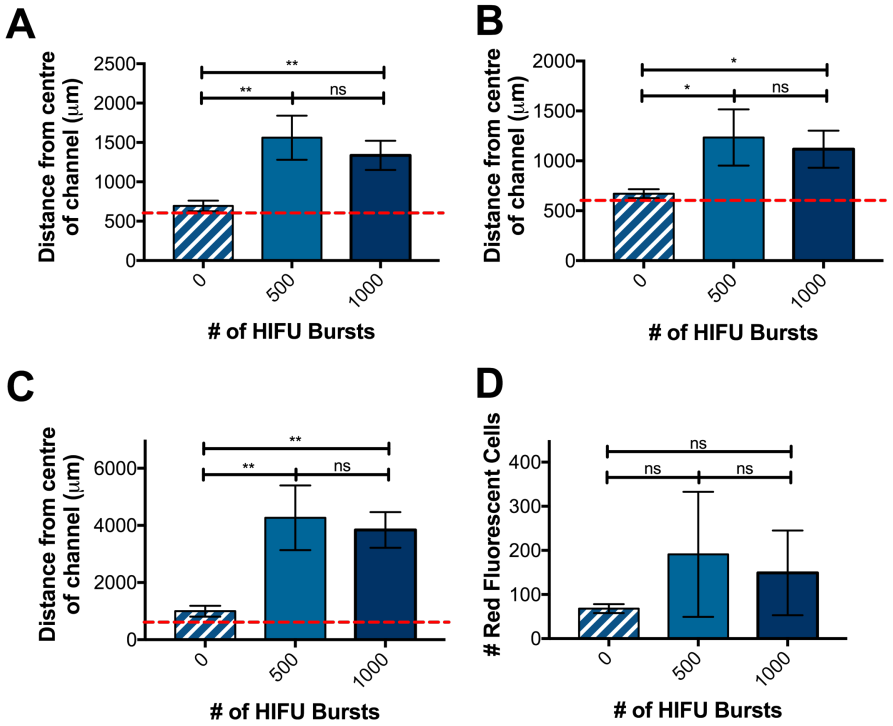

Figure 5.8: Quantification of RFP-expression after delivery of ColoAd-RFP + SSPs to a cell-embedded gel with and without US exposure. ColoAd and SSPs were flowed through channels within a cell-embedded gel, where multiple spots along each channel were exposed to focused US, for a duration of 50s (500 bursts) or 100s (1000 bursts). 6-days post exposure to ColoAdRFP, channels were excised from gel and imaged with fluorescence microscopy. The resulting images were processed in ImageJ, red fluorescent cells (RFP+) were counted, and distance to centre of channel was measured. Mean (A), median (B), and maximum distances (C) from channel centre to RFP+ cells were quantified. Red dashed line represents the outer edge of the channel. Panel D shows quantification of total number of infected cells. For the 0 (no US) and 500 burst conditions, a total of 3 spots were exposed (n = 3), while for the 1000 burst condition, a total of 4 spots were exposed (n = 4). Error bars represent standard deviation (SD). Statistical significance was assessed with one-way ANOVA followed by post-hoc Tukey's multiple comparisons test. ** = $p < 0.01$, * = $p < 0.05$, ns = $p > 0.05$, all p-values were adjusted for multiple comparisons.

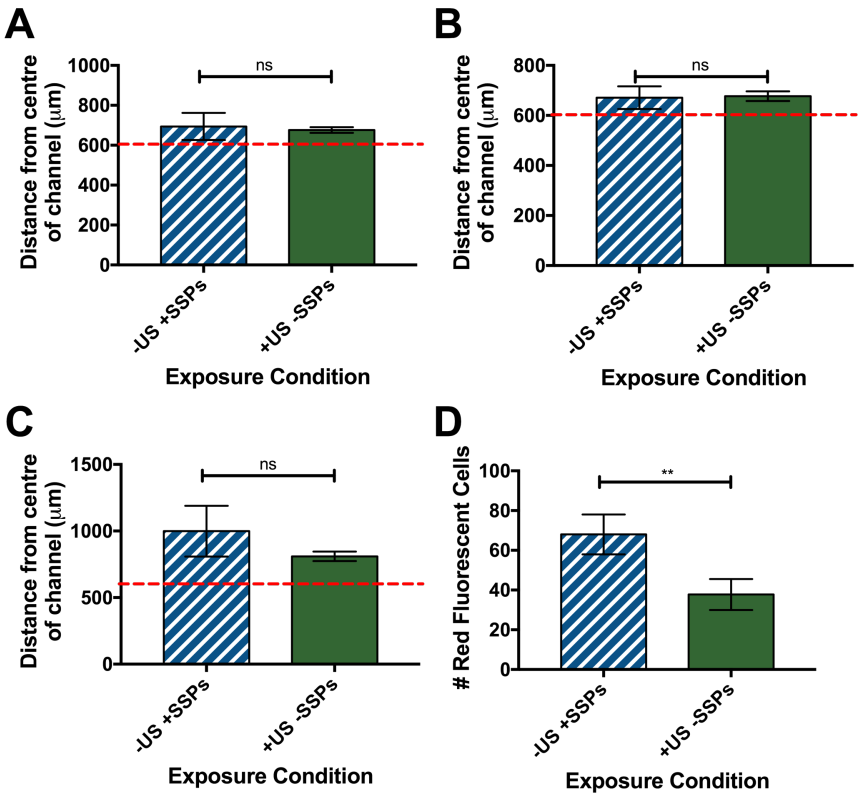

Figure 5.9: Quantification of RFP-expression after delivery of ColoAd-RFP to a cell-embedded gel without US but with SSP or with US but without SSPs. ColoAd + SSPs was flowed through channels within a cell-embedded gel, with no exposure to US (-US +SSPs), i.e. cavitation nuclei but no cavitation. ColoAd (with no SSPs) was also flowed through a single additional channel where multiple spots along each channel were exposed to focused US (+US -SSPs), for a duration of 50s (500 bursts) or 100s (1000 bursts), i.e. US but no cavitation. 6-days post exposure to ColoAdRFP (5-days for +US -SSPs group), channels were excised from gel and imaged with fluorescence microscopy. The resulting images were processed in ImageJ, red fluorescent cells (RFP+) were counted, and distance to centre of channel was measured. Mean (A), median (B), and maximum distances (C) from channel centre to RFP+ cells were quantified. Red dashed line represents the outer edge of the channel. Panel D shows quantification of total number of infected cells. For the -US + SSPs condition, a total of 3 spots were quantified (n = 3), while for the +US -SSPs condition, a total of 4 spots were quantified (n = 4). Error bars represent standard deviation (SD). Statistical significance was assessed with unpaired two-tailed t tests, ** = $p < 0.01$, ns = $p > 0.05$.

5.2 In vivo delivery of ColoAd with US-mediated cavitation

As with in vitro studies, past in vivo studies of oncolytic adenovirus delivery using US + CN used microbubble US contrast agent SV as a cavitation nuclei [178, 134],

and although these studies provided compelling evidence for the potential of US-mediated cavitation to enhance delivery of adenovirus into solid tumours, they suffered two potential limitations to translation. Firstly, these studies relied on the use of the Ad5 serotype which has a neutralization and clearance profile in human blood so rapid that any systemic administration strategy would require protective surface modification [128], a requirement with scientific, scale-up, and regulatory complexities. In the studies reported here, an Ad vector with improved circulation in humans was used, however it is important to note that in mice the circulation kinetics of ColoAd are comparable to those of Ad5, so the benefits of extended circulation are not captured in this model. The second limitation of previous studies is their reliance on the use of microbubble formulations as CN. Microbubbles are potentially limited in their application to US-mediated drug delivery in a clinical setting (as discussed in sections 4.2 and 5.1). Despite these limitations, as SV has demonstrated success in pre-clinical models of adenovirus delivery, it was used here as a positive control for cavitation-mediated delivery of ColoAd.

As shown in Section 5.1.2 solid gas-entrapping SSPs can be used in lieu of microbubbles to seed cavitation, and enhance delivery of ColoAd in vitro. Moreover, in Chapter 4, SSPs were shown to provide greater enhancement of delivery (compared to SV) of a therapeutic antibody, and targeted nanoparticle. Here, the effects of SSPs and SV on US-mediated delivery of ColoAd were investigated and compared in two different treatment regimes. An additional control of 'inactive' SSPs (which do not entrap gas) was also included in this study, to control for any potential effect of US in the absence of cavitation.

5.2.1 Experimental design

In Chapter 4, a bilateral tumour model was used to isolate the effect of US and cavitation on delivery of a therapeutic, while controlling for other random effects which contribute to variance in delivery between animals. A bilateral tumour model

is also used here. CD-1 nude mice were implanted with subcutaneous bilateral xenograft DLD-1 tumours. These tumours were allowed to grow for just over two weeks, until the majority of tumours reached a volume between 75-150 mm^3. There was a large variability in tumour size and shape observed between mice, and between the two bilateral tumours per mouse. Mice with the most closely matched tumour sizes were chosen to be treated with virus and active cavitation nuclei (SV or SSPs), and were assigned to a treatment group such that group means of US and non-US treated tumours were approximately equal with comparable variances. Mice with only one tumour of appropriate size were treated with ColoAd and inactivated SSPs (iSSPs), and though this group lacked an internal 'no-US' control tumour, the levels of viral delivery can be compared to the other treatment groups, and provide a background level of delivery in the presence of US and iSSP but absence of cavitation.

The US set-up used here was identical to the setup used for antibody/nanoparticle delivery in Chapter 4 and is shown in Fig. 4.5. After mounting in the water tank, and alignment of the treatment (HIFU) and PAM transducers, animals were dosed i.v. with ColoAd and CN, immediately after which one of two bilateral tumours was treated with focused US (note, the dose was split into two injections, one at the onset of US treatment, and the second halfway through the treatment time). At the onset of treatment (following ColoAd + CN injection), the transducers were focused on the largest region of the tumour, but after injection of CN, the mouse holder was slowly moved in 3 dimensions, in order to allow the HIFU focus to treat all regions of the tumour. Post-treatment, the tumours were examined for any signs of bruising or other damage. ColoAd variants expressing a luciferase transgene (under the control of either i) the major late promoter and splice acceptor sequence [SA], or ii) the human cytomegalovirus promoter [CMV]) were kindly provided by Egon Jacobus (ColoAdSALuc and ColoAdCMVLuc). ColoAd expressing a luciferase transgene was deemed optimal for these studies as it allows for tracking of virus delivery over

time (indirectly via imaging of transgene production) without the need for sacrifice of animals at each time point. Mice were imaged for luciferase production up to 11 days after virus dosing. After the final imaging session, mice were culled and tumours were collected for ex vivo processing of luciferase content, qPCR analysis of virus genome copies and immunohistochemistry (IHC) staining.

Two treatment regimes were investigated: both regimes used the same US parameters (Table 5.1), with the exception of PRFP, which was adjusted in the second treatment regime to optimize cavitation levels in real-time. The regimes are described in Section 2.10.1, and outlined in Table 5.2.

Frequency (MHz)	**PRF (Hz)**	**Duty Cycle (%)**	**# Cycles/Burst**
0.5	0.5	5	50 000

Table 5.1: US parameters kept constant between in vivo US treatment regimes.

.

Regime	**Virus**	**US Time (min)**	**PRFP (MPa)**
1	ColoAdCMVLuc	10	1.5
2	ColoAdSALuc	5	1.5-2

Table 5.2: Parameters varied between in vivo US treatment regimes. Note that doses of SV and iSSPs/SSPs were kept constant for each regime. Other US parameters were also kept constant (detailed in Table 5.1)

.

5.2.2 Statistical analysis

The impact on internally controlling experiments by having two tumours, only one of which received US, on the independence of error and the statistical analysis used is described in detail in Section 4.2.2. The same principles were followed here. It was hypothesized that the response variable (tumour ColoAd transgene expression) was a function of two factors: treatment with a type of CN and exposure

to US. However, data was also collected at multiple time points, and as ColoAdSALuc/ColoAdCMVLuc are replication-competent, it is expected that time will also be a factor in determining the value of the response variable. These factors were all considered fixed effects. A mixed-effect model was constructed to describe the response variable (tumour transgene expression) in terms of the fixed effects of CN, US and Time, and the random effect of Subject. Here CN was restricted to two levels (SSPs, and SV), to elucidate the differences between the effect of SV and SSPs as CN. The application of US was assigned two levels (+ or -), and Time had multiple levels (depending on the number of imaging sessions). The model was constructed in RStudio (R Core Team, 2018) lme4 [184] using the restricted maximum likelihood approach. The Satterthwaite approximation for degrees of freedom was used to determine p-values.

In this study, the effect of US alone (in the absence of cavitation) on ColoAd delivery, was controlled for using an inactive form of SSPs (iSSPs). iSSPs are prepared in such a way that they do not entrap gas (as do SSPs), and are thus considered 'inactive' and do not give rise to appreciable levels of cavitation when exposed to the same acoustic regimes as SSPs or SV. This assumption was tested by analysis of acoustic data passively acquired during US exposure of mice treated with ColoAd + iSSPs (Fig. 5.11).

5.3 Tumoural delivery of ColoAd with US-mediated cavitation: Regime 1

As outlined in Table 5.2, mice in Regime 1 were treated with ColoAdCMVLuc (1 x 10^{10} VPs) co-administered with either SV, or 1.75 mg of SSPs/iSSPs.

5.3.1 Acoustic feedback

Representative traces of PAM magnitude over time from treatment of mice with iSSPs, SSPs, and SV are shown in Fig. 5.10. With SV (panel A), a peak in the PAM magnitude was observed immediately following injection (at the onset of treatment, and after approximately 4 minutes), which decayed rapidly back to baseline values. Fig. 5.10 shows the PAM magnitude over time from the US treatment for one representative mouse dosed with SSP (panel B). The dose was split between t = 0 and t = 240 seconds, and the cavitation was seen to spike at these time points and decay thereafter. Treatment with control iSSPs (panel C) showed very little evidence of any cavitation events, as expected.

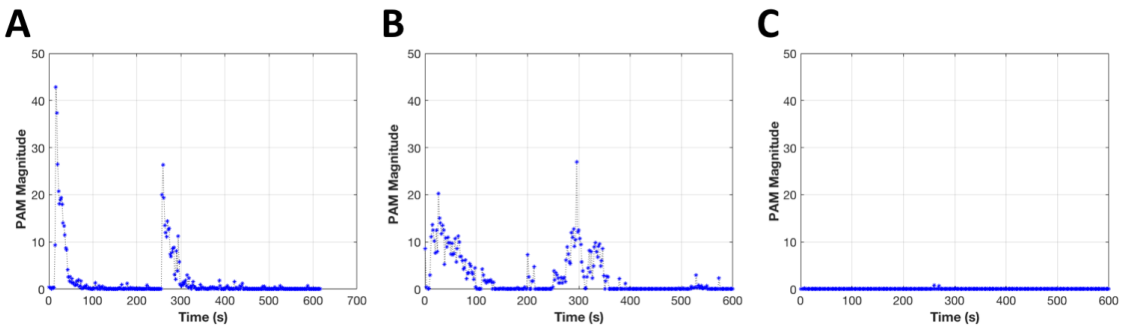

Figure 5.10: Acoustic data acquired during US- treatment of tumour-bearing mice with ColoAd + SV (A) or SSPs (B) or iSSPs (C). The magnitude of the maximum PAM pixel is plotted over time for duration of US-treatment of mice with ColoAd + SSPs.

From these PAM traces, as in Chapter 4, multiple metrics were quantified in order to compare the features of the cavitation recorded, with the aim of determining the optimal levels of cavitation required for successful enhancement of viral delivery (Fig. 5.11). Firstly, the maximum PAM magnitude and total (integrated) PAM magnitude recorded throughout treatment were compared for the different CN (and iSSP controls). While the total (cumulative) PAM magnitudes were not significantly different between SV and SSPs, the maximum PAM magnitude was significantly

higher with SV than with SSPs. The percentage of treatment time with cavitation activity over a threshold of 1 was significantly greater with SSPs than SV. Percentage of treatment time above a threshold of 10 was comparable between SV and SSPs.

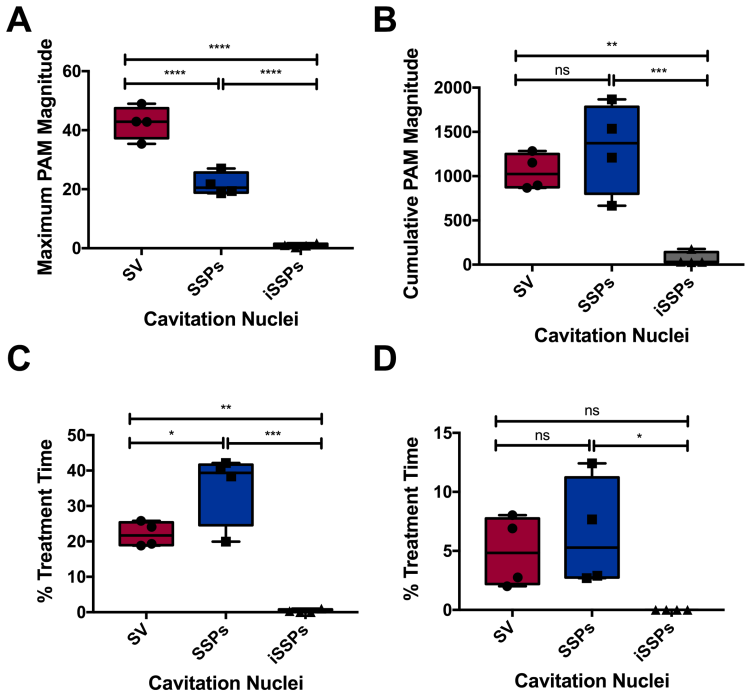

Figure 5.11: Quantification of acoustic data acquired during US- treatment of tumour-bearing mice dosed with ColoAd and CN. The maximum (panel A) and cumulative (panel B) PAM magnitudes are shown, as well as the percentage of treatment time that PAM magnitude was above a threshold of 1 (panel C) or a threshold of 10 (panel D). Box and whisker plots show median, first and third quartiles, and maximum and minimum values, while points show data from individual mice (n = 4, data from one iSSP mouse not shown due to data saving error). Statistical significance was assessed with one-way ANOVA followed by post-hoc Tukey's multiple comparisons test. ** = $p < 0.01$, * = $p < 0.05$, ns = $p > 0.05$, all p-values were adjusted for multiple comparisons.

Immediately post-treatment, tumours were inspected for bruising and photographed. Fig. 5.12 shows that there was significant bruising in tumours treated with SSPs + US. Very minimal bruising was seen with SV, and none with iSSPs. Notably, the level of bruising did not obviously correlate with maximum PAM magnitude, but instead appeared to be related to duration of cavitation activity, as this metric was increased with SSPs relative to SV. No other adverse effects were observed as a result

of US-treatment, and bruising resolved within approximately 3 days post-treatment.

Figure 5.12: Photographs taken of US-exposed tumours immediately post-treatment with SV, SSPs or iSSPs. Red arrows denote areas of bruising.

5.3.2 Tracking of ColoAd infection

In Section 5.1, a fluorescent reporter gene was used to track infection at a resolution sufficient to quantify individual infected cells. Expression of a fluorescent protein can also be used in vivo as well to track viral infection, however there is significant overlap between natural tissue auto-fluorescence and commonly used fluorophores, such as the RFP used in this thesis. Bioluminescence is a more sensitive alternative for in vivo imaging, with a considerably larger dynamic range. Luciferase is an enzyme which can be encoded in the genome of ColoAd, and when expressed, acts upon its substrate (luciferin) to catalyze a reaction which emits a photon of light. Infected cells in a mouse can be tracked by administration of luciferin and subsequent imaging using a high-sensitivity in vivo imaging system (IVIS). Here, the expression of luciferase from ColoAdCMVLuc was measured 2 and 6 days post-treatment with IVIS imaging (preceded by an i.p. injection of luciferin, see Section 2.11). 6 days post-treatment, mice were culled and tumours were excised and frozen. Tumour tissue was then homogenized and lysed, and luciferase content was assayed using a

well-plate assay and microplate reader.

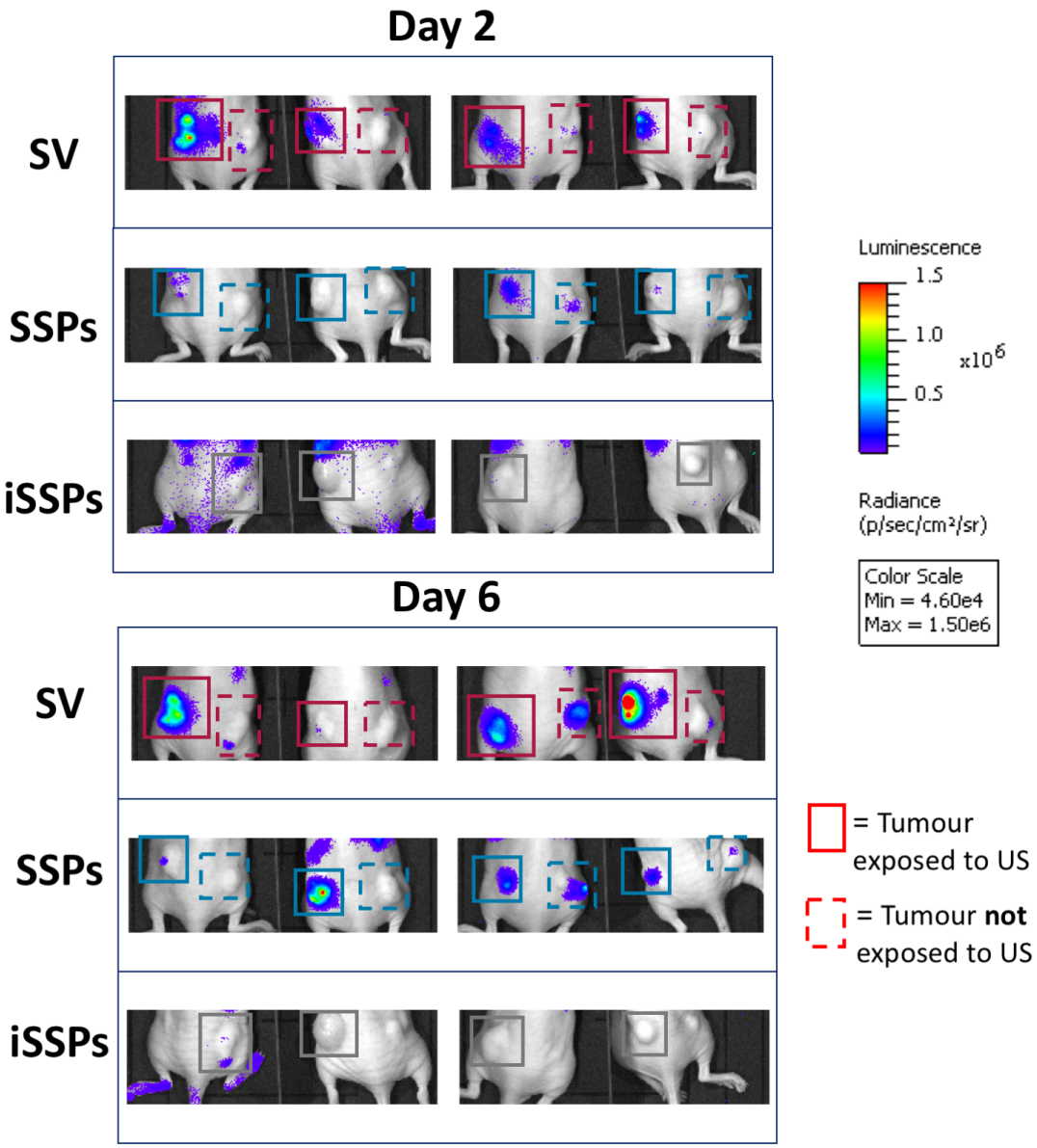

Figure 5.13: In vivo imaging of luciferase expression in tumour-bearing mice. 2 and 6-days post-treatment with ColoAd + CN +/- US mice were injected i.p. with luciferin, and imaged using IVIS. Solid squares denote tumours that were subject to treatment with US, dashed squares denote tumours that were not exposed to US.

The variant of ColoAd used in this regime (ColoAdCMVLuc) has the luciferase transgene under the control of a CMV promoter, which is uncoupled from the virus life cycle, and so the luciferase can be expressed quickly and before replication of

virus has begun. This is in contrast to the virus used in Regime 2 (ColoAdSALuc), wherein the luciferase transgene is coupled to the major late transcription unit (under the control of the major late promoter (MLP)) and is only expressed when the virus is replicating. Given these differences, luciferase transgene signal should be detectable slightly earlier in tumours infected with ColoAdCMVLuc than with ColoAdSALuc. Fig. 5.13 shows that 2 days post-treatment, a strong IVIS signal was readily observed in 4 out 4 tumours treated with SV + US. The IVIS signal in tumours treated with SSPs + US was lesser in magnitude, but is still enhanced (compared to non-US treated tumour) in 3 out of 4 mice.

Viral transgene production was quantified by measure of average radiance (referred to simply as radiance in the ensuing text) of each tumour (as shown in Fig. 5.14), and was quite variable, though the median radiance of the SV + US group was higher than all other treatment groups. Fig. 5.15 plots the radiance on day 6 of the US-treated and untreated tumours of each mouse that received an active CN. The lower limit of the y-axis in this plot is set to the mean background radiance across all mice.

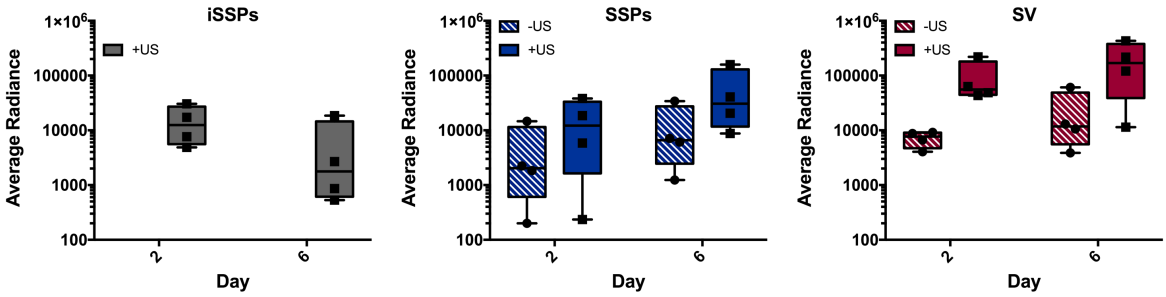

Figure 5.14: Quantification of in vivo luciferase production over 6 days using IVIS imaging. Mice were dosed i.v. with ColoAdCMVLuc + CN (iSSPs, SSPs, or SV), and one tumour was exposed to US while the other was not. Mice were imaged after i.p. injection of luciferin 2, and 6 days post-treatment. Luminescence is reported here as average radiance, in units of photons $\cdot \text{sec}^{-1} \cdot \text{cm}^{-2} \cdot \text{sr}^{-1}$. Box and whisker plots show median, first and third quartiles, and maximum and minimum values, while points show data from individual mice (n = 4).

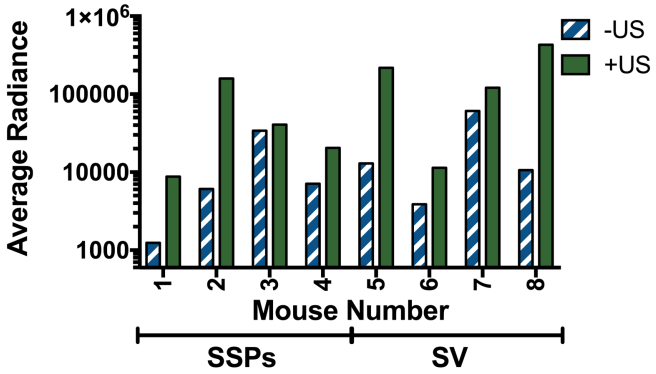

Figure 5.15: Quantification of in vivo luciferase production 6 days post-treatment using IVIS imaging. Mice were dosed i.v. with ColoAdCMVLuc + CN (SSPs, or SV), and one tumour was exposed to US while the other was not. Data shown here is from an IVIS imaging session 6 days post-treatment. Mice were imaged after i.p. injection of luciferin. Pairs of bars denote luminescence from each tumour (non-US and US-treated) of an individual mouse.Luminescence is reported here as average radiance, in units of photons $\cdot$ sec^{-1} $\cdot$ cm^{-2} $\cdot$ sr^{-1}.

Without transformation or further analysis of the data it appears as though cavitation provided a beneficial effect. Indeed, in 8 out of 8 mice, there was an increase in radiance in the US-treated tumour compared to its untreated 'internal control' (Fig. 5.14). However, there was also large variability in the absolute values measured in different mice, even between mice in the same group. In order to use linear regression modelling for data analysis the data must in fact be linear, and the residuals should be normally distributed and homoscedastic (variance of data should be the same across range of values). When the raw data was fit with the mixed effects model as described above, the Shapiro-Wilk test of normality of the residuals returned a p-value < 0.05, indicating the residuals were not normally distributed. Moreover, visual inspection of the residual plots revealed a significant deviation from homoscedasticity. The raw data would thus not be appropriately analysed using linear regression methods. Transformation of data is commonly used to normalize skewed data, particularly biological data that cannot have 'zero' or negative values [246]. The Box-Cox transform is a power transformation of the form y^{λ}, where the parameter λ can be estimated with a profile likelihood function to

provide a transformation that yields normal homoscedastic model residuals (this procedure is still however, a guide, and diagnostics still need to be performed post-transform to confirm desired result). Here, a λ of 0.101 was used to transform the IVIS radiance data, and when this transformation was applied the model residuals were normally distributed (Shapiro-Wilk test p-value > 0.05), and homoscedastic. The transformed IVIS data from 2 and 6 days post-treatment were analysed using a linear mixed effects model as discussed in Section 5.2.2.

Fixed Effect	**p**
CN	p = 0.0547
US	**p = 0.0004**
Time	**p = 0.0368**
CN:US	p = 0.2191
CN:Day	p = 0.4043
US:Day	p = 0.8043
CN:US:Day	p = 0.6701

Table 5.3: Type III ANOVA of fixed effects of transformed tumour radiance data for mice dosed with ColoAdCMVLUC and SV or SSPs.

Comparison	**Day 6**
SV +US vs. SV -US	p = 0.0601
SSP +US vs. SSP -US	p = 0.3243
SV +US vs. SSP +US	p = 0.6312
SV -US vs. SSP -US	p = 1

Table 5.4: Post-hoc multiple comparisons of EM means of mixed effects model of transformed tumour radiance data obtained 6 days post- treatment for mice dosed with ColoAdCMVLUC and SV or SSPs.. All reported p-values are corrected for multiple comparisons using the Bonferroni correction.

ANOVA of the fixed effects revealed significant main effects of US (p = 0.0004) and Time (p = 0.0368), while the main effect of CN was only slightly non-significant (p = 0.0547). Post-hoc t-tests of the estimated marginal (EM) means revealed no significant comparisons.

The fold increase between tumours treated with and without US was estimated from the model at day 6, and was found to be approximately 8-fold for SV + US (95% CI from 2- to 30-fold) and 5-fold for SSPs + US (95% CI from 1- to 21-fold). 95% CI of these fold-increases were estimated by parametric bootstrapping (5000 simulations).

Fixed Effect	p
CN	p = 0.1081
US	**p = 0.0180**
CN:US	p = 0.7588

Table 5.5: Type III ANOVA of fixed effects of transformed luminescence data from ex vivo luciferase assay for mice dosed with ColoAdCMVLuc with SV or SSPs.

Comparison	Day 6
SVY vs. SVN	p = 0.3434
SSPY vs. SSPN	p = 0.1841
SVY vs. SSPY	p = 0.7136
SVN vs. SSPN	p = 0.4224

Table 5.6: Post-hoc multiple comparisons of EM means from mixed effects model of transformed luminescence data from ex vivo luciferase assay for mice dosed with ColoAdCMVLuc with SV or SSPs. All reported p-values are corrected for multiple comparisons using the Bonferroni correction.

These results were confirmed by the analysis of the ex vivo luciferase assay (Fig. 5.16) conducted on tumours excised and homogenized at day 6: ANOVA of fixed effects revealed a signficant main effect of US (p = 0.018), while post-hoc tests found no significant comparisons.

Quantitative polymerase chain reaction (qPCR) analysis was conducted on DNA extracted from the excised and homogenized tumours from day 6 to directly quantify the number of virus genomes per milligram of tumour. Statistical analysis of the qPCR data confirmed the same trends observed with IVIS and ex vivo luciferase data: a significant main effect of US (p = 0.0178) by ANOVA and no significant comparisons by post-hoc testing.

Fixed Effect	p
CN	p = 0.1031
US	**p = 0.0178**
CN:US	p = 0.8135

Table 5.7: Type III ANOVA of fixed effects of transformed genome copy data from ex vivo qPCR analysis for mice dosed with ColoAdCMVLuc with SV or SSPs.

Comparison	Day 7
SVY vs. SVN	p = 0.3161
SSPY vs. SSPN	p = 0.1960
SVY vs. SSPY	p = 0.6368
SVN vs. SSPN	p = 0.4269

Table 5.8: Post-hoc multiple comparisons of EM means from mixed effects model of transformed genome copy data from qPCR analysis of mice dosed with ColoAdCMVLuc with SV or SSPs. All reported p-values are corrected for multiple comparisons using the Bonferroni correction.

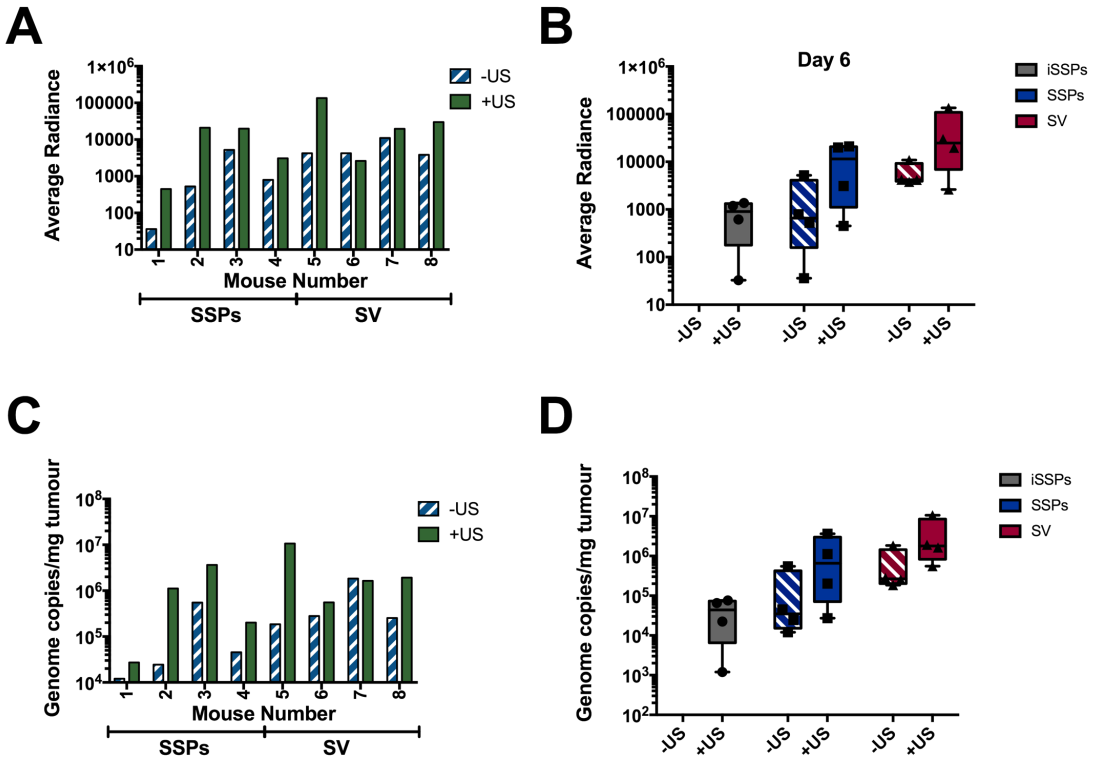

Figure 5.16: Ex vivo quantification of luciferase and viral genome copies 6 days post-treatment. Mice were dosed i.v. with ColoAdCMVLuc + CN (SSPs, or SV), and one tumour was exposed to US while the other was not. 6 days post-treatment, tumours were excised, homogenized, and analyzed for luciferase content and virus genome copies. Pairs of bars denote luminescence (A) or genome copies (C) from each tumour (non-US and US-treated) of an individual mouse. Aggregate data of luciferase (B) and genome copies (D) are shown.

Finally, the effect of US on tumour luciferase expression in the *absence* of cavitation was investigated, by comparing tumours treated with iSSPs and US to tumours treated with SSPs and no US (as the iSSP mice did not have untreated no US control tumours). Again, a linear mixed effects model was used to described the data, with the exclusion of CN as a fixed effect, as the iSSPs and SSPs differ only in the entrapment of gas, and should thus affect circulation of ColoAd in the same manner. ANOVA of fixed effects revealed a significant interaction between the factors of US and Time ($p = 0.021$), but post-hoc testing revealed no significant difference ($p = 0.3092$) between tumours treated with SSPs only (equivalent to iSSPs only) and tumours treated with iSSPs and US. A two-tailed unpaired t-test was used to compare luciferase expression and genome copies per mg of tumour between these two groups, and no statistically significant difference ($p = 0.8141$, and $p = 0.4632$ respectively) was found.

Fixed Effect	**p**
US	$p = 0.6931$
Time	$p = 0.6347$
US:Time	**$p = 0.0210$**

Table 5.9: Type III ANOVA of fixed effects of transformed tumour radiance data for mice dosed with ColoAdCMVLUC and iSSPs + US or SSPs -US.

Comparison	**Day 7**
iSSPY vs. SSPN	$p = 0.3092$

Table 5.10: Post-hoc multiple comparisons of EM means of mixed effects model of transformed tumour radiance data obtained 6 days post-treatment for mice treated with ColoAdCMVLUC and iSSPs +US or SSPs -US.

In summary, within this treatment regime (US of 1.5 MPa PRFP, and 10 minutes of US exposure), treatment with ColoAdCMVLuc + SSPs + US gave rise to an estimated 5-fold (95% CI from 1 to 21-fold) increase in tumour transgene expression as measured by IVIS imaging 6-days post-treatment. Treatment with ColoAd + SV + US also gave rise to an increase in transgene expression (approximately 8-fold, 95% CI from 2 to 30-fold). ANOVA of the fixed effects of a linear mixed effects model revealed significant main effects of US and Time, while post-hoc analysis

at day 6 showed no significant comparisons. These results were confirmed with ex vivo quantification of luciferase content and viral genome copies per milligram of homogenized tumour.

The cavitation activity seen in mice treated with SSPs in this regime was sustained for significantly longer than cavitation from tumours of mice treated with SV. Quantification of viral transgene expression by IVIS and ex vivo luciferase, as well as qPCR analysis of virus genome copies at day 6 post-treatment indicated an increase in ColoAd delivery for 4 out of 4 mice treated with SSPs.

Fold-increase in transgene expression after 6 days was slightly greater for mice treated with SV however, and there was substantially less bruising observed in US-treated tumours with SV versus SSPs. Considering the acoustic feedback from the US-treatments, cavitation activity with SV was significantly shorter in duration, but significantly greater in terms of maximum PAM magnitude. This suggests that substantial enhancement of delivery can occur with relatively short exposure to cavitation, and is potentially optimised by the generation of 'spikes' of cavitation (as seen immediately after administration of SV). In mice, ColoAd is cleared rapidly, with a half-life of approximately 2 minutes after i.v. injection [247]. Given this, it is likely that US-mediated cavitation will have the largest effect on delivery of ColoAd within the first two minutes post-injection. This could explain why there is no observed 'added benefit' of the more sustained cavitation seen with SSPs over the treatment time of 10 minutes, as was seen with cetuximab + SSPs in Chapter 4. To address these observations, a new treatment regime was proposed (Regime 2), wherein the tumour was exposed to US for only 5 minutes, ColoAd and CN (SV or SSPs) were administered at t = 0 and at t = 2.5 minutes, and the PRFP output by the HIFU transducer was varied between 1.5 MPa and 2 MPa (to increase PAM magnitude levels seen with SSPs). iSSPs were no longer included as a control, as no significant increase in tumour transgene expression was seen with iSSP + US treatment in the absence of significant cavitation.

5.4 Tumoural delivery of ColoAd with US-mediated cavitation: Regime 2

As outlined in Table 5.2, mice in Regime 2 were treated with ColoAdSALuc co-administered with either SV, or SSPs (same doses as in Regime 1). The PRFP was varied throughout treatment between 1.5 to 2 MPa, using real-time PAM feedback to keep cavitation activity of the SSPs consistent between PAM magnitudes of approximately 10 to 20. In order to try and compensate for the impact of the inter-mouse variation, the number per group was also increased from 4 to 8. As the effect evidenced in Regime 1 with SSPs appeared to be increasing with time, Regime 2 was taken out to 11 days.

5.4.1 Acoustic feedback

Fig. 5.17 shows the PAM magnitude over time from the US treatment for each of the 8 mice dosed with SSP. The dose was split between t = 0 and t = 150 seconds, though cavitation levels remained quite consistent throughout each treatment. Cavitation was also quite consistent between mice, and this is reflected in the 4 quantification metrics plotted in Fig. 5.18. Traces are not shown from mice treated with SV, as these results mirrored those obtained in Regime 1. With the increase in PRFP of the driving HIFU transducer (compared to Regime 1), the maximum PAM magnitude recorded for mice treated with SSPs was not significantly different from those mice treated with SV (as was the case for Regime 1). Moreover, the cavitation activity with SSPs was significantly greater ($p < 0.05$) than with SV by all other metrics (total PAM magnitude, and percentage of time above threshold of 1 or 10).

Immediately post-treatment, tumours were inspected for bruising and photographed (data not shown). Levels of bruising with SSPs matched those seen with Regime 1 (Fig. 5.12), while again very minimal bruising was seen with SV.

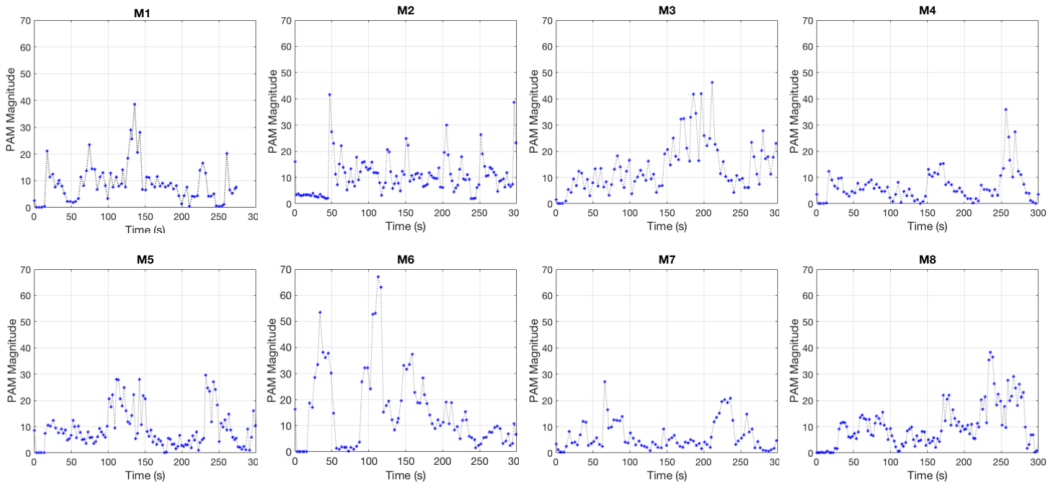

Figure 5.17: Acoustic data acquired during US- treatment of 8 tumour-bearing mice with ColoAd + SSPs. The magnitude of the maximum PAM pixel is plotted over time for duration of US-treatment of mice with ColoAd + SSPs.

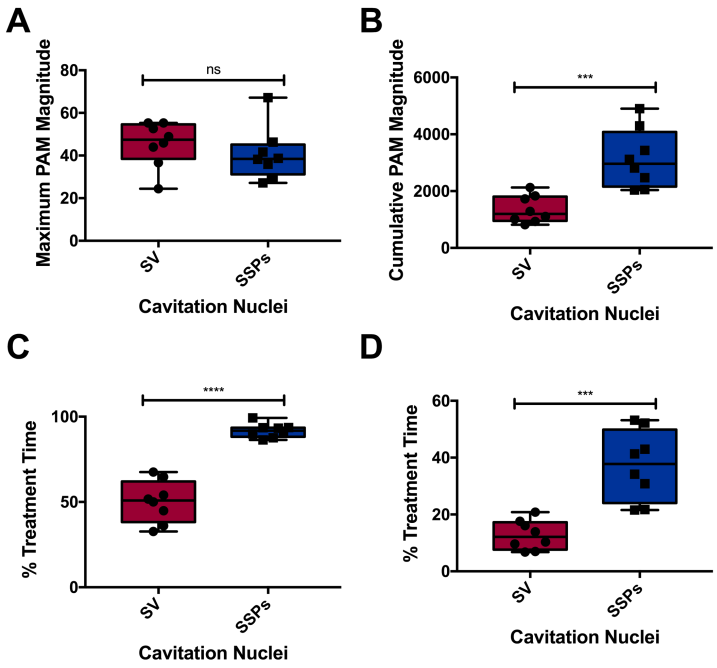

Figure 5.18: Quantification of acoustic data acquired during US-treatment of tumour-bearing mice with ColoAd and CN. The maximum (panel A) and cumulative (panel B) PAM magnitudes are shown, as well as the percentage of treatment time that PAM magnitude was above a threshold of 1 (panel C) or a threshold of 10 (panel D). Box and whisker plots show median, first and third quartiles, and maximum and minimum values, while points show data from individual mice (n = 8). Statistical significance was assessed with two-tailed unpaired t-tests. *** = $p < 0.001$, **** = $p < 0.0001$, ns = $p > 0.05$.

5.4.2 Tracking of ColoAd infection

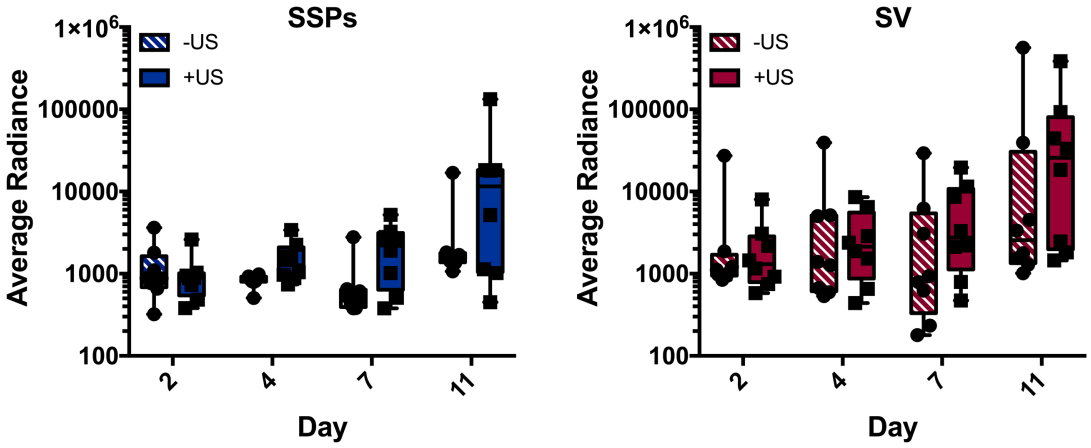

Figure 5.19: Quantification of in vivo luciferase production over 11 days using IVIS imaging. Mice were dosed i.v. with ColoAdSALuc + CN (SSPs, or SV), and one tumour was exposed to US while the other was not. Mice were imaged after i.p. injection of luciferin 2, 4, 7, and 11 days post-treatment. Luminescence is reported here as average radiance, in units of photons $\cdot$ sec^{-1} $\cdot$ cm^{-2} $\cdot$ sr^{-1}. Box and whisker plots show median, first and third quartiles, and maximum and minimum values, while points show data from individual mice (n = 8).

From Fig. 5.19, it is clear that despite the relatively consistent cavitation levels seen across mice, the delivery of ColoAd (as measured by IVIS imaging of transgene expression), was extremely variable. 11-days post-treatment however, the median radiance levels were higher for tumours treated with SV + US or SSPs + US compared to their corresponding untreated tumours. Fig. 5.20 plots the radiance values from each tumour for individual mice at day 11. Out of the 8 mice treated with SSPs, 3 mice had no luciferase transgene expression detectable by IVIS in either tumour: mice 2, 4, and 5 had radiance levels from both tumours less than a threshold of mean background radiance + 2 standard deviations (σ) calculated across mice. Of the 5 SSP mice with a detectable signal (defined as $>$ background radiance + 2σ), all mice had a greater signal from the US-treated tumour. It would appear that in this context, the effect of US is 'enabling': i.e. without US there is no expression of viral transgenes (detected by IVIS) in 1/8 tumours, and with US there

is substantial expression in 5/8 tumours.

The effect with SV treatment is even more variable: 6/8 mice had a detectable IVIS signal in at least one tumour. Out of these 6, 4 mice had an increased signal in the US-treated tumour (though the extent of this increase was highly variable).

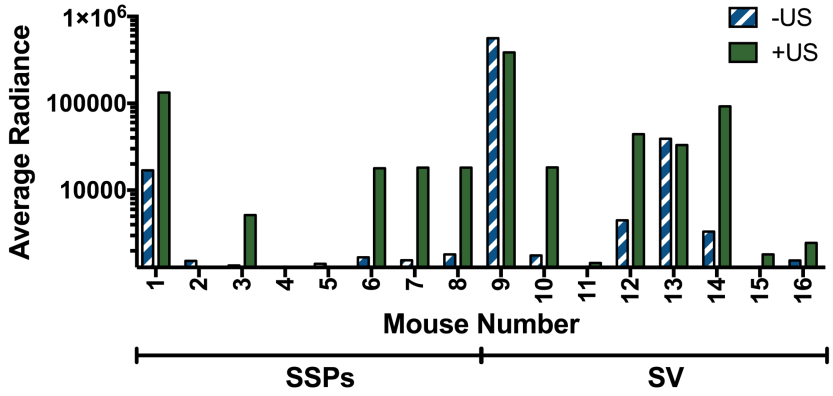

Figure 5.20: Quantification of in vivo luciferase production 11 days post-treatment using IVIS imaging. Mice were dosed i.v. with ColoAdSALuc + CN (SSPs, or SV), and one tumour was exposed to US while the other was not. Data shown here is from an IVIS imaging session 11 days post-treatment. Mice were imaged after i.v. injection of luciferin. Luminescence is reported here as average radiance, in units of photons $\cdot$ sec^{-1} $\cdot$ cm^{-2} $\cdot$ sr^{-1}.

A linear mixed effects model was fit to the (log-transformed) data across all 4 days of IVIS imaging to help analyze the factors affecting luciferase expression.

ANOVA of the fixed effects of the fitted model revealed significant main effects of US ($p < 0.001$) and Time ($p < 0.001$), and a significant interaction between US and Time ($p = 0.0196$). Post-hoc tests revealed a significant difference between SSP + US and SSP -US at day 11 ($p = 0.0423$).

The fold increase between tumours treated with and without US was estimated from the model at day 11, and was found to be approximately 11-fold for SV + US (95% CI from 2- to 57-fold) and 13-fold for SSPs + US (95% CI from 3- to 69-fold)

Although statistical analysis of the ensemble IVIS data across the whole cohort of mice revealed a statistically significant main effect of US, leading to a statistically significant increase in luciferase transgene expression for tumours treated with SSPs + US compared to SSPs alone, this effect was only seen in 5 out of 8 mice receiving

Fixed Effect	p
CN	p = 0.1440
US	**p < 0.001**
Time	**p < 0.001**
CN:US	p = 0.6082
CN:Day	p = 0.7461
US:Day	**p = 0.0196**
CN:US:Day	p = 0.8924

Table 5.11: Type III ANOVA of fixed effects of transformed tumour radiance data for mice dosed with ColoAdSALUC and SV or SSPs.

Comparison	Day 11
SV +US vs. SV -US	p = 0.0595
SSP +US vs. SSP -US	**p = 0.0423**
SV +US vs. SSP +US	p = 0.4942
SV -US vs. SSP -US	p = 0.4193

Table 5.12: Post-hoc multiple comparisons of EM means of mixed effects model of transformed tumour radiance data obtained 11 days post-treatment for mice dosed with ColoAdSALUC and SV or SSPs. All reported p-values are corrected for multiple comparisons using the Bonferroni correction.

this treatment (the remaining 3 mice having no IVIS signal above threshold). As there was no discernible trend in the cavitation data to explain this difference, it was hypothesized that the difference in response could stem from inherent biological variation between the tumours. To further investigate this, and to potentially investigate any impact of cavitation on the *distribution* of ColoAd, half of the tumours treated in this regime were fixed and stained for immunohistochemistry (IHC). To ensure an even representation of the variability seen between mice, 2 'responders' and 2 'non-responders' were chosen from both the SSP and SV groups for IHC analysis. The results of this analysis are discussed further in Section 5.4.3.

The remaining half of the tumours were excised (on day 11) and analysed for luciferase content and virus genome copies as before. Statistical analysis of the ex vivo luciferase assay and qPCR analysis (Fig. 5.21) revealed no significant main or interaction effects, and post-hoc analysis found no significant comparisons. However, given that 2 positive 'responders' were removed from each group (and 4 mice total from each group), the statistical power to detect an effect is greatly reduced from the analysis of the IVIS data.

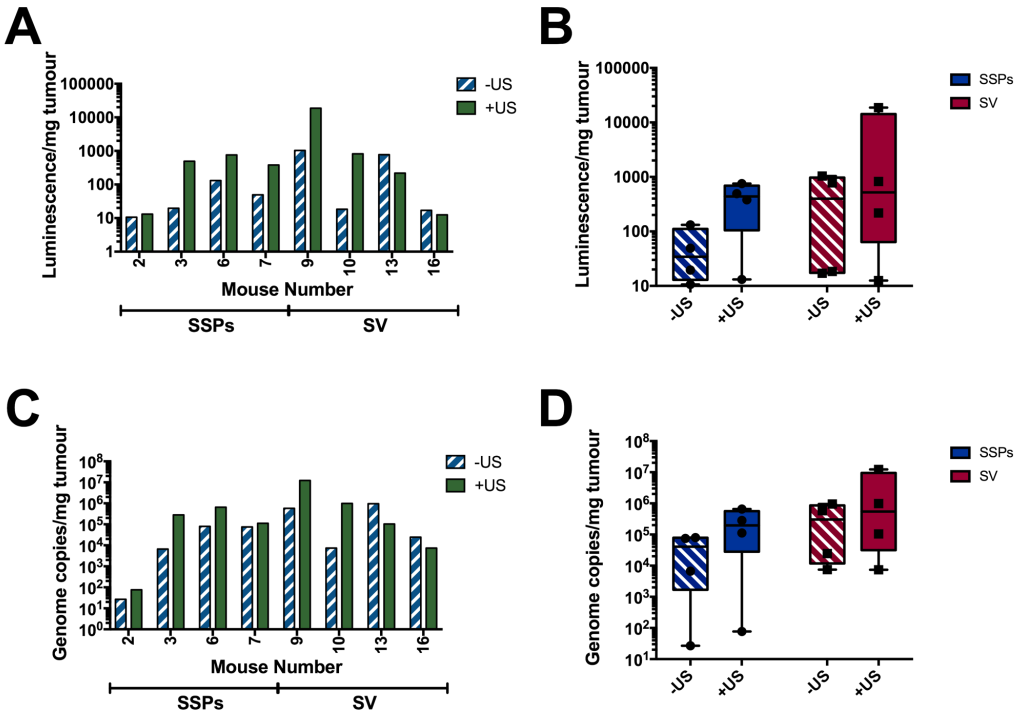

Figure 5.21: Ex vivo quantification of luciferase and viral genome copies 11 days post-treatment. Mice were dosed i.v. with ColoAdSALuc + CN (SSPs, or SV), and one tumour was exposed to US while the other was not. 11 days post-treatment, tumours were excised, homogenized, and analyzed for luciferase content and virus genome copies. Pairs of bars denote luminescence (A) or genome copies (C) from each tumour (non-US and US-treated) of an individual mouse. Aggregate data of luciferase (B) and genome copies (D) are shown. As tumours from 4 mice for each CN type group (SV and SSPs) were sent for staining, these data are from the 4 remaining mice for each CN type.

Fixed Effect	p
CN	p = 0.4788
US	p = 0.0656
CN:US	p = 0.7124

Table 5.13: Type III ANOVA of fixed effects of transformed luminescence data from ex vivo luciferase assay for mice dosed with ColoAdSALuc with SV or SSPs.

Comparison	Day 7
SV +US vs. SV -US	p = 0.9448
SSP +US vs. SSP -US	p = 0.4472
SV +US vs. SSP +US	p = 1
SV -US vs. SSP -US	p = 1

Table 5.14: Post-hoc multiple comparisons of EM means from mixed effects model of transformed luminescence data from ex vivo luciferase assay for mice dosed with ColoAdSALuc with SV or SSPs. All reported p-values are corrected for multiple comparisons using the Bonferroni correction.

Fixed Effect	p
CN	p = 0.3047
US	p = 0.1608
CN:US	p = 0.7173

Table 5.15: Type III ANOVA of fixed effects of transformed genome copy data from ex vivo qPCR analysis for mice dosed with ColoAdCMVLuc with SV or SSPs.

Comparison	Day 7
SV +US vs. SV -US	p = 1
SSP +US vs. SSP -US	p = 0.8445
SV +Us vs. SSP +US	p = 1
SV -US vs. SSP -US	p = 1

Table 5.16: Post-hoc multiple comparisons of EM means from mixed effects model of transformed genome copy data data from qPCR analysis for mice dosed with ColoAdSALuc with SV or SSPs. All reported p-values are corrected for multiple comparisons using the Bonferroni correction.

5.4.3 Immunohistochemistry

IHC analysis of remaining tumours looked at vascularization (by staining for endomucin, an endothelial marker), tumour viability (H&E staining), and viral delivery (by staining for hexon, a major viral capsid protein). Across all tumours, vascular-

ization was heterogenenous (see Fig. 5.22), though no trend was detected between tumours that 'responded' to US treatment and those that did not. Many tumours contained large necrotic areas devoid of positive staining for blood vessels, while some areas were almost completely viable and well perfused. Very little positive staining for ColoAd (detected by capsid protein hexon) was seen. Fig. 5.23 shows the virus staining from the US-treated tumour of the mouse (M1) with the greatest proportion of hexon staining (which also corresponded to a mouse with relatively high luciferase expression by IVIS, see Fig. 5.20). Within this section, 4 foci of infection were identified (enlarged in Fig. 5.23, panel A), and compared to the adjacent section stained for endomucin (panel B, co-registration was done manually in ImageJ). This analysis did not unfortunately provide much information about virus delivery after US treatment, as the levels of hexon staining were so low across tumours.

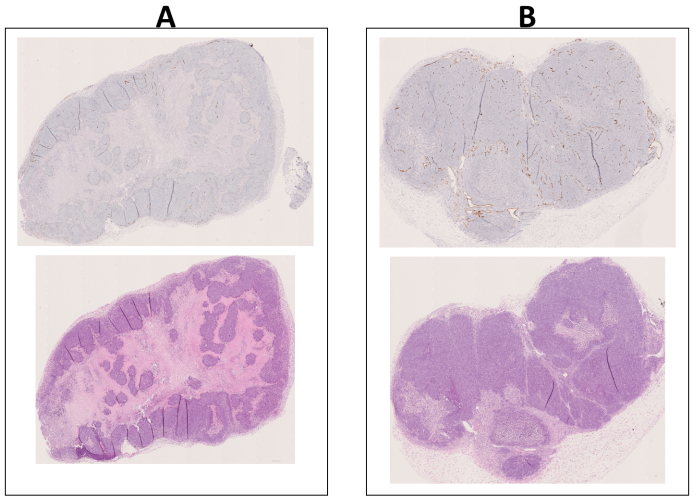

Figure 5.22: Representative sections of tumours stained for vasculature and viability. Top sections show immunostaining for endomucin (brown), while bottom sections show H%E staining. Panel A is a representative section with 'low' vascularity and viability, while panel B is a representative section with 'high' vascularity and viability.

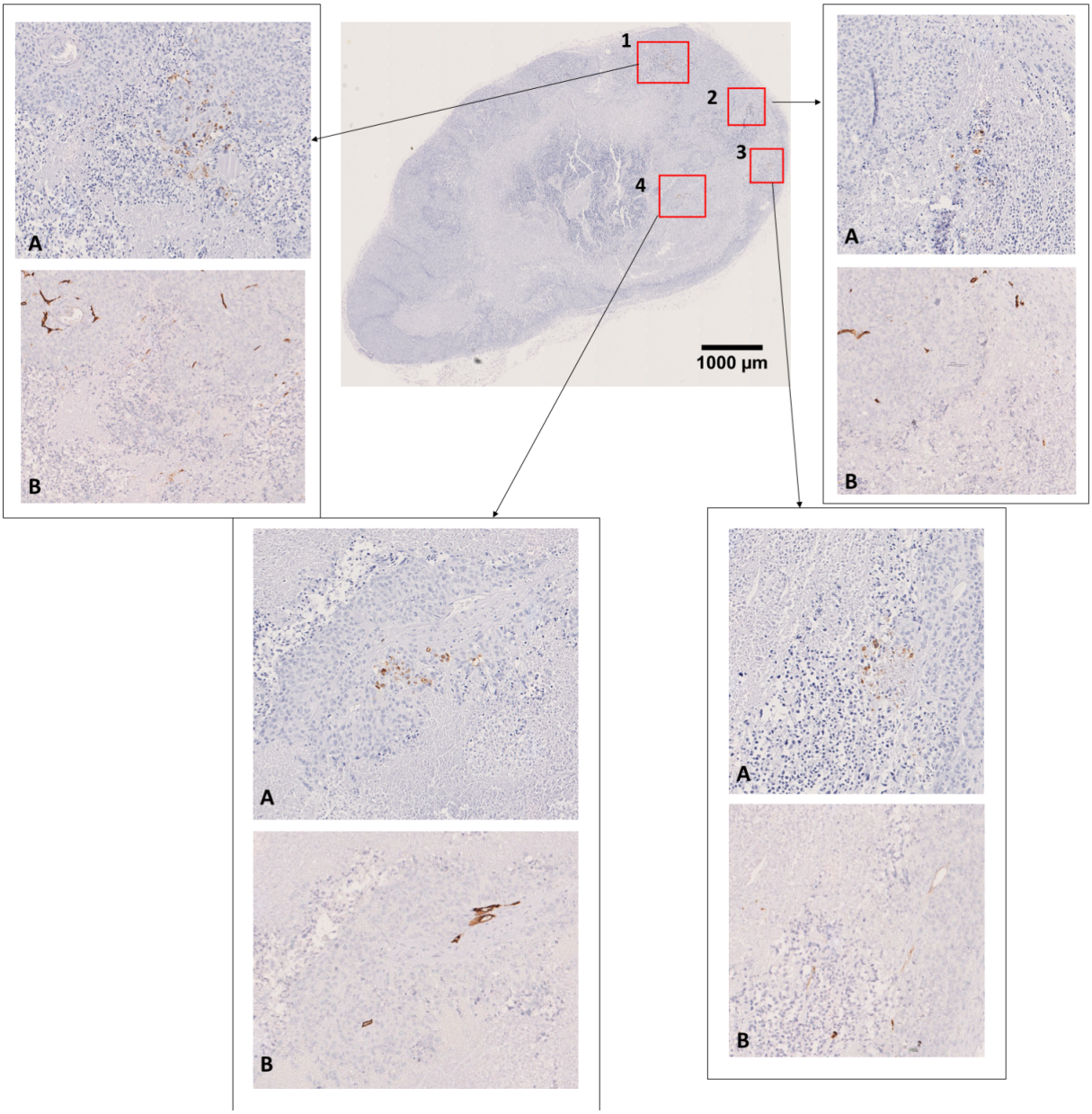

Figure 5.23: Section of tumour showing positive staining for hexon. For each infection foci, top sections (A) show immunostaining for hexon (brown), while bottom sections (B) show immunostaining for endomucin (brown). Four foci of infection were identified within this section.

In summary, within this treatment regime (US of 1.5-2 MPa PRFP over 5 minutes), treatment with ColoAdSALuc + SSPs + US gave rise to an estimated 13-fold (CI from 3 to 69-fold) increase in tumour transgene expression as measured by IVIS imaging 11-days post-treatment. Treatment with ColoAd + SV + US also gave rise to an increase in transgene expression (approximately 11-fold, CI from 2 to 57-fold).

ANOVA of the fixed effects revealed significant main effects of US and Time, while post-hoc analysis at day 11 showed a significant difference ($p = 0.0423$) between tumours treated with ColoAdSALuc + SSPs + US and corresponding tumours treated with ColoAdSALuc + SSPs alone (as measured by IVIS).

The cavitation activity seen in mice treated with SSPs and the variable PRFP in this regime, was very consistent across mice, was similar in maximum magnitude to and sustained for significantly longer than cavitation from tumours of mice treated with SV. Quantification of viral transgene expression by IVIS indicated an increase in ColoAd delivery for 5 out of 8 mice treated with SSPs, though 3/8 mice had no IVIS signal detected above threshold in either tumour. The apparent dichotomy of this response was somewhat unexpected, given the consistent cavitation response across mice. However, in personal communication with Dr. Sam Illingworth, the lower amenability of DLD tumours to ColoAd infection was discussed. IHC analysis revealed low levels of hexon staining for ColoAd across the 16 tumours analysed (each section at 4 levels throughout tumour).

5.5 Summary and discussion

Although ColoAd can be delivered i.v., it still faces significant barriers at the level of uptake into and penetration throughout the tumour. Drug penetration (especially of large biological therapeutics) in solid tumours is limited [12], and though oncolytic viruses such as ColoAd can self-replicate and spread throughout a tumour, voids of infection within a tumour have been identified as barriers to successful oncolytic virotherapy [131]. Mathematical modelling of intratumoral virus spread suggests that altering the density or size of tumour cell regions initially infected with oncolytic virus can positively impact upon anti-tumour efficacy of virotherapy [248]. In Chapter 4, it was shown that US + CN can significantly increase the delivered dose of therapeutic antibodies and targeted nanoparticles. In the literature, US has been used in conjunction with microbubbles to enhance the delivery of an oncolytic

adenovirus [178, 134, 135], though the level of enhancement showed variability between mice. The combination of US + SSPs has been shown to enhance the delivery of an oncolytic vaccinia virus 6-fold more than US + SV [173], while in Chapter 4 of this thesis, it was shown that US + SSPs can enhance the delivery of a therapeutic antibody 1.85-fold more than US + SV. These results, in combination with the practical clinical limitations of administering micron-sized UCAs to generate sustained cavitation, suggest that these solid gas-entrapping nanoparticles could provide a substantial benefit to US-mediated delivery of adenoviruses.

In this chapter, delivery of ColoAd with US-mediated cavitation was initially investigated in an vitro tissue-mimicking model. A tissue-mimicking agarose gel was used in a novel phantom holder, which incorporated three independent flow channels and optically and acoustically transparent windows for ease of US treatment and subsequent imaging. SSPs were used to seed cavitation, and gave rise to inertial cavitation, as determined by passive detection of broadband acoustic emissions. Delivery of ColoAdRFP to cancer cells embedded in a gel within this holder was investigated at driving HIFU frequencies of 0.5 and 1.6 MHz. Results obtained with 0.5 MHz were confounded by non-realistic cracking of the agar gel at the HIFU focus, though this did result in increased delivery of ColoAdRFP at depths away from the channel walls. With 1.6 MHz, the maximum, mean, and median delivery distances of ColoAdRFP (from the channel) were significantly enhanced when US was applied, and very little extravasation was seen in the absence of cavitation (diffusion-only scenario). The enhanced delivery was uni-directional (in the direction of US propagation).

The in vitro results shown here confirm that SSPs can be used successfully to enhance delivery of ColoAd. Furthermore, successful imaging of RFP-producing cells 6-days post-treatment indirectly demonstrates that US-mediated cavitation (within the parameters tested here) can be safely applied to cells within a visco-elastic matrix without causing membrane rupture and cell death.

US-mediated delivery of ColoAd (expressing a luciferase transgene) with cavitation seeded by SSPs was then investigated in vivo in a murine bilateral tumour model. During US-treatment, cavitation was detected in real-time using two orthogonally mounted linear arrays, and was mapped using PAM (as described in Section 2.7.1). A maximum magnitude PAM signal was extracted at each time point during the treatment, and this PAM magnitude was used to characterize cavitation during treatment of mice receiving either SV, SSPs, or control 'inactive' SSPs (iSSPs).

In the first instance, US-mediated delivery of ColoAdCMVLuc was investigated using US at 0.5 MHz driving frequency and a constant PRFP of approximately 1.5 MPa over a treatment time of 10 minutes. ColoAdCMVLuc was chosen for this study as production of luciferase transgene is uncoupled from the virus life-cycle, and can occur rapidly after infection. This allowed for early analysis of any delivery-benefit of US, as early expression of luciferase transgene would be largely independent of the additional factor of virus replication, and thus more representative of pure delivery. Analysis of acoustic feedback data revealed substantial variability between mice receiving SSPs, and although cavitation with SSPs was significantly more sustained than with SV, the maximum PAM magnitude was significantly reduced ($p < 0.05$). Viral delivery was assessed using IVIS imaging of luciferase expression 2- and 6-days post-treatment, as well as by ex vivo quantification of luciferase and viral genome copies 6-days post-treatment. Statistical analysis of these data sets was performed using a linear mixed effects model, and while ANOVA of the fixed effects revealed a significant main effect of US, post-hoc testing of the EM means of the model found no significant comparisons. The fold-increases in tumour radiance (from IVIS imaging) between tumours treated with and without US were estimated at 6-days post-treatment, using the EM means of the fitted model, and 95% CI were determined by parametric bootstrapping. SSPs + US gave rise to a 5-fold (CI from 1- to 21-fold) increase in tumour radiance, while SV gave rise to an 8-fold (CI from

2- to 30-fold) increase in tumour radiance. Any effect of US alone (in the absence of CN) was controlled for by comparing the levels of tumour radiance from tumours treated with iSSPs + US to tumours treated with SSPs without US, as iSSPs are simply 'inactive' SSPs which do not entrap gas and thus cannot nucleate cavitation. ANOVA of the fixed effects within these two groups measured over time revealed no significant main effect of US alone, and post-hoc comparison was insignificant (this was confirmed with ex vivo luciferase and qPCR quantification).

US-mediated delivery of ColoAd was subsequently investigated using US again at 0.5 MHz driving frequency but with a variable PRFP between approximately 1.5 to 2 MPa over a treatment time of 5 minutes. As an improvement of delivery of ColoAdCMVLuc was seen with SSPs and SV in Regime 1, a more clinically-relevant virus was chosen for further investigation in Regime 2. Transgene expression from ColoAdSALuc is tied to viral replication (as transgene is under control of the major late promoter), and is thus as tumour selective as ColoAd itself [249]. Analysis of acoustic feedback data showed less variability between mice receiving SSPs with the varying PRFP than seen with the constant PRFP. Cavitation with SSPs was significantly more sustained than with SV, and the maximum PAM magnitude was not significantly different between the two CN ($p > 0.05$). Viral delivery was again assessed using IVIS imaging of luciferase expression (2, 4, 7, and 11 days post-treatment). Variability in luciferase expression between mice within the same group was very large, and the effect of US + SSPs appeared to be 'enabling': only 1 out of 8 tumours receiving SSPs but no US had a tumour radiance above background threshold. Statistical analysis of these data sets was again performed using a linear mixed effects model, and again ANOVA of the fitted model revealed a significant main effect of US. Post-hoc testing of the EM means of the model found a significant difference between tumours treated with SSPs + US and those treated with SSPs without US ($p < 0.05$). The fold-increases in tumour radiance (from IVIS imaging) between tumours treated with and without US were estimated at 11-days post-

treatment as above. SSPs + US gave rise to a 13-fold (CI from 3- to 69-fold) increase in tumour radiance, while SV gave rise to an 11-fold (CI from 2- to 57-fold) increase in tumour radiance. These results do not recapitulate those seen by Myers et al. whereby delivery of vaccinia virus was 6-fold greater with SSPs + US than with SV + US. Indeed, the effects of cavitation with SSPs or SV on ColoAd delivery more closely ressemble the trend seen with delivery of cetuximab-GNPs in the previous chapter (large variability, 'enabling' effect, small difference between SSPs and SV).

IHC analysis was performed on half of the tumours treated in Regime 2, and though the results of this highlighted the inter-tumour variabilty in viability and vascularization, few meaningful conclusions about US-mediated delivery could be drawn. IHC is, however, a limited technique for quantifying delivery, as it is practically impossible to sample all regions of the tumour, and it is possible that the sections chosen for analysis were simply not where infection foci are location. However, given that a relatively high number of tumours (n = 16) were analysed, and all tumours were sectioned at 4 levels 1 mm apart throughout the tumour, the results are expected to be relatively representative of the actual distribution of viral infection. The results of this analysis again underscore the scale of the delivery challenge.

The next chapter will examine a strategy to enhance the density of ColoAd, with the aim of improving its cavitation-mediated delivery, as past studies have shown that increased density can have a positive effect on cavitation-mediated transport [135, 193].

Chapter 6

Development and evaluation of a method for modifying the density of an oncolytic adenovirus

The work of Mo et al. showed that extensive surface modification of Ad5 with polymer-modified 5 nm gold nanoparticles (GNPs) could improve the pharmacokinetics and ultrasound-enhanced delivery of Ad5 into tumours by over 100-fold [135]. This suggested that increasing the density of a therapeutic agent may substantially increase the response of the agent to US-induced cavitation. Lea-Banks et al. showed through in silico modelling and in an in vitro agar-phantom model, that density plays a role in the US-mediated delivery of particles. This work confirmed that in the presence of US and microbubbles (the combination of which can give rise to microstreaming – one of the possible mechanisms in this transport strategy), denser particles travel farther into a viscoelastic matrix [193].

Although coating Ad5 with GNPs enhanced its ultrasound-mediated delivery of Ad5, a corresponding increase in tumour infection (and by consequence, therapeutic benefit) was not observed using this thorough and non-specific modification approach [135]. This is hypothesized to be due to a failure of the reduction-dependent de-stealthing mechanism required to reactivate the virus. The work in this chapter explores the possibility of using GNPs to achieve a similar density increase but by applying an alternative, more specific, means of modification of the viral capsid to maintain infectivity. Here a new strategy for surface modification of adenovirus is proposed and evaluated for enadenotucirev (ColoAd), a virus with superior circulation kinetics to Ad5, and demonstrated safety and virus delivery in the clinic [130, 250, 251]. Specifically, anti-adenovirus antibodies were investigated as possible linkers to attach dense GNPs to regions of the virus protein capsid not

involved in the main infection pathway. It was hypothesized that by using antibodies which bind specifically to the hexon protein region as linkers, the addition of GNPs to the virus surface would not significantly abrogate infectivity. The success of such an approach is dependent on GNP modification of the antibody not reducing its capacity to bind to its target hexon epitope. To mitigate against this possibility two alternative conjugation strategies were employed. First, a simple method of functionalizing GNPs with antibodies was examined, wherein the antibodies were conjugated to the GNP surface through their lysine residues in a one-step, but random and orientation-independent fashion. Subsequently, an alternative method was developed (based on the results presented in Chapter 3 for site-specific modification of cetuximab), whereby antibodies were site-specifically PEGylated prior to conjugation with GNPs. In the sections below, both methods are evaluated for the ability of their resulting antibody-GNP constructs to bind and modify the surface and density of ColoAd.

6.1 Proposed design

Figure 6.1 illustrates the proposed strategy for modifying the surface of an adenovirus in a specific fashion to increase its density without compromising infectivity. In this approach, spherical GNPs, surface-functionalized with N-hydroxysuccinimide (NHS) ester groups, are reacted with the solvent-exposed lysine residues of a monoclonal anti-adenovirus antibody. These antibody-GNP constructs are then combined with ColoAd, and attach specifically to regions of the virus capsid not involved in the main infection pathway: a specific region of the hexon coat protein.

Figure 6.2 illustrates the second proposed strategy for modifying the surface of an adenovirus with GNPs. In this approach, antibodies are first site-specifically PEGylated, with a heterobifunctional 3.4 kDa PEG linker capable of binding covalently to gold. Bare spherical GNPs are then reacted with the PEGylated anti-adenovirus antibody, and capped with a short (2 kDa) methoxy-terminated PEG.

These antibody-PEG-GNP constructs are then combined with ColoAd.

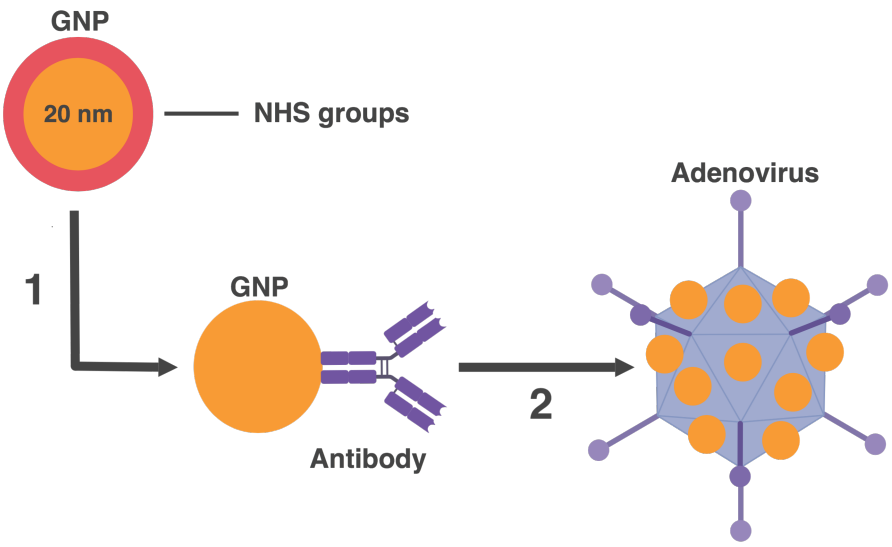

Figure 6.1: Schematic of proposed surface modification (1) of ColoAd with GNPs. 1) 20 nm diameter GNPs functionalized with NHS groups are combined with monoclonal anti-adenovirus antibodies to create an antibody-GNP construct. Non-reacted NHS groups are allowed to hydrolyze before further synthetic steps. 2) antibody-GNP constructs are combined with adenovirus in order to coat the surface of the virus at specific regions of the capsid not involved in cell-entry and infection. This contrasts with the random surface modification utilized by Mo. et al [135]

.

ColoAd is a group B chimeric adenovirus derived from Ad3 and Ad11p [129]. Its capsid is derived entirely from Ad11p – a serotype of adenovirus to which the general population has reduced levels of pre-existing immunity (as compared to other serotypes, such as Ad5) [130]. Thus, compared to Ad5 particularly, ColoAd has improved haemocompatibility, and has already been delivered intravenously to patients in Phase I trials [251, 250, 242]. In Chapter 5 it was shown that the delivery of ColoAd can be enhanced using US-mediated cavitation. Despite this enhancement however, a large area of opportunity for further improving delivery remains, the effect of US + CN on ColoAd delivery was variable between mice, and IHC analysis revealed that the majority of tumoural area remains unexposed

to virus 11-days post-treatment. It was thus hypothesized that the specific density modification strategy proposed in Section 6.1 could be used to alter the density of ColoAd, and thereby ultimately enhance its ultrasound-mediated delivery. Notably, the density modification would likely not need to provide any chemical stealthing of the virus, as ColoAd is not restricted by poor circulation kinetics and bloodstream compatibility to the same extent as Ad5 in humans [130, 242]. This strategy may be predicted to enhance the therapeutic efficacy of cancer therapy with ColoAd.

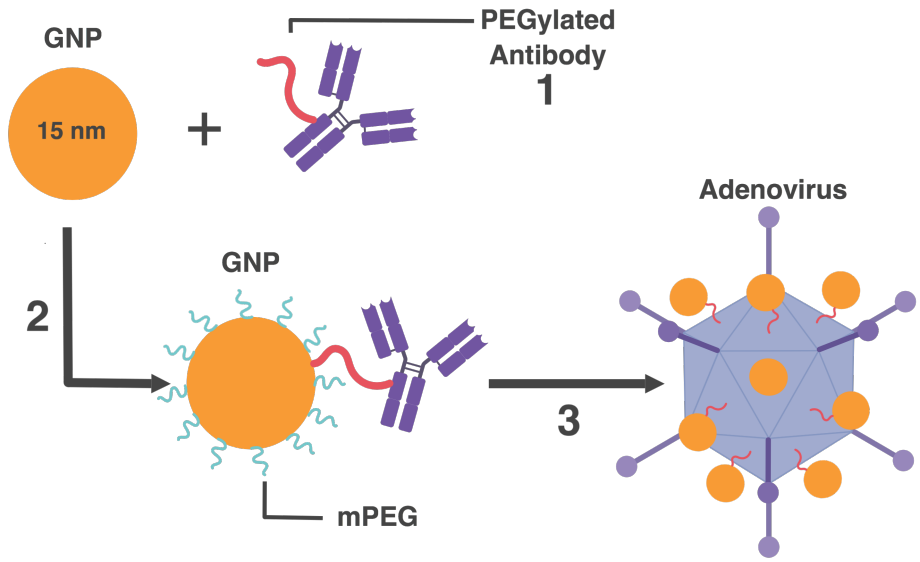

Figure 6.2: Schematic of proposed surface modification (2) of ColoAd with GNPs. 1) Anti-adenovirus antibodies are site-specifically PEGylated. 2) PEGylated antibodies are reacted with 15 nm diameter bare GNPs to create an antibody-PEG-GNP construct. 3) Antibody-PEG-GNP constructs are combined with adenovirus in order to coat the surface of the virus at specific regions of the capsid not involved in cell-entry and infection.

6.2 Characterization of anti-ColoAd antibodies

6.2.1 Specificity of anti-ColoAd antibodies

In the first instance, an antibody with non-neutralising specificity for hexon protein of ColoAd needed to be identified. The capsid of ColoAd is derived entirely

from Ad11p [130], which is a group B adenovirus. No commercially available anti-Ad11 antibodies were identified, so the selection criteria was broadened to antibodies raised against any group B adenoviruses. MAB8052 is a monoclonal antibody raised against hexon protein isolated from Ad3 (group B), and selected for reactivity against the hexon protein of all known adenovirus serotypes. Monoclonal antibody ab7428 was raised against whole Ad3 virion (according to the manufacturer, Abcam).

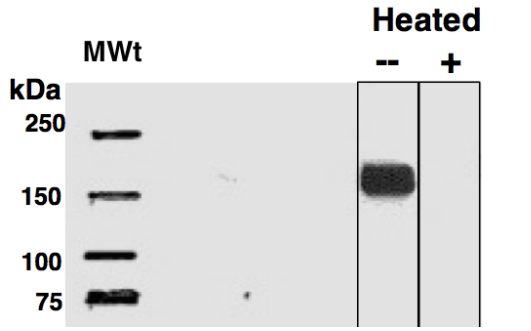

(a)

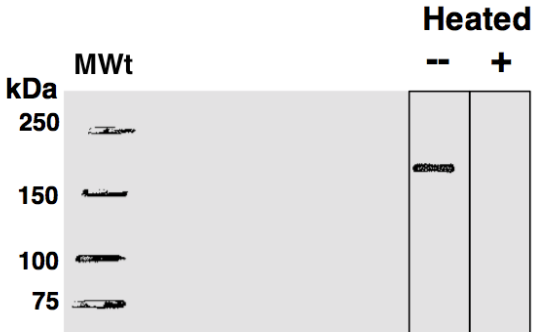

(b)

Figure 6.3: Western blot analysis of antibody binding to ColoAd. ColoAd samples (5 x 10^8 VPs) were separated by SDS-PAGE, transferred to a nitrocellulose membrane and probed with anti-Ad antibodies, either a) MAB8052 or b) ab7428. Membranes were washed and subsequently probed with anti-mouse IgG Horseradish Peroxidase-conjugated antibody (HRP-IgG). Binding of the HRP-IgG indicates presence of primary antibody. The MAB8052 and ab7428 antibodies did not bind to heat denatured samples of ColoAd (denoted with '+'), but did bind to the non-denatured, native hexon protein of the unheated samples (denoted with '–'). The leftmost lane denoted 'MWt' shows the protein standard ladder.

It was thus hypothesized that MAB8052 and ab7428 should have binding activity to the hexon protein of the ColoAd virus, but in order to confirm this, and to

confirm that the antibodies bind to intact native hexon (i.e. accessible external capsid regions), a western blot analysis of ColoAd was conducted with MAB8052 and ab7428 as the primary detection antibodies. Results in Fig. 6.3 show that both MAB8052 and ab7428 only bind to unheated samples of ColoAd. Specifically, Fig. 6.3 shows successful binding of both antibodies to unheated hexon trimers at approximately 190 kDa. Crucially, no interaction with heated, denatured virus proteins was observed, indicating that both the MAB8052 antibody and ab7428 antibody bind specifically to ColoAd hexon in its native form.

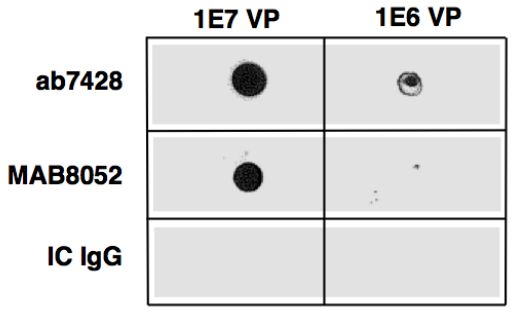

Figure 6.4: Dot Blot analysis of antibody binding to ColoAd. 1 x 10^7 and 1 x 10^6 ColoAd virus particles (VP) were spotted onto three separate nitrocellulose membranes and probed with either ab7428, MAB8052 or an isotype control mouse IgG (IC IgG). Membranes were washed and subsequently probed with anti-mouse IgG Horseradish Peroxidase-conjugated antibody (HRP-IgG). Binding of the HRP-IgG indicates presence of antibody.

In addition to determining the specificity of the two anti-virus antibodies, it was also necessary to confirm that the antibody chosen to act as a negative control did not have any affinity or specificity for the ColoAd virion. A dot blot was performed whereby ColoAd was spotted onto three separate nitrocellulose membranes at two different concentrations. The membranes were probed with ab7428, MAB8052, and the isotype control IgG (IC IgG). Fig. 6.4 shows that while both anti-virus antibodies bind to the spotted ColoAd (at the highest concentration tested: 1 x 10^7 VP per spot), the negative control antibody, IC IgG, does not bind to ColoAd. Fig. 6.4 also shows that while ab7428 still binds to ColoAd at the lower concentration tested (1 x 10^6 VP per spot), MAB8052 is no longer bound (to a detectable level). This could

indicate a higher affinity of ab7428 compared to MAB8052 for whole intact ColoAd virion.

6.2.2 Effect of anti-ColoAd antibodies on infectivity of ColoAdRFP

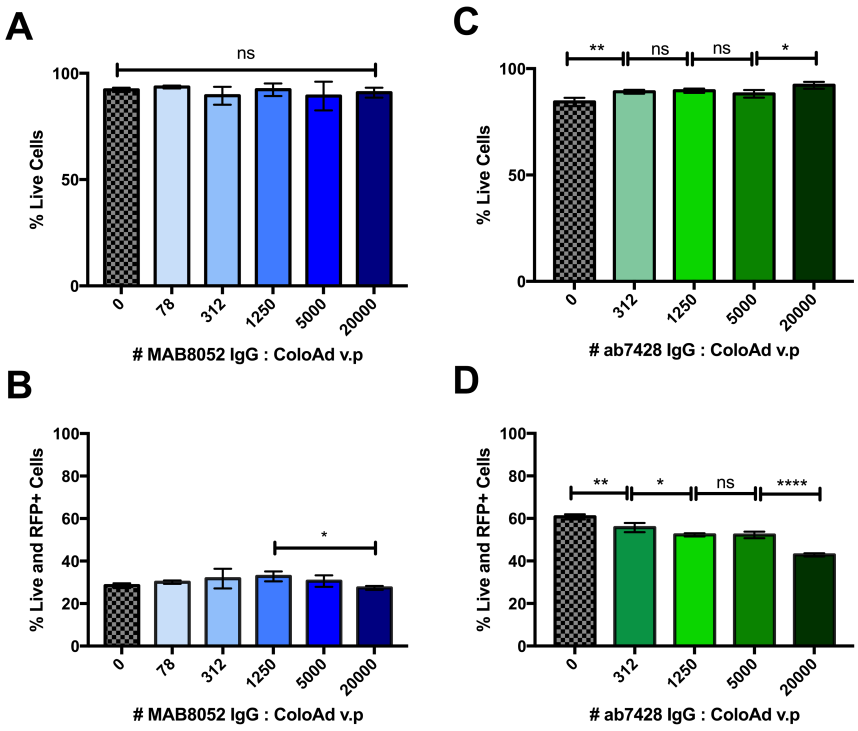

Figure 6.5: Impact of MAB8052 : ColoAd (Panels A and B) and ab7428 : ColoAd (Panels C and D) ratio on ability of ColoAdRFP to infect A549 cells. ColoAdRFP and either of the two antibodies were mixed for 1 hour prior to incubation with cells. RFP expression was measured 24 hours post-infection using flow cytometry with a BD FACSCalibur Flow Cytometer as described in Section 2.13.3. Untreated cells were used as negative controls to gate for cellular debris and RFP expression. Panels A and C present the percentage of gated single cells, while Panels B and D presents the RFP positivity for each antibody dilution. 10,000 cells were analysed for each sample. **A** and **B**: Mean of N=5 wells, error bars represent standard deviation (SD). No substantial difference in infectivity or cell viability was evident in any group, and ANOVA analysis with Tukey post-test revealed only one pairwise comparison with a significant difference (Panel B: 1250 MAB8052 vs 20000 MAB8052, $p < 0.05$). **C** and **D**: Mean of N=4 wells, error bars represent standard deviation (SD), ns = $P > 0.05$, * = $P < 0.05$, ** = P< 0.01, **** = P< 0.0001 as analysed using a one-way ANOVA with Tukey comparison of all columns. All p-values are corrected for multiple comparisons.

After determining that both ab7428 and MAB8052 bind with specificity to native hexon protein of ColoAd, and to whole ColoAd virion, their effect on infectivity needed to be elucidated. To this end, ColoAd virus was incubated with varying titres of ab7428 or MAB8052, ranging from approximately 0 to 20,000 IgG molecules per viral particle. ColoAd expressing a red fluorescent protein reporter gene (ColoAd-RFP) was used in these experiments to allow for quantification of infected cells. Flow cytometry was used to identify and count single and red-fluorescent cells. Untreated cells were used as a negative control in order to gate for single cells. Within the gated population of single cells, histogram gating was applied to control for any cellular autofluorescence present in the untreated control. For the MAB8052 study (Fig. 6.5 panels A and B), 5 separate samples from each treatment group were analysed, while for ab7428 study (Fig. 6.5 panels C and D) 4 separate samples were used. The results shown in Fig. 6.5 panel B demonstrate that even with high titres of MAB8052, neutralization of ColoAd infection was not evident, with no substantial differences in infectivity evident regardless of the concentration of antibody added. Though it remains possible that even higher titres of MAB8052 might have an effect on ColoAd infectivity (as measured by cellular transgene expression), the range investigated here completely encompasses the ratios of antibody to virus particle that would be used in order to attach antibody-functionalized GNPs to the virus capsid. In contrast, the results shown in Fig 6.5 panel D indicate that ab7428 has a small but significant effect on ColoAd infectivity. At the lowest ratio of ab7428 to ColoAd VP tested (312:1), pre-treatment with ab7428 resulted in a decrease in infectivity as of approximately 8%, while at the highest ratio tested (20000:1) ab7428 resulted in a decrease in infectivity of 29%. Clearly, ColoAd can be pre-treated with ab7428 at ratios at or below 312:1 IgG per VP without substantially abrogating its infectivity, potentially making this antibody a good candidate for use in this strategy. The difference in levels of infection reduction achieved using the two antibodies is in accordance with the differences in binding that were observed in Fig. 6.4, and may

relate to differences in the targeted capsid epitope.

6.2.3 Relative affinities of anti-ColoAd antibodies

Though the results of the anti-ColoAd antibody binding experiments conducted by dot blot analysis (Section 6.2.1) and in vitro infectivity experiments (Section 6.2.2) indicated that ab7428 has a higher affinity for ColoAd than MAB8052, this remained to be confirmed quantitatively. Enzyme-linked immunoassays (ELISAs) are a method whereby the interaction between an antibody and its antigen can be probed quantitatively. ELISA analysis can be used to determine the relative binding affinities of antibodies to their antigens, as measured by their relative dissociation constants, K_d, as was discussed in Section 3.3.2.

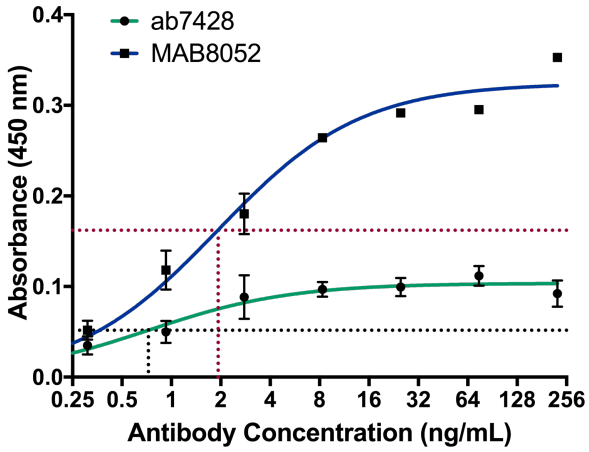

Figure 6.6: Indirect ELISA analysis of ab7428 or MAB8052 binding to immobilized ColoAd. ColoAd was coated onto a polystyrene Immunosorp-coated 96-well plate, which was blocked with 1% BSA prior to incubation with a range of concentrations of ab7428 (circular marker) and MAB8052 (square marker). See Section 2.13.4 for details of ELISA. Least-squares nonlinear regression in GraphPad PRISM was used to fit data sets, these fits are depicted by the green (ab7428) and blue (MAB8052) traces. Dashed lines show point of half-maximal saturation for MAB8052 (red line) and ab7428 (black line).

Fig. 6.6 shows the binding curves of MAB8052 and ab7428 to immobilized ColoAd. Absorbance at 450 nm is proportional to the amount of bound antibody (as detected by an HRP-conjugated anti-mouse secondary antibody), and thus K_d was determined empirically by fitting the data with a hyperbola of the form of Eq 3.3.

Table 6.1 shows that the K_d of ab7428 is approximately 2.6-fold lower than the K_d of MAB8052, suggesting a higher affinity of this antibody for ColoAd.

Antibody	**Relative K_d (ng/mL)**	**95% CI of K_d (ng/mL)**
ab7428	0.7259	0.3793 to 1.301
MAB8052	1.923	1.392 to 2.636

Table 6.1: Estimates of relative dissociation constants of ab7428 and MAB8052 from indirect ELISA

6.3 Functionalization and characterization of NHS-GNPs

Though both MAB8052 and ab7428 were shown to bind to hexon protein of ColoAd, and did not substantially reduce infectivity of ColoAd over a large range of antibody titres, ab7428 was chosen as the optimal antibody to link GNPs to hexon protein on ColoAd capsid. Firstly, the dot blot analysis in Section 6.2.1 indicated that ab7428 might have a higher affinity for intact ColoAd virion, as it was detected bound to ColoAd at lower concentrations of virus than MAB8052. Secondly, the infectivity assays presented in Section 6.2.2 showed that ab7428 did have a modest effect on the infectivity of ColoAd, while MAB8052 did not have any detectable effect. While this might simply be due to MAB8052 binding to the hexon-protein capsid in a configuration that does not impact regions involved in infectivity at all, it could also be due to a potential higher affinity of ab7428 for the ColoAd virion than MAB8052. Finally, ELISA determination of the relative K_d values of ab7428 and MAB8052 for ColoAd provided strong evidence for the hypothesis of ab7428 having a higher affinity for intact ColoAd than MAB8052.

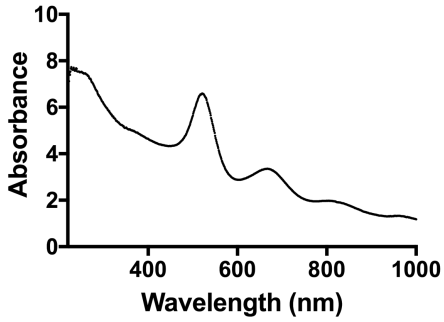

Figure 6.7: UV-Vis absorbance spectrum of NHS-coated GNPs functionalized with ab7428. Absorbance is measured in a UV-transparent microplate in a BMG Labtech plate reader, and corrected to a path-length of 1 cm, and is plotted as a function of wavelength.

Thus, GNPs were functionalized with ab7428 as described in Section 2.14. Additionally, a separate batch of GNPs were functionalized with the mouse IC IgG which – as it has no specificity for ColoAd as shown in Section 6.2.1 – should control for any linking of ab7428-GNPs to ColoAd due to non-specific interaction of the antibody-GNP with ColoAd. Antibody was added in molar excess to GNPs, to help drive the functionalization reaction, and to account for the multiple orientations with which the antibodies can bind to the GNP surface. Of note, the GNPs were originally purchased dry, and had to be resuspended in PBS prior to functionalization with antibody, however the GNPs were quite prone to aggregation and despite addition of DMSO (5%) and sonication, a sub-population of particles remained aggregated. This phenomenon is readily apparent in the UV-Vis absorbance spectrum of the particles, as shown in Fig. 6.7 (data shown for ab7428-GNPs, and the same trend was seen with IC IgG-GNPs). As discussed in Chapter 3, monodisperse GNPs of sizes 5-100 nm display one single absorbance peak at a wavelength corresponding to the surface plasmon resonance (SPR) band for that particuar size [226]. For 20 nm particles, the SPR band occurs at approximately 525 nm, and this peak is still visible in Fig. 6.7. There is also, however, a broad second peak appearing at approximately 670 nm (and possibly a third peak >800 nm); these peaks indicate aggregation of the gold nanoparticles [252]. Interestingly however, the degree of ag-

gregation appeared to remain constant over time, and so gentle centrifugation was used to remove large aggregates prior to further analysis (for example, with HPLC in Section 6.4.2).

6.3.1 Dot blot analysis of antibody-GNP loading

After the NHS-coated GNPs were reacted with ab7428 or IC IgG, the constructs were centrifuged and washed six times with a solution of 1% PBS and 0.1% Tween-20. Fig. 6.8 presents a dot blot of the functionalized and purified GNPs. Samples of both GNP constructs were taken throughout the purification process and spotted onto a nitrocellulose membrane. This membrane was subsequently probed with an anti-mouse HRP-conjugated antibody in order to detect any ab7428 or IC IgG. The spotted samples in the first column (left-most) are from the pre-washed constructs, and are clearly positive for ab7428 and IC IgG. The samples in the second column are taken from the supernatant of the constructs following the first centrifugation step. Again, these samples are clearly positive for ab7428 or IC IgG – this represents free excess antibody which did not bind to GNPs, and therefore was not pulled down in the centrifugation step. The samples in the third column are taken from the supernatant of the construct following the sixth and final wash and centrifugation, and are negative for ab7428 or IC IgG. This indicates that there was no detectable free antibody in the final supernatant, and validates the success of the washing procedure. Finally, the samples in the fourth column are taken from the final resuspended pellet containing GNPs, and indicate that the purified GNPs have been bound to ab7428 or IC IgG. Thus the final GNP constructs are functionalized with ab7428 or a control IC IgG, and are free of residual antibody in solution.

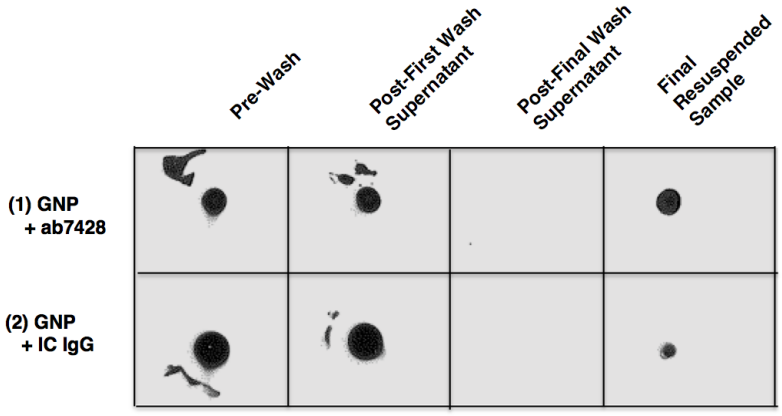

Figure 6.8: Dot blot analysis of antibody-functionalized GNPs. Samples were taken from ab7428-GNP or IC IgG-GNP formulations 1) before purification steps, 2) from sample supernatant after first centrifugation, 3) from sample supernatant after final centrifugation, and 4) from final product resuspended in DPBS. GNP samples were spotted onto a nitrocellulose membrane and probed with an anti-mouse IgG HRP-conjugated antibody. Binding of the HRP-IgG indicates presence of antibody. Absence of binding of HRP-IgG in the post-final wash supernatant indicates that there was no detectable free antibody in solution, while positive binding in the final resuspended sample indicates successful functionalization of GNPs with ab7428 or IC IgG.

6.4 Characterization of GNP + ColoAd constructs

6.4.1 Density analysis of GNP + ColoAd constructs: CsCl gradient

A common method for small-scale purification of adenovirus is CsCl banding; a method which allows for separation of particles of different density by ultracentrifugation through a CsCl density gradient. Adenovirus particles can be spun into a tight band between two CsCl layers of different density , and can thus be extracted from cellular debris and other detritus with differing density. This method was used by both Mo et al., and Saini et al. to demonstrate the density increase of gold-coated adenoviruses [135, 253]. Though it has already been shown here that ab7428 binds to ColoAd VPs, these experiments were all performed in either DPBS (with and without 10% skim milk as blocking buffer) or growth media (DMEM + 10% FBS). Prior to attempting to determine the density of ab7428-GNP + ColoAd constructs

using CsCl banding, any effect of the components of the CsCl gradient on ab7428 binding to ColoAd needed to be elucidated.

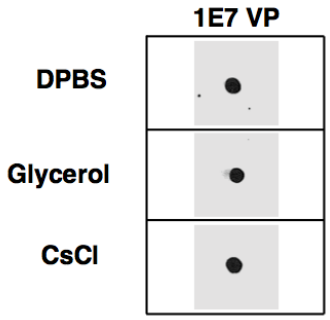

Figure 6.9: Dot blot analysis of ab7428 binding to ColoAd in the presence of DPBS, CsCl, or glycerol. 1 x 10^7 ColoAd VPs were spotted onto three separate nitrocellulose membranes and probed with ab7428 at a concentration of 1 μg/mL in 10% blocking buffer and either 1.47 g/cm^3 CsCl solution, 40% glycerol, or DPBS for 1 hour. Membranes were washed and subsequently probed with anti-mouse IgG HRP-conjugated antibody. Binding of the HRP-IgG indicates presence of antibody.

Fig. 6.9 shows a dot blot analysis of ab7428 binding to ColoAd VPs spotted onto a nitrocellulose membrane, in the presence of either DPBS, 40% glycerol, or 1.47ρ CsCl solution (i.e. the three components used in the CsCl gradient as described in Section 2.15.2). The presence of glycerol, or high CsCl salt concentrations, does not abrogate binding of the ab7428 antibody to ColoAd in this assay. These results suggest that CsCl banding could be an appropriate method to determine whether or not GNPs functionalized with ab7428 can bind to and increase the density of ColoAd, and to purify non-modified ColoAd capsids away from GNP-modified ColoAd capsids.

After determining that the ab7428 antibody can bind to hexon protein on the ColoAd capsid (even in the presence of glycerol and CsCl), and successfully functionalizing GNPs with ab7428, the ab7428-GNP constructs (and control IC IgG-GNP constructs) were combined with ColoAd virus at a ratio of approximately 100 GNPs per VP. These formulations were mixed for 1 hour at 37 °C. The GNP + ColoAd formulations were then spun through a gradient of CsCl in order to determine their

density, and separate modified ColoAd VPs from unmodified VPs. The gradient was made with two layers of different density CsCl: 1.32 g/cm^3 and 1.47 g/cm^3. Naked adenovirus has a density of approximately 1.37 g/cm^3, and will form a tight band between the two CsCl layers when spun at high rcf through this CsCl gradient. Addition of any GNP to the surface of the ColoAd would change the density of the virus, causing it to travel further through the CsCl gradient. Given the high density of the 20 nm GNPs (calculated to be approximately 18.4 g/cm^3), the addition of just one GNP would increase the density of the GNP-ColoAd construct to approximately 1.76 g/cm^3 – denser than the densest layer of the CsCl gradient. Thus, if any of the ab7428-GNPs were to successfully bind ColoAd, if spun for adequate time these GNP-ColoAd constructs should pellet out at the bottom of the centrifuge tube. Quantitative polymerase chain reaction (qPCR) can be used to determine the number of virus copies in a sample, and so by sampling the CsCl gradient at different heights after ultracentrifugation, it can be determined whether or not any GNPs have successfully increased the density of ColoAd VPs. Moreover, by performing the same analysis on ColoAd + IC IgG constructs, any non-specific interaction of the GNPs and ColoAd can be accounted for.

The photos shown in Fig. 6.10 indicate no change in the density of ColoAd pre-incubated with either ab7428-GNPs or the control IC IgG-GNPs – a single sharp white band is seen in either case, where naked virus has banded out at a density between the two CsCl layers. Moreover, GNPs (which are a deep burgundy colour) can be seen in both cases at the bottom of the centrifuge tubes. The virus bands were aspirated from the gradient with a wide bore needle and collected. A separate needle was then used to carefully remove the GNPs from the bottom of the centrifuge tubes. The samples were then digested, and any viral DNA was extracted using the GenElute Mammalian Genomic DNA Miniprep Kit Protocol from Sigma-Aldrich.

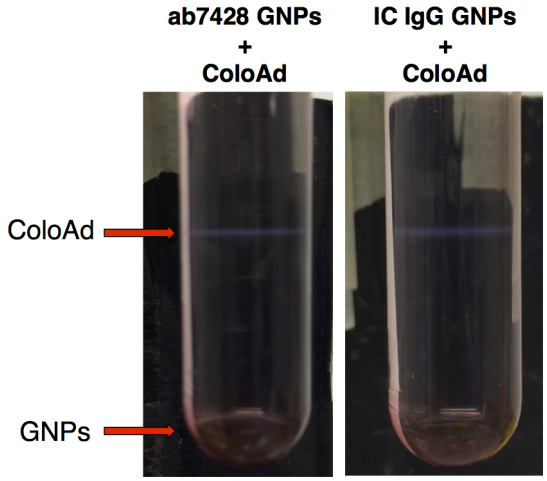

Figure 6.10: CsCl density gradient ultracentrifugation of antibody-functionalized GNPs and ColoAd virus. Gradients were made of 40% glycerol, 1.32 g/cm^3 CsCl,and 1.47 g/cm^3 CsCl as described in Section 2.15.2. Centrifuge tubes containing the gradients overlaid with samples of ab7428-GNP + ColoAd (left) or IC IgG-GNP + ColoAd (right) were spun at 25000 rpm for 1 hour. The photos in this figure show the centrifuge tubes immediately following centrifugation. The demarcated white bands are virus banding at a density between 1.32 g/cm^3 and 1.47 g/cm^3, while the GNPs can be seen at the bottom of each tube.

A qPCR analysis of the eluted DNA (as compared to standards prepared from known concentrations of ColoAd and extracted following the same protocol as the samples) was run and the results are presented in Table 6.2. Approximately 90% of ColoAd VPs that were added to the two centrifuge tubes were recovered in the two samples taken from each tube. Unsurprisingly, the vast majority (96%) of the recovered VPs were found in the samples taken from the virus band, while less than 4% of the VPs ended up in the pellet along with the GNPs. Moreover, given that 4% of VPs were found in the pellet from the tube containing ab7428-GNPs *and* the control IC IgG-GNPs, even this small amount of higher density ColoAd cannot be attributed to any specific binding of GNPs to the ColoAd capsid via the ab7428 antibody.

GNP Functionalization	% of VPs Recovered	% of Recovered VPs in Pellet	% of Recovered VPs in Band
ab7428	$91 \pm 3\%$	$3.7 \pm 0.2\%$	$96 \pm 4\%$
IC IgG	$90 \pm 3\%$	$3.7 \pm 0.2\%$	$96 \pm 5\%$

Table 6.2: Copies of ColoAd DNA found in either the band or pellet of ultracentrifuged CsCl gradients and quantified by qPCR. The first column of this table indicates the functionalization of the GNPs that were combined with ColoAd and added to each gradient. The second column shows the VP DNA copies that were recovered from the centrifuge tube, calculated as a percentage of the number of copies added to the centrifuge tube originally. The third and fourth column shows the percentage of the recovered VP copies that were found in the GNP pellet or in the virus band, respectively. All samples and standards were digested and processed using GenElute Mammalian Genomic DNA Miniprep Kit Protocol from Sigma-Aldrich as described in Section 2.15.2. qPCR was run on an Applied Biosystems StepOnePlus^{TM} Real-Time PCR System.

Though ab7428 was shown to be capable of binding to ColoAd in the presence of CsCl and glycerol by dot blot, a more quantitative approach was needed to rule out an effect of CsCl or glycerol on the affinity of ab7428-GNPs for ColoAd. High concentration ionic solutions can be used to dissociate antibody from its antigen, as the binding domain of antibodies often attach to their antigen using electrostatic interactions which can be effectively disrupted in solutions of high ionic strength (due to charge shielding) [254] [255]. Though the dot blot analysis showed that the ab7428 *can* bind to ColoAd in CsCl and glycerol, this kind of analysis does not reveal anything about potential changes in the affinity of this interaction.

Fig. 6.11 shows the binding curves of ab7428 to immobilized ColoAd in 1.47ρ CsCl, 40% glycerol, or PBS. It is evident from the curves that both glycerol and CsCl have a significant impact on the binding of ab7428 to ColoAd. In the presence of 40% glycerol, saturation of binding is still observed and a relative K_d can be determined (Table 6.3); this relative K_d value indicates an affinity of interaction approximately 6-fold lower than in PBS (note that all incubations with HRP-conjugated secondary antibody were performed in PBS with 1% BSA following washing to remove glycerol or CsCl).

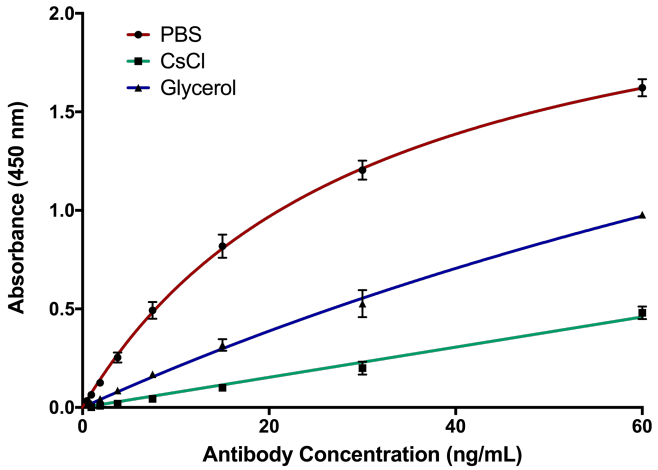

Figure 6.11: Indirect ELISA analysis of ab7428 binding to immobilized ColoAd in PBS, CsCl, or glycerol. ColoAd was coated onto a polystyrene Immunosorp-coated 96-well plate, which was blocked with 1% BSA prior to incubation with a range of concentrations of ab7428 diluted in either PBS (circular markers), CsCl (square markers), or glycerol (triangular markers). Antibody bound to ColoAd was detected with an HRP-conjugated anti-mouse secondary antibody. After addition of TMB-substrate and sulfuric acid as a stop solution, absorbance was measured at 450 nm and related to total antibody concentration. Least-squares nonlinear regression in GraphPad PRISM was used to fit data sets, these fits are depicted by the coloured traces (red, green, and blue for PBS, CsCl, and glycerol respectively).

Solvent	**Relative K_d (ng/mL)**	**95% CI of K_d (ng/mL)**
PBS	30.45	27.01 to 34.44
Glycerol	182.9	122.9 to 321.8
CsCl	–	–

Table 6.3: Estimation of relative dissociation constants of ab7428 incubated with ColoAd in PBS, 40% glycerol, or 1.47ρ CsCl from indirect ELISA

In the presence of 1.47ρ CsCl, an approximately linear relationship between absorbance at 450 nm (proportional to the amount of bound antibody) and total antibody concentration is observed. This indicates that while there is some positive antibody-antigen interaction (as observed in the dot blot analysis), the affinity of this interaction is greatly reduced to the point where the data is described only ambiguously with Eq. 3.3, and it is thus not appropriate/informative to use a K_d

value to describe this interaction.

6.4.2 Chromatographic analysis of ColoAd + GNPs

Given the clear impact of glycerol and CsCl on ab7428 binding to ColoAd determined by indirect ELISA (Fig. 6.11), the results of the CsCl density gradient analysis of ColoAd + GNPs in Section 6.4.1 (which showed no meaningful alteration to the density of ColoAd after incubation with ab7428-GNPs) are perhaps not representative of the state of ColoAd + ab7428-GNPs when in a solution of comparatively lower ionic strength, such as PBS or plasma. Thus, an alternative assay to assess the success (or failure) of ab7428-GNPs binding to ColoAd was required.

Anion-exchange high-performance liquid chromatography (HPLC) is a method used for purification, quantification, and characterization of adenoviruses [256]. This method relies upon interaction of negatively-charged residues of the viral capsid with positively charged groups in the stationary phase of the column. As a gradient of increasing salt concentration is applied to the column, the increasing ionic strength gradually weakens electrostatic interactions, and the virus particles are eluted. This method can be used to distinguish between adenoviruses of different serotypes, as shown in Fig. 6.12. Blanche et al. described a correlation between retention time and the degree of negative charge of the hexon protein (adenoviruses with more negative hexon proteins were retained longer). The authors hypothesized that the hexon protein is largely responsible for interaction of virus capsid with column, as it is highly negatively charged and is abundant in the viral capsid [256]. Given that the hexon protein likely plays an integral role in the interaction of adenovirus with an anion-exchange column, if the negative charge of hexon is masked or altered by modification with GNPs, a change in virus retention time is likely to result. Thus, anion-exchange HPLC can be used to detect successful surface modification of ColoAd with GNPs. Moreover, if modification with GNPs alters viral retention time sufficiently such that modified ColoAd can be resolved from naked ColoAd, HPLC

can be used for purification of a gold-modified construct away from unmodified virus – an important step if the in vitro and in vivo infectivity and efficacy of a gold-modified construct are to be assessed.

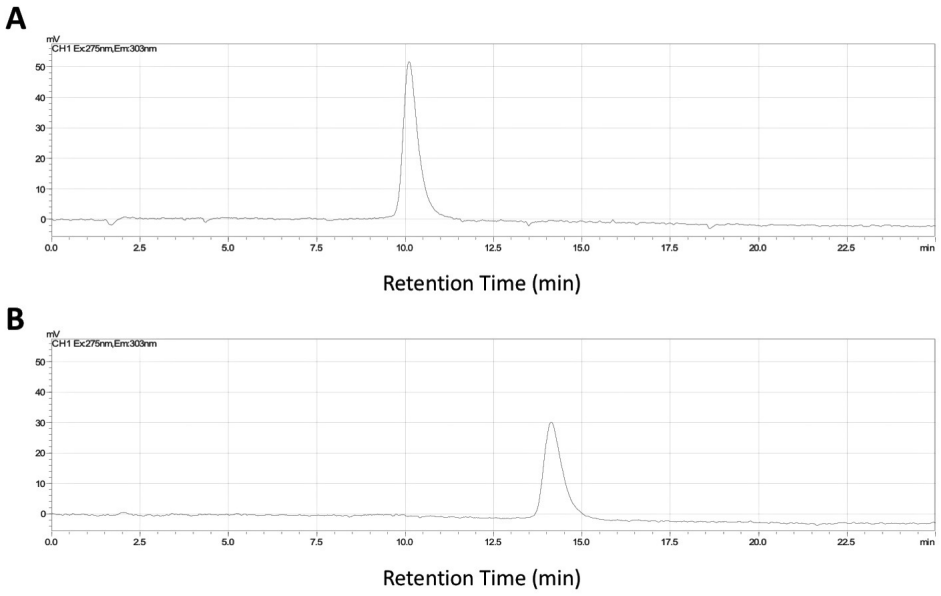

Figure 6.12: HPLC analysis of ColoAd (panel A) and Ad5 (panel B). VPs of ColoAd and Ad5 were loaded on to a RESOURCE Q anion exchange chromatography column packed with SOURCE 15Q (anion exchanger) and were eluted with a linear gradient of sodium chloride buffered with HEPES at pH 7.4 (gradient details in Section 2.15.4). ColoAd VPs were eluted at approximately 10 minutes (panel A), while Ad5 particles were more strongly retained and are eluted at approximately 14 minutes. Peaks were detected using a fluorescence detector with Ex/Em wavelengths of 275/303 nm. Arbitrary units (mAU) of fluorescence are shown on y-axis.

Though anion-exchange HPLC can be used as a method to detect modification of ColoAd with GNPs attached via covalent NHS-chemistry (as shown in Fig. 6.13), detection of successful modification of ColoAd with ab7428-GNPs could be susceptible to the confounding effect of the ionic strength of the mobile phase used to elute ColoAd on antibody-antigen interactions (as observed with CsCl analysis in Section 6.4.1). Thus, as in Section 6.4.1, an indirect ELISA was performed to assess the affinity of the interaction between ab7428 and immobilized ColoAd in the presence of either PBS or HPLC mobile phase.

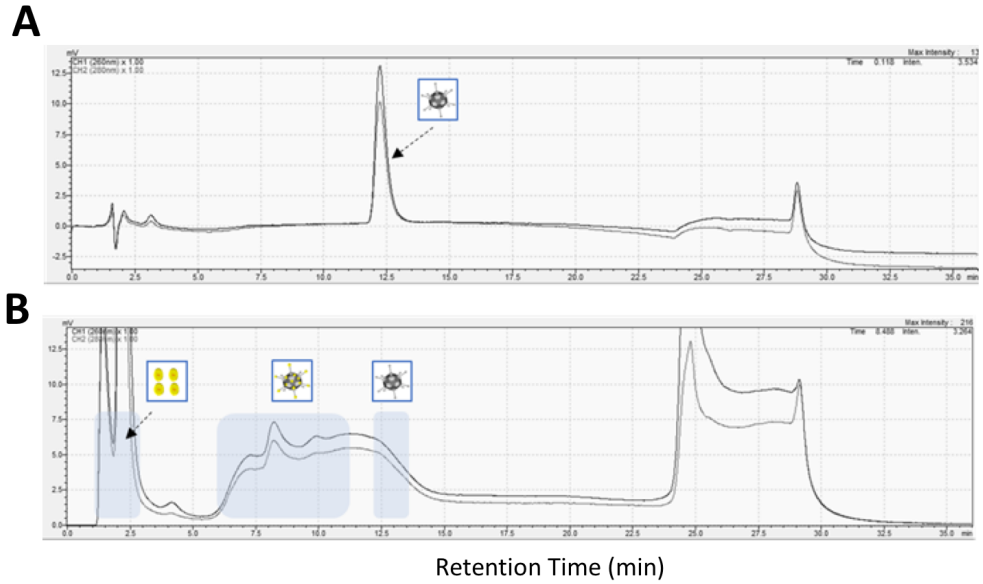

Figure 6.13: HPLC analysis of ColoA (panel A) and ColoAd + GNP (panel B). VPs of ColoAd and ColoAd covalently linked via NHS-chemistry to GNPs were loaded on to a RESOURCE Q anion exchange chromatography column packed with SOURCE 15Q (anion exchanger) and were eluted with a linear gradient of sodium chloride buffered with HEPES at pH 7.4 (note gradient used here differs from that used in other analyses here and described in Section 2.15.4). Naked ColoAd (A) is eluted at approximately 12 minutes, while ColoAd modified with GNPs eluted over a large range of retention times. Peaks are detected using a fluorescence detector with Ex/Em wavelengths of 275/303 nm. Arbitrary units (mAU) of fluorescence are shown on y-axis, and retention time (min) is shown on x-axis. Image was provided by Dr. Brian Lyons.

From Fig. 6.12, it was determined that ColoAd elutes at a mobile phase composition of slightly less than 10% Mobile Phase B (see Section 2.15.4 for gradient details), thus binding of ab7428 diluted in 10% Mobile Phase B (in 90% Mobile Phase A) was investigated and compared to PBS. The composition of mobile phase at 10% Mobile Phase B contains a concentration of approximately 420 mM NaCl: a 3-fold greater concentration than is present in PBS. The results presented in Fig. 6.14 suggest that the interaction between ab7428 and immobilized ColoAd is indeed affected by the higher salt content of the HPLC mobile phase (compared to PBS). As shown in Table 6.4, the relative K_d value of this interaction in HPLC mobile phase is approximately 2.8-fold higher than that determined in PBS alone. Though this result indicates that ab7428-GNPs will likely have a lower affinity for ColoAd in the HPLC

mobile phase gradient than in PBS, the saturatable behaviour of antibody in this medium (as compared to the behaviour of ab7428 in CsCl as shown in Fig 6.11) and relative K_d value suggest that at sufficiently high antibody:antigen ratios, ab7428-GNPs could still bind to ColoAd despite the ionic strength of the media. Moreover, while (relative) measurements of K_d are helpful when discussing affinity of interactions, this parameter refers only to the thermodynamics of the interaction (i.e. the state of the system at equilibrium), and gives no information about reaction kinetics. If the ab7428-GNPs are allowed to react with and bind to ColoAd in PBS, and the dissociation kinetics of ab7428 from ColoAd are sufficiently slow, its conceivable that GNP-modification of ColoAd could still be readily discerned by anion-exchange HPLC with a a salt gradient, despite the disruptive effect of high salt concentrations of antibody-antigen equilibria.

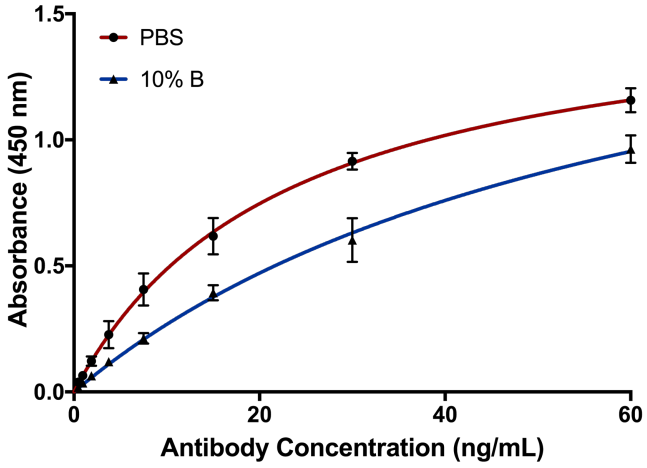

Figure 6.14: Indirect ELISA analysis of ab7428 binding to immobilized ColoAd in of PBS, or HPLC mobile phase. ColoAd was coated onto a polystyrene Immunosorp-coated 96-well plate, which was blocked with 1% BSA prior to incubation with a range of concentrations of ab7428 diluted in either PBS (square markers), or 10% Mobile Phase B in 90% Mobile Phase A (triangular markers). Antibody bound to ColoAd was detected with an HRP-conjugated anti-mouse secondary antibody. After addition of TMB-substrate and sulfuric acid as a stop solution, absorbance was measured at 450 nm and related to total antibody concentration. Least-squares nonlinear regression in GraphPad PRISM was used to fit data sets, these fits are depicted by the coloured traces (red, or blue for PBS, and 10% Mobile Phase B respectively).

Solvent	Relative K_d (ng/mL)	95% CI of K_d (ng/mL)
PBS	22.77	19.21 to 27.14
10% Mobile Phase B	62.97	47.25 to 87.64

Table 6.4: Estimation of relative dissociation constants of ab7428 incubated with ColoAd in PBS, or 10% Mobile Phase B from indirect ELISA

Fig. 6.15 depicts the chromatograms obtained when ColoAd (alone or pre-incubated with GNPs) is loaded onto an anion-exchange column and eluted with an increasing salt gradient. When substances pass through the column they are detected with both a diode array detector (which measures UV absorbance), and a fluorescence detector (of excitation/emission wavelengths of 275/303 nm). Fig. 6.15 shows the chromatograms recorded by the fluorescence detector, as fluorescence is more sensitive than UV absorbance for detecting proteins (due to fluorescence of aromatic amino acid residues). Fig. 6.16 shows the UV-Vis absorbance spectrum of the peaks detected and shown in Fig. 6.15, which can be used to distinguish peaks due to protein or GNPs, as GNPs of 20 nm absorb strongly at a wavelength of approximately 525 nm, while protein does not have a strong absorbance at this wavelength. As shown in Fig. 6.15 panel A, ColoAd alone elutes as a single peak with a retention time of 10.105 minutes. GNPs (non-functionalized) are not well retained and elute largely with the solvent front (two broad peaks spread between approximately 1.2 and 5 minutes, Fig. 6.15 panel B). Additionally however, a small but extremely broad signal is apparent in panel B between 9 and 16 minutes, indicating some interaction between the GNPs and the column. In panel C, the chromatogram of a sample of ColoAd pre-incubated for 1 hour at 37 °C with blank GNPs shows GNPs eluting with the solvent front, while a clear peak of ColoAd eluting at a retention time of 10.001 minutes is also seen. Although there is a slight decrease in retention time compared to ColoAd alone (10.001 versus 10.105 min), this is likely due to superposition of the broad GNP signal between minutes 9-16 seen in panel B with

the ColoAd signal seen in panel A. Additionally, the UV-VIS absorbance spectrum of the ColoAd + blank GNPs sample at the ColoAd peak (RT = 10.001, Fig. 6.16 panel C1) does not show a peak at 525 nm.

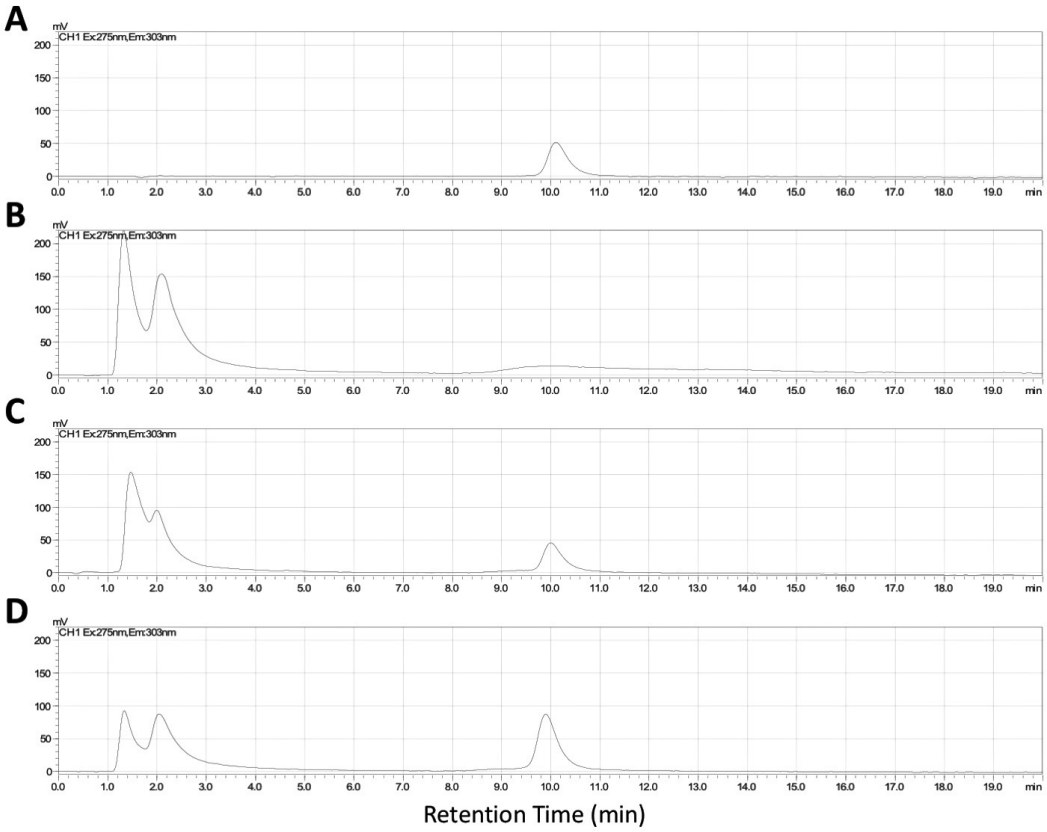

Figure 6.15: HPLC analysis of ColoAd and GNPs. VPs of ColoAd were pre-incubated for 1 hour with a 100-fold excess of with blank GNPs or GNPs functionalized with ab7428 before before chromatographic analysis as in Section 2.15.4. The chromatograms of the following samples are presented here: A) ColoAd alone, B) blank (non-functionalized) GNPs, C) ColoAd pre-incubated with blank GNPs, D) ColoAd pre-incubated with ab7428-GNPs. Peaks are detected using a fluorescence detector with Ex/Em wavelengths of 275/303 nm, arbitrary units (mAU) of fluorescence are shown on y-axis.

Thus, a non-specific interaction of blank GNPs with ColoAd is not detected with this method of anion-exchange HPLC. In panel D however, the chromatogram of ColoAd pre-incubated with ab7428-GNPs for 1 hour at 37 °C also does not show a large shift in the retention time (9.891 versus 10.105 min) or change in the UV-Vis

absorbance profile of the ColoAd peak (Fig 6.16 panel D1), certainly not to the extent evident with the covalent modification of ColoAd with NHS-GNPs (Fig. 6.13). As the chromatogram of ColoAd + ab7428-GNPs (Fig. 6.15 panel D) does not differ appreciably from that of ColoAd + blank GNPs (panel C), it must therefore be concluded that either this detection method is not sensitive enough to detect the modification of ColoAd by specific attachment of a low number of GNPs (particularly in the presence of a higher ionic strength salt solution that could be negatively impacting GNP attachment), or that the modification strategy was unsuccessful. The limitations of the detection method are difficult to address, but given the success of HPLC in separating adenoviruses with different serotypes (Fig. 6.12) and adenovirus covalently modified with GNPs from naked virus (Fig. 6.13) it seems improbable that a successful modification of ColoAd with enough GNPs to significantly alter its density such that it would benefit from enhanced ultrasound-mediated transport would remain undetected by this chromatographic analysis.

This first modification strategy reported here relies on orientation-independent addition of antibodies (via the reaction between lysine residues on the antibody molecule and NHS esters on the GNP surface). This has advantages in terms of ease of formulation and seems to have provided an effective strategy for achieving Ab-GNP conjugation. However, it also has the potential limitation that many of the conjugated antibodies will be oriented in a direction such that their antigen binding Fab regions are not accessible, resulting in antibody-GNP constructs which are functionally useless. This would thus result in a low yield of functional antibody-GNP constructs, which might explain why the ab7428-GNP constructs were seemingly unable to successfully attach to and alter the density (or surface charge) of ColoAd VPs.

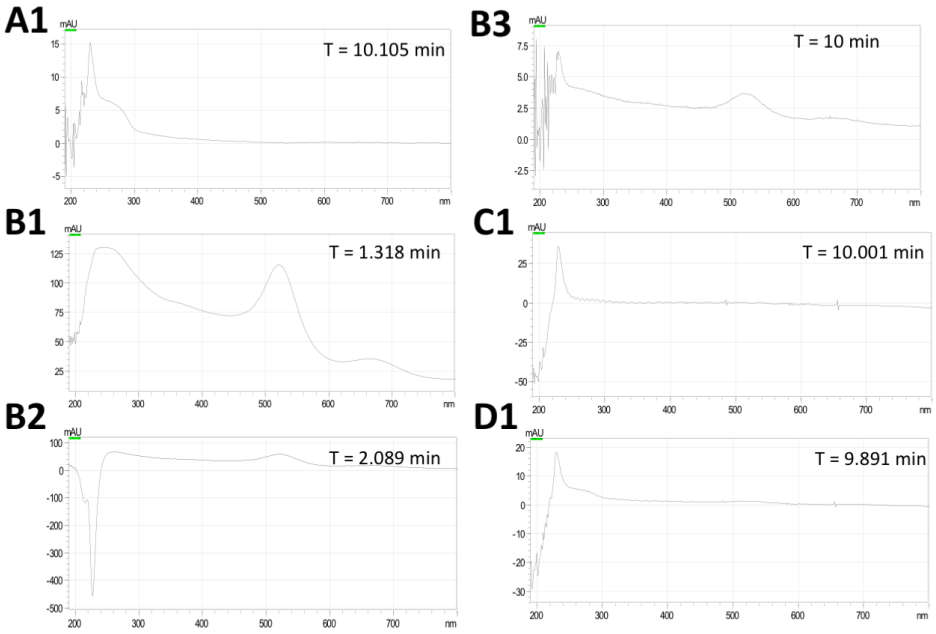

Figure 6.16: UV-Vis spectrum of peaks of ColoAd and GNPs separated by anion-exchange HPLC. VPs of ColoAd were pre-incubated for 1 hour with a 100-fold excess of blank GNPs or GNPs functionalized with ab7428 before chromatographic analysis as in Section 2.15.4. The resulting chromatograms are shown in Fig. 6.15, and the UV-Vis absorbance spectrums of peaks at different retention times (RT) taken from these chromatograms are presented here: A1) ColoAd alone (RT = 10.105 min), B1) blank GNPs (RT = 1.318 min), B2) blank GNPs (RT = 2.089 min), B3) blank GNPs (RT = 10 min), C1) ColoAd pre-incubated with blank GNPs (RT = 10.001 min), D1) ColoAd pre-incubated with ab7428-GNPs (RT = 9.891 min), arbitrary units (mAU) of absorbance are are shown on y-axis.

An additional potential limitation is that steric hindrance could be preventing the antibody-GNP constructs from attaching to the VP surface. Adenoviruses are icosahedron-shaped, with a distance of approximately 40 nm between vertices (where the fibres are located), and a face area on the order of 800 nm^2 (this is calculated using the density and MW of adenoviruses to obtain the volume of their icosahedron shape). So while the 20-nm diameter GNPs should theoretically fit well onto the faces of the icosahedron, it is possible that the larger hydrodynamic diameter of the GNPs, compounded with any steric effects due to the fibre shaft and knob, could

prevent the GNP from getting close enough to the hexon protein to allow antibody binding. The second (orientation-dependent) modification strategy addresses both these potentially limiting factors, by efficiently functionalizing smaller GNPs (15 nm) with anti-ColoAd antibody in a direction-controlled fashion, with the use of a 3.4 kDa heterobifunctional polyethylene glycol (PEG) spacer.

6.5 Functionalization of GNPs with site-specifically PEGylated anti-ColoAd antibody

Figure 3.1 illustrates the second strategy for modifying the surface of an adenovirus in a specific fashion with GNPs. In this approach, N-linked glycan moieties within conserved glycosylation sites on Fc regions of the anti-ColoAd antibodies were first oxidized to create aldehyde groups within conserved glycosylation sites on Fc regions. The oxidized antibodies were then reacted with a hydrazide on a heterobifunctional PEG linker (3.4 kDa) to form a hydrazone bond. These PEGylated antibodies were then reacted with citrate-stabilized unmodified spherical gold nanoparticles (GNP); a lipoic acid group on the unattached end of the PEG linker was chosen to react with the surface of the gold particles to form a stable covalent bond. The particles were then capped with a shorter methoxy-terminated PEG-thiol (2 kDa) to stabilize them in solution. These antibody-GNP constructs were then combined with ColoAd, in order to achieve specific attachment to the hexon coat protein (Fig. 6.2).

6.5.1 PEGylation of anti-ColoAd antibodies

As discussed in Section 3.3, the degree of antibody oxidation can be modulated by adjustment of pH, temperature, and concentration of oxidant (sodium metaperiodate $NaIO_4$). As in Chapter 3, oxidation of ab7428 was carried out at at pH 5.6, in order to maximize potential for successful PEGylation. The reaction conditions used here replicated those used by Wolfe et al.; oxidation was carried out in 20 mM

acetate buffer, supplemented with 0.15 M NaCl and pH adjusted to 5.6 [211].

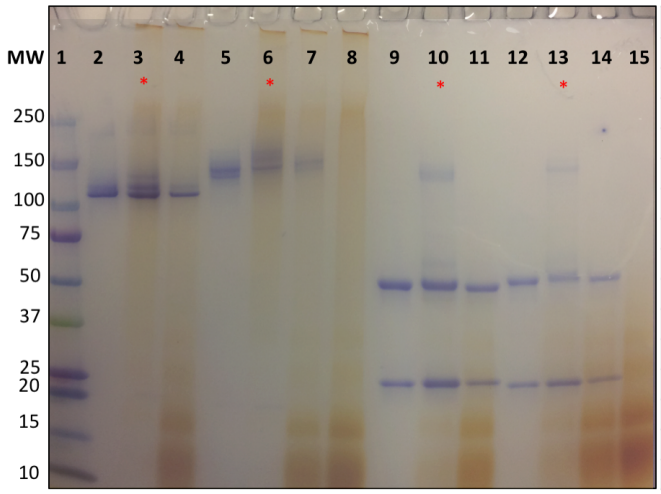

Lane #	Sample Identity
1	Molecular weight marker
2	Non-oxidized IC IgG
3	PEGylated IC IgG
4	Non-oxidized IC IgG + LA-PEG-Hyd
5	Non-oxidized ab7428
6	PEGylated ab7428
7	Non-oxidized ab7428 + LA-PEG-Hyd
8	LA-PEG-Hyd
9	Non-oxidized IC IgG
10	PEGylated IC IgG
11	Non-oxidized IC IgG + LA-PEG-Hyd
12	Non-oxidized ab7428
13	PEGylated ab7428
14	Non-oxidized ab7428 + LA-PEG-Hyd
15	LA-PEG-Hyd

Figure 6.17: SDS-PAGE and Coommassie/barium iodide staining characterization of PEGylated antibodies. Non-reduced samples (lanes 2–8) were diluted 3:1 in 4x Laemmli sample buffer, while reduced samples (lanes 9-15) were diluted 3:1 in 4x Laemmli sample buffer supplemented with 10% β-mercaptoethanol, and heated to 95 °C for 10 minutes (denoted with text box filled in blue). Gels were run as described in Section 2.2.2. Staining was performed first for PEG (barium iodide stain), and second for protein (Coommassie stain), and images of the gel after the two separate staining steps are co-registered and overlaid here. $\star$ denotes lanes containing antibody-PEG conjugates.

PEGylation of antibodies was performed as described in Section 2.16. After completion of the PEGylation reaction, PEGylated antibodies were analysed by sodium dodecyl sulfate–polyacrylamide gel electrophoresis (SDS-PAGE), as described in Section 2.2.2. As in Chapter 3, gel was stained first with barium iodide to identify PEG migration bands, then with Coommassie stain to identify protein. Fig. 6.17 is a composite of the photographs of the gel after (brown, PEG) barium iodide staining and (blue, protein) Coommassie staining. Attachment of PEG can change apparent MW of the protein [216], and barium iodide staining overlaps with Coommassie staining of a PEGylated protein [220] [216] [190]. Lanes 2-8 contain unreduced samples, while samples in lanes 9-15 were reduced by heating to 95 °C in 2.5% β-mercaptoethanol (BME). In lanes 3 and 6 in Fig. 6.17 (at about 120 or 150 kDa

respectively) a small increase in MW (and smearing) of the unreduced protein band can be observed, when compared to lanes 1 and 4 or lanes 5 and 7 respectively (which contain non-oxidized antibody [1 and 5], and non-oxidized antibody mixed with LA-PEG-Hyd [4 and 7]). As an unmodified antibody already has a MW of 150 kDa, addition of a PEG of 3.4 kDa would likely not alter MW significantly, so it is unsurprising that a large change in MW is not observed. Comparison of the reduced and PEGylated antibodies to reduced and untreated antibodies does not reveal a significant alteration to MW (lanes 9 and 10, and 12 and 13). A faint band slightly below 150 kDa is apparent in lanes 10 and 13 which could be an aggregate or unreduced antibody. An extremely faint second band immediately above the heavy chain is seen in lane 10 for PEGylated IC IgG – similar to the heavy chain bands seen with PEGylated cetuximab in Chapter 3, though with greatly reduced intensity. The results of the barium iodide staining for PEG show no distinct brown band associated with protein is seen in any of the PEGylated protein lanes (3, 6, 10, and 13). However, there are clearly changes to the migration patterns of the protein bands and some positive staining in these lanes, which occurs despite thorough washing of the PEGylated antibodies and is not present in the control lanes, which could indicate successful association of PEG with antibody. The barium iodide staining of the gel also validates successful washing of the non-reacted LA-PEG-Hyd away from PEGylated antibodies, as the strong barium iodide staining visible in the lanes with free LA-PEG-Hyd (8 and 15), as well as the lanes with free LA-PEG-Hyd added to un-oxidized antibody (4, 7, 11, and 14) at low MW (< 20 kDa) is largely removed. Notably, when a 30 kDa MWCO filter is used instead of 100 kDa for these washing steps, this low MW barium iodide staining is completely retained.

6.6 Functionalization and characterization of GNPs

15 nm bare citrate-capped GNPs were functionalized with ab7428 as described in Section 2.17, and a separate batch of GNPs were functionalized with IC IgG. LA-

PEG-antibody was added in molar excess to GNPs (20:1), to help drive the functionalization reaction. LA-PEGylated antibodies were added to GNPs and allowed to react overnight, before 2 kDa mPEG-SH was added to cap remaining surface of GNPs to provide colloidal stability. As in Chapter 3, mPEG-SH was added at a ratio 2-fold greater than the amount predicted to provide complete coverage of the GNP surface [225]. A batch of 'blank' GNPs were made, which did not have any LA-PEGylated antibody added, but were simply capped with mPEG-SH. After 20 minutes incubation with mPEG-SH, particles were centrifuged and washed with PBS + 0.05% Tween-20.

6.6.1 UV-Vis

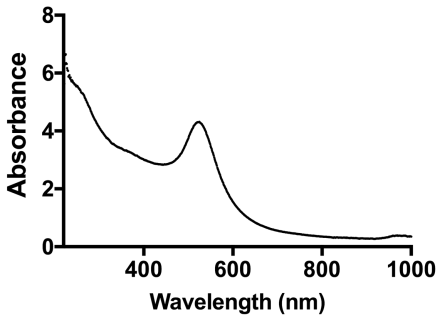

Figure 6.18: UV-Vis absorbance spectrum of GNPs functionalized with LA-PEG-ab7428 and capped with mPEG-SH. Absorbance is measured in a UV-transparent microplate in a BMG Labtech plate reader, and corrected to a path-length of 1 cm, and is plotted as a function of wavelength.

The UV-Vis absorption spectrum of a representative batch of antibody-PEGylated GNPs is shown in Fig. 6.18 (this batch was functionalized with a ratio of antibody to GNP of 20:1). Unlike the functionalized NHS-GNPs (Fig. 6.7), the PEGylated GNPs functionalized with LA-PEG-ab7428 (or LA-PEG-IC IgG control, data not shown) had a single absorption peak at 523, in good agreement with the predicted SPR band of 15 nm GNPs [226], which indicates a non-aggregated and monodisperse population of particles.

6.6.2 SDS-PAGE analysis of antibody-PEG-GNP loading

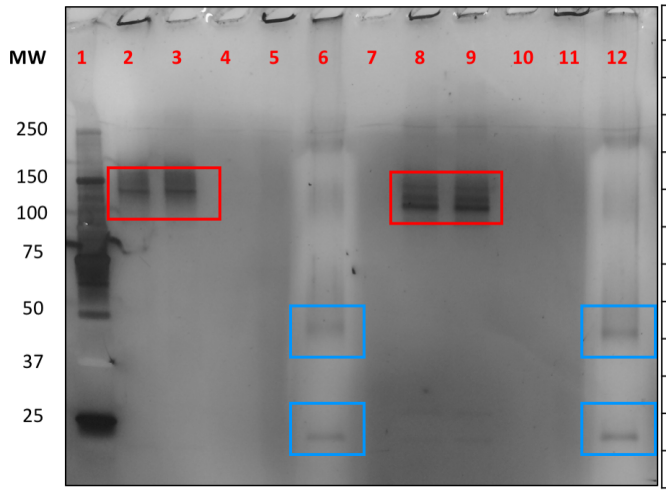

Lane #	Sample Identity
1	Molecular weight marker
2	ab7428-GNPs unwashed
3	Sup. 1rst wash ab7428-GNPs
4	Sup. final wash ab7428-GNPs
5	ab7428-GNPs washed
6	ab7428-GNPs washed
7	Blank
8	IC IgG-GNPs unwashed
9	Sup. 1rst wash IC IgG-GNPs
10	Sup. final wash IC IgG-GNPs
11	IC IgG-GNPs washed
12	IC IgG-GNPs washed

Figure 6.19: SDS-PAGE and silver staining characterization of antibody-PEG-GNP conjugates. SDS-PAGE and silver staining was performed with samples as described in Section 2.17.2. Samples in lanes 6 and 12 are diluted in reducing Laemmli sample buffer (denoted with text box filled in blue), while the remaining samples are in non-reducing Laemmli buffer. The red boxes correspond to unreduced antibody bands, while the blue boxes correspond to the reduced heavy and light chain antibody fragments.

Functionalization and removal of free antibody was verified by dot blot as in Section 6.3.1 (data not shown), and by SDS-PAGE analysis with silver staining for protein. Samples were taken from pre-washed antibody-GNP solutions (lanes 2 and 8), from supernatants of antibody-GNP solutions after the first centrifugation (lanes 3 and 9), from supernatants after final wash and centrifugation (lanes 4 and 10), and from the final washed antibody-GNP constructs (lanes 5 and 11). These samples were all diluted in non-reducing Laemmli sample buffer. In antibody-PEG-GNP samples prior to washing (lanes 2 and 8), as well as supernatants from the first wash (lanes 3 and 9), a clear intact antibody band is apparent at a MW slightly less than 150 kDa in Fig. 6.19. In the final wash supernatant samples (lanes 4 and 10), no protein staining is seen indicating successful washing of samples to remove

unreacted antibody. Lanes 5 and 11, which were loaded with antibody functionalized GNPs (functionalized with ab7428 and IC IgG respectively) which had been washed, also show no protein staining. The absence of staining further validated the washing procedure and demonstrates no low-affinity non-specific binding of antibody to the GNPS. The GNPs themselves are too large to migrate into the gel, as can be seen in the sample wells at the top of the gel. When washed antibody-GNP samples are diluted in reducing sample buffer (final concentration of 2.5% BME) and heated to 95 °C for 10 minutes, bands corresponding to the light and heavy chains of the antibody can be seen (lanes 6 and 12, blue boxes). As discussed in Chapter 3, thiol-containing BME can displace the lipoic acid of LA-PEG-Hyd and release PEGylated antibodies from the GNP surface. Thus, presence of antibody heavy chain in lanes 6 and 12 (reduced antibody-GNPs), but not in lanes 5 and 11 (non-reduced antibody-GNPs), provides strong evidence of GNP functionalization with ab7428 or IC IgG through the proposed mechanism.

6.7 Characterization of GNP + ColoAd constructs

6.7.1 Chromatographic analysis of GNP + ColoAd constructs

As in Section 6.4.2, washed antibody-PEG-GNP was incubated with ColoAd (at a ratio of approximately 100:1), and the resultant mixtures were analysed by anion exchange HPLC. Fig. 6.20 depicts the chromatograms obtained when 2.5 x 10^9 VPs of ColoAd were pre-incubated with GNPs functionalized with PEGylated antibodies (functionalized at a ratio of 20:1 antibodies per GNP). Panel A shows the expected elution profile of ColoAd with a characteristic virus peak at RT = 10.105 min. As with NHS-GNP experiments (see Figs 6.15 and 6.16), the PEGylated GNPs are not well retained by the column and elute with the solvent front (one peak between 1 and 3 minutes with strong fluorescence in panels B to D, and also UV-Vis absorbance at 525 nm as shown in Fig. 6.21 panel B1).

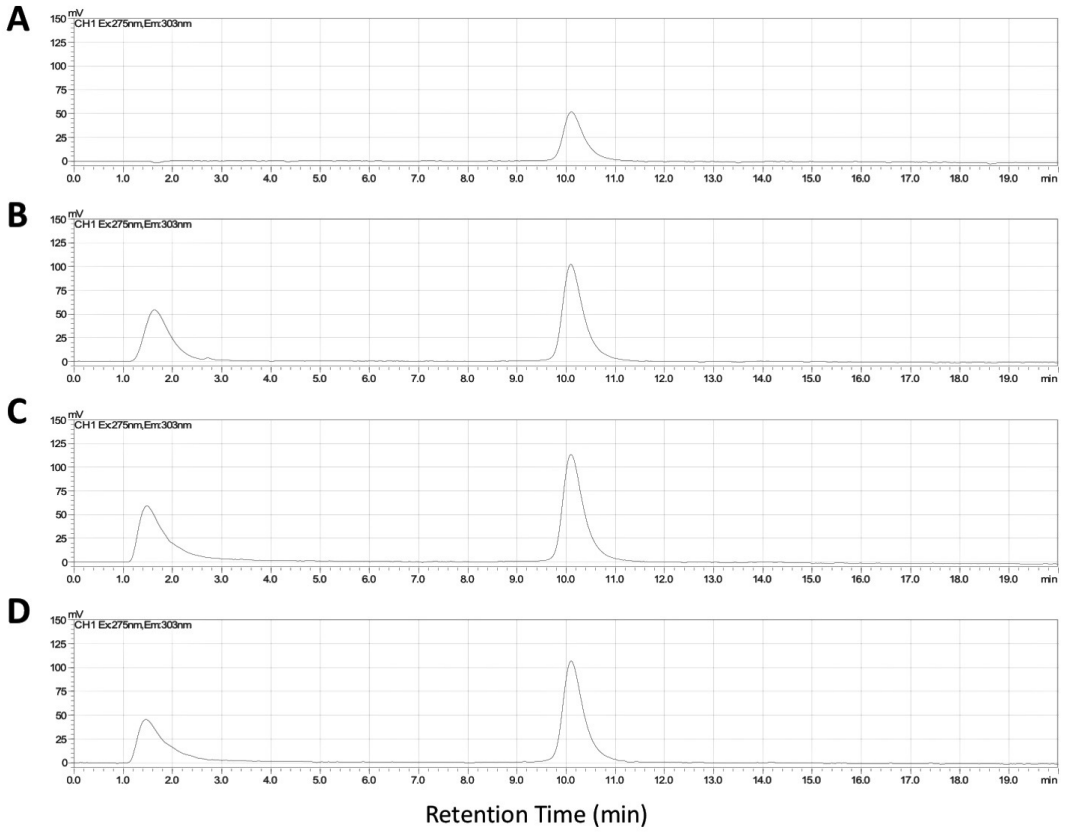

Figure 6.20: HPLC analysis of ColoAd and GNPs. 2.5 x 10^9 VPs of ColoAd were pre-incubated for 1 hour with a 100-fold excess of blank GNPs, GNPs functionalized with ab7428, or GNPs functionalized with IC IgG before chromatographic analysis as in Section 2.15.4. The chromatograms of the following samples are presented here: A) ColoAd alone, B) ColoAd pre-incubated with blank (PEGylated with mPEG-SH, but no antibody) GNPs, C) ColoAd pre-incubated with IC IgG-GNPs , D) ColoAd pre-incubated with ab7428-GNPs. Peaks are detected using a fluorescence detector with Ex/Em wavelengths of 275/303 nm. Arbitrary units (mAU) of fluorescence are shown on y-axis.

In panel B of Fig. 6.20, the chromatogram of a sample of ColoAd pre-incubated for 1 hour at 37 °C with blank GNPs shows GNPs eluting with the solvent front (RT = 1.625 min), while a clear peak of ColoAd eluting at a retention time of 10.092 minutes is also seen (ColoAd alone eluted at 10.105 min). The chromatograms of ColoAd pre-incubated with IC IgG-PEG-GNPs and ab7428-PEG-GNPs (panels C and D respectively), are nearly identical, and no substantial shift in retention time of ColoAd is seen among any of the conditions tested. However, when the UV-Vis

absorbance spectra of the ColoAd peaks (RT ≈ 10 min) from the different samples were examined (Fig. 6.21), a slight peak in absorbance at 525 nm was observed in ColoAd + IC IgG-PEG-GNPs or + ab7428-PEG-GNPs samples (panels C1 and D1, see red arrows), but not with ColoAd + blank GNPs (panel B2) or ColoAd only (panel A1) samples.

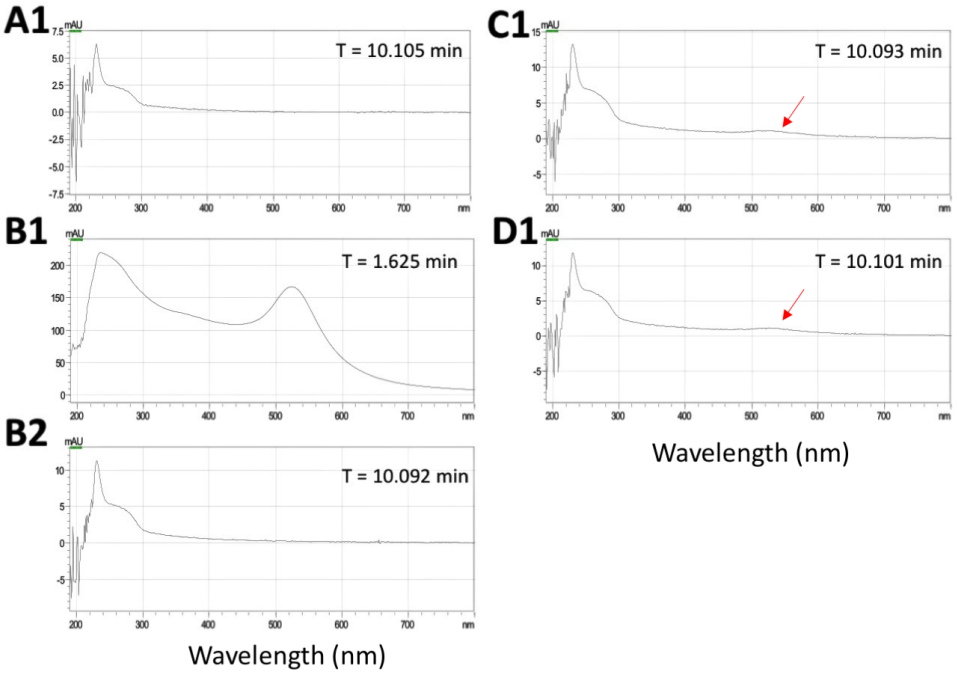

Figure 6.21: UV-Vis spectrum of peaks of ColoAd and GNPs separated by anion-exchange HPLC. 2.5 x 10^9 VPs of ColoAd were pre-incubated for 1 hour with a 100-fold excess of blank GNPs, GNPs functionalized with ab7428, or GNPs functionalized with IC IgG before before chromatographic analysis as in Section 2.15.4. The resulting chromatograms are shown in Fig. 6.20, and the UV-Vis absorbance spectra of peaks at different retention times (RT) taken from these chromatograms are presented here: A1) ColoAd alone (RT = 10.105 min), B1) ColoAd pre-incubated with blank (PEGylated with mPEG-SH, but no antibody) GNPs (RT = 1.625 min), B2) ColoAd pre-incubated with blank GNPs (RT = 10.092 min), C1) ColoAd pre-incubated with IC IgG-GNPs (RT = 10.093) , D) ColoAd pre-incubated with ab7428-GNPs (RT = 10.101). Arbitrary units (mAU) of absorbance are shown on y-axis.

The presence of this peak indicates association of GNPs with ColoAd, but as it is

seen with both the ColoAd specific antibody (ab7428) and isotype control antibody (IC IgG) functionalized GNPs, it is likely due to non-specific interaction of the antibody-coated GNPs with the VPs.

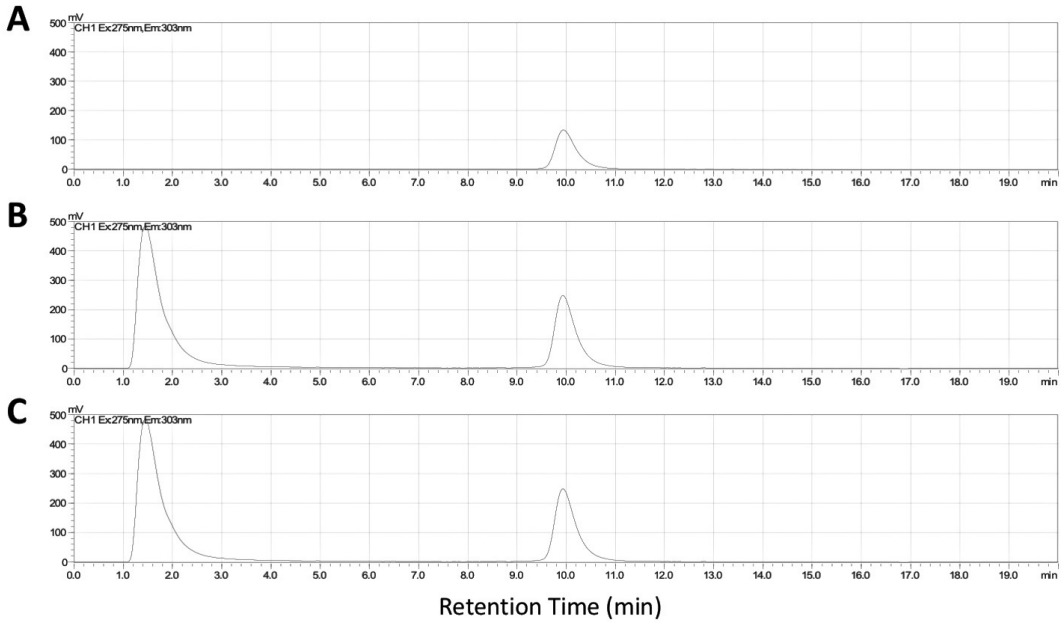

Figure 6.22: HPLC analysis of ColoAd and GNPs. 5 x 10^9 VPs of ColoAd were pre-incubated with a 130-fold excess of blank GNPs, GNPs functionalized with ab7428-PEG, or GNPs functionalized with IC IgG-PEG before chromatographic analysis as in Section 2.15.4. The chromatograms of the following samples are presented here: A) ColoAd alone, B) ColoAd pre-incubated with IC IgG-PEG-GNPs , C) ColoAd pre-incubated with ab7428-GNPs. Peaks are detected using a fluorescence detector with Ex/Em wavelengths of 275/303 nm. Arbitrary units (mAU) of fluorescence are shown on y-axis.

As no successful specific attachment of GNPs to ColoAd was observed, a fresh batch of functionalized GNPs were prepared (as above) by incubating PEGylated ab7428 or IC IgG with GNPs at a higher ratio of 40:1. These GNPs were then incubated with 5 x 10^9 VP of ColoAd at a ratio of approximately 130:1, before running through the anion exchange column as before. Fig 6.22 shows the resultant chromatograms; ColoAd alone (panel A), ColoAd + IC IgG-PEG-GNPs (panel B), and ColoAd + ab7428-PEG-GNPs (panel C). The results from this attempt mirror

the results from the previous attempt: there is no appreciable shift in retention time of virus pre-incubated with IC IgG-PEG-GNPs or ab7428-PEG-GNPs (RT = 9.94, 9.937 and 9.928 for ColoAd alone, + IC IgG-GNPs, or ab7428-PEG-GNPs respectively).

UV-Vis analysis of the ColoAd peaks was again performed and although a peak at 525 nm was again seen in the UV-VIS absorbance spectrum of ColoAd pre-incubated with ab7428-PEG-GNPs, a similar peak was seen for ColoAd pre-incubated with the control IC IgG-GNPs again indicating a non-specific interaction. It is hard to ascribe this interaction to electrostatic binding as it seems resistant to the presence of 0.4 M salt. However, as the binding lacks selectivity there is little value in pursuing it further as the methodology was specifically designed to ensure selective attachment that would not compromise infectivity. Moreover, as absorbance is linearly related to concentration through Beer's law ($A = c\epsilon$, for a path length of 1 cm, where A is absorbance, c is concentration and ϵ is the molar extinction coefficient), the concentration of GNPs co-eluting with ColoAd at RT $\approx$ 10 min can be roughly approximated. Thus, the absorbance of the GNPs eluted with the solvent front at RT $\approx$ 1.5 min was compared to the absorbance of the ColoAd peak. Evidently, the GNPs associated with ColoAd represent a tiny fraction the total GNPs added (approximately 0.3%, which at a ratio of 130 GNPs:VP, would be roughly equal to only 0.5 GNPs per virus). The existence of this minor but non-specific interaction between GNPs with ColoAd is similar to the results observed upon CsCl density gradient separation of ColoAd and GNPs (Section 6.4.1), where approximately 3.7% of VPs were recovered from the pellet of the centrifuged ColoAd + antibody-GNP samples.

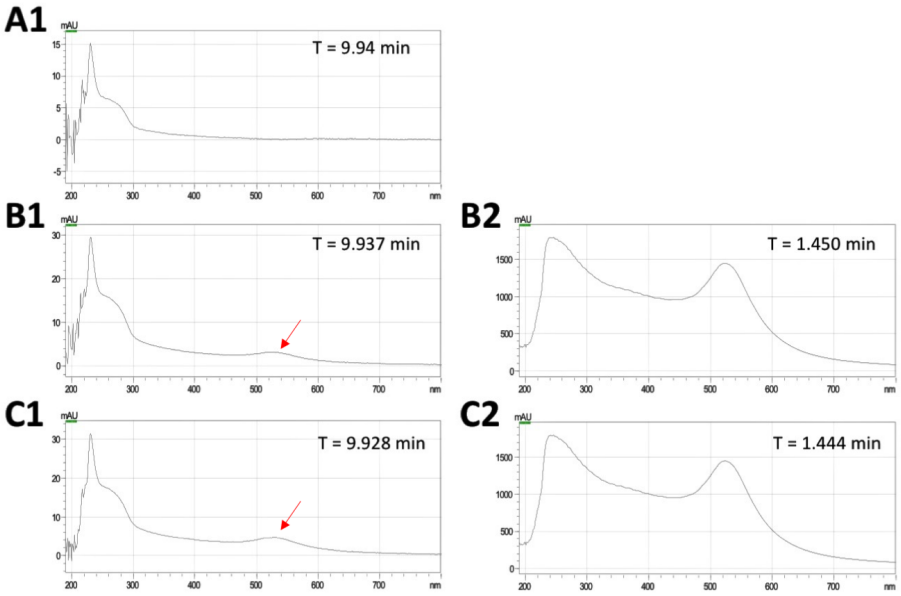

Figure 6.23: UV-Vis spectrum of peaks of ColoAd and GNPs separated by anion-exchange HPLC. 5 x 10^9 VPs of ColoAd were pre-incubated with a 130-fold excess of blank GNPs, GNPs functionalized with ab7428, or GNPs functionalized with IC IgG before chromatographic analysis as in Section 2.15.4. The resulting chromatograms are shown in Fig. 6.22, and the UV-VIS absorbance spectrums of peaks at different retention times (RT) taken from these chromatograms are presented here: A1) ColoAd alone (RT = 9.94 min), B1) ColoAd pre-incubated with IC IgG-PEG-GNPs (RT = 9.937 min), B2) ColoAd pre-incubated with IC IgG-PEG-GNPs (RT = 1.45 min), C1) ColoAd pre-incubated with ab7428-PEG-GNPs (RT = 9.928), C2) ColoAd pre-incubated with ab7428-PEG-GNPs (RT = 1.444 min). Arbitrary units (mAU) of absorbance are shown on y-axis.

6.8 Summary and discussion

The need to enhance the bloodstream stability and tumour accumulation of therapeutic adenoviruses has long been recognized [121]. A range of polymer coating and genetic modification strategies to achieve this have been reported [257, 258, 126]. GNP modification of adenoviruses has been explored by Saini et al. and Mo et al. as a means of enhancing the clinical utility of these vectors [135, 253]. The approach of Saini et al. requires the scientific and regulatory complexities involved in genetically modifying the virus to provide an attachment point for the gold. The approach of Mo et al. does not suffer this limitation but the chemistry utilized for attachment

causes a large decrease in infectivity of the adenovirus, limiting its ultimate utility. An important feature of the work of Mo et al. using adenovirus type 5 (Ad5) was the requirement that the GNPs provide a dense coat around the adenovirus to 'stealth' the VP from bloodstream components and increase its circulation time. Although the gold coating strategy presented by Mo et al. succeeded in improving circulation kinetics of Ad5, it also abrogated the natural infection mechanisms of the virus, thereby diminishing its oncolytic ability. In this chapter, a method for modifying the surface of adenoviruses in a specific fashion was investigated. This method aimed to use anti-adenovirus antibodies with specificity against the hexon protein – a region of the virus capsid not involved in the main cell entry pathway of the virus – as linkers to attach GNPs to the adenovirus surface. The goal of this strategy was to modify adenovirus in such a way that the virus could still utilize its natural mechanisms of infection and cell entry, while benefiting from an increase in density that could potentiate its ultrasound-mediated transport [135, 193]. An important corollary of this approach is however, that the viral surface modification is likely to not be as thorough as the modification achieved by Mo et al., and thus a lower degree of protection from bloodstream components would be conferred. Consequently, an alternative type of adenovirus was investigated; one with superior blood compatibility and circulation kinetics to Ad5, that would not require a thorough protection from blood components. ColoAd (enadenotucirev), a chimeric adenovirus derived from Ad11p/Ad3, was kindly provided by Prof. Len Seymour's group within the Department of Oncology of the University of Oxford. Two anti-Ad3 antibodies were investigated (ab7428 and MAB8052) and found to have specificity for hexon protein of ColoAd. Only ab7428 had dose-dependent neutralizing activity against ColoAd, while MAB8052 had no effect on infectivity over a wide range of antibody titres. Furthermore, indirect ELISA analysis indicated a higher relative affinity of ab7428 versus MAB8052 for ColoAd. Thus, the ab7428 antibody was selected as a linker and GNPs were functionalized with ab7428 using firstly, simple orientation-independent

lysine modification. The ab7428-functionalized GNPs were then combined with ColoAd (alongside isotype control IgG-functionalized GNPs). Both control IC IgG-GNP + ColoAd and ab7428-GNP + ColoAd formulations were subjected to CsCl density gradient ultracentrifugation, to determine if the addition of ab7428-GNPs could increase the density of ColoAd VPs. The results indicated that the density of the ab7428-GNP + ColoAd constructs had not been altered from the density of the control IC-IgG-GNP + ColoAd constructs. ELISA analysis of ab7428 binding to ColoAd in the presence of CsCl and glycerol indicated however, that the antibody-antigen interaction is significantly hindered in the presence of the high ionic strength CsCl (and also, though to a lesser degree, the glycerol solution). Consequently, high performance liquid chromatography (HPLC) performed using an anion-exchange column, and a salt gradient as mobile phase was investigated as an alternative method for monitoring successful modification of ColoAd with GNPs. Though ELISA analysis indicated that the salt concentrations in the mobile phase gradient could negatively affect the virus-antibody interaction, binding was not completely abrograted, so it was hypothesized that at high titres of ab7428-GNP, modified virus might still be detectable by this method. The employed anion-exchange HPLC method was able to resolve different adenovirus serotypes (Ad5 and ColoAd), and could resolve ColoAd covalently and non-site specifically modified with GNPs from naked ColoAd, however, pre-incubation of ColoAd with ab7428-GNPs did not result in an appreciable shift in retention time, or alteration to the UV-absorbance spectrum of the eluted ColoAd. Thus, despite careful consideration and characterization of the chosen antibody linker, and use of different analysis techniques, successful modification of ColoAd with GNPs using an antibody linker could not be demonstrated using this strategy. Two limitations of the GNP-antibody-virus construct formulation process were identified. Firstly, steric hindrance could prevent binding of the relatively large 20 nm GNP to the hexon coat protein of the virus, and secondly, reaction of NHS-coated GNPs with antibody in a non-direction controlled fashion could lead to

modification of antigen binding domains and low yields of functional GNP-antibody constructs. The second proposed GNP modification strategy was designed to address these potential limitations. Hence, a smaller GNP and a PEG spacer were used to prevent possible steric hindrance, and a site-specific PEGylation of antibody was used to improve the yield of functional GNPs. The heterobifunctional PEG linker (LA-PEG-Hyd) that was synthesized and characterized in Chapter 3 was used. The 'active' ab7428 and 'control' IC IgG were PEGylated and used to functionalize 15 nm bare citrate-stabilized GNPs. Functionalization of the GNPs through the proposed mechanism was confirmed using SDS-PAGE analysis of the washed antibody-PEG-GNP constructs. UV-Vis absorbance spectroscopy was used to demonstrate superior colloidal stability of the PEGylated GNP constructs as compared to the previously-used functionalized NHS-GNPs. Subsequently, anion-exchange HPLC was used to analyze the binding of ab7428-PEG-GNPs to ColoAd. In two separate experiments, no substantial difference in retention time or antibody-specific change in the UV-VIS absorbance spectrum was detected for samples containing ColoAd incubated with ab7428-PEG-GNPs, ColoAd incubated with control GNPs, or ColoAd alone. The ColoAd-antibody-GNP conjugate that could be identified was non-specifically associated and represented such a small proportion of the total input constituent parts that there was no value in pursuing the approach further. The conclusion of this work is thus that the strategy and tools used in this chapter for achieving a specific density modification of ColoAd with antibody-modified GNPs are not viable.

Though appealing due to their high-specificity, this body of work demonstrates the limitations of antibodies for use as linkers in bio-conjugation strategies. Despite demonstrating a high-affinity for ColoAd hexon protein, the antibody-antigen interaction was susceptible to the effects of ionic strength. This made both functionalization and characterization of a GNP-ColoAd construct challenging. Future work on modification of adenovirus through specific strategies designed to preserve infectivity could look at use of genetic engineering (as used by Saini et al. [253])

to introduce conjugation sites into the hexon protein. Alternatively, strategies to create a modified adenovirus requiring 'destealthing' could be revisited. Mo et al. investigated the use of a linker susceptible to reduction, and had limited success with this strategy in vivo. Other linkers such as enzymatically-cleavable linkers have been successfully employed in other bio-conjugation contexts [259], and could prove helpful here, though this strategy re-introduces the dependency on the (often heterogeneous) character of the tumour microenvironment. An ultrasound-labile linker [260] could be explored, however the US-sensitivity of this linker would need to be finely tuned in order for a GNP-virus construct to benefit from the potentiating effect of increased density on US-mediated transport.

Chapter 7

Conclusions and Future Work

7.1 Summary of findings and conclusions

Currently, drug development for cancer is tending towards highly targeted biological therapeutics, including antibodies and oncolytic viruses, which can selectively treat tumours while mitigating some of the devastating off-target effects commonly seen with conventional small-molecule chemotherapeutics. Moreover, in the last couple of decades, the promise of 'enhanced permeability and retention' of nanoscale therapeutics has led many researchers to formulate (or reformulate) nanoparticulate drugs or drug carriers. It is theorized that these 'passively' targeted nanoparticles can be made more selective by 'actively' targeting through decoration with cancer selective ligands or antibodies. However, as the size and complexity of cancer therapeutics become increases, the challenge of delivery also increases. The tumour microenvironment – though potentially suited for passive accumulation of drug as a result of its leaky vasculature – is also characterized by high interstitial fluid pressure, dense extracellular matrix components, and reduced lymphatic drainage. This ultimately results in a reduction in convective flow and an increased reliance on diffusion for drug delivery and penetration [12]. This effect has been shown with therapeutics as varied as antibodies [35, 36], liposomes [261], and viruses [131], and is likely to significantly reduce the delivery, and potentially the efficacy, of these complex and painstakingly engineered modern therapeutics. Recently, US-mediated cavitation has been proposed and evaluated as a non-invasive external stimulus to improve delivery of drugs. Depending on the acoustic parameters applied, cavitation can be used to open the blood brain barrier for drug delivery [155], or can be used to

transport drugs out of the vasculature and into the tumour [178]. Notably, artificial cavitation nuclei can be used to seed cavitation at relatively low pressures; this allows cavitation levels capable of enhancing drug transport to be achieved without causing damage to tissue [167].

In this thesis, the effects of US-mediated cavitation on delivery of a range of therapeutics into solid tumours was investigated. Two classes of cavitation nuclei were employed: clinically approved microbubble ultrasound contrast agents (SV), and sonosensitive gas-entrapping nanoparticles (SSPs). The therapeutics tested here cover a spectrum of current targeted therapeutics for selective treatment of cancer, with vastly different characteristics in vivo. The therapeutics tested here comprised (in order of increasing complexity), a cancer-targeting mAb (cetuximab), an actively targeted nanoparticle (cetuximab-GNPs), and an oncolytic virus (ColoAd). Furthermore, site-specific density-modification of ColoAd was investigated, in an attempt to further enhance its cavitation-mediated transport.

7.1.1 Development and characterization of targeted gold nanoparticles

Reports in the literature suggest that nanoparticle-conjugated antibodies have enhanced target binding and consequent bioeffects, and that targeting nanoparticles with antibodies can enhance cell-uptake and cancer cell kill [186, 187, 188, 189]. Many studies however, have conjugated antibodies non-specifically, which can lead to reduced antibody efficacy (due to blocking or modification of antigen binding site), and decreased colloidal stability. To avoid these potential limitations, a site-specific conjugation strategy was used here, whereby antibodies were first site-specifically modified with a heterobifunctional PEG linker, prior to conjugation with GNPs. Use of this strategy with cetuximab was previously reported, and indicated that site specific conjugation to GNPs could enhance the bioeffects of cetuximab in vitro [189, 186].

Here, a new heterobifunctional PEG linker with the ability to site-specifically

modify an antibody on one end, and stably attach to the surface of GNPs on the other, was synthesized. Characterization of this linker (LA-PEG-Hyd) demonstrated a high-yield of functional product with the synthesis protocol reported here.

Subsequently, a rigorous and in-depth characterization of site-specific modification of cetuximab was performed. Glycoprofiling of cetuximab has repeatedly shown the presence of two glycosylation sites on this antibody (one in the Fc region, and the other in the antigen binding region). It is intriguing that reports in the literature describing conjugation to cetuximab via oxidized N-linked glycans fail to consider the presence of the second possible conjugation site [186, 191, 189]. Comparison of the number of potential conjugation sites generated by periodate oxidation of cetuximab vs trastuzumab (which contains only one glycosylation site) showed a greater number on cetuximab at all conditions tested. This suggests the potential for conjugation to cetuximab via this other glycosylation site. Therefore, analysis of cetuximab binding to its target antigen (EGFR) post-PEGylation was conducted to determine if the presence of the second conjugation site compromises antigen-binding activity. Although a small decrease in functional antibody affinity was observed post-PEGylation, this was also observed with PEGylated trastuzumab, suggesting that this site-specific method of antibody conjugation is appropriate for use with cetuximab, despite the possibility of conjugation to the antibody binding domain. Site-specific modification of the heavy-chain of cetuximab was confirmed, as no changes in MW by SDS-PAGE or retention time by UP-LC were seen with the light chain, but significant changes to the heavy chain were observed only when antibody was first oxidized and then reacted with the LA-PEG-Hyd linker.

PEGylated cetuximab was conjugated to GNPs, and the resulting constructs were characterized. Conjugation of cetuximab through the proposed mechanism was confirmed by SDS-PAGE analysis, and a lower limit of antibody loading per GNP was estimated. DLS, TEM, and UV-Vis spectroscopy were used to characterize the size, monodispersity, and colloidal stability of the particles. Finally,

the biological activity of the cetuximab-GNPs was verified with an in vitro assay that demonstrated a dose-dependent blocking of EGF binding to cancer cells by cetuximab-GNPs. Given the lower limit estimates for cetuximab loading on the GNPs, the particles were less effective than free cetuximab at blocking EGF binding, which was surprising given the reports in the literature of increased anti-cancer efficacy of nanoparticle-conjugated cetuximab [186, 187, 188, 191, 189]. However, the differences observed between the effects of free versus conjugated cetuximab were not so great as to discount the potential of the cetuximab-GNPs, and it is possible that alternative assays looking at inhibition of cell proliferation, or internalization and degradation of EGFR might reveal a greater efficacy of cetuximab-GNPs consistent with reports in the literature. Enhanced efficacy via conjugation to a nanoparticle may be a function of the balance between affinity lost as a consequence of modification or blocking or antigen binding groups, and avidity gained by improving target receptor clustering. The site specific modification described here certainly provides a good route to minimizing the former. Future work may be beneficial in developing this approach to improve the latter.

The conclusions of the work presented in Chapter 3 can be summarized as follows:

- A heterobifunctional PEG linker capable of site-specifically conjugating antibodies (or any glycoprotein/aldehyde-containing molecule) to gold surfaces can be readily synthesized from commercially available PEG molecules using the protocol presented here.

- Cetuximab can be site-specifically modified with this PEG linker while retaining high affinity for its antigen, despite the (under-reported) presence of a second glycosylation site within the antigen binding domain.

- PEGylated cetuximab can be loaded onto GNPs, and retain the ability to block EGF binding to the EGF receptor.

Delivery of the cetuximab-GNP construct formulated and characterized in this

chapter was examined in the subsequent chapter.

7.1.2 In vivo assessment of cavitation-mediated delivery of antibodies and targeted nanoparticles

In vivo delivery of cetuximab-GNPs and free cetuximab was investigated, firstly in the absence of US-mediated cavitation, and subsequently in combination with US-mediated cavitation. The US-mediated cavitation was seeded using either SV microbubbles or SSPs, and characterized using PAM. Analysis of circulation kinetics of cetuximab-GNPs revealed poor circulation of the cetuximab-GNPs compared to the extended circulation time of free cetuximab (approximately 20% vs 100% of ID remains in circulation 5 minutes after injection). Perhaps as a consequence, passive tumour accumulation of cetuximab-GNPs was poor, with only 0.13±0.08 percent of the ID accumulating within the tumour after 24 hours (in comparison to 1.87±0.80% of the ID of free cetuximab). These findings suggest a large area of opportunity for improving the delivery of these cetuximab-GNP constructs (or similar therapeutics suffering from poor circulation kinetics and low passive tumoural accumulation).

The effects of US-mediated cavitation on delivery of cetuximab-GNPs and free cetuximab were investigated in a bilateral tumour model, wherein one tumour was exposed to US, while the other was not. This design allowed for comparison of each US-treated tumour to its internally controlled unexposed tumour, and potentially allows for a more powerful analysis of the effects of interest in the presence of significant inter-subject variability. As with the study of circulation kinetics and passive tumoural accumulation, ELISA was used to directly quantify the concentration of cetuximab (free or conjugated to GNPs), and thus calculate the percentage of injected dose recovered from tumours. Such precise quantification of US-mediated delivery of an antibody therapeutic has not previously been reported in settings outside blood brain barrier work.

Delivery of cetuximab (with SV or SSPs) was enhanced with US in 8 out of

8 mice treated. Mice receiving SSPs had a greater fold increase of cetuximab in US-treated tumours (approximately 3.6-fold higher than untreated tumours) than mice receiving SV (approximately 2-fold higher). Analysis of cetuximab delivery as a function of cavitation activity (quantified by the cumulative PAM magnitude over treatment), suggested a potential predictive role of PAM feedback of cavitation activity for therapeutic delivery, irrespective of CN type used to seed cavitation.

Comparison of cetuximab recovered from tumours after just 12 minutes of treatment with US + CN versus after 24 hours of passive accumulation showed that treatment with US + SSPs or SV resulted in delivery comparable to the level achieved after 24 hours of passive accumulation.

Delivery of cetuximab-GNPs (with SV or SSPs) was also greatly enhanced with US, and the effect of US + CN appeared to be 'enabling'. Only 2 out of 8 tumours receiving CN but no US had a tumoural concentration of cetuximab-GNPs above the detection limits of the ELISA. Though the ultimate percentage of the injected dose recovered from tumours receiving cetuximab-GNPs + US + CN was lower than with free cetuximab + US + CN, the relative benefit compared to the case without US was greater for cetuximab-GNPs, indicating that US could potentially have a large positive impact on delivery of therapeutics that do not circulate or passively accumulate efficiently. Specifically, the median % ID per gram of tumour recovered from tumours treated with with US + SSPs or US + SV was greater than the dose recovered of cetuximab-GNPs passively accumulating over 1 hour.

For both cetuximab and cetuximab-GNPs, the use of SSPs as cavitation nuclei gave rise to a greater median recovered dose of drug compared to SV. This difference was statistically significant for free cetuximab ($p < 0.01$), but not for cetuximab-GNPs (as the difference in this group was small, and within-group variance was very large). Focusing on the case of free cetuximab, this could be due to the significantly greater cumulative PAM magnitude detected over treatment with SSPs vs SV ($p < 0.01$). There was however, significant bruising seen in tumours after treatment with

US + SSPs (though much of this bruising was more localized to the skin). Future studies could look at quantifying the total percentage of injected dose successfully bound to EGFR within the tumour to discern if the presence of bruising artificially increases the level of delivered cetuximab quantified.

The conclusions of the work presented in Chapter 4 can be summarized as follows:

- Circulation kinetics and passive tumour accumulation of cetuximab-GNPs were found to be substantially poorer than free cetuximab.

- US and CN were found to have a substantial (3.6 and 2.0-fold for SSPs and SV, 95% CI from 2.5 to 6.2-fold and 1.3 to 3.7-fold respectively) and significant effect ($p< 0.01$, for SSPs) on the percentage of ID of cetuximab recovered in tumours. Cumulative PAM magnitude as a measure of cavitation activity was found to be a significant predictor of cetuximab delivery.

- The effects of US + CN were found to 'enable' delivery of cetuximab-GNPs (at the 12 minute time point investigated here). Without US, only 2 out of 10 tumours had a tumoural concentration of cetuximab-GNPs above the detection limits of the ELISA. US-mediated cavitation may have a large role to play in enhancing the delivery of therapeutics that do not passively accumulate effectively.

- Treatment with US + SSPs gave rise to a greater tumoural delivery of cetuximab than treatment with US + SV.

7.1.3 In vitro and in vivo assessment of cavitation-mediated delivery of an oncolytic adenovirus

Past studies have shown that US + SV can enhance the delivery of Ad5 both in vitro and in vivo [167, 177, 178, 134], though the necessity for repeated administrations of SV was identified as a limiting factor to the clinical translation of this strategy. Moreover, rapid neutralization of Ad5 by human blood components limits

the clinical utility of this virus as an oncolytic therapeutic [241]. Here cavitation-mediated transport of an oncolytic adenovirus amenable to i.v. delivery in the clinic (ColoAd) [242] was investigated both in vitro and in vivo. In vitro, delivery of ColoAdRFP with US + SSPs to a tissue-mimicking flow phantom was investigated. In vivo, delivery of luciferase-expressing ColoAd variants was investigated in a bi-lateral tumour model as described for cetuximab, with both SV and SSPs as CN.

In vitro, delivery of ColoAdRFP to cancer cells embedded in a tissue-mimicking agar gel was investigated at driving HIFU frequencies of 0.5 and 1.6 MHz, with SSPs to seed cavitation. Results obtained with 0.5 MHz (though somewhat confounded by non-realistic cracking of the agar gel at the HIFU focus) showed increased delivery of ColoAdRFP at depths away from the channel walls. With 1.6 MHz, the maximum, mean, and median delivery distances of ColoAdRFP (from the channel) were significantly ($p < 0.05$) enhanced when US was applied. Virtually no extravasation beyond the walls of the channel was seen in the absence of cavitation, re-emphasizing the scale of the delivery challenge faced.

In vivo, delivery of ColoAd was investigated within two regimes. Firstly, US-mediated delivery of ColoAdCMVLuc was investigated using US at 0.5 MHz driving frequency and a constant PRFP of approximately 1.5 MPa over a treatment time of 10 minutes. Within this regime, an increase in viral delivery (as assessed with IVIS imaging of in vivo luciferase transgene production) was evident in 8 out of 8 tumours treated with US, though there was significant inter-subject variability in the size of this effect, in line with previous studies of Ad5 delivery with US + CN [178, 134]. In contrast to the results in Chapter 4, whereby use of SSPs to seed cavitation gave rise to greater delivery than the use of SV, the estimated fold-increase in tumour radiance was greater here with SV than with SSPs. Analysis of the acoustic feedback data revealed that while SSPs gave rise to more sustained cavitation, the maximum PAM magnitude was consistently higher with SV. As ColoAd has a half-life of only 2 minutes in mice [247], it was hypothesized that within this regime the short duration

but high magnitude cavitation activity of SV was sufficient to increase delivery of ColoAd, and that the sustained cavitation activity of SSPs had little added value. This hypothesis is consistent with results in Chapter 4, whereby delivery of long-circulating cetuximab was increased with longer duration cavitation activity afforded by SSPs.

Thus, in a second regime, US-mediated delivery of ColoAd was investigated using US with a variable PRFP between approximately 1.5 to 2 MPa (as in Chapter 2) over a treatment time of only 5 minutes. Furthermore, a more clinically-relevant virus (ColoAdSALuc) was used, whereby transgene expression is tied to viral replication and is thus tumour selective [249]. With a PRFP adjusted in real-time based on PAM feedback, cavitation activity was very consistent across mice, and maximum PAM magnitude was not significantly different between mice receiving SV or SSPs. Variability in luciferase expression between mice within the same group was still very large (as assessed by IVIS imaging). However, as with cetuximab-GNPs, the effect of US + SSPs appeared to be 'enabling': only 1 out of 8 tumours receiving SSPs but no US had a tumour radiance above background threshold, while 5 out of 8 tumours receiving SSPs + US had substantial luciferase expression. The effect with US + SV also showed high variability, with 4 mice showing an increased signal in the US-treated tumour. The fold-increase in tumour radiance with US was estimated and it was found that SSPs + US and SV + US gave rise to similar fold increases (13-fold vs. 11-fold, 95% CI from 2 to 57-fold and 3 to 39-fold respectively). This finding is similar to the results of delivery of cetuximab-GNPs presented in Chapter 4. This result sits somewhat below the levels reported by [134] and [173], which may reflect differences in the vascularization of the tumour models used, or the PK of the viruses being tested. Indeed, for these short circulating therapeutics, the greater duration of cavitation activity with SSPs does not seem to result in a large increase in delivery compared to SV. This contrasts with the significant difference in delivery with SSPs compared to SV seen with long-circulating free cetuximab. ColoAd is cleared rapidly

in mice at a similar rate to Ad5 [247]. In humans, conversely, ColoAd has improved haemocompatibility compared to Ad5 [130] and demonstrated delivery after i.v. administration [242], thus use of SSPs as CN might therefore provide an even greater advantage in the clinic than is apparent in pre-clinical models. Finally, tumours from half of the mice treated in this regime were analysed with IHC. Large variability was seen across tumours in terms of the percentage of viable tissue, and the degree of vascularity (as determined by staining for endothelial marker, endomucin). This analysis is beneficial in understanding the high variation seen in IVIS measurements. It is notable that despite such variation in tumour composition and vascularization, PAM feedback could be used to adjust and maintain very reproducible levels of cavitation. As may be expected from single dosing, in non-clodronate treated mice with poorly vascularized tumours, only small foci of virus infection were detected by IHC, once again underlining the vast delivery challenge faced.

The conclusions of the work presented in Chapter 5 can be summarized as follows:

- US + SSPs can be used to enhance the delivery of ColoAd to a tissue-mimicking gel.
- US + SSPs or US + SV can be used in vivo to enhance the delivery of ColoAd to tumours, though the size of the effect is subject to large variability.
- The benefit of the sustained cavitation activity from SSPs may be related to the circulation time of the drug being delivered.
- The large variability in delivery as assessed by in vivo luciferase tracking, ex vivo quantification of luciferase production, ex vivo qPCR quantification of viral genomes, and IHC analysis of tumour characteristics and viral spread, all suggest that there remains a significant area of opportunity for further improving the enhancement of delivery afforded by treatment with US + CN.

In the final chapter, a strategy to further enhance US-mediated transport of ColoAd by increasing its density [135, 193] was explored.

7.1.4 Development and evaluation of a method for modifying the density of an oncolytic adenovirus

Mo et al. showed that modification of Ad5 with GNPs could improve the pharmacokinetics and US-enhanced delivery of Ad5 into tumours by over 100-fold [135]. This work suggested that the density of a therapeutic agent may play a role in its response to US-mediated cavitation. Work by Lea-Banks et al. confirmed that in the presence of US and microbubbles, denser particles travel greater distances into a viscoelastic matrix [193]. In this chapter, density modification as a means to improve the cavitation-mediated delivery of ColoAd was investigated. As the work of Mo et al. suffered the limitation of reduced virus activity after heavy surface modification with GNPs, a more site-specific modification strategy was pursued here. Anti-adenovirus antibodies were investigated as possible linkers to attach GNPs to particular regions of the ColoAd protein capsid not crucial for infection. Two alternative conjugation strategies were employed. First, a simple method wherein antibodies were conjugated to NHS-GNPs through their lysine residues in a one-step, but random and orientation-independent fashion was investigated. Subsequently, the method developed in Chapter 3 for site-specifically PEGylating antibodies prior to conjugation with GNPs was used. Two non-neutralizing antibodies with selectivity for ColoAd hexon protein were identified, one of which was prioritized for use as a linker due to evidence of increased affinity for ColoAd. GNPs were successfully functionalized with anti-ColoAd antibodies through both methods, though colloidal stability was greater with the selective-conjugation method. The ability of antibody-GNP constructs to bind to ColoAd was assessed with CsCl density gradient ultracentrifugation (as in [135, 253]), and with chromatographic analysis using anion exchange liquid chromatography. No significant proportion of ColoAd was specifically bound to GNPs regardless of whether orientation dependent or independent antibody-GNP constructs were used, or which analysis method was used. It was concluded that there was no value in pursuing the approach further.

The conclusions of the work presented in Chapter 6 can be summarized as follows:

- Though highly-specific, antibodies are not a viable option for use as linkers to attach GNPs to the surface of ColoAd. The interaction is relatively weak compared to covalent linkers, and is susceptible to high ionic strength solutions.
- Formulation, characterization, and purification of a GNP-modified virus is very challenging, and future studies should further investigate the added-value of density modification in vivo before further work is done to create such a construct.

7.2 Future work

This thesis presents an examination of US-mediated delivery of three therapeutic classes: a therapeutic mAb (cetuximab), an actively targeted nanoparticle (cetuximab-GNP), and an oncolytic virus (ColoAd). Notably, these agents represent some of the most novel and clinically impactful classes of drug being developed for the treatment of cancer. However, they all have significant challenges to overcome in terms of their delivery into and throughout solid tumours. This thesis also presents the development and extensive characterization of advanced protocols for loading GNPs with antibodies, both randomly, and site-specifically. Here, some of the limitations encountered are discussed and future work is proposed to address these limitations and extend the work presented in this thesis.

- Analysis of cetuximab-GNP stability in human plasma at 37 °C revealed a small but significant release of antibody over time. Sodium cyanoborohydride was used here to reduce and further stabilize the bond between the PEG linker and the oxidized cetuximab to enable chromatographic analysis at low pH and high-temperatures. This method could be used to increase stability of antibody-GNP conjugates [191].

- Quantification of delivered gold by inductively coupled plasma mass spectrometry (ICP-MS) would more directly confirm the results of the study of cetuximab-GNP delivery, as the current ELISA method will not discriminate between free cetuximab and cetuximab-GNPs.

- Potency of cetuximab-GNP constructs could potentially be enhanced by conjugation of an additional therapeutic to the nanoparticle surface. Similar to an ADC, this construct could provide targeted delivery of a potent therapeutic, and potentially enhance its delivery into EGFR-expressing cells (as cetuximab-GNP constructs have been shown to be preferentially uptaken into EGFR+ cells [186]). An increase in potency could help to compensate for low tumour accumulation. US + CN could be used to increase delivery of this targeted antibody-drug-nanoparticle conjugate.

- The analysis presented here describing the relationship between tumour uptake of cetuximab and cavitation activity (as measured by the cumulative PAM magnitude over treatment) suggested that cavitation activity could be predictive of therapeutic delivery. The study presented here was underpowered to definitively outline a relationship, though the data acquired was reasonably consistent across mice and normally distributed, suggesting that the setup and analysis methods used here could be a good platform for further probing the relationship between cavitation feedback and therapeutic delivery. Data acquired with shorter-circulating therapeutics such as cetuximab-GNPs and ColoAd were much more variable, and would thus be more difficult to definitively correlate with cavitation activity. Future work could probe the delivery of cetuximab over a greater range of 'cavitation doses' to fully elucidate the relationship between cavitation and delivery. It is hoped it may ultimately be possible to link PAM feedback to therapeutic outcome, providing a tool of great clinical utility.

- Although the use of US + CN was shown here to substantially increase the percentage of the injected dose of cetuximab delivered to the tumour, this amount was not significantly different from the percentage that accumulated passively within the tumour over 24 hours. This comparison is somewhat facile, as there is no reason to think that US-treated tumours would not also benefit from passive accumulation in addition to US-mediated delivery. However, if US-mediated cavitation is to be further pursued as a clinical tool for use with therapeutic mAbs, the effects of US beyond simple delivery should be further probed. Literature has shown that tumoural distribution of mAbs can be heterogeneous, and is greatest in perivascular regions and very low in regions of hypoxia (especially when lower doses are administered) [36, 35]. Tumoural distribution of cetuximab (or other therapeutic mAbs) should be investigated after exposure to US-mediated cavitation, and compared to distribution achieved by passive accumulation. Finally, a study of the efficacy of cetuximab + US + CN to control the growth of or reduce the size of EGFR-overexpressing tumours, as compared to cetuximab without US, would more definitively determine the potential of the enhanced delivery this strategy provides in terms of therapeutic outcome and the value of further translation.

- Similarly, an efficacy study of ColoAd + US + CN would provide additional evidence of the benefits of US + CN as a strategy to improve virotherapy. IHC analysis presented here demonstrates the scale of the delivery problem, even for therapeutics that can self-replicate. Repeat dosing of ColoAd + US + CN could increase the effect size seen and decrease the variability between mice. Additionally, a tumour model more permissive to ColoAd replication (HCT-116 cells, for example), might help reduce variability between mice, and more closely recapitulate results seen with vaccinia virus + US + CN [173].

- Finally, although the study of Mo et al. provided compelling evidence for the

benefits of increased density on US-mediated transport, the virus modification in this study also provided a huge benefit to circulation kinetics of Ad5. It is difficult to separate the effects of having a greater dose in circulation during US exposure from the effect that density may have on US-mediated transport. The work of Lea-Banks et al. provided solid evidence for a positive role of density on transport through in silico modelling, and in an in vitro model. In vivo results were, however, confounded by large inter-subject variability and small group sizes (personal communication). Before further work is conducted on modification of a complex therapeutic to increase its density, the benefit of increased density to US-mediated transport should be further probed in vivo. Such a study would ideally compare the delivery of particles identical in all respects except for density. Gold-shelled particles are commercially available, which have a low-density core, but are coated in gold and have the same surface properties as a solid GNP. ICP-MS could be used to quantify the tumoural delivery of these two constructs after delivery with US + CN, and these results could inform future strategies for enhancing US-mediated delivery of biological therapeutics through density modification.

Ultimately, the work presented in this thesis both underscores some of the challenges to effective cancer therapy with biological therapeutics, and provides compelling evidence and support for the further investigation of US-mediated cavitation as an effective tool for improving the delivery of biological therapeutics into tumours.

References

[1] J. M. Brown, A. J. Giaccia, *Cancer Res* **58**, 1408 (1998).
[2] P. Carmeliet, R. K. Jain, *Nature* **407**, 249 (2000).
[3] P. Baluk, S. Morikawa, A. Haskell, M. Mancuso, D. M. McDonald, *Am J Pathol* **163**, 1801 (2003).
[4] M. W. Dewhirst, *et al.*, *Int J Radiat Oncol Biol Phys* **17**, 91 (1989).
[5] H. Hashizume, *et al.*, *Am J Pathol* **156**, 1363 (2000).
[6] C. H. Heldin, K. Rubin, K. Pietras, A. Ostman, *Nat Rev Cancer* **4**, 806 (2004).
[7] R. Carlisle, C. C. Coussios, *Ther Deliv* **4**, 1213 (2013).
[8] A. J. Leu, D. A. Berk, A. Lymboussaki, K. Alitalo, R. K. Jain, *Cancer Res* **60**, 4324 (2000).
[9] P. A. Netti, D. A. Berk, M. A. Swartz, A. J. Grodzinsky, R. K. Jain, *Cancer Res* **60**, 2497 (2000).
[10] R. K. Jain, *Nat Med* **7** (2001).
[11] O. Tredan, C. M. Galmarini, K. Patel, I. F. Tannock, *J Natl Cancer Inst* **99**, 1441 (2007).
[12] A. I. Minchinton, I. F. Tannock, *Nat Rev Cancer* **6**, 583 (2006).
[13] P. Vaupel, O. Thews, M. Hoeckel, *Medical Oncology* **18**, 243 (2001).
[14] P. Vaupel, *Semin Radiat Oncol* **14**, 198 (2004).
[15] S. Loges, M. Mazzone, P. Hohensinner, P. Carmeliet, *Cancer Cell* **15**, 167 (2009).
[16] D. Fukumura, R. K. Jain, *J Cell Biochem* **101**, 937 (2007).
[17] A. J. Primeau, A. Rendon, D. Hedley, L. Lilge, I. F. Tannock, *Clin Cancer Res* **11**, 8782 (2005).
[18] H. Maeda, *Adv Enzyme Regul* **41**, 189 (2001).
[19] H. Maeda, H. Nakamura, J. Fang, *Adv Drug Deliv Rev* **65**, 71 (2013).
[20] H. Maeda, *J Control Release* **65**, 271 (2000).
[21] Y. Barenholz, *J Control Release* **160**, 117 (2012).
[22] A. A. Gabizon, *Cancer Invest* **19**, 424 (2001).
[23] S. Dromi, *et al.*, *Clin Cancer Res* **13**, 2722 (2007).
[24] S. M. Graham, *et al.*, *J Control Release* **178**, 101 (2014).
[25] C. M. Dawidczyk, *et al.*, *J Control Release* **187**, 133 (2014).
[26] E. Miele, G. P. Spinelli, E. Miele, F. Tomao, S. Tomao, *Int J Nanomedicine* **4**, 99 (2009).
[27] T. Lammers, F. Kiessling, W. E. Hennink, G. Storm, *J Control Release* **161**, 175 (2012).
[28] U. Prabhakar, *et al.*, *Cancer Res* **73**, 2412 (2013).
[29] J. W. Nichols, Y. H. Bae, *J Control Release* **190**, 451 (2014).
[30] S. Wilhelm, *et al.*, *Nat Rev Mater* **1**, 16014 (2016).
[31] J. E. Zuckerman, *et al.*, *Proc Natl Acad Sci U S A* **111**, 11449 (2014).
[32] D. Goren, *et al.*, *Clin Cancer Res* **6**, 1949 (2000).
[33] C. A. Hudis, *N Engl J Medicine* **357**, 39 (2007).
[34] F. Morschhauser, *et al.*, *J Clin Oncol* **26**, 5156 (2008).
[35] C. M. Lee, I. F. Tannock, *BMC Cancer* **10**, 255 (2010).
[36] J. H. Baker, *et al.*, *Clin Cancer Res* **14** (2008).
[37] M. Juweid, *et al.*, *Cancer Research* **52**, 5144 (1992).
[38] T. M. Allen, P. R. Cullis, *Adv Drug Deliv Rev* **65**, 36 (2013).
[39] N. Ferrara, K. J. Hillan, W. Novotny, *Biochem Biophys Res Commun* **333**, 328 (2005).

[40] R. K. Jain, D. G. Duda, J. W. Clark, J. S. Loeffler, *Nat Clin Pract Oncol* **3**, 24 (2006).
[41] S. Goel, *et al.*, *Physiol Rev* **91**, 1071 (2011).
[42] T. Roy Chaudhuri, *et al.*, *Molecular Cancer Therapeutics* **15**, 84 (2016).
[43] S. Mo, C. C. Coussios, L. Seymour, R. Carlisle, *Expert Opin Drug Deliv* **9**, 1525 (2012).
[44] P. C. Lyon, *et al.*, *Lancet Oncol* **19**, 1027 (2018).
[45] J. S. Ross, *et al.*, *Oncologist* **14**, 320 (2009).
[46] J. Baselga, *Eur J Cancer* **37, Supplement 4**, 16 (2001).
[47] G. J. Weiner, *Semin Hematol* **47**, 115 (2010).
[48] R. M. Srivastava, *et al.*, *Clin Cancer Res* **19**, 1858 (2013).
[49] Y. Kawaguchi, *et al.*, *Int J Cancer* **120**, 781 (2007).
[50] A. M. Scott, J. D. Wolchok, L. J. Old, *Nat Rev Cancer* **12**, 278 (2012).
[51] D. J. Slamon, *et al.*, *N Engl J Med* **344**, 783 (2001).
[52] M. L. Telli, S. A. Hunt, R. W. Carlson, A. E. Guardino, *J Clin Oncol* **25**, 3525 (2007).
[53] C. S. Karapetis, *et al.*, *N Engl J Med* **359**, 1757 (2008).
[54] J. Galon, *et al.*, *Science* **313**, 1960 (2006).
[55] L. Zhang, *et al.*, *N Engl J Med* **348**, 203 (2003).
[56] D. M. Pardoll, *Nat Rev Cancer* **12**, 252 (2012).
[57] C. J. Nirschl, C. G. Drake, *Clin Cancer Res* **19**, 4917 (2013).
[58] M. A. Postow, M. K. Callahan, J. D. Wolchok, *J Clin Oncol* **33**, 1974 (2015).
[59] C. Robert, *et al.*, *Lancet* **384**, 1109 (2014).
[60] T. Okazaki, T. Honjo, *Int Immunol* **19**, 813 (2007).
[61] F. S. Hodi, *et al.*, *N Engl J Med* **363**, 711 (2010).
[62] S. L. Topalian, *et al.*, *J Clin Oncol* **32**, 1020 (2014).
[63] J. R. Brahmer, *et al.*, *N Engl J Med* **366**, 2455 (2012).
[64] H. L. Kaufman, *et al.*, *Lancet Oncol* **17**, 1374 (2016).
[65] A. Rittmeyer, *et al.*, *Lancet* **389**, 255 (2017).
[66] T. Powles, *et al.*, *JAMA Oncol* **3**, e172411 (2017).
[67] S. L. Topalian, C. G. Drake, D. M. Pardoll, *Curr Opin Immunol* **24**, 207 (2012).
[68] J. Delyon, *et al.*, *Ann Oncol* **24**, 1697 (2013).
[69] P. Sharma, *Cancer J* **22**, 68 (2016).
[70] E. L. Sievers, P. D. Senter, *Annu Rev Med* **64**, 15 (2013).
[71] R. A. de Claro, *et al.*, *Clin Cancer Res* **18**, 5845 (2012).
[72] L. Amiri-Kordestani, *et al.*, *Clin Cancer Res* **20**, 4436 (2014).
[73] A. D. Ricart, *Clin Cancer Res* **17**, 6417 (2011).
[74] I. E. Krop, *et al.*, *J Clin Oncol* **30**, 3234 (2012).
[75] S. A. Hurvitz, *et al.*, *J Clin Oncol* **31**, 1157 (2013).
[76] P. A. Baeuerle, C. Reinhardt, *Cancer Res* **69**, 4941 (2009).
[77] A. Thakur, L. G. Lum, *Curr Opin Mol Ther* **12**, 340 (2010).
[78] L. Zitvogel, A. Tesniere, G. Kroemer, *Nat Rev Immunol* **6**, 715 (2006).
[79] K. Brischwein, *et al.*, *Mol Immunol* **43**, 1129 (2006).
[80] K. Brischwein, *et al.*, *J Immunother* **30**, 798 (2007).
[81] C. Haas, *et al.*, *Immunobiology* **214**, 441 (2009).
[82] T. Dreier, *et al.*, *Int J Cancer* **100**, 690 (2002).
[83] R. Bargou, *et al.*, *Science* **321**, 974 (2008).
[84] M. S. Topp, *et al.*, *J Clin Oncol* **29**, 2493 (2011).
[85] M. S. Topp, *et al.*, *J Clin Oncol* **32**, 4134 (2014).

[86] A. Krishnamurthy, A. Jimeno, *Pharmacol Ther* **185**, 122 (2018).
[87] K. Garber, *Nat Rev Drug Discov* **13**, 799 (2014).
[88] R. Linke, A. Klein, D. Seimetz, *MAbs* **2**, 129 (2014).
[89] T. Dao, *et al.*, *Nat Biotechnol* **33**, 1079 (2015).
[90] M. Aleksic, *et al.*, *Eur J Immunol* **42**, 3174 (2012).
[91] N. Liddy, *et al.*, *Nat Med* **18**, 980 (2012).
[92] E. McCormack, *et al.*, *Cancer Immunol Immunother* **62**, 773 (2013).
[93] G. Bossi, S. Buisson, J. Oates, B. K. Jakobsen, N. J. Hassan, *Cancer Immunol Immunother* **63**, 437 (2014).
[94] J. Oates, N. J. Hassan, B. K. Jakobsen, *Mol Immunol* **67**, 67 (2015).
[95] S. J. Russell, K. W. Peng, *Trends Pharmacol Sci* **28**, 326 (2007).
[96] T. Nakamura, *et al.*, *Nat Biotechnol* **23**, 209 (2005).
[97] C. Springfeld, *et al.*, *Cancer Res* **66**, 7694 (2006).
[98] T. G. Huang, M. J. Savontaus, K. Shinozaki, B. V. Sauter, S. L. Woo, *Gene Ther* **10**, 1241 (2003).
[99] T. Wirth, *et al.*, *Cancer Res* **63**, 3181 (2003).
[100] R. Rodriguez, *et al.*, *Cancer Res* **57**, 2559 (1997).
[101] D. F. Stojdl, *et al.*, *Cancer Cell* **4**, 263 (2003).
[102] R. Cawood, *et al.*, *PLoS Pathog* **5**, e1000440 (2009).
[103] C. Sheridan, *Nat Biotechnol* **33**, 569 (2015).
[104] B. D. Lichty, C. J. Breitbach, D. F. Stojdl, J. C. Bell, *Nat Rev Cancer* **14**, 559 (2014).
[105] R. J. Prestwich, *et al.*, *Hum Gene Ther* **20**, 1119 (2009).
[106] Z. S. Guo, Z. Liu, D. L. Bartlett, *Front Oncol* **4**, 74 (2014).
[107] M. Toda, S. D. Rabkin, H. Kojima, R. L. Martuza, *Hum Gen Ther* **10**, 385 (1999).
[108] N. N. Senzer, *et al.*, *J Clin Oncol* **27**, 5763 (2009).
[109] T. S. Miest, R. Cattaneo, *Nat Rev Microbiol* **12**, 23 (2014).
[110] J. D. Dias, *et al.*, *Clin Cancer Res* **16**, 2540 (2010).
[111] G. R. Simpson, *et al.*, *Br J Cancer* **106**, 496 (2012).
[112] S. Guedan, *et al.*, *Mol Ther* **18**, 1275 (2010).
[113] A. Tedcastle, S. Illingworth, A. Brown, L. W. Seymour, K. D. Fisher, *Mol Ther* **24**, 796 (2016).
[114] H. H. Chen, *et al.*, *Mol Ther* **19**, 67 (2011).
[115] M. Bazan-Peregrino, *et al.*, *Cancer Gene Ther* **20**, 461 (2013).
[116] W. Lu, *et al.*, *World J Gastroenterol* **10**, 3634 (2004).
[117] I. Haralambieva, *et al.*, *Mol Ther* **15**, 588 (2007).
[118] C. L. White, *et al.*, *Gene Ther* **15**, 911 (2008).
[119] G. Fulci, *et al.*, *Proc Natl Acad Sci U S A* **103**, 12873 (2006).
[120] S. J. Russell, K. W. Peng, J. C. Bell, *Nat Biotechnol* **30**, 658 (2012).
[121] R. C. Carlisle, *et al.*, *Blood* **113**, 1909 (2009).
[122] M. C. Sprangers, *et al.*, *J Clin Microbiol* **41**, 5046 (2003).
[123] L. Evgin, *et al.*, *Mol Ther* **23**, 1066 (2015).
[124] A. Danielsson, *et al.*, *Gene Ther* **17**, 752 (2010).
[125] M. A. Thomas, *et al.*, *Molecular Therapy* **16**, 1665 (2008).
[126] D. M. Roberts, *et al.*, *Nature* **441**, 239 (2006).
[127] T. S. Miest, *et al.*, *Mol Ther* **19**, 1813 (2011).
[128] K. Doronin, E. V. Shashkova, S. M. May, S. E. Hofherr, M. A. Barry, *Hum Gene Ther* **20**, 975 (2009).
[129] I. Kuhn, *et al.*, *PLoS One* **3**, e2409 (2008).

[130] Y. Di, L. Seymour, K. Fisher, *Gene Ther* **21**, 440 (2014).
[131] A. Miller, *et al.*, *Mol Ther Oncolytics* **1**, 14005 (2014).
[132] C. C. Heise, A. Williams, J. Olesch, D. H. Kirn, *Cancer Gene Ther* **6**, 499 (1999).
[133] M. Bazan-Peregrino, R. C. Carlisle, L. Purdie, L. W. Seymour, *Gene Ther* **15**, 688 (2008).
[134] R. Carlisle, *et al.*, *J Natl Cancer Inst* **105**, 1701 (2013).
[135] S. Mo, *et al.*, *J Control Release* **210**, 10 (2015).
[136] C. E. Engeland, *et al.*, *Mol Ther* **22**, 1949 (2014).
[137] A. T. Power, J. C. Bell, *Gene Ther* **15**, 772 (2008).
[138] H. T. Ong, K. Hasegawa, A. B. Dietz, S. J. Russell, K. W. Peng, *Gene Ther* **14**, 324 (2007).
[139] J. Qiao, *et al.*, *Gene Ther* **15**, 604 (2008).
[140] E. J. Ilett, *et al.*, *Gene Ther* **16**, 689 (2009).
[141] E. J. Ilett, *et al.*, *Clin Cancer Res* **17**, 2767 (2011).
[142] S. H. Thorne, R. S. Negrin, C. H. Contag, *Science* **311**, 1780 (2006).
[143] J. Garcia-Castro, *et al.*, *Cancer Gene Ther* **12**, 341 (2005).
[144] J. Garcia-Castro, *et al.*, *Cancer Gene Ther* **17**, 476 (2010).
[145] E. K. Mader, *et al.*, *J Transl Med* **11**, 1 (2013).
[146] C. Willmon, *et al.*, *Mol Ther* **17**, 1667 (2009).
[147] N. P. Restifo, M. E. Dudley, S. A. Rosenberg, *Nat Rev Immunol* **12**, 269 (2012).
[148] M. J. Besser, *et al.*, *Clin Cancer Res* **16**, 2646 (2010).
[149] R. A. Morgan, *et al.*, *Mol Ther* **18**, 843 (2010).
[150] L. A. Johnson, *et al.*, *Blood* **114**, 535 (2009).
[151] V. Prasad, *Nat Rev Clin Oncol* **15**, 11 (2018).
[152] W. G. Pitt, G. A. Husseini, B. J. Staples, *Expert Opin Drug Deliv* **1**, 37 (2004).
[153] G. ter Haar, C. Coussios, *Int J Hyperthermia* **23**, 85 (2007).
[154] R. O. Illing, *et al.*, *Br J Cancer* **93**, 890 (2005).
[155] K. Hynynen, N. McDannold, N. A. Sheikov, F. A. Jolesz, N. Vykhodtseva, *Neuroimage* **24**, 12 (2005).
[156] K. E. Hitchcock, *et al.*, *Ultrasound Med Biol* **37**, 1240 (2011).
[157] A. J. Coleman, J. E. Saunders, *Ultrasonics* **31**, 75 (1993).
[158] T. Leighton, *The acoustic bubble* (Academic press, 2012).
[159] C. C. Coussios, C. H. Farny, G. Ter Haar, R. A. Roy, *Int J Hyperthermia* **23**, 105 (2007).
[160] M. Gyongy, M. Arora, J. A. Noble, C. C. Coussios, *2008 IEEE Ultrasonics Symposium*, pp. 871–874.
[161] C. D. Arvanitis, M. S. Livingstone, N. McDannold, *Phys Med Biol* **58**, 4749 (2013).
[162] M. Gyongy, C. Coussios, *IEEE Trans Biomed Eng* **57**, 48 (2010).
[163] C. Coviello, *et al.*, *J Acoust Soc Am* **137**, 2573 (2015).
[164] S. A. Elder, *J Acoust Soc Am* **31**, 54 (1959).
[165] P. Marmottant, S. Hilgenfeldt, *Nature* **423**, 153 (2003).
[166] C. C. Coussios, R. A. Roy, *Annu Rev Fluid Mech* **40**, 395 (2008).
[167] C. D. Arvanitis, M. Bazan-Peregrino, B. Rifai, L. W. Seymour, C. C. Coussios, *Ultrasound Med Biol* **37**, 1838 (2011).
[168] D. R. Morel, *et al.*, *Invest Radiol* **35**, 80 (2000).
[169] G. Dimcevski, *et al.*, *J Control Release* **243**, 172 (2016).
[170] J. J. Kwan, *et al.*, *Small* **11**, 5305 (2015).
[171] J. J. Kwan, *et al.*, *Phys Rev E Stat Nonlin Soft Matter Phys* **92**, 023019 (2015).
[172] C. Mannaris, *et al.*, *Adv Healthc Mater* **7**, e1800184 (2018).

[173] R. Myers, *et al.*, *Mol Ther* **24**, 1627 (2016).
[174] J. Y. Lee, *et al.*, *Adv Mater* **27**, 5484 (2015).
[175] H. A. Hancock, *et al.*, *Ultrasound Med Biol* **35**, 1722 (2009).
[176] S. Wang, *et al.*, *J Control Release* **162**, 218 (2012).
[177] M. Bazan-Peregrino, C. D. Arvanitis, B. Rifai, L. W. Seymour, C. C. Coussios, *J Control Release* **157**, 235 (2012).
[178] M. Bazan-Peregrino, *et al.*, *J Control Release* **169**, 40 (2013).
[179] R. Myers, *et al.*, *Int J Nanomedicine* **13**, 337 (2018).
[180] M. Kinoshita, N. McDannold, F. A. Jolesz, K. Hynynen, *Proc Natl Acad Sci U S A* **103**, 11719 (2006).
[181] M. Kinoshita, N. McDannold, F. A. Jolesz, K. Hynynen, *Biochem Biophys Res Commun* **340**, 1085 (2006).
[182] C. D. Arvanitis, *et al.*, *Proc Natl Acad Sci U S A* **115**, E8717 (2018).
[183] G. M. Hale, M. R. Querry, *Applied Optics* **12**, 555 (1973).
[184] D. Bates, M. Machler, B. Bolker, S. Walker, *arXiv preprint arXiv:1406.5823* (2014).
[185] A. Kuznetsova, P. B. Brockhoff, R. H. B. Christensen, *J Stat Softw* **82** (2017).
[186] T. Yokoyama, *et al.*, *PLoS One* **6**, e25507 (2011).
[187] H. W. Kao, *et al.*, *Nanotechnology* **25**, 295102 (2014).
[188] Y. Qian, *et al.*, *Sci Rep* **4**, 7490 (2014).
[189] L. Garcia-Fernandez, *et al.*, *Nanoscale* **9**, 6111 (2017).
[190] N. Chattopadhyay, *et al.*, *Mol Pharm* **7**, 2194 (2010).
[191] S. H. Tseng, M. Y. Chou, I. M. Chu, *Int J Nanomedicine* **10**, 3663 (2015).
[192] K. Sokolov, *et al.*, *Cancer Res* **63**, 1999 (2003).
[193] H. Lea-Banks, B. Teo, E. Stride, C. C. Coussios, *Phys Med Biol* **61**, 7906 (2016).
[194] W. Eck, *et al.*, *ACS nano* **2**, 2263 (2008).
[195] S. Kumar, J. Aaron, K. Sokolov, *Nat Protoc* **3**, 314 (2008).
[196] F. Higel, A. Seidl, F. Sorgel, W. Friess, *Eur J Pharm Biopharm* **100**, 94 (2016).
[197] D. K. Kolmel, E. T. Kool, *Chem Rev* (2017).
[198] J. Kalia, R. T. Raines, *Angew Chem Int Ed Engl* **47**, 7523 (2008).
[199] Z. Li, R. Jin, C. A. Mirkin, R. L. Letsinger, *Nucleic Acids Res* **30**, 1558 (2002).
[200] B. Garcia, *et al.*, *Chem Commun (Camb)* pp. 369–71 (2005).
[201] G. Zhang, *et al.*, *Biomaterials* **30**, 1928 (2009).
[202] S. Zalipsky, *Bioconjug Chem* **4**, 296 (1993).
[203] Z. J. Kaminski, *et al.*, *J Am Chem Soc* **127**, 16912 (2005).
[204] V. Schepkin, T. Kawabata, H. J. Tritschler, L. Packer, *Free Radic Res* **25**, 195 (1996).
[205] S. Zalipsky, S. Menon-Rudolph, *Poly(ethylene glycol)* **680**, 318 (1997).
[206] J. Qian, *et al.*, *Anal Biochem* **364**, 8 (2007).
[207] D. Ayoub, *et al.*, *MAbs* **5**, 699 (2013).
[208] R. Gahoual, *et al.*, *MAbs* **5**, 479 (2013).
[209] W. Wang, *et al.*, *Mol Immunol* **48**, 860 (2011).
[210] Q. Zhou, *et al.*, *Bioconjug Chem* **25**, 510 (2014).
[211] C. A. Wolfe, D. S. Hage, *Anal Biochem* **231**, 123 (1995).
[212] H. W. Morehead, K. W. Talmadge, D. J. O'Shannessy, C. J. Siebert, *J Chromatogr* **587**, 171 (1991).
[213] R. Abraham, *et al.*, *J Immunol Methods* **144**, 77 (1991).
[214] A. Dirksen, S. Dirksen, T. M. Hackeng, P. E. Dawson, *J Am Chem Soc* **128**, 15602 (2006).
[215] P. Crisalli, E. T. Kool, *J Org Chem* **78**, 1184 (2013).

[216] C. Zheng, G. Ma, Z. Su, *Electrophoresis* **28**, 2801 (2007).
[217] B. Friguet, A. F. Chaffotte, L. Djavadi-Ohaniance, M. E. Goldberg, *J Immunol Methods* **77**, 305 (1985).
[218] I. Suarez, A. Salmeron-Garcia, J. Cabeza, L. F. Capitan-Vallvey, N. Navas, *J Chromatogr B Analyt Technol Biomed Life Sci* **1032**, 155 (2016).
[219] B. Skoog, *Vox sanguinis* **37**, 345 (1979).
[220] M. M. Kurfurst, *Anal Biochem* **200**, 244 (1992).
[221] A. Martinez-Ortega, *et al.*, *Journal of Pharmaceutical Analysis* **6**, 117 (2016).
[222] B. Bobaly, M. Lauber, A. Beck, D. Guillarme, S. Fekete, *J Chromatogr A* **1549**, 63 (2018).
[223] E. J. Park, D. H. Na, *Anal Chem* **88**, 10848 (2016).
[224] S. Fekete, A. Beck, E. Wagner, K. Vuignier, D. Guillarme, *J Sep Sci* **38**, 1 (2015).
[225] R. G. Nuzzo, B. R. Zegarski, L. H. Dubois, *J Am Chem Soc* **109**, 733 (1987).
[226] W. Haiss, N. T. Thanh, J. Aveyard, D. G. Fernig, *Anal Chem* **79**, 4215 (2007).
[227] B. N. Khlebtsov, N. G. Khlebtsov, *Colloid Journal* **73**, 118 (2011).
[228] T. Zheng, S. Bott, Q. Huo, *ACS Appl Mater Interfaces* **8**, 21585 (2016).
[229] F. R. Luo, *et al.*, *Cancer Chemother Pharmacol* **56**, 455 (2005).
[230] M. C. Prewett, *et al.*, *Clin Cancer Res* **8**, 994 (2002).
[231] G. Sonavane, K. Tomoda, K. Makino, *Colloids Surf B Biointerfaces* **66**, 274 (2008).
[232] W. S. Cho, *et al.*, *Toxicol Appl Pharmacol* **236**, 16 (2009).
[233] L. Yang, *et al.*, *Sci Rep* **7**, 3303 (2017).
[234] J.-M. Gorce, M. Arditi, M. Schneider, *Invest Radiol* **35**, 661 (2000).
[235] D. Elbes, C. Paverd, R. Cleveland, C. Coussios, *J Acoust Soc Am* **141**, 3550 (2017).
[236] B. Winter, *arXiv preprint arXiv:1308.5499* (2013).
[237] S. G. Luke, *Behav Res Methods* **49**, 1494 (2017).
[238] S. E. Lazic, *BMC Physiol* **8**, 16 (2008).
[239] A.-L. Fabricius, L. Duester, B. Meermann, T. A. Ternes, *Anal Bioanal Chem* **406**, 467 (2014).
[240] A. I. Bush, *et al.*, *PLoS ONE* **3**, e2175 (2008).
[241] T. C. Liu, E. Galanis, D. Kirn, *Nat Clin Pract Oncol* **4**, 101 (2007).
[242] R. Garcia-Carbonero, *et al.*, *J Immunother Cancer* **5**, 71 (2017).
[243] M. O. Culjat, D. Goldenberg, P. Tewari, R. S. Singh, *Ultrasound Med Biol* **36**, 861 (2010).
[244] M. Maaloum, N. Pernodet, B. Tinland, *Electrophoresis* **19**, 1606 (2005).
[245] J. Narayanan, J.-Y. Xiong, X.-Y. Liu, *J Phys Conf Ser* **28**, 83 (2006).
[246] J. W. Osborne, *Practical Assessment, Research & Evaluation* **15**, 2 (2010).
[247] S. Illingworth, *et al.*, *Mol Ther Oncolytics* **5**, 62 (2017).
[248] B. Lichty, *et al.*, *PLoS ONE* **8**, e73759 (2013).
[249] N. Marino, *et al.*, *PLoS One* **12**, e0177810 (2017).
[250] E. Calvo, *et al.*, *Ann Oncol* **25**, iv367 (2014).
[251] V. Boni, *et al.*, *Ann Oncol* **25**, iv368 (2014).
[252] T. J. Norman, *et al.*, *J Phys Chem B* **106**, 7005 (2002).
[253] V. Saini, *et al.*, *Small* **4**, 262 (2008).
[254] A. Dejaegere, L. Choulier, V. Lafont, E. De Genst, D. Altschuh, *Biochemistry* **44**, 14409 (2005).
[255] R. Reverberi, L. Reverberi, *Blood Transfus* **5**, 227 (2007).
[256] F. Blanche, *et al.*, *Gene Ther* **7**, 1055 (2000).
[257] K. D. Fisher, L. W. Seymour, *Adv Drug Deliv Rev* **62**, 240 (2010).
[258] P. H. Kim, *et al.*, *Biomaterials* **32**, 2314 (2011).

[259] J. R. McCombs, S. C. Owen, *AAPS J* **17**, 339 (2015).
[260] T. Manouras, M. Vamvakaki, *Polym Chem* **8**, 74 (2017).
[261] T. D. Tailor, *et al.*, *Mol Cancer Ther* (2010).